UNIVERSITÀ
DEGLI STUDI
DI PADOVA

Sede Amministrativa: Università degli Studi di Padova

Dipartimento di Astronomia

Scuola di dottorato di ricerca in: Astronomia
Indirizzo: Extra-Galattico
Ciclo XXIII

GAS ORIGIN IN THE EXTENDED NARROW LINE REGION OF NEARBY SEYFERT GALAXIES

Direttore della scuola: Ch.mo Prof. Giampaolo Piotto
Supervisore: Ch.mo Prof. Piero Rafanelli
Dott. Stefano Ciroi

Dottorando: Valentina Cracco

Dipartimento di Astronomia

Facoltà di Scienze Matematiche Fisiche Naturali

Università di Padova

789° Anno Accademico

GAS ORIGIN IN THE EXTENDED NARROW LINE REGION OF NEARBY SEYFERT GALAXIES

Thesis submitted by

Valentina Cracco

as a requirement for the degree of

Philosophy Doctor in Astronomy Science

MCCXXII

Thesis supervisors:

- Prof. Piero Rafanelli
  Dipartimento di Astronomia, Università di Padova, Italy, EU
- Dr. Stefano Ciroi
  Dipartimento di Astronomia, Università di Padova, Italy, EU

Riassunto

La Extended Narrow Line Region (ENLR) dei Nuclei Galattici Attivi (AGN) è una regione di gas ad alta ionizzazione, di forma conica o biconica con dimensioni fino a 15-20 kpc e gli apici in direzione del nucleo attivo. Questa struttura, detta anche coni di ionizzazione, è una prova della validità del Modello Unificato (Antonucci 1993), che predice che il flusso della radiazione ionizzante emessa dal nucleo sia collimato dal toro di polveri. La struttura della ENLR è complicata e sono numerose le questioni irrisolte, per esempio non è chiara l'origine del gas ionizzato presente in queste regioni. Il gas potrebbe essere parte del mezzo interstellare della galassia ospite, ed essere semplicemente ionizzato dal nucleo attivo, oppure potrebbe essere mezzo intergalattico acquisito dall'esterno in seguito a interazioni gravitazionali. Finora sono state scoperte solo 25 Seyfert 2 con coni di ionizzazione. Questo basso numero di oggetti potrebbe essere dovuto a un effetto di selezione, oppure all'assenza di gas distribuito su larga scala nella galassia ospite, ma potrebbe anche indicare che servono particolari condizioni per formare la ENLR. In questo lavoro abbiamo studiato l'orgine del gas utilizzando dati spettroscopici integral field (IFU), longslit e echelle. A causa del piccolo campo di vista dei dati IFU c'è bisogno di un confronto con immagini broad band dell'intera galassia, per poter meglio interpretare l'informazione ottenuta dal dato spettroscopico. Abbiamo ridotto e analizzati i dati, che sono stati ottenuti nell'ambito della nostra campagna osservativa di galassie di Seyfert vicine. I dati IFU sono stati acquisiti con lo spettrografo MPFS al telescopio di 6-mt del SAO, i dati longslit con AFOSC al telescopio di 1.8-mt dell'Osservatorio Astrofisco di Asiago e i dati echelle con MagE al telescopio Magellan di 6.5-mt. Le immagini sono state in parte ottenute con SCORPIO al telescopio di 6-mt del SAO e in parte dall'archivio ING. Il lavoro è basato sul seguente metodo: (i) analisi delle proprietà fisiche del gas (densità, temperatura e metallicità), (ii) analisi dei rapporti di righe, (iii) studio della cinematica del gas e delle stelle, (iv) analisi morfologica. Abbiamo applicato questo metodo a due galassie che mostrano emissione di [O III] estesa, NGC 7212 una Seyfert 2 e MRK 6 una Seyfert 1.5. Abbiamo ottenuto valide prove di un origine esterna del gas ionizzato per entrambi gli oggetti. L'origine esterna è attesa nel caso di NGC 7212 che è una galassia in un sistema fortemente interagente, comunque abbiamo trovato anche in MRK 6 indizi di un possibile merger. Abbiamo poi sfruttato il vantaggio offerto dai dati IFU che permettono di campionare spazialmente la ENLR in regioni da $1'' \times 1''$ e abbiamo poi selezionato 12 Seyfert 2 per effettuare uno studio statistico delle proprietà spettroscopiche di un elevato numero di queste regioni. Dall'analisi di 848 sub-regioni abbiamo notato che la maggior parte mostra proprietà simili a quelle della NLR. Tutti questi risultati suggeriscono che siano necessarie particolari condizioni iniziali per formare delle NLR con dimensioni dell'ordine di alcuni kpc.

Abstract

The Extended Narrow Line Region (ENLR) of Active Galactic Nuclei (AGN) is a conical or bi-conical region of highly ionized gas with a size of few up to 15–20 kpc and the apexes pointing towards the active nucleus. This region is also called ionization cones. These cones are an evidence of the Unified Model (Antonucci 1993) that predicts an anisotropic escape of ionizing photons from the nucleus confined in a conical flow by a dusty torus. Many details about the complex structure of the ENLR still remains unveiled. For example it is not clear which is the origin of the ionized gas. This is an important issue, being related to the fuelling of the active nucleus. The gas could be simply part of the interstellar medium of the host galaxy, ionized by the active nucleus or by shocks; or it could be intergalactic medium acquired by the surroundings of the host galaxy through gravitational interactions. Up to now only 25 Seyfert 2 galaxies with ionization cones are known and studied. The lack of cones in Seyfert 2 galaxies could be a selection effect, or it could be due to the absence of gas distributed over large scales in the host galaxy, but it can also indicate that some particular initial conditions are needed in order to form an ENLR. In this work we tackle the question of the origin of the gas, by combining the information obtained from IFU, longslit and echelle spectra. Being the IFU field of view typically small, in order to correctly interpret the spectroscopic results we analyse also broad band images. We reduced and analyzed the collected data from our observational campaign of nearby Seyfert galaxies. IFU spectra were taken with MPFS at SAO 6-mt telescope, longslit spectra with AFOSC at the 1.8-mt telescope of Asiago Astrophysical Observatory and the echelle spectra with MagE at 6.5-mt Magellan telescope. The broad band images were taken with SCORPIO at SAO 6-mt telescope and from the ING archive. This work is based on: (i) analysis of gas physical properties (density, temperature and metallicity), (ii) analysis of emission lines ratios, (iii) study of gas and stars kinematics, (iv) morphological analysis. We applied this method to two Seyfert galaxies showing extended [O III] emission, NGC 7212, a Seyfert 2 galaxy and MRK 6 a Seyfert 1.5 galaxy. We obtained strong proof of an external origin for the ionized gas in both cases. This is more likely to occur in NGC 7212 because it is in a strongly interacting system, however also in MRK 6 we found hints of a past merger. We took advantage of integral field data which allow to spatially sample the ENLR in $1'' \times 1''$ emission line sub-regions and we selected 12 Seyfert 2 galaxies to perform a statistical study of spectroscopic properties of a large number of these regions. From the analysis of about 850 sub-regions we pointed out that most of them share the properties generally observed in the NLR of Seyfert galaxies. All these results strongly suggest that particular initial conditions are mandatory in order to generate a kpc-size NLR.

Contents

1

Introduction

In this chapter we introduce the scientific rationale and scientific aims of this PhD thesis. The main topic of this work concerns a spectroscopic study of the Extended Narrow Line Region (ENLR) of Seyfert galaxies. This is an elongated region of highly ionized gas extended up to 15-20 kpc from the active nucleus. The first Section is an overview about Active Galactic Nuclei and Seyfert galaxies, the second Section concerns the properties of the ENLR, and finally the third Section describes the aims and methods of this work.

1.1 Active Galactic Nuclei

The Active Galactic Nuclei (AGN hereafter) are among the most powerful energy sources in the universe. They are compact regions in the nuclei of galaxies, characterized by very high luminosity over all the electromagnetic spectrum: their emission of radiation involves radio, infrared, optical, ultraviolet, X-ray and Gamma-ray bands. These energetic phenomena cannot be attributed to the stars, on the contrary, it is thought to be a result of accretion onto a supermassive black hole located in the centre of the host galaxy. This class includes both bright quasars, with luminosity exceeding 10^{47} erg s^{-1}, as well as faint LINERs (low-ionization nuclear emission line regions) emitting no more than 10^{41} erg s^{-1}. It is generally accepted that an object belongs to the AGN family when it shows at least one of the following characteristic: strong energy emission (between $10^{41} - 10^{47}$ erg s^{-1}); a luminous compact nuclear region; a non-stellar continuum emission; nuclear emission lines, indicating ionization by non-stellar continuum; variability of emission lines and continuum (Netzer 1990).

A classification scheme is shown in Figure 1.1. The principal subdivision is based on the F_{5GHz}/F_B flux ratio: when the ratio is $\gtrsim 10$, AGN are called radio-loud, otherwise they are radio-quiet (Urry & Padovani 1995). Within the radio-quiet group we can distinguish between Seyfert 1 and QSO on one side and Seyfert 2 and LINER on the other. Seyfert 1 galaxies have relatively low luminosity and therefore are seen only nearby, where the host galaxy can be resolved, instead QSO have higher luminosity and are seen at greater distances, rarely showing an obvious galaxy surrounding the bright central source (Urry & Padovani 1995). Both of them exhibit a strong non-stellar continuum, emitting from far-infrared (FIR)

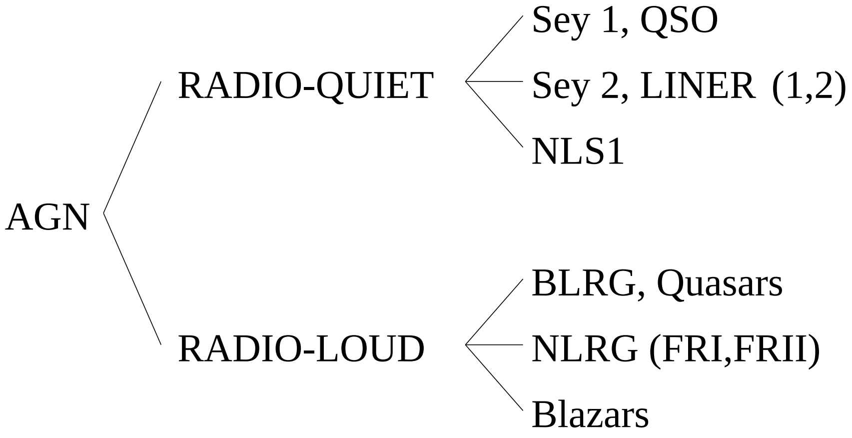

FIGURE 1.1— The scheme of the AGN classification.

to X-rays, low polarization and variability, and strong emission lines (Lawrence 1987). The permitted lines are broad, with FWHM $\sim 10^4$ km s^{-1}, while the forbidden lines are narrow (FWHM $\lesssim 10^3$ km s^{-1}) (Antonucci 1993). Seyfert 2 galaxies have nuclei with no or weak continuum, but strong emission lines, all of which are narrow, and no variability (Lawrence 1987). LINER represents the least luminous AGN ($\lesssim 10^{41}$ erg s^{-1}). Their strongest emission lines are of low ionization species and are somewhat narrower (200 – 400 km s^{-1}) than the narrow lines of Seyfert galaxies (Netzer 1990). A peculiar case are the Narrow-Line Seyfert 1 galaxies (NLS1), generally characterized by steeper 0.1-2.4 keV (soft X-rays) continuum slopes than normal Seyfert 1, emission lines from Fe II or higher ionization iron lines as [Fe VII] λ6087 or [Fe X] λ6375 often seen in Seyfert 1, and generally not in Seyfert 2, [O III]/H$\beta < 3$, but the permitted lines only slightly broader than the forbidden ones (Boller et al. 1996). The radio-loud AGN are commonly hosted in elliptical galaxies. They can be organized into a similar classification as done for radio-quiet AGN. The counterparts of Seyfert 1 and QSO are the Broad Line Radio Galaxies (BLRG) at low luminosities and radio quasars at high luminosities. Radio loud type 2 AGN are called Narrow Line Radio Galaxies (NLRG), which include two different morphological types: the Fanaroff -Riley type I and II radio galaxies (FR I and FR II) (Urry & Padovani 1995). The FR I are the lower luminosity lobe dominated radio sources: they exhibit very extended twin lobe structures, the ends of which show the steepest radio spectra and appear faint in radio maps. Their lobes are connected to the central optical galaxy by smooth and continuous double-sided jets. The FR II are the more powerful radio lobe dominated sources: their lobes differ significantly from these of the FR I in that the steepest spectrum radio emission is found at the inner regions. The ends of the lobes are frequently edge-brightened and shows hot spots at their outer extremities. Unlike the FR I, the jets, more collimated and dominated by bright knots, appear usually single-sided, or, when double, one side is many times brighter than the other (Robson 1996). Another class of radio-loud objects exist, generally called blazars and characterized by dramatically fast variability, high polarization, strong continuum and superluminal motions. Among blazars we can distinguish between sources with broad and strong emission lines, like the Optically Violently Variable quasars (OVV), High Polarized Quasars (HPQ) and Flat Spectrum Radio Quasars (FSRQ), and those with very weak or absent emission lines, like BL Lacertae (BL Lac).

At the present, the approximate structure of an AGN is known. The prevailing picture (Figure 1.2),

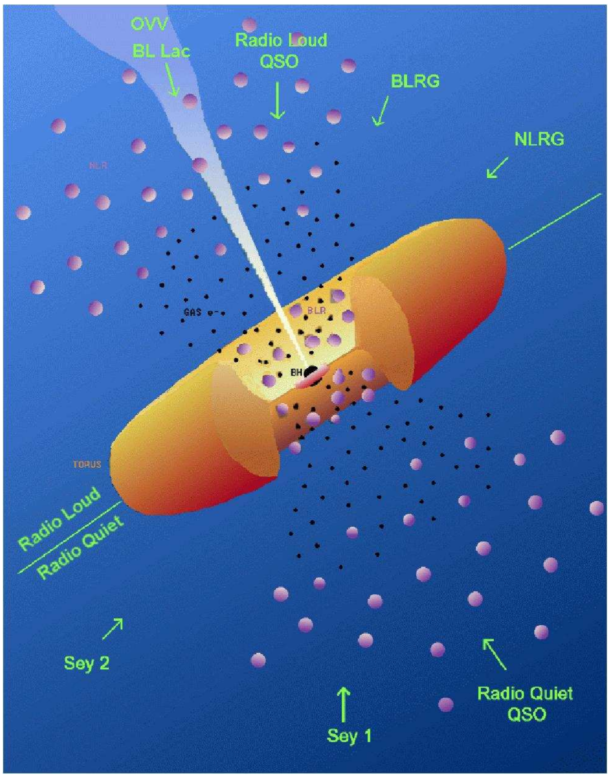

FIGURE 1.2— Structure of an AGN, according to the Unified Model (Antonucci & Miller 1985; Antonucci 1993).

named the Unified Model (Antonucci & Miller 1985; Antonucci 1993), provides for a central supermassive black hole (SMBH), whose gravitational potential energy is the ultimate source of the AGN luminosity: matter falling into the SMBH loses angular momentum through viscous and turbulent processes in an accretion disk, resulting into emission of photons at ultraviolet (UV), soft-X and hard-X ray wavelengths. Strong optical and ultraviolet emission lines are produced in clouds of gas rapidly moving in the potential of the SMBH, the Broad Line Region (BLR). Along some line of sight the optical and ultraviolet radiation is obscured by a torus or a warped disk of gas and dust, with a radius larger than the accretion disk and containing the BLR. Narrow emission lines are produced in slower moving clouds of gas, beyond the torus, the Narrow Line Region (NLR). Along the poles of the disk outflows of energetic particles form collimated radio-emitting jets and sometimes giant radio sources when the host galaxy is an elliptical, but only very weak radio sources when the host is a spiral. The plasma in the jets streams outward at very high velocities, beaming radiation relativistically in the forward direction. This axisimmetric model of AGN implies a different aspect at different angles: in practice, the observed apparently disparate classes of AGN can be unified considering them to have a fundamentally identical structure seen at different orientation (Antonucci 1993; Urry & Padovani 1995). Seyfert galaxies are the nearest and hence the most throughly studied type of AGN. They are separated from QSO according to the definition by Schmidt & Green (1983), which fixes the borderline at absolute magnitude $M_B = -23$. The main spectral classification into Seyfert 1 and 2 was later improved by introducing the intermediate

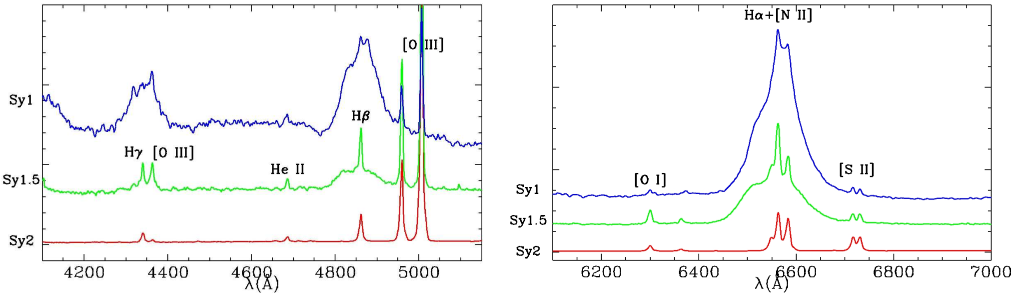

Figure 1.3— Left: three examples of spectra in Hγ and Hβ region for a Seyfert 1 (blue line), an intermediate type Seyfert (green line) and for a Seyfert 2 (red line) galaxy. Right: three examples of spectra in Hα+[N II] region for a Seyfert 1 (blue line), an intermediate type Seyfert (green line) and for a Seyfert 2 (red line) galaxy.

types 1.5, 1.8 and 1.9 which show composite profiles (broad+narrow) in their permitted emission lines with a progressively decreasing intensity in the broad component (Figure 1.3). The narrow lines must be emitted in a region, the already mentioned NLR, in which the density is low enough that forbidden lines are not collisionally de-excited and the range of internal velocity is small. Typical values for the NLR are T $\sim 10^4$K and $N_e \sim 10^4$ cm^{-3}. The mean size and mass are r $\sim 10^2$pc and M $\sim 10^6$ M$_\odot$; they are derived from measurements of Hβ luminosity. The broad lines are emitted in a region of high electron density, the BLR, in which all the forbidden lines are so weakened by collisional de-excitation as to be unobservable and the gas has a large range of internal velocity. Typical values for the BLR are T $\sim 10^4$ K and $N_e \sim 10^{10} - 10^{12}$ cm^{-3}. The mass of the BLR and its size, the latter estimated through studies of variability in Seyfert 1 galaxies, are M $\sim 10^3$M$_\odot$ and r $\sim 3 \times 10^{-2}$ pc (Frank et al. 1985; Osterbrock 1989). A very important advance in the unification of the different types of Seyfert galaxies was the discovery by Antonucci & Miller (1985) that in plane-polarized radiation the Seyfert 2 NGC 1068 has the spectrum of a Seyfert 1 object, with broad Hβ and Fe II emission. It was the first case of a hidden BLR, whose radiation is obscured to our line of sight, but can escape in other directions and is scattered toward us by free electrons above and below the obscuration. In NGC 1068 the position angle of the plane of polarization is perpendicular to the observed position angle of the radio jets, indicating that photons escape along the axis of the jets.

1.2 The Extended Narrow Line Region

Contrary to the BLR, which is confined within a parsec far from the SMBH, and it is therefore not resolved even by space observations of very nearby AGN, the NLR which has a typical extension larger than 100 pc up to 10 kpc offers the great advantage to be observed with ground-based telescopes in nearby galaxies. In fact, during the last twenty years several imaging surveys have been carried out through broad-band UBVR and narrow band interference filters at [O III] λ5007 and Hα, which have disclosed blue elongated structures with a conical or even bi-conical shape in a handful of Seyfert 2 galaxies (see e.g. Pogge 1989; Mulchaey, Wilson & Tsvetanov 1996; Schmitt et al. 2003) (Figure 1.4). The appearence of one-sided cones is easily understood geometrically. Given the large amounts of obscuring material that might be present in the host galaxy mid-planes, only the sides of the cones emerging more or less toward us from the near side of the host galaxies should be visible (Pogge 1989).

These structures, later named Ionization Cones, are a fundamental proof of the validity of the Unified Model, which predicts an anisotropic escaping of photons from the AGN confined in a conical flow by the optically thick dusty torus. Until now, twenty-five active nuclei (see Table 1.1), at redshift lower than 0.04, have been discovered to show a bright extended NLR. Fifteen out of twenty-five are Seyfert 2, two are Seyfert 1.9 and eight are Seyfert 1.5. Summarizing the morphological properties of ionization cones, we point out that both bi-cones and single (one-sided) cones are found, with opening angles, projected on the sky, ranging between $\sim 40^\circ$ and $\sim 100^\circ$. In the case of one-sided cones, the observed cone projects against the far side of the galaxy disk, suggesting that a counter-cone may be present but hidden by obscuration in the disk. It may thus be that all cases are intrinsically bi-conical. When a bi-cone is seen, the two cones share the same axis. The linear extents of the known cones lie between ~ 70 pc and ~ 20 kpc. The emission line gas in the NLR has a large linewidth (FWHM of a few hundred km s^{-1}) and high intensity; more distant from the nucleus, in the Extended Narrow Line Region, the [O III] emission has typically a lower intensity, a narrower line profile and a smaller velocity gradient. Indeed, the ENLR can be separated from the NLR on the basis of both its kinematics and spatial extent. The other important characteristic of the ENLR is the high excitation, with a spectrum similar to that of a Seyfert 2 nucleus, which distinguishes it from the regions associated with extranuclear starbursts (Wilson 1988). Unger et al. (1987) found that the ENLR emission is highly elongated with extremely narrow lines. The orderly, slowly-varying velocity field suggests that the gas is undergoing normal galactic rotation. The similarity of the emission-line spectra of the nebulosities to those of Seyfert 2 nuclei strongly suggests that the gas is photoionized by collimated source of ionizing radiation, supporting the Unified Model (e.g. Antonucci 1993). Ionization cones with sharp, straight edges (e.g. NGC 5252, Tadhunter and Tsvetanov 1989; NGC 5728 Wilson 1996) are hard to understand if matter-bounded and are almost certainly radiation-bounded. The properties of the linear sources and the ionization cones provide valuable constraints on the nuclear disks or tori which are presumably responsible for their collimation. The relationship between these structures and the disk of the parent galaxy is also relevant to the origin of the nuclear disks. Other arguments, such as those based on the energy balance of the emission-line gas (e.g. Wilson et al. 1988; Kinney et al. 1991) often favor an anisotropic source of nuclear radiation. A different interpretation, in situ ionization of the extended gas by local ionizing shocks (e.g. Sutherland et al. 1993), is possible in individual cases, but it is unclear how sharp-edged, triangular morphologies can be accounted for. Most ionization cones are associated with type 2 Seyfert galaxies. In the simplest picture, ionization cones are not expected in type 1 Seyfert galaxies: assuming the cones result from shadowing by the same dusty torus that blocks our view of the nucleus in Seyfert 2's, type 1 Seyfert galaxies would correspond to cases in which our line of sight lies within the cones. If the illuminated gas fills the cone (ionization-bounded case), we then expect to observe "halo" morphologies for the extended narrow line regions in Seyfert 1's. However there is evidence for ionization cones in a few Seyfert 1.5–the best case is NGC 4151 (Evans et al. 1993), with NGC 4253 (Mulchaey et al. 1996) and MRK 6 (Meaburn et al. 1989) being possible examples. There are a number of possible explanations for the presence of cones in type 1 Seyfert galaxies. The blocking torus could have a lower density atmosphere and our line of sight passes through this atmosphere (Evans et al. 1993). The atmosphere is envisaged to have a column density of 10^{20}–10^{21} cm^{-2}, which is sufficient to be optically thick at all wavelengths between the Lyman edge and soft X-rays. The atmosphere can thus collimate the ionizing radiation, with our line of sight lying outside the resulting cones. For normal gas-to-dust ratios, extinction will not have much impact until gas

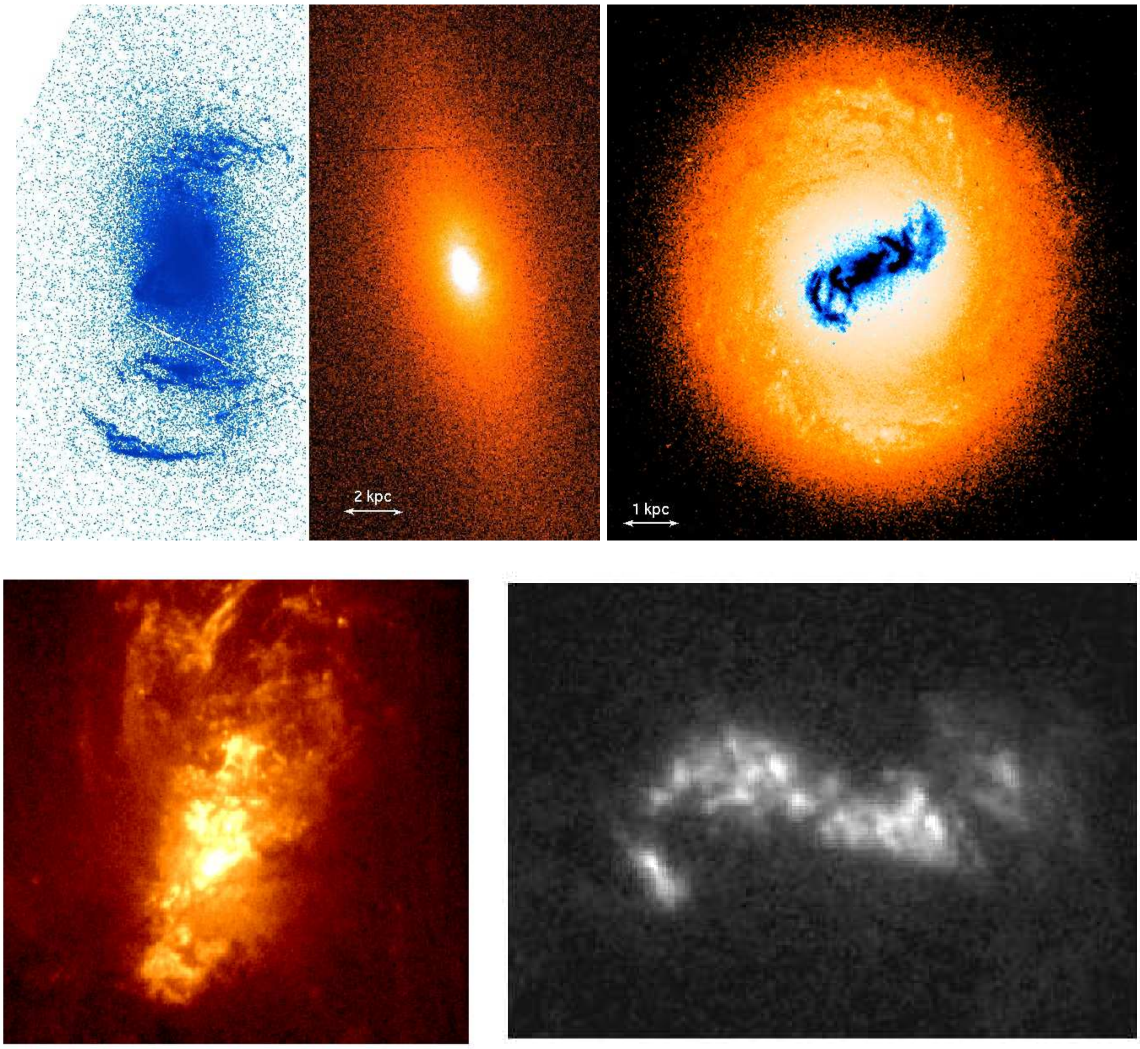

Figure 1.4— Four examples of Extended Narrow Line Region in Seyfert 2 galaxies observed with HST. From up-left: NGC 5252 ([O III], left; continuum, right), MRK 573 (continuum in orange and [O III] in blue), NGC 1068 (UV+[O III]) and MRK 3 ([O III]).

column densities exceed several times 10^{21} cm^{-2}. Consequently, lines of sight falling within the cones defined by the shadow of the opaque torus, but exterior to the ionization cones, will have a relatively clear view of the central regions; in particular the broad line region will still be visible. The gas being illuminated by the ionization cones could be in a disk-shaped configuration. The triangular morphology of the ionized gas results from the intersection of the ionization cone with the gas disk. In this case, “ionization triangles” are expected even when our line of sight lies within the cone of escaping ionizing radiation (i.e. in Seyfert 1 galaxies). Robinson et al. (1994) explain the 25″ long emission-line string seen in ground-based observations of NGC 4151 in terms of such a model, in which the ionization cone grazes the gas disk. The radiation could not be collimated by a dusty torus but by a disk-like broad-line region or a hole in the broad-line region (see Kriss et al. 1992 and Evans et al. 1993). Alternatively, the UV source itself could be intrinsically anisotropic radiator (Madau, 1988). Projection effects can affect the observed emission-line morphologies. For spherical gas distributions, emission-line cones are only seen when our line of sight lies outside the ionization cone. The apparent opening angle of cones with axis close to the plane of the sky is close to the true opening angle of the ionizing radiation. However, for a fixed opening angle of the ionizing radiation, the apparent opening angle of the emission-line structure increases as the angle between the cone axis and the line of sight decreases. This result implies that direct measurement of cone angles will tend to overestimate the true opening angle when the gas is more or less spherically distributed. When the gas lies in a thin disk, the ionizing radiation does not always intersect the disk. For geometries in which the cones and disk do overlap and the gas disk is not viewed edge-on, “bi-triangular” morpohologies are seen, whether our line of sight lies inside or outside of the cone. When the axis of the cone does not lie in the plane of the disk, the observed opening angles are usually smaller than the true opening angle of the cone. This is the opposite of the trend noted for spherical distributions. Projection effects can thus significantly affect the morphology of the observed cones and can differ for different gas distributions. Various works have indicated that the emission from the NLR of Seyfert galaxies is generally aligned with the radio axes (e.g. Unger et al. 1987). The NLR gas is found to be associated with the linear radio sources on the tens of pc to kpc scale (e.g. Haniff et al. 1988; Whittle et al. 1988; Wilson & Tsvetanov 1994). The walls of the torus might be responsible for collimation of radio ejecta in some objects. An alternative mechanism to explain the ionization cones suggests that the radio ejecta plasma acts to scour clear a channel from the central continuum source toward the outer regions of the nucleus, through which radiation may preferentially escape along a conical path. Probably the radiation field is first locally collimated by an obscuring torus, with the radio ejecta clearing away material in front of the collimated radiation, thus acting to further enhance the collimating effect. In the absence of a channel scoured clean by a radio-jet it is hard to imagine that ionizing radiation could make its way through the interstellar matter (ISM) surrounding the nucleus and still be able to strongly ionize clouds many kpc from the nucleus (Pogge 1989). The close connection between the radio ejecta of Seyfert nuclei and their narrow-line regions (NLRs) initially became apparent from their similar spatial extents and from strong correlations between radio luminosities and [O III] λ5007 luminosity and line width (de Bruyn & Wilson 1978; Wilson & Willis 1980; Whittle 1985, 1992). Spectroscopic studies of the NLR (Baldwin, Wilson, & Whittle 1987; Whittle et al. 1988) have revealed that the kinematics of the gas are often clearly affected by the radio jets. Such interactions could play a role in determining the structure of the NLR within the region ionized by the nucleus. In a handful of cases, HST has shown a clear spatial correspondence between the radio and emission-line distributions (e.g. NGC 5929, Bower

Object name	RA (J2000.0)	Dec (J2000.0)	z (NED)	Seyfert type
MRK 348	00:48:47.1	+31:57:25	0.015034	Sy2
MRK 573	01:43:57.8	+02:21:00	0.017179	Sy2
NGC 1068	02:42:40.7	-00:00:48	0.003793	Sy2
ESO 362-G8	05:11:09.1	-34:23:36	0.015748	Sy2
ESO 362-G18	05:19:35.8	-32:39:28	0.012445	Sy1.5
NGC 2110	05:52:11.4	-07:27:22	0.007789	Sy2
MRK 3	06:15:36.3	+71:02:15	0.013509	Sy2
MRK 6	06:52:12.2	+74:25:37	0.018813	Sy1.5
MRK 78	07:42:41.7	+65:10:37	0.037150	Sy2
UGC 3995	07:44:09.3	+29:14:48	0.015844	Sy2
NGC 3227	10:23:30.6	+19:51:54	0.003859	Sy1.5
NGC 3281	10:31:52.1	-34:51:13	0.010674	Sy2
NGC 3516	11:06:47.5	+72:34:07	0.008836	Sy1.5
NGC 4051	12:03:09.6	+44:31:53	0.002336	Sy1.5
NGC 4151	12:10:32.6	+39:24:21	0.003319	Sy1.5
NGC 4253	12:18:26.5	+29:48:46	0.012929	Sy1.5
NGC 4258	12:18:57.5	+47:18:14	0.001494	Sy1.9
NGC 4388	12:25:46.7	+12:39:44	0.008419	Sy2
NGC 5252	13:38:15.9	+04:32:33	0.022975	Sy1.9
Circinus	14:13:09.9	-65:20:21	0.001448	Sy2
NGC 5643	14:32:40.8	-44:10:29	0.003999	Sy2
NGC 5728	14:42:23.9	-17:15:11	0.009353	Sy2
MRK 315	23:04:02.6	+22:37:28	0.038870	Sy1.5
NGC 7582	23:18:23.5	-42:22:14	0.005254	Sy2
NGC 7212	22:07:01.3	+10:13:52	0.026632	Sy2

TABLE 1.1— List of the 25 Seyfert galaxies showing ionization cones. **MRK 6**: Ulvestad & Wilson (1984), and Meaburn et al. (1989), confirmed in this work. **NGC 7212**: This work.

et al. 1994; Mrk 78, Capetti et al. 1994, 1996; Mrk 1066, Bower et al. 1995; Mrk 3, Capetti et al. 1996; ESO 428-G14, Falcke et al. 1996), indicating that the radio ejecta strongly perturb the ionized gas, at least in these objects. It has also been suggested that the hot gas associated with the shocks generated by the interaction between the radio ejecta and the ambient medium is a significant source of ionizing radiation (e.g. Dopita 1995; Dopita & Sutherland 1995; Bicknell et al. 1998; see also reviews in Morse, Raymond, & Wilson 1996 and Wilson 1996). In objects like Mrk 573, for example (Capetti et al. 1996), the lobelike radio features are clearly associated with concave arcs of emission whose apex lies at the position of the radio source and which suggests strongly that, as in Herbig-Haro objects, these are in fact bow shocks formed at the working surface of the advancing radio lobes. Equally convincing is the structure of the emission-line regions associated with Seyfert galaxies, which shows radio jets, e.g., Mrk 3, Mrk 348 (Capetti et al. 1996), in which the NLR also takes the form of a linear structure that is essentially cospatial with the radio jet. First, narrow-band imaging and spectroscopy have shown that in many cases not only are the physical sizes of the radio structure and the line-emitting gas in the NLR comparable, but the line-emitting gas also has a tendency to be elongated in the same direction as the radio ejecta (Wilson & Heckman 1985). Secondly, there are a few galaxies in which discrete velocity components seen in the [O III] λ5007 line profile are closely associated with individual radio components as for example in NGC 5929 (Whittle et al. 1986). The key issue is whether the radio plasma and ionizing photons are collimated on the same or different spatial scales. The most stringent limit on the collimation of radio ejecta in Seyferts is provided by VLBI observations of NGC 4151 (Harrison et al. 1986), which show that the collimation occurs on a scale $<$ 2 pc. HST observations of NGC 1068 (Evans et al. 1991), NGC 4151 (Evans et al. 1993), and NGC 5728 (Wilson et al. 1993) indicate that the ionization cones are formed $<$ 20 pc from the nucleus. Both emission and absorption models of the collimation of the ionizing photons are consistent with this observational limit.

1.3 Aims of this work

As previously seen, twenty-five active nuclei, at redshift lower than 0.04, have been discovered to show a bright extended NLR. Their very small number could be caused by a selection effect, since an extended NLR is visible only in nearby galaxies, or by the absence of large scale interstellar medium within the cone of ionizing photons in most of the active galaxies, so that their NLR has a very small extension appearing as a point-like source from ground-based observations, or finally by the necessity of particular initial conditions able to generate a kpc-size NLR. For example, about the third hypothesis, Morse et al. (1998) argued that the spectacular ionization cones of NGC 5252 were likely to be formed as a consequence of a merger process with a gas rich dwarf galaxy. Another merger seems to be the cause of the ionization cones in the early-type Seyfert 2 galaxy Mrk 3 (Di Mille, PhD Thesis 2007). Other examples of Seyfert galaxy in which the ENLR is probably caused by gravitational interactions are NGC 4388 (Yoshida et al. 2002; Ciroi et al. 2003) and MRK 315 (Ciroi et al. 2005). Recently Fu & Stockton (2007) were able to study the NLR of the quasar 4C 37.43 (z=0.37) and suggested an external origin for this gas, likely obtained through a merger with a late-type gas rich galaxy. Thanks to the Hubble Space Telescope it has been possible to see in more detail the structure of the ENLR, that appears to be made of filaments of gas with a complex structure. Indeed a lot of problems concerning the ENLR are still open. It is important to determine whether ENLR emission is present in all Seyfert galaxies, or whether it occurs preferentially in particular galaxy types. This requires a deeper search of more objects. Two-dimensional mapping is required to determine how elongated the ENLR emission is and how closely the ENLR is aligned with the radio axis. Furthermore, it is still unclear which is the origin of the ionized gas. Until now a specific research was never really handled to understand if the NLR gas is simply interstellar medium (ISM) belonging to the host galaxy and photoionized by the powerful energy source of the active nucleus, or it is material ejected by the nucleus itself in strong interaction with radio-jet, or material acquired directly from intergalactic medium (IGM) or through gravitational interactions with companion galaxies. These questions are strongly related to the mechanisms of AGN feeding. Ther are no specific papers on the ENLR gas origin in literature, since it is not simple to disentagle among these hypotheses.

We present a possible approach to handle the problem of the NLR origin, based on the analysis of the spectral properties, the kinematics and metallicity of the ionized gas. We stress that a powerful method of investigation is the generally called “3D spectroscopy”, which includes integral-field spectroscopy through arrays of fibers, or fibers+lenses, or image slicers, and Fabry-Perot spectroscopy through narrow band filters. 3D spectroscopy is very suitable for this science case, because it gives spectrophotometric and kinematic information of extended sources, allowing to perform a more reliable analysis not affected by the orientation of the spectrograph as in long-slit spectroscopy, and offering the great chance to map and model areas of the sky with a size ranging from few arcsecs up to an arcmin, depending on the instrument used. It is useful to perform two-dimensional observations of the bright extended cones in nearby Seyfert galaxies, mapping the kinematics and flux ratios or the emission clouds populating the NLR of these AGN. Through the analysis of these data we expect to add a significant contribution to the general understanding of the ionization cones structure and physical processes at work within them.

Understanding the physical processes occurring in the NLR is not a simple question, but it is important because it can be related to the gas origin. This goal could be achieved by means of spectrophotometric technique. Optical spectra of the NLR show several recombination, forbidden and semi-forbidden emission lines. In particular, in optical the recombination lines are emitted by hydrogen and helium, while forbidden lines are emitted mainly by oxygen, nitrogen and sulphur. Calculating and plotting emission line ratios between forbidden and recombination lines or between forbidden lines, like for example [O III] 5007/Hβ, [N II] 6584/Hα, [O II] 3727/[O III] 5007 ratios introduced by Baldwin, Phillips and Terlevich (1981) and by Veilleux and Osterbrock (1987) in their famous BPT and VO diagnostic diagrams, allow to clearly distinguish between ionization by a thermal continuum, by a power-law continuum or by shock waves. In particular, in these diagrams AGN are well separated by Hii regions and supernova remnants, showing gas with higher ionization degree. The mechanism which is believed to determine the emission in the NLR of AGN is the photoionization by a power-law continuum. Indeed, the emission line ratios suggest that the spectral energy distribution cannot be thermal, since a large amount of high energy ionizing photons are necessary to produce atomic species like e. g. [O III] or [Ne III], which require energies larger than 50 eV, that is photons of the Extreme Ultraviolet spectral range and beyond. Analysis of the NLR physical conditions as a function of the distance from the nucleus suggest that the ionization parameter, adimensional quantity given by the ratio of the ionizing photon flux to the hydrogen density, decreases outward in most of the cases. This confirms that the dominant source of ionization is the nuclear one, since the emitted photons are geometrically diluted during their spread through the NLR clouds and the lower is the ionization flux, the lower is the gas ionization degree, and the ionization parameter, which assumes typical values of some 10^{-3}. The detection of forbidden lines like [O III] 4959,5007, [O II] 3726,3729, [N II] 6548,6584, [S II] 6716,6731, etc. is a strong indication that the NLR is a relatively low density medium, with expected values around 10^3 – 10^4 e^- cm^{-3}, and therefore the [O III] 4959+5007/4363 ratio can be effectively used to determine the temperature. In fact, high densities would suppress [O III] 4959,5007 with respect to [O III] 4363, which has a higher critical density ($N_c \sim 10^7$ cm^{-3}). Typical temperature values measured for the clouds of the NLR are in range 1 – 2×10^4 K. This is also a proof in favor of the photoionization mechanism, since the collisional excitation of the forbidden transitions cause the radiative cooling of the gas, which keep the temperature within the above mentioned range. Otherwise, to produce [O III] by means of collisional ionization, temperatures larger than 0.5 – 1 $\times 10^5$ K are required. Studying in detail the gaseous properties of the NLR as a function of the distance from the nucleus, it is frequent to find a high ionization degree even several kpc far from the ionization source. This is unexpected and strongly suggests that additional ionization mechanisms should occur in the NLR. Several authors invoked the effects of shock waves (see e.g. Viegas-Aldrovandi & Contini 1989, or Dopita & Sutherland 1995): a fast radiative shock compresses and heats the gas to temperatures of about 10^6 – 10^7 K, which diffuses UV/soft X-ray ionizing photons from the hot post-shock region; the photons moving upstream encounter the preshock gas and produce a precursor ionized region with a temperature of some 10^4 K. Let us consider an outflow process at velocity v_s = 500 km s^{-1}. The mass of the ionized gas involved can be roughly estimated by means of the reddening corrected luminosity of Hβ emission line and the electron density. By assuming n_e = 100 cm^{-3} and the case B recombination at 10^4 K, and taking into account that typical values of L(Hβ) are 10^{39} – 10^{42} erg s^{-1}, we obtain about 10^5 – 10^8 $M_\odot$, which implies a kinetic energy of 10^{53} – 10^{56} erg. Now, if the NLR has a size of 1 kpc the dynamical timescale t_{dyn} will be 10^6 yr and the input momentum rate of the ionized gas 10^{32} – 10^{35} dyn. If we compare this value with the input momentum rate caused by the accretion onto the SMBH , we obtain that an accretion rate 10^{-3} – 1 $M_\odot$ yr^{-1} can sustain an outflow of gas with these assumed properties. Such accretion values are typically observed in Seyfert galaxies. We must take into account that outflows are not exclusive effects of the AGN accretion mechanism, since also starbursts can be drivers of this phenomenon. In particular, in case of star formation, by estimating the rate of momentum injection into the circumnuclear environment from SNe and stellar winds (Veilleux et al. 2005) for solar metallicity, it is easy to verify that a SFR between 0.1 and 10 $M_\odot$ yr^{-1} can also sustain the outflow of gas of this example. But we cannot forget that the emission line ratios of the NLR indicate mostly AGN ionization. Moreover, nuclear starburst outflows are observed to be oriented orthogonally to the galactic plane, while AGN outflows are randomly oriented, since the torus axis is in general not aligned with the axes of the host galaxy.

The different origin of the NLR gas is expected to affect the kinematics of its ionized clouds: in case of host galaxy ISM, the kinematics of the ionization cones should be dominated by rotational velocity driven by the gravitational potential of the galaxy, while in case of material ejected by the nucleus or acquired from outside, the inflow/outflow processes should generate one or more significant non-rotational components. Mrk 573, for example, shows an extended NLR (larger than 4 kpc) whose external side follows a smooth velocity field with very narrow emission lines, while the internal side is characterized by very disturbed kinematics with much broader emission lines especially in the areas where the radio ejecta lobes are located (Ferruit et al. 1999). Non-circular motions have been detected by us in the extended NLR of Mrk 3 up to ~3 kpc from the center, both with low-resolution integral-field spectra (~500 km s^{-1}) and with high resolution long-slit spectra (~40 km s^{-1}), by means of which at least three independent components could be fit to the [O III] λ5007 lines (Di Mille PhD Thesis, 2007). Fabry-Perot observations of NGC 4388 revealed the presence of a bipolar outflow in the ionization cones (Veilleux et al. 1999). Indeed, Ciroi et al. (2003) showed that its South-West cone is characterized by a mixture of low density colliding clouds and that the high ionization observed in the outer edges can be explained by a combination of photoionization and shock. Ciroi et al. (2005) detected in Mrk 315 an extended region (up to 7 kpc) of highly ionized and collimated gas moving radially at high velocity (~ +500 km s^{-1}) with respect to rotation of the galaxy and producing clear effects of gas compression and shock ionization. More recently, Smirnova et al. (2007) by means of panoramic 3D spectroscopy discovered that the NLR of the Seyfert 2 galaxy Mrk 533 is composed of at least two (probably three) kinematically separated regions. In particular, they detected stratified outflows having different velocities (from 20-50 km s^{-1} to 600-700 km s^{-1}), at different radial distances (~2.5 and ~1.5 kpc), and with the faster outflow corresponding to the position of the observed radio jet. Spectral emission lines of NLR show Full Width at Half Maximum (FWHM) typically ranging from 200 up to 800 km s^{-1}. A few AGN show even higher FWHMs, which can reach 1000 km s^{-1}. The widths of these lines cannot be an effect of atomic thermal motions, because in this case the Doppler broadening would require temperatures around 10^6–10^7 K, which are not observed. The ratio between the FWHM of NLR emission lines and the total velocity range covered by the ionized gas, was used to give a rough measure of the relative importance of turbulent velocities to large scale motions. Values larger than 1 were found by Durret & Warin (1990) in 12 out of 20 nearby AGN with extended NLR, and were interpreted as accreted matter not yet on stable rotating orbits. The emission from the NLR of the Seyfert galaxies is generally observed aligned with the radio axes. The NLR gas is found to be associated with the “linear” radio sources on tens of pc to kpc scales. Bow shocks or cocoons driven by a radio jet can accelerate the line emitting gas to 100 – 1000 km s^{-1}. In this case, the gas is shocked by the expanding jet and we observe a clear kinematic and morphologic association between radio and optical emission regions. It is well known already from medium resolution spectra (R ~ 1000 – 5000, corresponding to 60 – 300 km s^{-1}) that high excitation emission lines, like [O III] lines in the optical domain, show often asymmetric profiles with clear blue or red wings, which indicate the presence of additional kinematical components in the NLR. Therefore, there are strong evidences that the NLR is made by several kinematic components moving radially inward or outward. Scanning Fabry-Perot observations have already demonstrated their capability when the emission line profiles have to be studied in detail. Unfortunately they are limited by a very small spectral range and by time consuming observations caused by the scanning procedure. Integral-field spectroscopy is favourite, but it does not generally offer a high resolution. In addition it is mandatory to have a velocity field of the stellar component of the host galaxy, since this is the only way to understand if the gas is following the gravitational potential of the host, or if it is decoupled showing for example counter-rotations which are generally ascribed to accretion of matter from the surroundings of the galaxy.

Estimate the metallicity of the NLR is a key point because the feeding process of the SMBH is expected to influence the chemical conditions of the host galaxy. For example, if the gas is accreted from the non-processed ISM of a nearby galaxy or from the intergalactic medium, we should measure sub-solar metallicity, while in case of gas processed by stars belonging to the host galaxy, it should be solar or super-solar. Unfortunately, the metallicity determination in AGN is not simple as in case of Hii regions, where there is a good understanding of the ionizing sources (essentially O, B stars), photoionization models treating the physics of these regions are quite well-developed, and therefore the correlation of emission line ratios with abundances in Hii regions is reasonable. On the contrary, in AGN the situation is markedly different, because the ionizing source is not as well understood, and has a much greater range in luminosity. The ionizing spectrum is also harder than that produced by stars, and shocks are also more likely to contribute to the ionization state. Also, the shape of the AGN ionizing continuum and the density distribution of the clouds are generally unknown. Therefore, in the past observations of the circum-nuclear and extra-nuclear Hii regions were preferred and the nuclear abundances were obtained by means of extrapolation to the center of radial abundance profiles. Results from these and previous works show for Seyfert 2 and LINER nuclei a clear overabundance of oxygen (up to 2-3 times solar) and of nitrogen and sulphur (up to 4-5 times) (Storchi-Bergmann & Pastoriza 1989, 1990). Nevertheless, we mention that Komossa & Schulz (1997), following a different method, have found that the oxygen is underabundant by a factor of ~2, while the N/O ratio is a factor 1.5-2.0 above the solar value. This observed N/O overabundance is expected in case of enrichment by recent starburst episodes associated with AGN. The bursts could be triggered by gas moving toward the nuclear region and falling onto the accretion disk around the black hole, modifying therefore the chemical abundances of the host galaxy (Matteucci & Padovani 1993). Oliva et al. (1999) derived reliable metallicities in Circinus galaxy by applying grids of photoionization models to spectra including a large number of line ratios. Even if they show that a degeneracy exists between the continuum shape and the density distribution of ionized gas, the use of combined optical and near-infrared emission line ratios allows to successfully constrain gas elemental abundances regardless of the assumptions behind the photoionization calculations. More recently, Groves et al. (2006), applying dusty, radiation pressure dominated models to a large sample (~23000) of Seyfert 2 galaxies observed by SDSS were able to find only 40 active nuclei with sub-solar metallicity, confirming that most of the AGN at least in the local Universe seems to be characterized by solar/super-solar metallicities.

In this work, we tried to tackle the open question about the origin of the NLR gas in AGN. This topic has been handled by different authors on single-case objects or list of objects, but never systematically analyzing different aspects of sample of targets. We showed here a possible method to investigate this issue, making use of a modern investigation technique, called integral-field spectroscopy. The 2D spectroscopic data must be analyzed with photometric and longslit data in order to better understand the properties of the objects. The ensemble of all these information is expected to offer a clue to the physical conditions which lead to the formation of the NLR and/or the extended NLR. In Chapter 2 the basic characteristic of 3D spectroscopy are described, our data properties are listed and the reduction and analysis procedures are explained. In Chapter 3 and Chapter 4 we applied the just mentioned analysis to two Seyfert galaxies, NGC 7212 and MRK 6, respectively. We studied in detail the ENLR gas of a type 2 and of an intermediate type Seyfert galaxy, finding in both cases that the ionized gas has probably an external origin. In Chapter 5 we focused on the structure and properties of sub-regions of ENLR, by means of integral field spectra of a sample of 12 nearby Seyfert 2 galaxies. In Chapter 6 we summarized and discussed our results.

2

Data reduction and analysis

Being interested in studying ionization cones, we need to map a spatial extended field and to collect spectroscopic information in the whole area. In this case, integral field spectroscopy (IFS) is a very powerful method of investigation: it permits to obtain simultaneous spectra over a two-dimensional field (e.g. Bacon et al. 1995). The data are in three dimensions, two spatial (α, δ) and one spectral (λ), in contrast with the usual longslit aperture technique, which is limited to only one spatial dimension, along the slit. Regardless of the method used to obtain the data, the final product is a data-cube, with axes of x, y (or RA, Dec; the two spatial axes) and wavelength (or velocity) (see Figure 2.1).

In this chapter the basic characteristic of IFS are explained, our data properties are listed and the reduction and analysis procedures applied to IFS data are described.

2.1 Integral Field Spectroscopy

The recording of the spectrophotometric information content of celestial objects is, in the general case, a three dimensional problem (x, y, λ). However, present detectors are of a two-dimensional nature and this explains the still prevalent use of classical longslit spectrographs, despite total loss of one of the spatial coordinates (across the slit width) and because of their perfect geometrical match with available digital detectors. Traditional spectroscopy is based on dispersing the image of a slit (single or multiple) so that a spectrum is produced for whatever fraction of the light from the target of interest falls within the aperture defined by the slit. While this is satisfactory for many applications, it makes poor use of the incident light when the object is extended, either intrinsically or due to poor seeing and suffers from wavelength-dependent slit-losses due to differential atmospheric refraction (DAR). In these cases, what is really required is to record a spectrum from each part of an extended object. This cannot be done with a longslit except in one dimension defined by the length of the slit. Moreover, seeing and sky transparency may change from one long slit exposure to another, possibly leading to errors when comparing the data.

IFS avoids this restriction by decoupling the slit width from the field shape reformatting a two-dimensional field into a linear pseudoslit. Most of the advantages of the IFS technique are direct consequences of the simultaneity when recording spatial and spectral information. The simultaneity not only

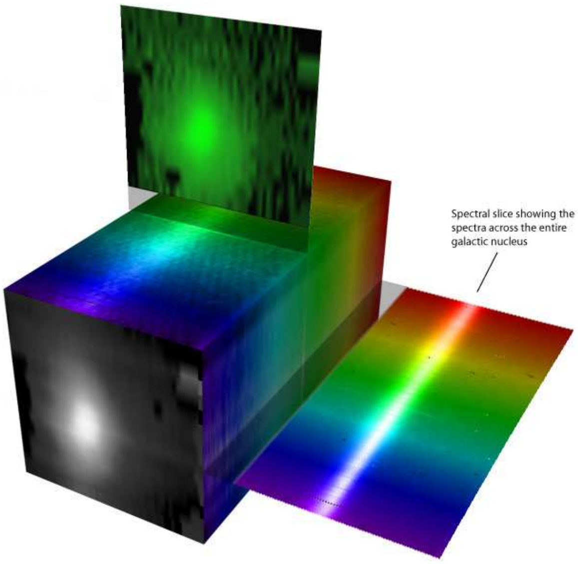

Spectral slice showing the spectra across the entire galactic nucleus

Figure 2.1— The final result obtainable with IFU data: the datacube. In x and y axes there are the spatial coordinates, so the green extracted slice is an image obtained by integrating the 2D spectrum in a well defined spectral range. The z axis is the dispersion axis, along this direction, we can see the 1D spectrum of each fiber or aperture.

implies a more efficient way of observing but, more importantly, it guarantees a great homogeneity in the data, because the data are collected in the same conditions of observations. So, accurate centering in the slit and to adapt the slit width (spectral resolution) to the seeing conditions are no longer needed. Furthermore the atmospheric dispersion effects can be corrected without loss of light by manipulation of the datacube. The global velocity field is recovered without bias imposed by the observer's choice of slit position and orientation. The main limitation is the small field of view (f.o.v), ranging from several arcsec (e.g. PMAS) to about one arcmin (e.g. VIMOS), small compared to the typical f.o.v. of some arcmins of longslit spectrograph, but it is enough for many types of objects (Vanderriest, 1998). The small field of view implies that in order to map more extended region a number of exposures with different pointings must be mosaiced.

The term 3D spectroscopy is used to indicate any technique that produces spatially-resolved spectra over a two-dimensional field. Integral field spectroscopy is that subset of 3D spectroscopy in which all the data for one pointing of the telescope are obtained simultaneously. The other methods, such as Fabry-Pérot Interferometry (FPI) and imaging Fourier transform spectroscopy (IFTS), use the time domain to step through wavelength space (or a Fourier conjugate). The Fabry-Pérot scanning allows a large field of view (e.g. 5 arcmin) to be surveyed at high spatial resolution in a single exposure but only at a single wavelength so that the required data volume with axes labelled by x-position, y-position and wavelength must be built up by scanning through the desired wavelength range. This technique can achieve a very high spectral and spatial resolution and high throughput. Historically, Fabry-Pérot scanning have been less popular than the other IFS techniques because it has proved extremely difficult to perform accurate flat-fielding and flux calibration of the data. Another method is the *y*-scanning longslit in which the 2D spatial information is obtained by stepping the position of the slit in order to map all the field, but this process is slow and time-consuming, since the effective exposure time is multiplied by roughly the ratio of the object size to the width of the slit.

All these techniques use the time as the third dimension, in the sense that they require repetitive integrations to obtain full spectra. Therefore, observations with such methods suffer a lot from varying atmospheric conditions and high quality spectra for faint objects are almost impossible to record (Eisenhauer et al. 2000). Nevertheless a wide field can be covered in one pointing, in contrast with IFS, which encodes all the spectral and spatial information in the same exposure but in a smaller field of view for a given detector format.

2.1.1 IFS configurations

An integral field spectrograph consists of two components: the spectrograph and an integral field unit (IFU). The IFU divides the 2D spatial plane into a continuous array. Each spatial element of an IFU is called spaxel, this term is used to distinguish between a spatial element on the IFU and a pixel on the detector. Several approaches to IFS have been developed (see Figure 2.2), based on the use of optical fibres to transform the bidimensional field into a pseudo-slit at the entrance of a classical longslit spectrograph (e.g. Vanderriest & Lemmonier 1988; Barden & Wade 1988; Arribas et al. 1991), a microlenses array as a spatial sampler (e.g. Courtès 1982 and Bacon et al. 1995), micro-mirrors (e.g. Weitzel et al. 1996; Content 1998), or mixed solutions (e.g. Allington-Smith et al. 1997).

Historically, the first one to be employed, chiefly by the Lyon group (Courtès et al. 1988; Bacon et al. 1995), uses an array of lenslets to segment an image formed by the telescope and produce separate images of the telescope pupil. These images are dispersed by the spectrograph into several spectra which would overlap unless the direction of dispersion is altered to avoid the principal axes of symmetry in the lenslet array. This technique allows the input image to be sampled contiguously, the throughput and spectral resolution can be optimised, but the length of the spectrum that can be produced without overlapping is very small. The maximum length of a spectrum is determined by the ratio between the size of the pupil image and the spacing between the subimages, fixed by the element size. This system, which does not make optimal use of the detector surface, because overlaps between spectra must be strictly avoided through the provision of unilluminated pixels between spectra, is best suited to applications where a long spectrum is not required, such as studies requiring either low spectral resolution over a large wavelength range or high resolution over a small wavelength range. Examples include studies of the individual absorption lines in galaxies (e.g. to obtain indices for abundances analysis) or kinematics from single absorption or emission lines (Allington-Smith & Content 1998). Recent examples of such an instrument include SAURON (Bacon et al. 2001) at the William Herschel Telescope (WHT), OASIS (McDermid et al. 2004) at the Canadian-France-Hawaii Telescope (CFHT), OSIRIS (Larkin et al. 2003) at the Keck Observatory, and Kyoto 3DII (the Kyoto tridimensional spectrograph II, Sugai et al. 2006) at the Subaru Telescope.

The second approach uses a fiber array, this is currently the most common technique in use. Optical fibers arranged in a close-packed bundle at the telescope focus, transfer the light of the input image to the slit of the spectrograph. The flexibility of the fibres allows the round/rectangular f.o.v. to be reformatted into one (or more) “slits”, from where the light is directed to the spectrograph; the spectra are obtained without wavelength shifts between them, resembling a longslit spectrum. Because of the linear format,

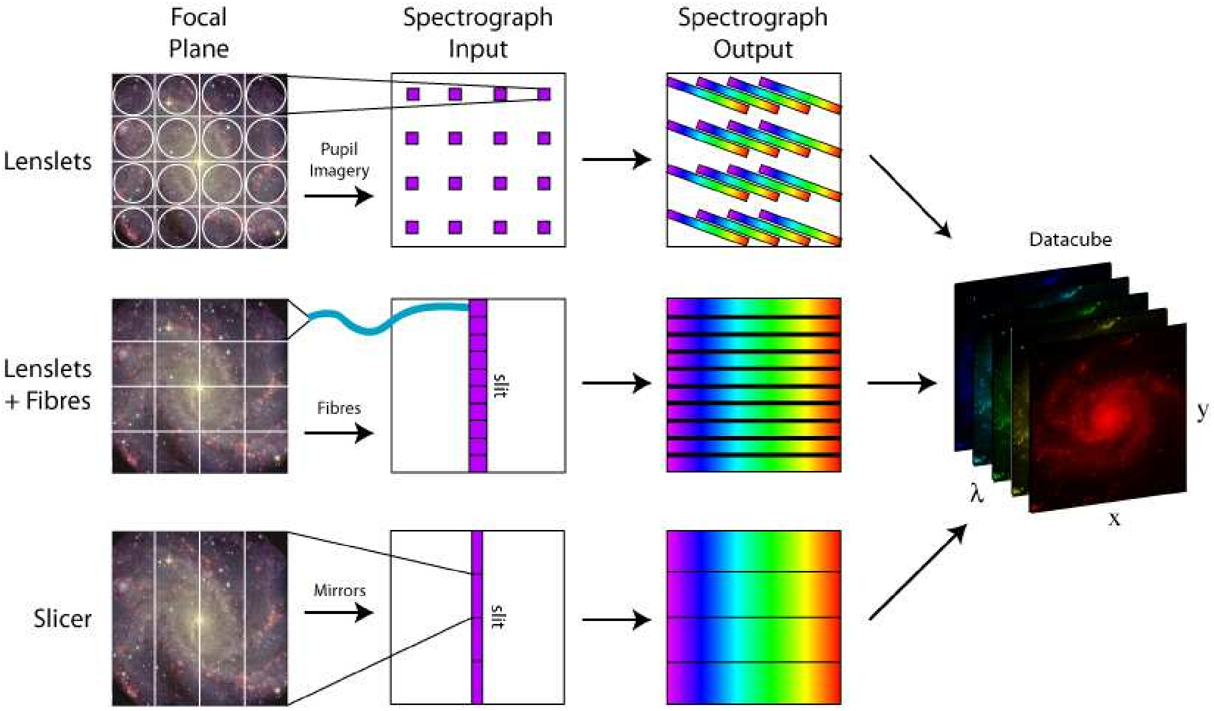

FIGURE 2.2— A clear scheme of the three main IFS configuration: the lenslets (upper-line), the lenslets+fiber (middle-line) and the slicer (lower-line). For each configuration, the way in which the f.o.v. is sampled, the spectrograph input, and the spectrograph output are shown. All these techniques finally result in a datacube.

the spectrum can be as long as the detector size allows. This technique requires less dead space and hence has the potential to increase the information density. The main disadvantage of this system is the filling factor: the geometrical fraction of the field that transmits light. It is directly related to the diameter of the fiber core and the outer diameter of the fiber, it is typically no greater than 63-75%, when the system is used in the optical wavelength range (Allington-Smith & Content 1998). Other disadvantages of this technique are that the sampling of the sky is not contiguous since there are gaps between the fibre cores and that the fibres do not work efficiently at the slow focal ratios at which most telescopes work resulting in focal ratio degradation (FRD). A clever modification of the previous principle uses a lenslet at the input of the fibers. The input lenslets provide better matching between the fiber and the telescope. In this way, all the light collected by each lenslet is focused into the fibre. An additional benefit of this variation is that the microlenses slow the telescope focal beam, minimising the FRD. Since the lenslets form a two-dimensional contiguous array, the advantage over fiber-only IFUs is that the filling factor is maximized, but there is the disadvantage of greater manufacturing difficulty. In particular, the lenslets must be accurately registered with the fibers to avoid transmission loss due to a displacement between the pupil image and the fiber core (Lee et al. 1998, Allington-Smith & Content 1998). The first instrument with this kind of configuration was the MPFS (Afanasiev et al. 2001) for the Russian 6-m telescope. Other optical instruments are GMOS (Allington-Smith et al. 1997) for the Gemini telescope, PMAS (Roth et al. 2005) installed at the Calar Alto Observatory, SPIRAL (Saunders et al. 2004, Kenworthy et al. 2001) at the Australian Astronomical Observatory and IMACS-IFU (Schmoll et al. 2004) at the Las Campanas Observatory. Near Infrared (NIR) instruments include SMIRFS (Haynes et al. 1999) at the UK Infrared Telescope and VIMOS (Le Fevre et al. 2003) at the VLT. Future instruments include the Gemini Planet Imager (GPI) at the Gemini telescope and the BIGRE-type IFS of the Planet Finder SPHERE for the VLT.

Another technique, which is especially applicable to wavelengths beyond 1.8 μm, where instruments must be cooled to reduce their thermal background, is to use an image slicer employing only reflective optics. This technique was pioneered by MPE with the 3D spectrograph (Weitzel et al. 1996; Krabbe 1997) mounted at the Anglo-Australian Telescope (AAT).The image formed by the telescope is incident on a mirror that is segmented in thin horizontal sections consisting of a number of narrow slices. Each mirror slice is set at a slightly different angle so that the diverging beam from each slice exits in a different direction. A second segmented mirror is arranged to reformat the slices so that, instead of being above each other they are now laid out end to end to form the slit of the spectrograph, actually a virtual slit. So the overall effect is to rearrange the rectangular field into a long thin field made up of all the slices arranged end to end (Allington-Smith & Content 1998). The main advantage of this system is that the reflecting optics make it suitable for use in cryogenic instruments. Another important advantage is that full spatial information is maintained along the slit. Furthermore with this technique the FRD is avoided and the slicing arrangement gives contiguous coverage of the field at potentially high spatial resolution. The disadvantages are that it is hard to make the design compatible with existing spectrograph designs, and that the optical system might be bulky and difficult to fabricate. Furthermore there is a shadowing effect at the step of the first mirror, which leads to unavoidable light losses and increases with smaller mirrors and a large field of view (Eisenhauer et al. 2000). The existing optical instruments are ESI (Sheinis et al. 2002, 2006) at the Keck Observatory and the Wide Field Spectrograph (WiFeS) (Dopita et al. 2007) at the 2.3 mt telescope of the Siding Spring Observatory. Future optical instruments include

MUSE (Bacon et al. 2004 and reference therein) at VLT. Existing NIR instruments include PIFS (Murphy et al. 1999) at the Palomar Observatory, UIST (Ramsay Howat et al. 2006) at the UK Infrared Telescope, NIFS (Mc-Gregor et al. 2003) and GNIRS (Allington-Smith et al. 2004) for Gemini telescope, and SPIFFI (Eisenhauer et al. 2003, Iserlohe et al. 2004) and SINFONI (Eisenhauer et al. 2003, Bonnet et al. 2004) for VLT. Future NIR instruments include KMOS (Sharples et al. 2004) for VLT, FRIDA at the Gran Telescopio Canarias (GTC), MIRI a multi-mode instrument to be used on JWST and METIS that is the proposed mid-IR instrument for E-ELT.

An alternative to image slicers is a hybrid between a lenslet array and image slicer system a microslice system (Content 2006). The aim is to get the large number of spaxels of a lenslet array with the efficient packing of spectra obtainable with a slicer. The solution is to make the lenslets so that they emulate a slicer. This uses lenslet arrays to divide the field in 2D and allow each pupil image to be replaced by a slice which contains spatial information along its length. The first lens array would be made of rectangular lenslets (the microslice) so that information in the spatial direction is not lost. Then a second array reimage the microslices on the spectrograph input focal plane again to maintain the spatial information that is lost if the pupil is imaged instead. They also demagnify the images to leave space for dispersion. A third array would reimage the pupil at the spectrograph stop. This provides many of the benefits of the image slicer in terms of reducing dead-space between spectra, but not to the same extent because the spectra are distributed over a 2D field and overlaps must be avoided since the wavelengths are not continuous between slices.

An important development of the basic IFS concept is the provision of multiple, independently deployable, IFUs called multiple integral field spectroscopy. Although it is possible to devise multiple IFUs using an image slicer approach, it is relatively straightforward to design a system using the fiber-lenslet technique. In such a system, a conventional pick-and-place robot would be used to position bundles of fibers coupled to lenslet arrays as required. Clearly the number of elements within each integral field subunit is limited by the area of the spectrograph's detector. In general terms, the minimum field size of each subunit should be a few arcsec^2, to compete with slit spectrographs with sub-arcsecond slit width. Adopting a design similar to that proposed for the GMOS-IFU, a total (non-contiguous) field of 60 arcsec^2 could be divided into 20 units, each with a field of 3 arcsec^2, sampled at $0''.2$ and containing $\sim$100 elements (Allington-Smith et al. 2002).

The different method of IFS can be compared. It can be seen that image slicers approach the theoretical maximum performance. Fiber systems are as efficient in terms of specific information density (SID) as lenslet arrays but slicer systems are much more efficient than either. The microslice IFU offers a compromise between the excessive numbers of unique components and performance which may prove suitable for wide-field surveys with IFS. The fiber-lenslet technique provides significant benefits over lenslet-only systems (e.g. SAURON, Bacon et al. 2001) in terms of the efficiency with which the detector surface is addressed and of the length of spectrum that can be obtained without overlaps between spectra. It ensures that the field is contiguous, with unit filling factor, and maximizes throughput by optimal coupling to both the telescope and spectrograph.

2.1.2 IFS scientific applications

IFS can be used to study extended objects, like galaxies, star forming regions, planetary nebulae, etc., to search for emission-line sources and obtain spectra of several objects in very crowded fields (Parry

1998). Any astronomical object for which spatially resolved spectroscopic information is required is suited for study with IFS, for example:

- Pre-main sequence objects: e.g. UIST@UKIRT for a study of stars in the Braid Nebula star formation region in Cygnus OB7 (Aspin et al. 2009); a study of kinematics and physical conditions of HH110 an Herbig-Haro object in Orion with PMAS (López et al. 2010).
- Resolved stellar populations: e.g. PMAS for a study of the luminous HII regions in M33 (Relaño et al. 2010); NIFS for studying the central arcsecond of compact elliptical galaxies (Davidge et al. 2008).
- Normal Galaxies: e.g. SINFONI for a study of the morphology and kinematics of nuclear star formation rings (Böker et al. 2008); Kyoto3DII for a study of nearby E+A (post-starburst) galaxies (Goto et al. 2008); SAURON for a study of the stellar kinematics of elliptical and lenticular galaxies (Emsellem et al. 2004).
- Active Galaxies: e.g. INTEGRAL to characterize the central regions of the Seyfert 1 radio galaxy 3C 120 (Garcia-Lorenzo et al. 2005); GMOS for studying the stellar kinematics of the nuclear region of active galaxies (Barbosa et al. 2006); PMAS to study the extended Ly-α emission around bright quasars (Christensen et al. 2006).
- Groups and cluster of galaxies: e.g. Kyoto3DII for studying the metal enrichment in the starbursts of an interacting galaxy system (Sugai et al. 2004); VIMOS to study the diffuse intracluster light in the galaxy cluster Abell 2667 (Covone et al. 2006); VIMOS for a study of the morphology, kinematics and ionization state of the extended emission-line region surrounding the radio source PKS1932–46 (Inskip et al. 2007).
- High redshift galaxies: e.g. SINFONI for a study of the rotation curves and dynamical evolution of UV-selected galaxies at $z \sim 2$ (Förster Schreiber et al. 2006); the SINS survey with SINFONI to study the rapid secular galaxy evolution at $z \sim 2$ (Genzel et al. 2008).
- Gravitational lensing: e.g. PMAS for integral field spectrophotometry of gravitationally lensed QSOs (Wisotzki et al. 2004); INTEGRAL for a 2D spectroscopy of the gravitational lens system Q2237+0305 (Mediavilla et al. 1998).

2.1.3 Recent developments

Integral field spectroscopy (IFS) has increased in importance as the use of large telescope apertures allows high signal-to-noise ratios to be obtained despite the division of the integrated light from discrete sources in both the spectral and (two-dimensional) spatial domains. Thus spatially resolved spectroscopy can be attempted even for faint, distant objects (e.g. Eisenhauer et al. 2004; Bower et al. 2004). Improvements in image quality through adaptive optics (AO) also increase the relevance of IFS by allowing the effective use of IFS on extremely large telescopes (ELTs). A key instrumental ability for ELTs will be multiplexed IFS. IFS near the diffraction limit is a key technique for the study of intermediate black holes in dense star clusters and in resolving stars in extragalactic systems where the combination of spectral and spatial information helps to overcome confusion. At the diffraction limit even modest fields of a few tens of arcminutes contain 10^9-10^{11} spaxels, and it is not feasible to sample the whole field simultaneously. Instead a number of sub-fields of a few arcseconds will be selected for high resolution imaging or IFS. This puts an even greater emphasis on performance since the total numbers of spaxels must be greatly increased to provide both a useful field for each IFU (say $(2/0.05)^2 \sim 2000$ spaxels) and a useful number of sub-fields (say 50, requiring $\sim 10^5$ spaxels in total). There are two main technologies under development to do this: articulated arms (Sharples et al. 2004) each of which relays a small field to a fixed IFU; or an array of "beam-steering" mirrors which subdivides the field and relays a portion of it to an IFU. An alternative technology is to use fiber-based IFUs with a pick-and place robot (Pasquini et al. 2000). The problem of addressing the large number of data samples (volume elements, voxels) making up a datacube obtained via a 3D technique with a finite number of detector pixels is well known (e.g. Allington-Smith 2006). At the diffraction limit, the number of potential spaxels available at the focal surface is $\sim 10^{10}$, requiring $\sim 10^{13}$ voxels, each of which should be addressed by at least 2^3 detector pixels for optimum sampling at the Nyquist-Shannon limit. This implies an unaffordable detector array of $10^7 \times 10^7$ pixels. Since this will exceed the detection capabilities of any realistic instrument, the field must be dilutely sampled by a factor $10^{-6} - 10^{-4}$ to extract spectroscopic data from selected regions of interest. This can be achieved by directing light from movable sub-fields into a number of spectrographs which may be independently optimised as required. An example is the pickoff scheme used in KMOS (Sharples et al. 2006) in which 24 sub-fields of a few arcsec are directed by articulated arms containing an optical relay to fixed image slicing integral field units (IFUs) and from there into three spectrographs. Each sub-field covers roughly 400 spaxels and 400000 voxels, or 10^4 spaxels and 10^7 voxels in total equivalent to a dilution factor of $\sim 3 \times 10^{-6}$. The scientific return will be maximised if the sampling pattern provides an adaptable combination of separated independent spaxels and larger contiguous sub-fields, seamlessly combining integral-field and multiple-object spectroscopy. This is called Diverse Field Spectroscopy. Diverse Field Spectroscopy allows the observer to target only the interesting bits so that the spectrograph's capabilities are used most effectively. The instrumentation needed for DFS is illustrated by the Celestial Selector concept which uses massive monolothic fibre bundles and networks of optical switches to select the desired parts of the field and feed the light to the slit of the spectrographs (see Figure 2.3). The celestial selector simply routes input light from the telescope focal surface to one of a number of outputs which feed spectrographs optimised for different types of spectroscopy. The concept consists of an input fibre bundle with a very large number of short, broadband fibres in a single monolithic unit, an array of optical switches which either permits light from selected inputs to go through to the output or redirects it into an available output channel; and a set of output bundles containing a much smaller number of fibres feeding a variety of spectrographs. Although envisaged here as a fibre system it is possible to consider an alternative realisation in which either the input or output fibre systems are replaced by direct optical feeds. An earlier example of such a system is the Honeycomb system of Bland-Hawthorn et al. (2004) in which output fibre bundles are plugged into a very large lenslet array.

2.1.4 MPFS

In this work we analyzed integral field data obtained in different runs of observations at the 6-mt telescope of the Special Astrophysical Observatory (SAO RAS) in Russia with the Multi Pupil Fiber Spectrograph (MPFS). The MPFS (Afanasiev et al. 2001) is the Russian instrument to perform IFS with a lenslet-array+optical fibers configuration (see Figure 2.4), designed and developed by the Spectroscopy and

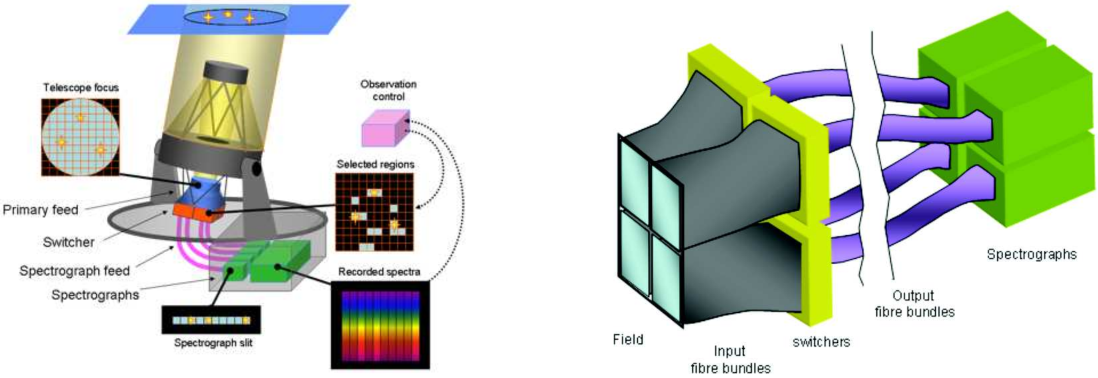

FIGURE 2.3— On the left: the Celestial Selector concept. On the right: the scheme of the Celestial Selector using fibre technology. This example has 4 tiles, each of which maps through a separate switcher to a single spectrograph.

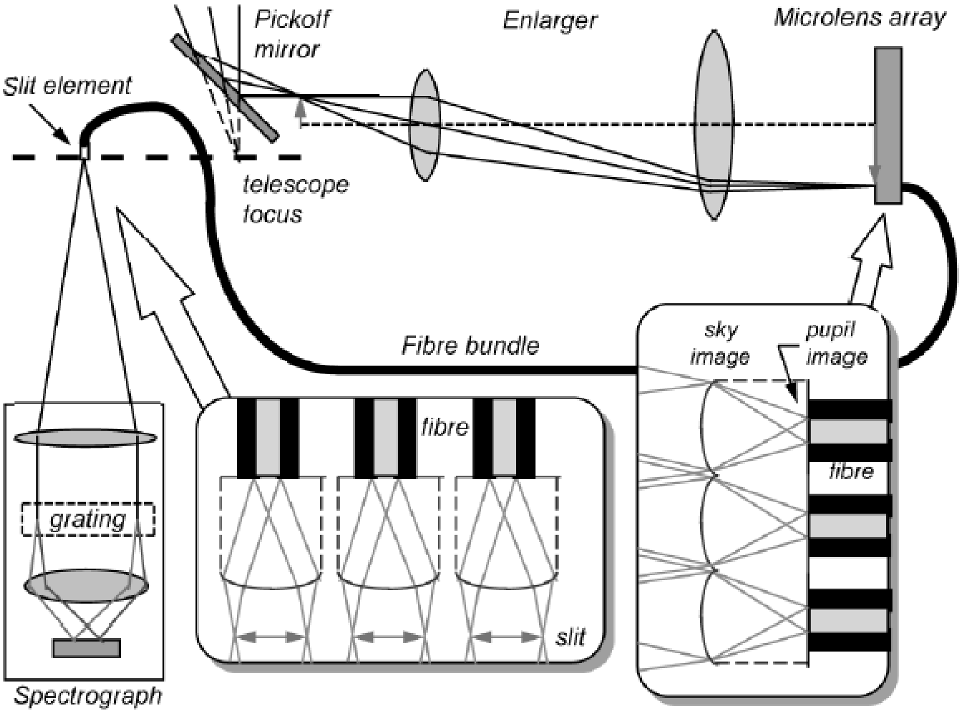

FIGURE 2.4— The configuration lenslet array plus optical fibers (Allington-Smith & Content 1998).

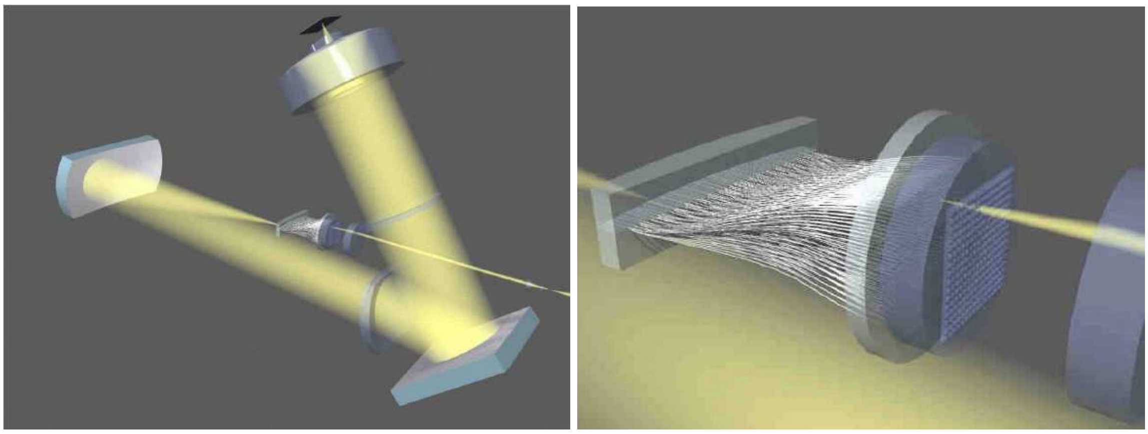

FIGURE 2.5— The MPFS optical layout: the 256 optical fibers, connected to the array of microlenses, are rearranged into a pseudoslit.

Photometry Laboratory of the SAO and mounted at the primary focus of the BTA, the 6-mt telescope, located near Mt. Pastukhova (Caucasus) at an altitude of 2070 m above the sea level. The MPFS is based on a matrix of contiguous microlenses which decomposes the image of an object into a definite number of micro-pupils. The array has 16×16 lenses, each lens is directly connected to its fiber, which carries the incoming signal, and all the fibers are rearranged into a pseudoslit (see Figure 2.5). This integral-field unit takes simultaneous spectra from 256 spatial elements. The field of view is $16'' \times 16''$ with a spatial sampling of $1''$.

2.2 Spectroscopic Data

The aim of this work is to carry out an integral-field spectroscopic study of few nearby Seyfert 2 galaxies ($z < 0.03$) with possible ionization cones or at least extended [O III] emission, taking adavantage of the MPFS in order to map the emission and investigate the physical and kinematical properties of the ENLR gas. We extracted the targets from the literature looking at [O III] emission line images obtained from the HST snapshot survey by Schmitt et al. (2003), selecting the objects showing elongated [O III] emission. We stress that in several cases the NLR size seems small and in principle not suitable for groundbased observations, but it must be taken into account that this survey is very shallow, as it can be verified by comparing the [O III] map of the ionization cone in NGC4388, extended up to 5-6 arcsec from the nucleus, with our integral-field data where the cone appears extended more than 10 arcsec (Ciroi et al. 2003).

Our idea was to observe the targets with a longslit spectrograph, setting the slit along the direction of the elongated emission, taking the position angle (PA) from the images of Schmitt et al. (2003). In this way we could verify how extended the emission is and select the objects to be observed at the 6-mt Russian telescope, planning a new long-term observational program at the SAO using the MPFS (in Appendix, one of the accepted proposals is shown) starting with the idea of study in detail the physical properties of ionization cones in nearby Seyfert 2 galaxies.

As a first test, we chose the Seyfert 2 NGC 7212. We compared the [O III] image of this object

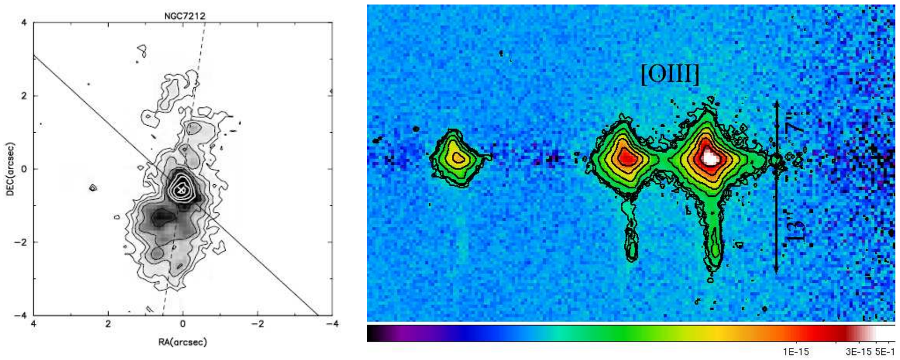

FIGURE 2.6— [O III] image of NGC 7212 taken from Schmitt et al. (2003) (left, North is up and East is to the left) compared with the continuum-subtracted NTT longslit spectrum (Bennert et al. 2006) in the Hβ+[O III] spectral region (right, North is down).

published by Schmitt et al. 2003 (see Figure 2.6), whose emission is extended up to 5″ (∼ 2.5 kpc) with lower limit of the measured flux of ∼ 6.5×10^{-14} erg s^{-1} cm^{-2} $arcsec^{-2}$, with a longslit spectrum taken with EMMI at NTT (see Bennert et al. 2003) along the direction of the [O III] emission at PA=170°. In the longslit spectrum (see Figure 2.6) the [O III] emission is more extended, up to 20″ (∼ 10 kpc), 7″ in the South direction and 13″ in the North direction, with the lower limit of the measured flux of about 6×10^{-18} erg s^{-1} cm^{-2} $arcsec^{-2}$. This object was the first candidate to be observed at the Russian 6 mt telescope with MPFS. By analysing these IFU data, and reconstructing the ionization map (the map of [O III]/Hβ), we have pointed out for the first time the presence of an ionization cone extended up to 12″, ∼6 kpc (see Chapter 3).

This test confirmed that our approach could give remarkable results in finding new ionization cones. So we decided to apply this method. First we selected a list of possible Seyfert 2 or intermediate type galaxies, observable in the northern emisphere, with a redshift z<0.03 and showing an elongated emission in [O III]. A redshift z<0.03 corresponds to a scale < 0.6 kpc/″ (assuming H_0 = 75 km sec^{-1} Mpc^{-1}); with a seeing of ∼2″, we expected to have a resolution <1 kpc. Such a resolution should be sufficient to map extended emissions. With this first list, we planned an observational program at the 1.8 mt telescope of the Asiago Astrophysical Observatory, (in Appendix one of the accepted proposals is shown) using the Asiago Faint Object Spectrograph (AFOSC). We used the grism 4 that covers the range 3500–8500 Å, with typical exposure time of 1–2 hours for each object. We estimated the position angle of the emission looking at the images in [O III] and we set the slit along the direction of the major axis of the emission to check how extended is (see Figure 2.7). We observed 12 Seyfert galaxies in 5 observational runs between 2007 and 2008. In October 2007 we observed MRK 1058, MRK 6 and NGC 7674; in December 2007 we observed MRK 79. In March 2008 we observed six objects: MRK 622, MCG-01-24-012, UGC 6100, NGC 3516, NGC 5347 and IRAS 16288+3929. Finally, UGC 10889 and MCG+03-45-003 were observed in July and in August 2008, respectively. All the galaxies observed with AFOSC are shown in Table 2.1, in particular in this table the PA of the slit and the total size (in kpc) of the extended [O III] emission are listed for each galaxy, $\Delta\lambda$ is the spectral resolution in Åand $\delta\lambda$ is the dispersion in Å/px.

From the first set of AFOSC data we extracted an interesting object: MRK 6. Even if this galaxy

Object name	RA (J2000.0)	Dec (J2000.0)	z (NED)	scale	Type	Slit	Spectral range	$\Delta\lambda$	$\delta\lambda$	T_{exp}	PA	size	flux
MRK 1058	02:49:51.8	+34:59:17	0.017139	0.33 kpc/″	Sy2	1″.26	3500–7800 Å	12 Å	4.24 Å/ px	2×3600 s	45°	2.9 kpc	3.0
MRK 6	06:52:12.2	+74:25:37	0.018813	0.36 kpc/″	Sy1.5	1″.26	3500–7800 Å	12 Å	4.24 Å/ px	2×2700 s	0°	11.7 kpc	3.0
MRK 79	07:42:32.8	+49:48:35	0.022189	0.43 kpc/″	Sy1.2	1″.26	3500–7800 Å	12 Å	4.24 Å/ px	4×1800 s	10°	9.6 kpc	2.5
MRK 622	08:07:41.0	+39:00:15	0.023229	0.45 kpc/″	Sy2	2″.10	3500–7800 Å	25 Å	4.24 Å/ px	2×1800 s	66°	4.5 kpc	3.0
MCG-01-24-012	09:20:46.2	-08:03:22	0.019644	0.38 kpc/″	Sy2	2″.10	3500–7800 Å	25 Å	4.24 Å/ px	2×1800 s	65°	4.0 kpc	4.5
UGC 6100	11:01:34.0	+45:39:14	0.029500	0.57 kpc/″	Sy2	2″.10	3500–7800 Å	25 Å	4.24 Å/ px	3×1800 s	0°	10.0 kpc	3.0
NGC 3516	11:06:47.5	+72:34:07	0.008836	0.17 kpc/″	Sy1.5	2″.10	3500–7800 Å	25 Å	4.24 Å/ px	4×1800 s	30°	7.0 kpc	3.0
NGC 5347	13:53:17.8	+33:29:27	0.007789	0.15 kpc/″	Sy2	2″.10	3500–7800 Å	25 Å	4.24 Å/ px	4×1800 s	37°	2.0 kpc	3.0
IRAS 16288+3929	16:30:32.6	+39:23:03	0.030558	0.59 kpc/″	Sy2	2″.10	3500–7800 Å	25 Å	4.24 Å/ px	3×1800 s	65°	9.6 kpc	4.0
UGC 10889	17:30:21.4	+59:38:24	0.028306	0.55 kpc/″	Sy2	1″.26	3500–7800 Å	12 Å	4.24 Å/ px	4×1800 s	113°	3.6 kpc	10.0
MCG+03-45-003	17:35:32.7	+20:47:48	0.024323	0.47 kpc/″	Sy2	1″.26	3500–7800 Å	12 Å	4.24 Å/ px	2×1800 s	20°	5.4 kpc	20.0
NGC 7674	23:27:56.7	+08:46:45	0.028924	0.56 kpc/″	Sy2	1″.26	3500–7800 Å	12 Å	4.24 Å/ px	2×3600 s	108°	9.3 kpc	3.0

TABLE 2.1— The AFOSC sample data. The last column is the limit flux in units of 10^{-18} erg cm^{-2} s^{-1} arcsec^{-2}

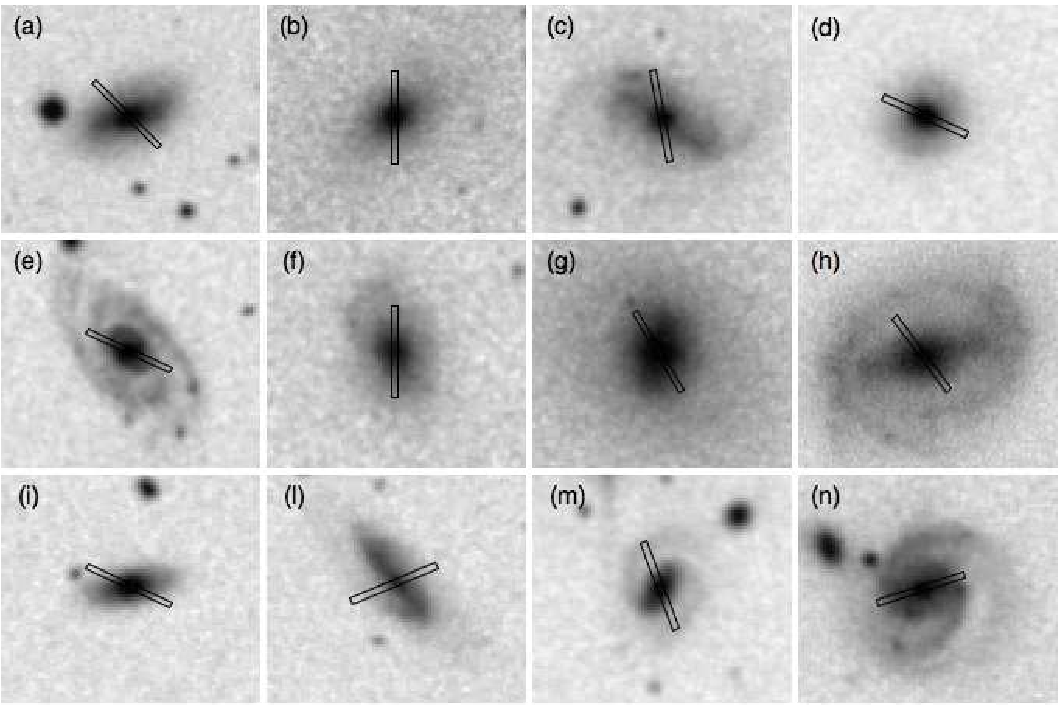

FIGURE 2.7— DSS images of the AFOSC sample galaxies. North is up and East is to the left. The rectangle indicates the PA of the slit, its length corresponds to 30″. The images order is the same as in Table 2.1.

is an intermediate type Seyfert, it shows in our longslit spectrum a very extended [O III] emission (see Figure 2.9) up to 32″ (~12 kpc, assuming H_0=75 km s^{-1} Mpc^{-1}). We found and collected both low and high resolution MPFS data from the SAO archive, furthermore we requested new high resolution observations off-centered to map the elongated emission visible in the [O III] emission images from Kharb et al. (2006) and Kukula et al. (1996), see Figure 2.9 in which the centered and off-centered f.o.v. are shown.

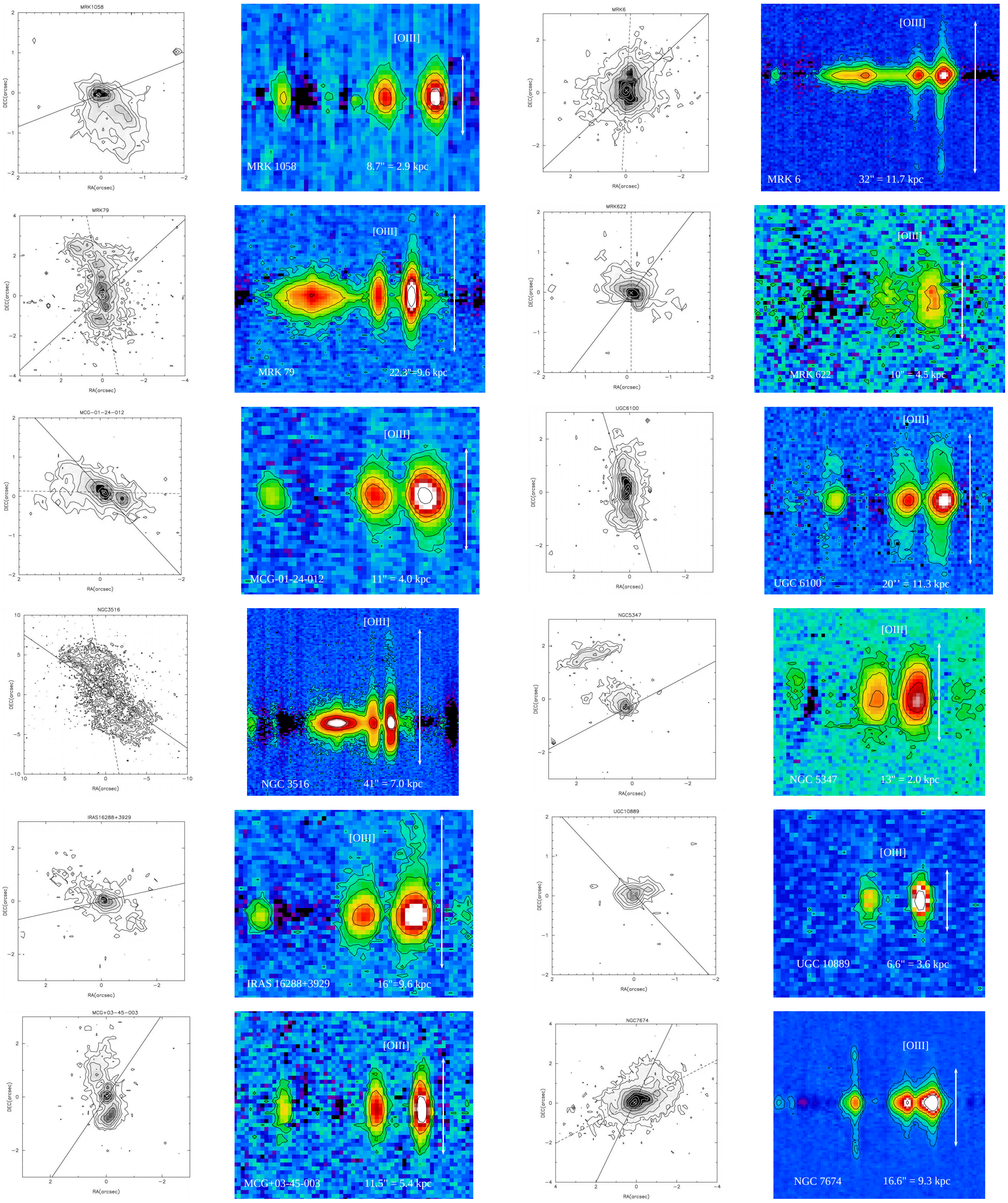

FIGURE 2.8— HST [O III] images (Schmitt et al. 2003) and Hβ+[O III] emission lines from AFOSC spectra.

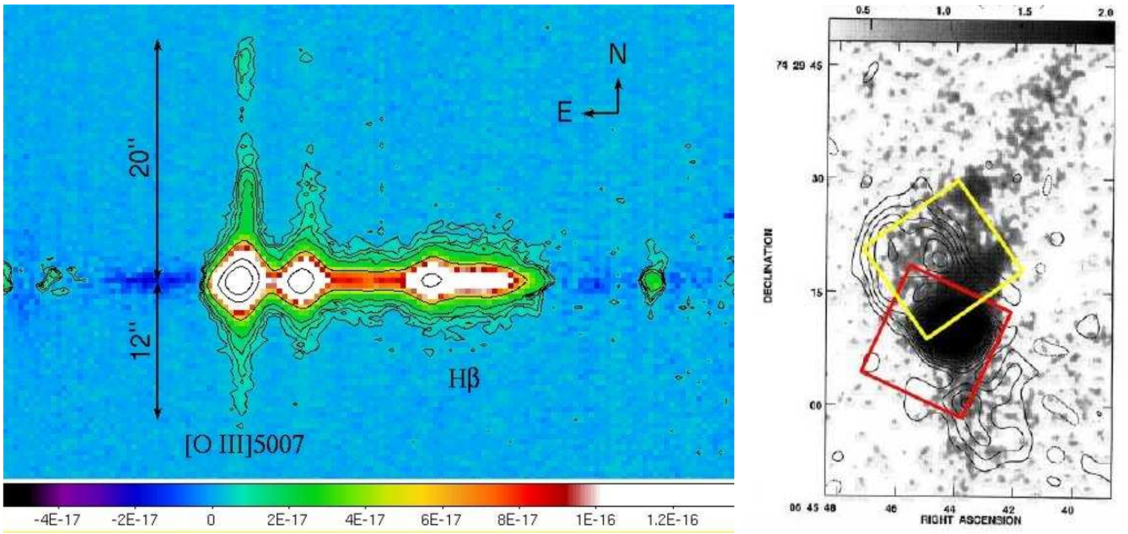

FIGURE 2.9— Continuum subtracted longslit spectrum of Mrk 6 taken at the 1.8-mt telescope of the Asiago Observatory. The [O III] emission line and radio image for MRK 6 (Kharb 2006) overlaid with the two fields of view (red and yellow squares). North is up and East is to the left.

Having found these two interesting objects, we decided to focus our attention on them, and perform a thorough analysis of their ENLR. First we focused on the physical and kinematics properties of the gas in NGC 7212 a Seyfert 2 which is expected to have ionization cones, according to the Unified Model. NGC 7212 was observed in the spectral range 3800–7300 Å with a low resolution grating (600 lines/mm) and in the spectral range 4000–7300 Å with a high resolution grating (1200 lines/mm), which give spectra with dispersion of 1.5 Å/px and 0.8 Å/px, and instrumental resolution of ~6 Å and ~3 Å, respectively. We took also a longslit spectrum of NGC 7212 with the B&C spectrograph at the 1.2-mt telescope of the Asiago Observatory in the spectral range 3400–7800 Å with a dispersion of 2.3 Å/px and instrumental resolution of 9 Å. We extracted from the NTT–ESO public archive another longslit spectrum obtained in two spectral ranges (3650–5350 Å and 4540–7060 Å). The dispersion is 1.84 Å/px in the blue and 1.58 Å/px in the red. The instrumental resolutions are ~13 Å and ~11 Å. The spatial resolution element is 0.37″ px^{-1} in the blue and 0.″33 px^{-1} in the red. The slit was oriented along the position angle of the maximum extent of the [O III] emission (PA~170°) taken from Schmitt et al. (2003). From HST-MAST archive also WFPC2 images in the F606W broad band filter have been obtained. Broad band BVR images have been obtained at the SAO 6-mt telescope with SCORPIO.

Then we analyzed in detail MRK 6, characterized by an intermediate type Seyfert spectrum but also by its unusually extended [O III] emission. MRK 6 was observed in the spectral range 3800–7300 Å with a low resolution grism (600 lines/mm) and in the spectral range 4000–7300 Å with a high resolution grism (1200 lines/mm), which give spectra with dispersion of 1.5 Å/px and 0.8 Å/px, and instrumental resolution of ~6 Å and ~3 Å, respectively. This galaxy was observed in two different fields of view: during the first run it was centered on the active nucleus, while in the second run it was off-centered by 8″ towards North with respect to the nucleus. This offset was applied in order to observe the [O III] emission extended about 30″–35″ in the N-S direction. This extended emission is clearly visible in our longslit spectrum taken with AFOSC at the 1.8-mt telescope of the Asiago Observatory (Figure 2.9) in the spectral range 3600–7800 Å (dispersion 4.7 Å/px, instrumental resolution 15 Å), and in the [O III] narrow-band image plus radio map published by Kharb (2006) and Kukula (1996) (see Figure 2.9). Broad band images have been obtained from the public archive of the Isaac Newton Group (ING).

For the second part of this work, we selected a sample of eleven Seyfert 2 galaxies, with extended [O III] emission, to be observed with the MPFS at the 6-mt telescope of the SAO or to be extracted from the SAO archive. The spectra we collected are obtained with the low resolution grating, in a spectral range from the [O II] λ3727 to the [Ar III] λ7135. Our aim was to perform a statistical analysis of the properties of the ENLR gas as a function of radial distance from the nucleus.

All the observational data and the archival data used in this work are listed in the Table 5.1, where $\Delta\lambda$ is the spectral resolution in Åand $\delta\lambda$ is the dispersion in Å/px.

2.2.1 Reduction procedures

Longslit spectra were reduced following the classical procedures (bias subtraction, flat-field correction, wavelength and flux calibration, sky subtraction and cosmic rays correction) and using IRAF (Image Reduction and Analysis Facility) tasks. The raw data from an IFS observation usually consists of multiple (anything from tens to thousands) spectra, each originating from an individual element of the IFU. In order to construct the data-cube, it is necessary to extract the individual spectra from the detector and rearrange them back into the geometric pattern that they held at the focal end of the telescope. In our case the raw data contain 272 spectra (256 object spectra and 16 sky spectra), therefore it is clear that an authomatic or semi-authomatic reduction procedure is needed.

In this work we applied two different approaches to reduce data: the first one running in IRAF environment and the second one written in IDL language. We tested that both give similar results, but the latter is more efficient. The steps to perform the reduction for IFU spectra are: bias subtraction, tracing, flat-field correction, wavelength and flux calibration, sky subtraction and cosmic rays correction.

The IRAF reduction package for MPFS data is called mpfs and it was created by our group. We subtracted the bias from our data following the usual procedure, we used the specific IRAF package for MPFS spectra. It is in general absolutely necessary to check the overlapping of the frames. In our case we already know that mechanical flexures of the instrument sometimes cause non-negligible shifts between the images. These shifts can become very dangerous, when the flat field geometry is used for example to extract the object spectra: due to their extreme closeness, information of different spectra can be mixed producing a completely wrong result. To solve the problem, the XCORR task was written, based on the cross-correlation method. This task correlates different images, calculates the relative differences and then shifts the images with respect to a reference image, which is usually a flat field.

After the correlation, the interactive DOMPFS task can be applied. This task was obtained by adapting the IRAF DOFIBERS task to MPFS configuration. It allows to do tracing, flat correction and wavelength calibration. It also allows to extract the monodimensional spectra. The main idea of this task is to use an internal flat field exposure as reference image to determine the geometrical scheme of the spectra arrangement; this scheme is subsequentely applied to the other frames in order to extract the 256 monodimensional spectra. First the tracing of the spectra must be done. In fact the spectra are not parallel to the lines of the CCD and the shift in y-direction for each spectrum must be calculated. A deviation with variable angle is in fact present; this angle decrease continuously from the bottom to the top of the frame,

Object name	RA (J2000.0)	Dec (J2000.0)	z (NED)	Instrument	Spectral range	$\Delta\lambda$	$\delta\lambda$	T_{exp}
MRK 348	00:48:47.1	+31:57:25	0.015034	MPFS	3700 – 6520 Å	6.5 Å	1.46 Å/ px	2×1200 s
				MPFS	4360 – 7310 Å	6.5 Å	1.46 Å/ px	4×900 s
MRK 1157	01:33:31.2	+35:40:06	0.015167	MPFS	3680 – 6300 Å	6.5 Å	2.54 Å/ px	3×1200 s
				MPFS	4650 – 7300 Å	6.5 Å	2.54 Å/ px	3×1200 s
UGC 2024	02:33:01.2	+00:25:15	0.022342	MPFS	3200 – 7450 Å	7 Å	1.43 Å/ px	6×1200 s
MRK 1066	02:59:58.6	+36:49:14	0.011946	MPFS	3700 – 6545 Å	7 Å	1.47 Å/ px	3×1200 s
				MPFS	4400 – 7325 Å	7 Å	1.47 Å/ px	2×1200 s
MRK 1073	03:15:01.4	+42:02:09	0.023343	MPFS	3700 – 5868 Å	6.5 Å	1.47 Å/ px	5×1100 s
				MPFS	4300 – 7280 Å	6.5 Å	1.47 Å/ px	5×1200 s
MRK 607	03:24:48.7	-03:02:32	0.008883	MPFS	3620 – 7500 Å	7 Å	1.43 Å/ px	3×1200 s
MRK 3	06:15:36.3	+71:02:15	0.013509	MPFS	3680 – 6300 Å	7 Å	2.55 Å/ px	4×1200 s
				MPFS	4720 – 7300 Å	7 Å	2.55 Å/ px	5×1200 s
MRK 620	06:50:08.6	+60:50:45	0.006138	MPFS	3660 – 6240 Å	6.5 Å	1.47 Å/ px	4×1200 s
				MPFS	4555 – 7500 Å	6.5 Å	1.47 Å/ px	3×1200 s
MRK 6	06:52:12.2	+74:25:37	0.018813	AFOSC	3600 – 7800 Å	15 Å	4.7 Å/ px	2×2700 s
				MPFS offset	4450 – 5965 Å	3 Å	0.75 Å/ px	6×1200 s
				MPFS offset	5845 – 7350 Å	3 Å	0.76 Å/ px	3×1200 s
				MPFS	4500 – 5830 Å	3 Å	1.34 Å/ px	2×900 s
				MPFS	5800 – 7140 Å	3 Å	1.34 Å/ px	3×1200 s
				MPFS	3768 – 6200 Å	6 Å	2.60 Å/ px	3×1200 s
				MPFS	4775 – 7380 Å	6 Å	2.61 Å/ px	3×1200 s
MRK 78	07:42:41.7	+65:10:37	0.037150	MPFS	3650 – 5855 Å	6.5 Å	1.46 Å/ px	6×1200 s
				MPFS	4350 – 7250 Å	6.5 Å	1.47 Å/ px	6×1200 s
MCG+03-45-003	17:35:32.7	+20:47:48	0.024323	MPFS	3730 – 5890 Å	6.5 Å	1.46 Å/ px	4×1200 s
				MPFS	4350 – 7290 Å	6.5 Å	1.47 Å/ px	4×1200 s
NGC 7212	22:07:01.3	+10:13:52	0.026632	NTT	3650 – 7100 Å	4 Å	1.6 Å/ px	1800 s
				B&C	3400 – 7800 Å	9 Å	2.3 Å/ px	3×1200 s
				MPFS	3780 – 5800 Å	6 Å	1.46 Å/ px	4×1200 s
				MPFS	4340 – 7310 Å	6 Å	1.47 Å/ px	6×900 s
				MPFS	4140 – 5650 Å	3 Å	0.76 Å/ px	4×1200 s
				MPFS	5765 – 7260 Å	3 Å	0.76 Å/ px	2×900 s
				MagE	3600 – 7000 Å	0.85 Å	–	6×1200 s
NGC 7319	22:36:03.5	+33:58:33	0.022507	MPFS	3690 – 6300 Å	7 Å	2.54 Å/ px	3×1200 s
				MPFS	4670 – 7300 Å	7 Å	2.54 Å/ px	7×1200 s

Table 2.2— The sample data

assuming as reference point the first bottom-left pixel. In addition the position of the centroid of each spectrum does not follow always a linear behaviour; this is true only in the central section of the frame. First the task plot the flat field across the dispersion direction, in order to see the peak of each spectrum. We identify the centroid of each spectrum, we fix the FWHM (in our case is ~ 4 px) and we centre all the spectra. Then the task traces the centroid of each spectrum for all the aperture along the dispersion. The tracing precision is strongly linked to the flat field quality: if the frame is not well illuminated the profiles can become so faint and noisy that the algorithm is not able to find the center anymore. In such bad cases, some points must be added by hand to complete the fitting over the whole dispersion, after having checked the centroid position at different columns. After the tracing has been done, DOMPFS extracts the 1–D spectra of the flat field, which will be used for correcting the pixel-to-pixel response and the differences in the fibers throughput. Later on all the spectra are averaged and the result is fitted with a smooth function; then the individual spectra are divided by this curve. This normalization procedure is necessary to remove the mean flat field shape, which otherwise would introduce changes of the count levels of the object. After the tracing, the flat spectrum is shifted according to the result of tracing; now we are sure that the information in each CCD line come from the same spectrum. The task goes to the next block of the reduction and extracts the arc calibration spectra, which are used to define the dispersion solution. Some spectral lines of the firts vector are interactively marked and a preliminary solution is found, then all the lines are automatically identified, using a database list of lines (in our case He-Ne-Ar lines), and the final solution can be determined. The fitting function usually applied is a Chebyshev polynomial typically with low orders like 3 or 5. Spectral lines with high residuals are removed until the RMS of the fitting goes down under a value of 10% of the nominal dispersion. Then this vector is taken as reference for the others: its identified features are in sequence reidentified in each single vector and a dispersion solution is found for all the spectra. In the end of this procedure a linear wavelength coordinate system is applied, defined by a start and end wavelength, a wavelength interval per pixel, and the number of the pixels. Now, DOMPFS can extract the spectra of the objects, which are corrected for the normalized flat field and calibrated in wavelegth. A task of the package SPECRED, named SKYSUB is used for the sky subtraction. This task selects the subset of the sky spectra and combines them into a usually average spectrum, which is subtracted from the spectra of the objects. To perform the flux calibration, at least one spectrophotometric standard star has to be observed. Its spectra are extracted, flat fielded, wavelength calibrated and sky subtracted. Then a task named VECADD is used to sum together the vectors in which the star is present in order to collect its total incoming flux. Then the usual step for the flux calibration (STANDARD and SENSFUNC) are applied to the standard stars and the flux calibration is applied to the object spectra using CALIBRATE.

The data of the second part of this thesis have been reduced using P3d (Sandin et al. 2010) that is a general data-reduction tool written in the IDL language. It has been developed to work with any fiber-fed IFU of any IFS. Currently the software has been configured and tested with PMAS, VIRUS-P and SPIRAL. For MPFS data some changes were done. P3d makes automatically the reduction steps, but allows us to interactively inspect and optimize parameters when required. The software, updates, documentation and tutorials can be found at the project web site: **http://p3d.sourceforge.net**.

The current version of P3d handles the following five data-reduction tasks:

- creation of a master bias;
- automatic finding and tracing spectra on the detector;
- creation of a dispersion mask for wavelength calibration;
- creation of a data set that is used to flat field the extracted spectra;
- extraction of object data, using different extraction methods.

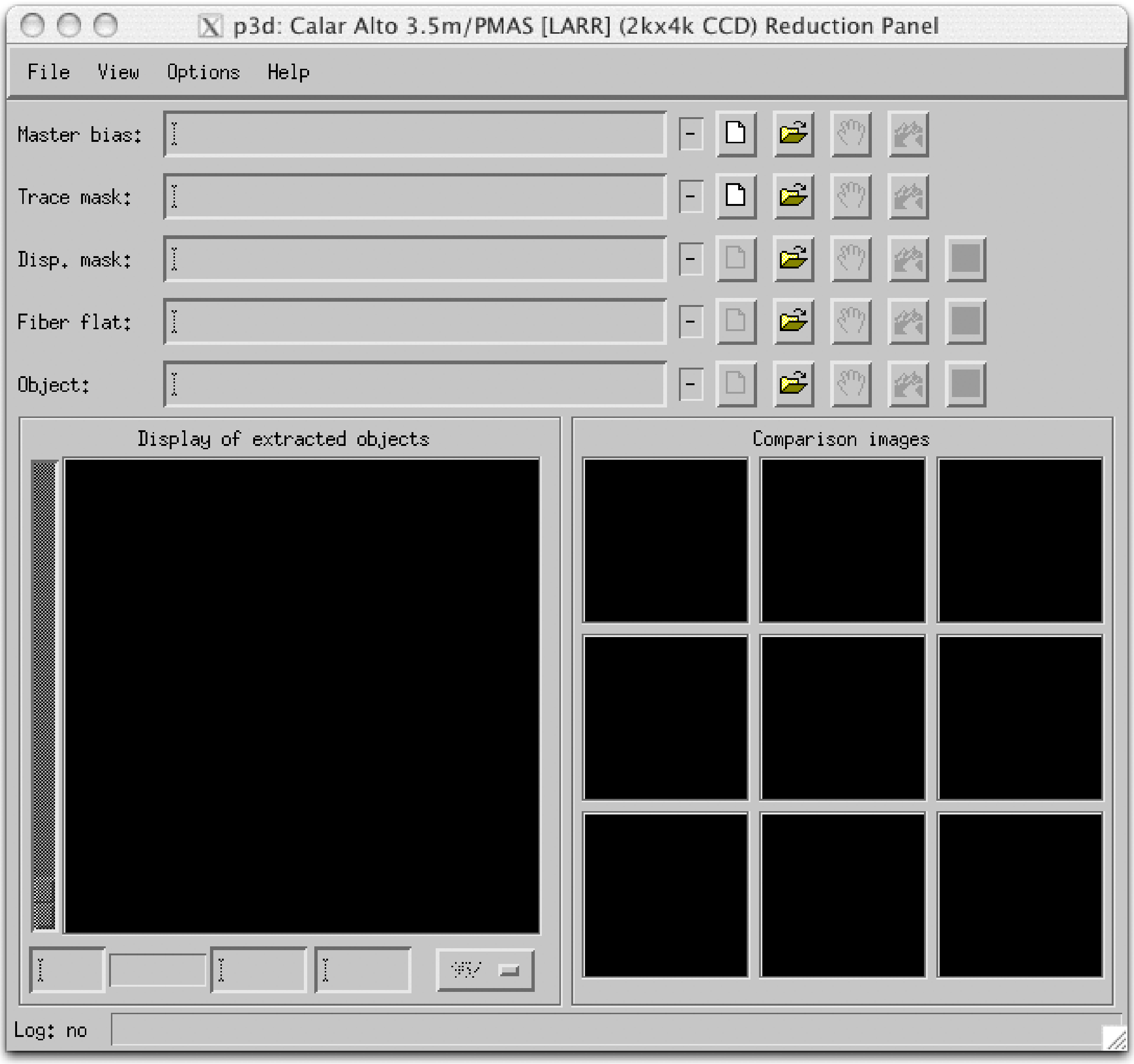

FIGURE 2.10— The graphical interface of P3d. Here calibration and object files can be inserted and the final calibrated images can be checked.

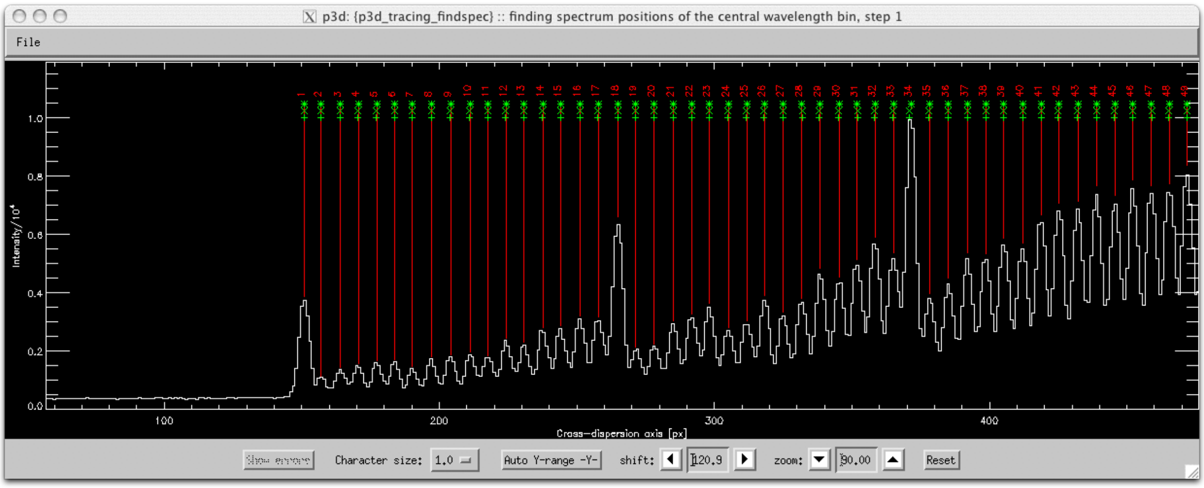
p3d: {p3d_tracing_findspec} :: finding spectrum positions of the central wavelength bin, step 1

Character size: 1.0

shift: 120.9

zoom: 90.00

FIGURE 2.11— An example of identification of the centroid of each spectrum, using the flat-field image. Each peak is a spectrum automatically identified by P3d.

P3d also provides several graphical tools to inspect the raw data and the output of the different tasks. Spectrum extraction can be done using either aperture extraction, or a modified optimal extraction, or using a multi-profile deconvolution optimal extraction. We used the aperture extraction, that is the same method applied in the IRAF case.

In the first step a master bias image is created by combining a set of at least three bias images. This master bias is subtracted from the raw data in all consecutive steps. In the second step the position of every spectrum is determined along the dispersion axis with a well-illuminated calibration exposure, using a flat field. The resulting trace mask is used in all consecutive steps when spectra are extracted. In the third step a dispersion correction is determined for every spectrum, using one or several arc lamp exposures. An extracted flat field image is created in the fourth step in order to correct for wavelength-dependent variations of every spectrum and for differences in the fiber-to-fiber throughput. In the final step all spectra are extracted from object exposures, optionally applying first the dispersion correction and thereafter the flat-field correction. This program does not take into account the shift of the whole image due to flexures of the telescope. So before to reduce the object spectra, we applied the task XCORR as explained before.

The main difference in the reduction procedure is the wavelength calibration step. An image with extracted spectra of an arc lamp exposure shows emission lines as curves across the cross-dispersion axis (Figure 2.12). In order to find a dispersion solution all spectra should be aligned and stretched to use the same starting wavelength and size of wavelength bins. P3d requires a list of lines with known wavelengths, some information about the expected wavelength range, and an arc lamp image to create a dispersion mask.

In a first step a list of lines with well known wavelengths is selected. In a second step a line mask curvature is determined by calculating positions for one or two lines in the arc frame. In a third step the line mask is shifted along the dispersion axis in order to achieve a rough match between the line mask and the emission lines of the lamp. If lines cannot be well matched across the entire dispersion axis the

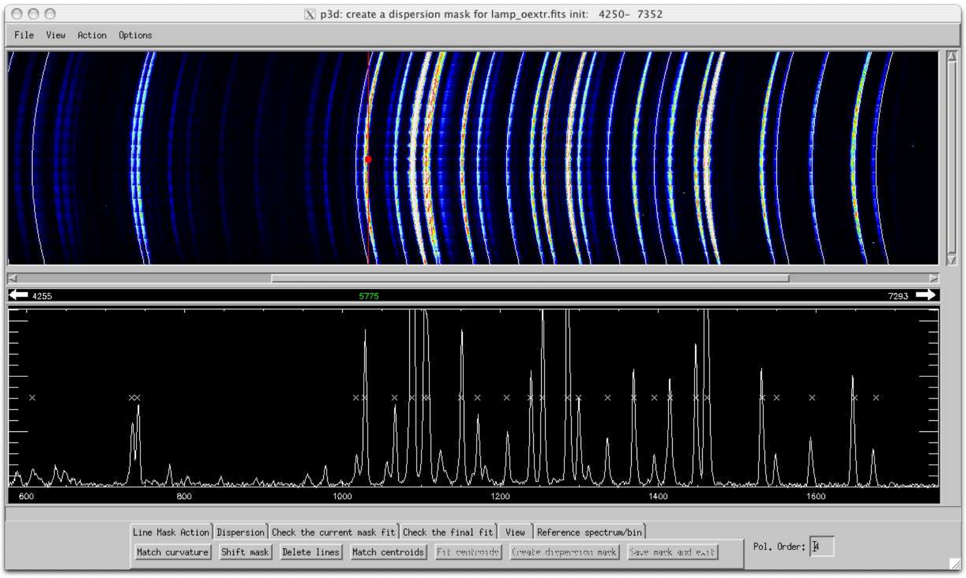

Pol. Order: 4

FIGURE 2.12— The first step of the dispersion correction. Upper panel: the extracted 2D spectrum of a comparison lamp, where we can clearly see that the emission lines are curved. Bottom panel: the identification of the emission lines, each lines is marked with a cross, in x there is the emission lines positions still in pixel.

dispersion can be changed manually. More precise pixel positions of entries in the line mask are then calculated by correlating every line in the line mask with the data, this is done for every spectrum. The final step is the creation of a dispersion mask. A linear polynomial of an usually low order is fitted to the pixel positions at all wavelengts, for every spectrum, in the line mask (Figure 2.13). So the solution is not re-applied to all spectra, but it is obtained for each spectrum by fitting along the curve profile. This is a more efficient method to perform the wavelength calibration.

Cosmic rays hit can be removed either by combining a set of raw data images, or using for example the approach of van Dokkum (2001) or Pych (2004).

After the reduction procedure, all these spectra have been corrected for Galactic reddening, using the IRAF task DEREDDEN and the value of *V*-band absorption (A_V) derived from NED, then we checked if the correction for atmospheric absorptions was necessary and we verified that this correction is needed for objects with redshift z $\sim$ 0.02: in fact at this redshift the [S II] doublet is in the range 6870–6880 Å where atmospheric absorption bands exist, which makes difficult to accurately measure the flux of these emission lines. The following objects: NGC 7212, MRK 348, MCG 03-45-003, MRK 1066, MRK 1073, NGC 7319, and UGC 2024 were corrected for atmospheric absorptions, by means of the IRAF tasks ATMO and RMAT, written by our group. First the task needs as input the flux-calibrated spectrum of the standard star. The continuum of the standard is fitted and the fit is divided by the stellar spectrum. The result is a spectrum with the mean value equal to 1 and the atmospheric absorption features in emission. Then all the intensity values at a λ shorter than 6700 Å is put equal to 1. Finally the corrected spectrum is obtained using the task RMAT that simply multiplies the observed spectrum by the output of ATMO.

After that, each spectrum has to be shifted at rest-frame. First we make the continuum emission

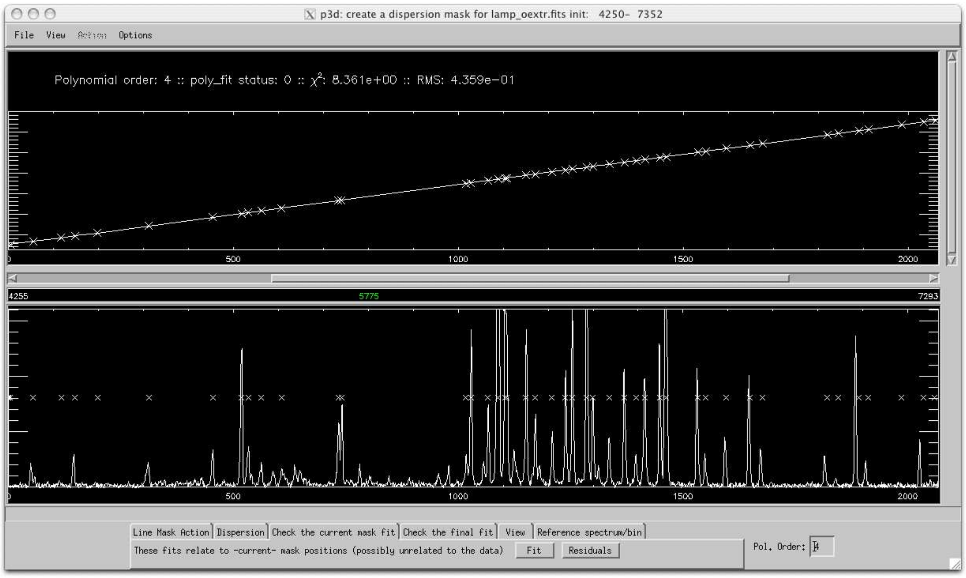

```
p3d: create a dispersion mask for lamp_oextr.fits init:   4250-  7352
```

```
Polynomial order: 4 :: poly_fit status: 0 :: χ²: 8.361e+00 :: RMS: 4.359e-01
```

```
These fits relate to -current- mask positions (possibly unrelated to the data)
```

FIGURE 2.13— The linear polynomial fit applied to the pixel positions of the emission lines. Upper panel: the fit and the best-fit parameters (order, χ^2 and rms). Bottom panel: the identified emission lines marked with a cross.

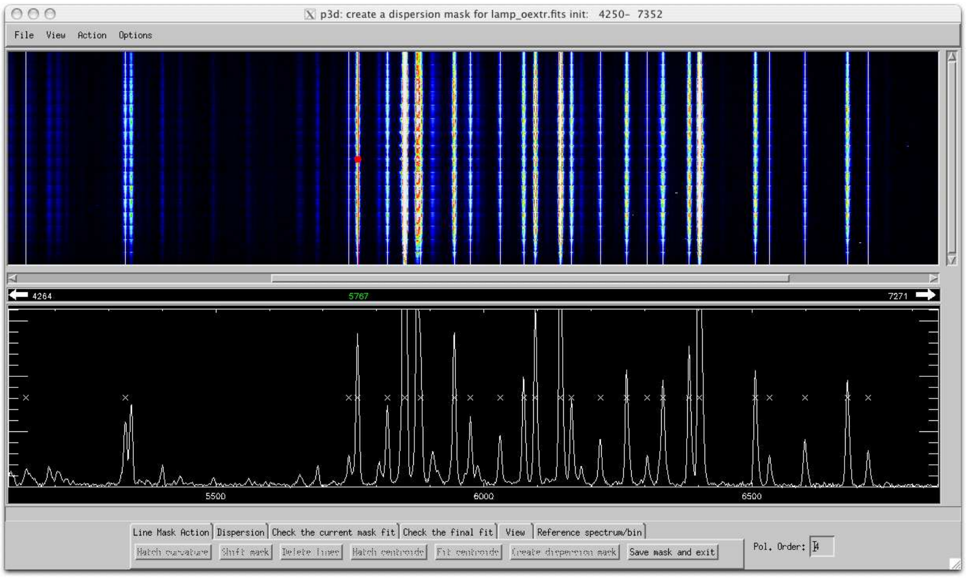

```
p3d: create a dispersion mask for lamp_oextr.fits init:   4250-  7352
```

FIGURE 2.14— The comparison spectrum after the wavelength calibration. Now the emission lines are straight lines (upper panel) and in the x-axis the emission lines position are in Ångstrom (bottom panel).

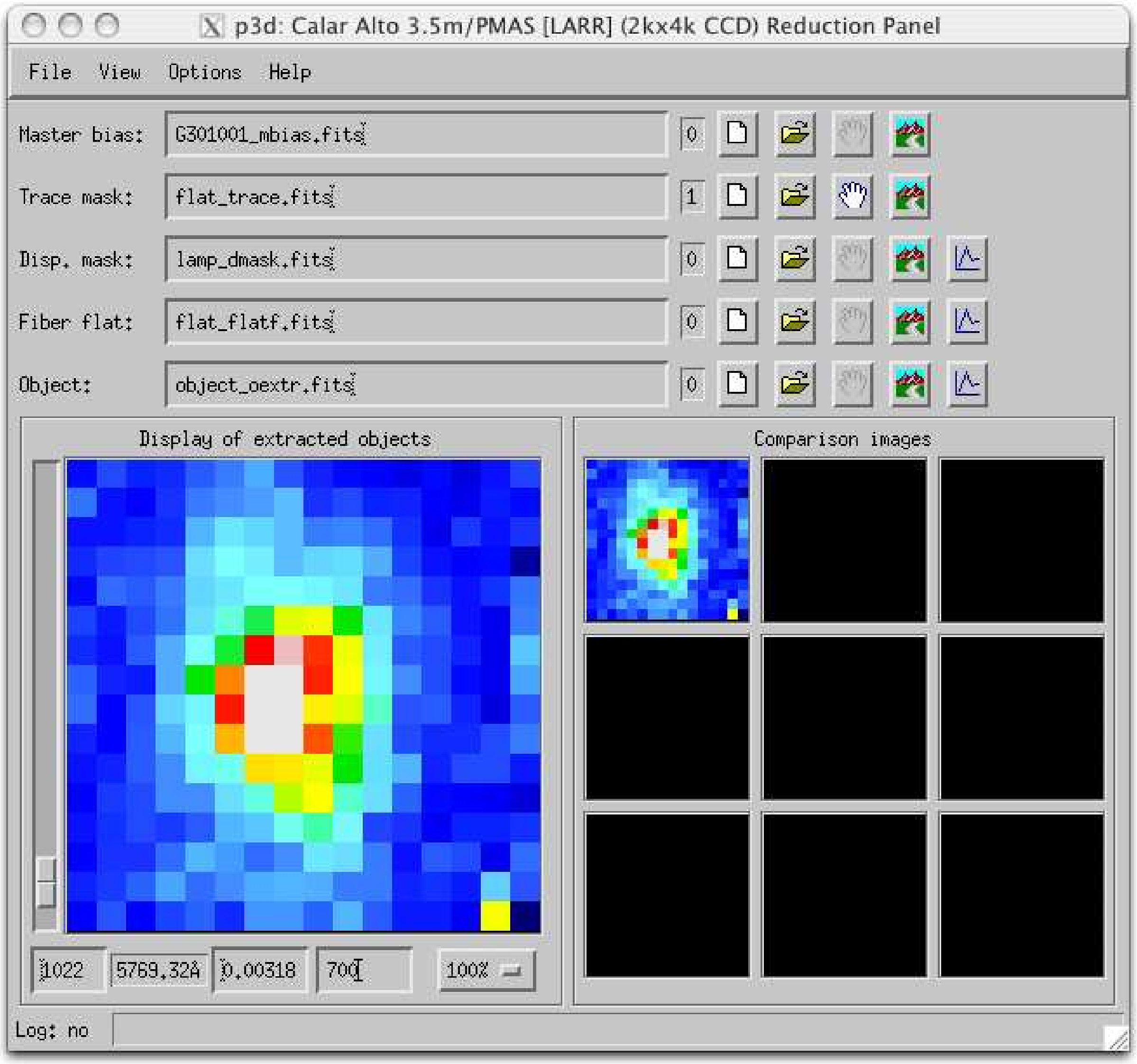

Master bias: G301001_mbias.fits 0
Trace mask: flat_trace.fits 1
Disp. mask: lamp_dmask.fits 0
Fiber flat: flat_flatf.fits 0
Object: object_oextr.fits 0

1022 5769.324 0.00318 700

Log: no

FIGURE 2.15— The first way to analyze the calibrated image. We can reconstruct the 2D maps in a wavelength range. We can compare up to 9 calibrated images.

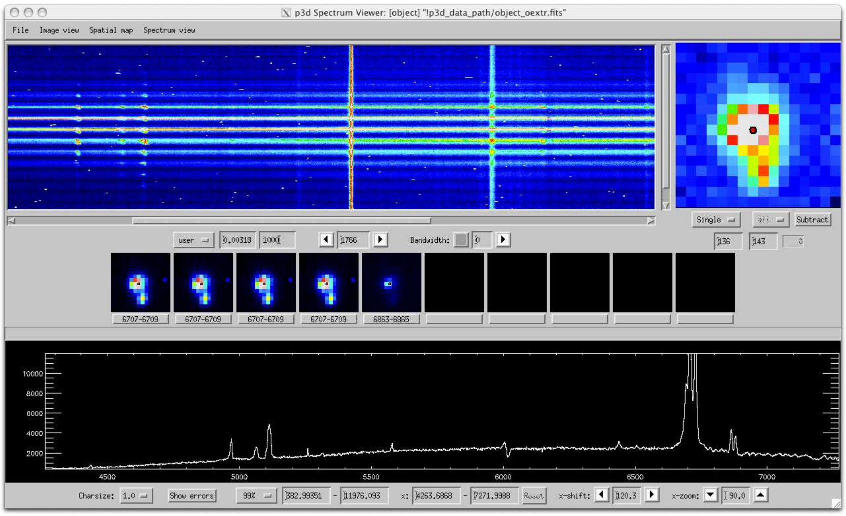

0.00318 1000
1766
Bandwidth: 0
136 143 0
Charsize: 1.0
382.99351 - 11976.093
x: 4263.6868 - 7271.9988
x-shift: 120.3
x-zoom: 90.0

FIGURE 2.16— The second and more complete way to check and visualize the calibrated spectrum. Upper-left: the calibrated 2D spectrum of an object. Upper-right: the 2D map of the same object integrated in a spectral range (these images can be saved in the middle-line boxes). Bottom: the 1D spectrum of the aperture defined by selecting a spaxel in the 2D images (in this case, it is the spectrum of the nuclear spaxel where the red dot is.). Changing the cursor position on the 2D spectrum, we can integrate in different spectral regions, and changing the cursor position on the 2D images, we can see different 1D spectra.

map at 5500 Å, finding the central spaxel for each object. Then we applied RVIDLINES to the nuclear spectrum both for emission and absorption lines deriving the redshift and we used NEWREDSHIFT to shift the spectra at the rest-frame.

We also checked if a correction for atmospheric refraction was necessary. To this aim, 2D maps of continuum emission centered at different wavelengths (3800 Å, 4200 Å, 4550 Å, 4800 Å, 5400 Å, 5700 Å, 6200 Å, 6450 Å, 6850 Å) were created and using IMCENTROID we calculated the centroid and the x and y shifts with respect to the reference image at 5400 Å. We decided to apply the correction when the shifts in the x or y direction were larger than about 1 spaxel. We corrected the following galaxies MCG 03-45-003, MRK 607, NGC 7319, UGC 2024, NGC 7212, MRK 1073 and MRK 78. We used two tasks written by us, running in the IRAF environment, named ACORR and DARCSPEC. The first task determines the correction to apply for atmospheric refraction, the latter applies this correction. In particular, ACORR creates images of the emission for 20–30 intervals centered at different λ along the dispersion direction, then it calculates the centroid of each image (x, y) using IMCENTROID and it allows us to interactively fit with a straight line the relations λ vs. x and λ vs. y, using NFIT1D. We verified that in some cases the fit should be done with an higher order function. DARCSPEC uses the x(λ) and y(λ) functions obtained from ACORR and for each λ along all the spectral range, makes an image, apply the needed shift (taking as reference the centroid at an intermediate λ, i.e. 5500 Å) and then transforms the image in a table with three columns: x, y, λ. From these output tables the spectrum corrected for atmospheric refraction is reconstructed by the task.

In order to measure accurately the emission lines, the underlying stellar component has to be subtracted from the spectra. This is particularly important in the case of hydrogen and helium Balmer lines. By applying the STARLIGHT software (Cid Fernandes et al. 2005, Cid Fernandes et al. 2007) the galactic stellar component was fitted and subtracted. Before being analyzed with STARLIGHT, the spectra dispersion has been modified to a value of 1 Å/px with DISPCOR. Then from the multi-aperture spectrum each 1D spectrum has been extracted and converted into text format using WSPECTEXT. These are the inputs of STARLIGHT, namely, for each aperture, a table with two columns, wavelength and flux. This software allows to fit an observed spectrum, with a model created with a number of spectral components from a predefined set of synthetic spectra. The model spectrum is a function of the stellar populations, the global and selective extinction (A_V and A_V^y) and of two kinematical parameters (v_* that is the velocity shift and σ_* that is the velocity dispersion). STARLIGHT reddens the synthetic spectra and convolves them by using a Gaussian function with a σ that allows to get the stellar velocity dispersion. Then makes a linear combination of these spectra. We used 45 synthetic spectra by combining 15 ages (from 10^6 yr up to 13×10^9 yr) with 3 metallicities (Z=0.004, 0.02 and 0.05 $Z_\odot$), and the Cardelli Clayton & Mathis (CCM, 1989) as extinction function. The synthetic spectrum of the stellar contribution obtained from STARLIGHT for each fiber was subtracted from the observed one to obtain a pure emission line spectrum, now the hydrogen and helium Balmer lines could be correctly measured. These procedures have been performed for low resolution spectra (see Figure 2.17 and Figure 2.18). For high resolution spectra, we did not apply STARLIGHT because in this case the stellar contribution was less important. In the case of MRK6 we did not apply STARLIGHT for both low and high resolution spectra, because the continuum was dominated by the AGN, being MRK 6 an intermediate type Seyfert galaxy. Therefore, for this object we faced the broad emission component problem (see chapter 4).

2.2.2 Measuring the emission lines

The data without the stellar component contribution are ready to be analyzed. As for the reduction procedures, also for measuring spectral lines we need an automatic software, indeed our IFS spectra are composed of 240 or 256 spectra and for each spectrum we have at least 10 emission lines to fit. There are different tasks to fit emission lines. For example SPLOT or NGAUSSFIT in IRAF or XALICE in MIDAS.

The IRAF tasks are useful for simple and regular emission lines profile without additional components. Actually also a multi-Gaussian fitting can be performed, for example the SPLOT task can deblend multiple line profiles (for example [N II] and Hα) using different functions (Gaussian, Lorentzian or Voigt profile) and allowing to hold fixed some parameters, for example the positions, or the FWHM. In particular it is possible to let all the parameters free or to fix some parameters to the same value, for example the FWHM. It is worth noting that for [N II] and Hα it should be useful to fix the FWHM of the [N II], letting the FWHM of Hα free. This cannot be done with SPLOT.

NGAUSSFIT allows to use multiple Gaussian functions to fit a line profile or more lines at the same time. Two function types can be used: “Gaussian”, in which all coefficients are given in absolute data units; and “cgauss” (constrained Gaussians), in which only the first component is given in absolute units and subsequent components are specified relative to the first (amplitudes as a factor of the first, and centers as an offset from the first). This latter form is useful when we need to keep fixed, during the fit, not the absolute values of the Gaussian coefficients, but their relative values, as when constraining spectral lines ratios by atomic physics values, or spectral line positions by their difference in wavelength. It is also possible to use an input table with initial guess, in order to use a previous obtained solution.

In the MIDAS software there is a package for spectral analysis that has been developed by Juan

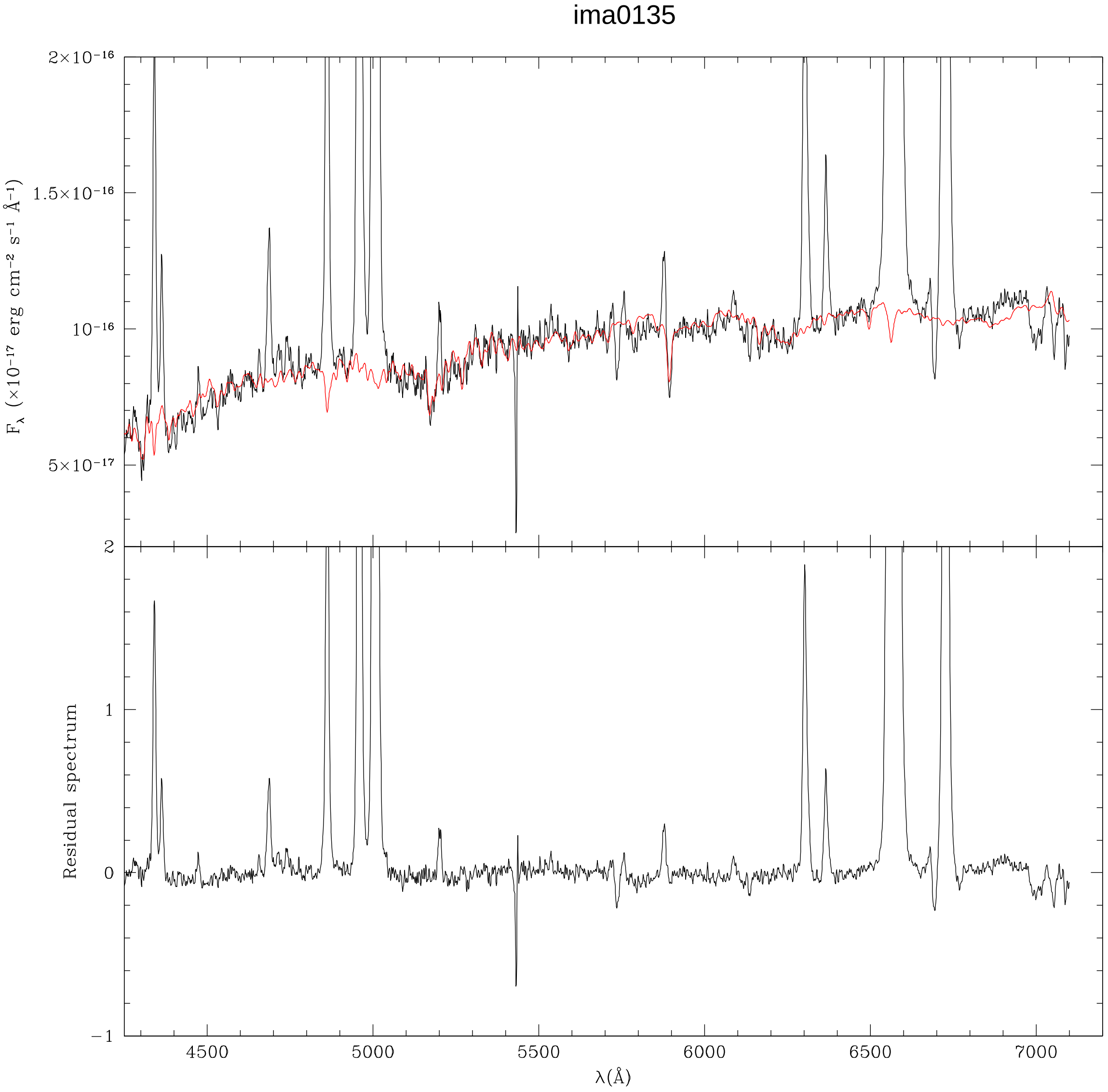

FIGURE 2.17— An example of fit with STARLIGHT applied to the nuclear spectrum of NGC 7212. The spectrum and the STARLIGHT fit are shown in the upper panel; the corrected spectrum is shown in the bottom panel.

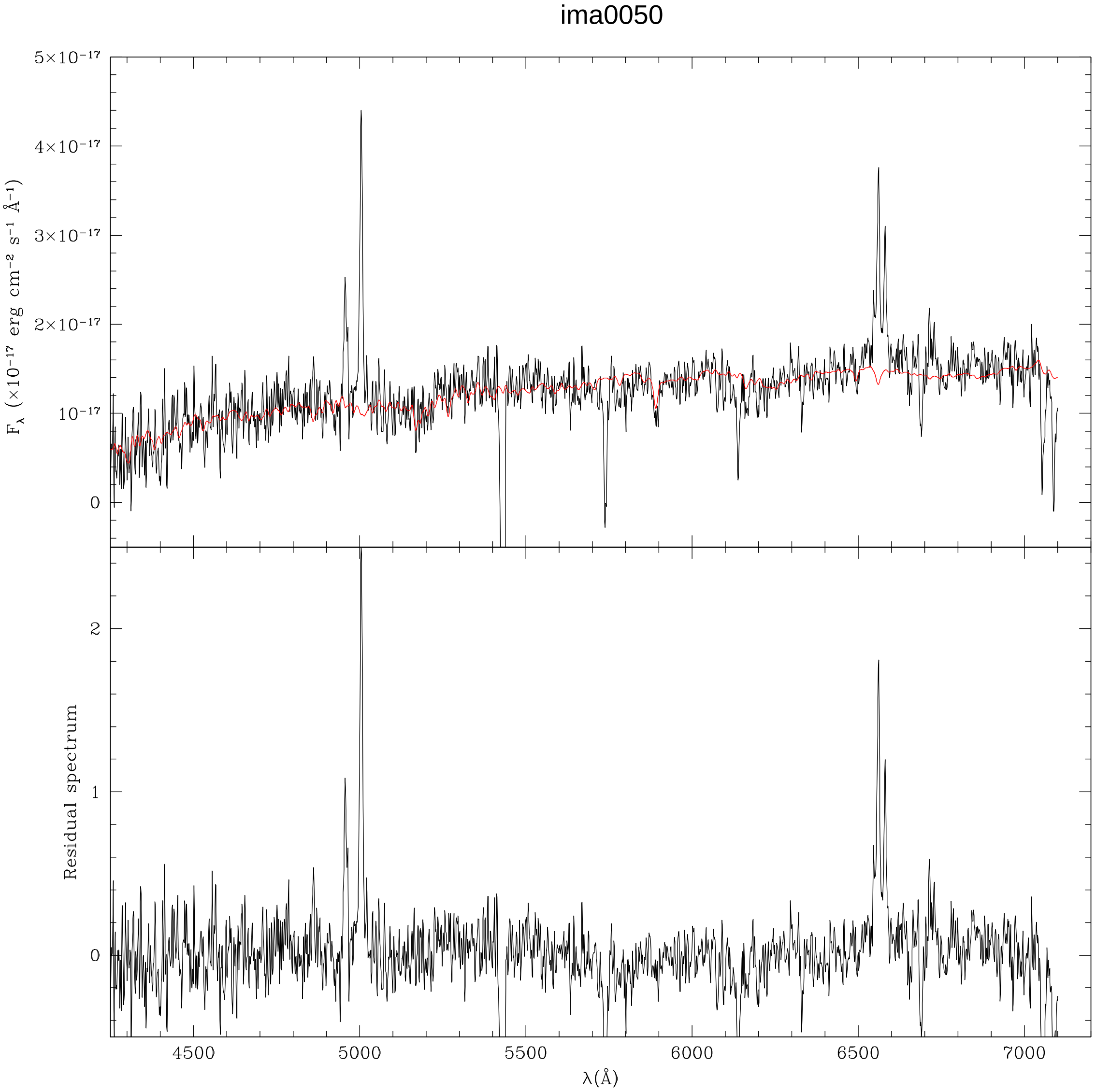

FIGURE 2.18— Another example of fit with STARLIGHT applied to an external spectrum of NGC 7212. The spectrum and the STARLIGHT fit are shown in the upper panel; the corrected spectrum is shown in the bottom panel.

Veliz at La Silla and is based on the graphical user interface XAlice. It provides basic functions for flux integration, including continuum fitting and determination of line parameters like FWHM, equivalent width, flux and continuum level. It allows to perform multiple-component fitting by a set of Gaussians. It is easier to use thanks to its graphical interface, and it allows to keep fixed or variable the intial guess parameters during the fit. It shows the solution, the components and the residuals too (see Figure 2.19). It is useful because the solutions applied to one spectrum can be easily applied to the following ones until the guess parameters are quite similar to the real ones. Indeed, the task is highly dependent to the initial guess in the sense that if the starting parameters are far from the real values, the solution is difficult to be obtained.

Among the different softwares for the analysis of integral field data, PAN (Peak ANalysis) an IDL-based general-purpose curve-fitting utility with a graphical user interface, based on Craig Markwardts MPFIT. PAN can be used to fit any of its own functions (straight line, Gaussian, Lorentzian, etc) or custom functions can be created to fit the data (e.g. Hα + [N II]). There is no limit to the number of functions that can be used simultaneously but for more functions it needs more computation time. PAN is particularly useful for IFU/MOS data since it has the ability to read in multiple spectra at once in an array format, and fit one initial guess to these spectra automatically. It can read in FITS data. The spectrum+fit, the residuals and the numerical results are displayed on-screen for each spectrum, the fit can be reviewed for each spectrum in a very visual manner (see Figure 2.20). The initial parameter guesses (amplitude, position and width) can be specified with the mouse. Our approach to fitting emission lines is:

- select the nuclear spectrum;
- choose the correct function to fit the emission line. For all the single emission lines we used a Gaussian; while for [N II] + Hα and [S II] we used an equation that allows to fit all the lines at the same moment, making a sort of deblending. In particular we used for [N II] + Hα a function in which we fixed equal the FWHM of the [N II] doublet, and the same for [S II] doublet;
- use the cursor to set the peak and the FWHM of the Gaussian;
- modify the parameters of the Gaussian to constrain the fit in order to assure the correct result. We usually let the central wavelength changing within a range of ~10 Å and we limited the minimum value for the flux to zero. For the FWHM we consider for each object a typical range 3 Å<FWHM<20 Å;
- fit the nuclear spectrum and then the software fit all the spectra by modifying the parameters to find the best solution for each spectrum;
- save the result in a table where we have the χ^2 of the fit, the flux, the central wavelength, the FWHM for each Gaussian used.

In this work, we used PAN for the data in which the emission lines have simple and regular profile, namely the data in which the fit can be done automatically and we do not need to check the spectra one by one. PAN is useful also because allow to let the parameters changing in a range of values, in this way we can control the fit, so we can apply the automatic fit being quite sure that the results will be correct. This is fast and for single Gaussian profile is accurate. But even if PAN allows to revise the result, it

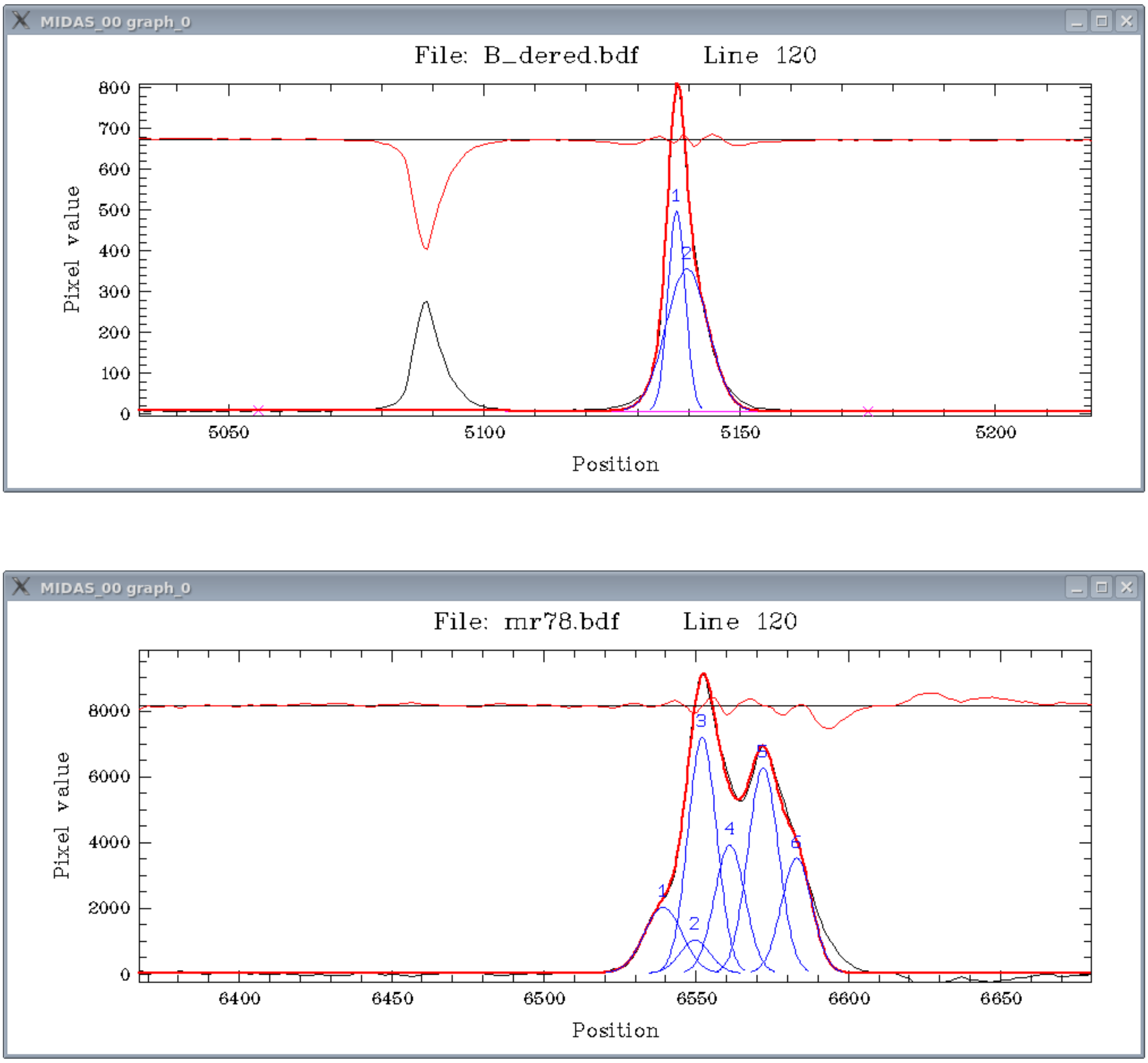

FIGURE 2.19— Two examples of the graphical interface of XAlice to check the results of multi-Gaussian fitting. Top panel: [O III] λ 5007 Å in a nuclear spectrum of NGC 7212. The profile is reproduced by means of a broader and a narrower component. The observed profile is the black line, the thick red line is the total model and the blue curves are the components. Finally the upper red line show the residuals. Bottom panel: Hα+[N II] in a nuclear spectrum of MRK 78. Here we used six components, two for each emission line.

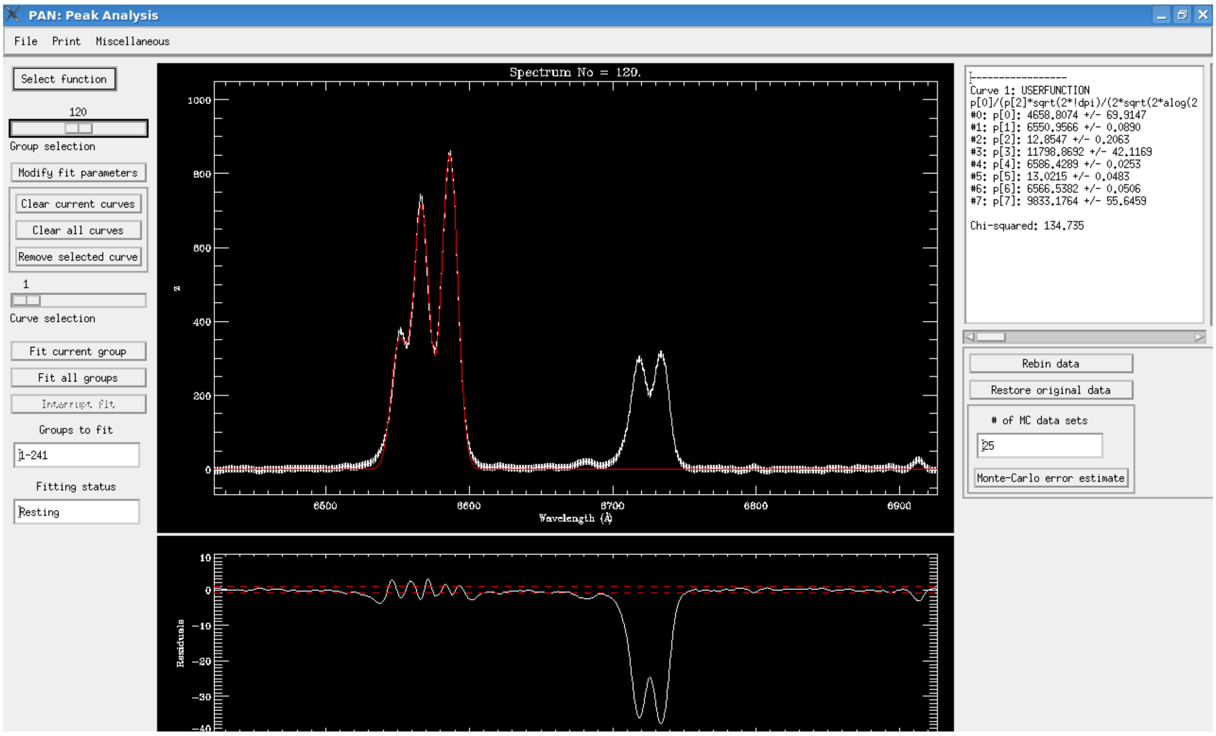

Group selection: 120

Curve selection: 1

Groups to fit: 1-241

Fitting status: Resting

# of MC data sets: 25

```
-----------------
Curve 1: USERFUNCTION
p[0]/(p[2]*sqrt(2*!dpi)/(2*sqrt(2*alog(2
#0: p[0]: 4658.8074 +/- 69.9147
#1: p[1]: 6550.9566 +/- 0.0890
#2: p[2]: 12.8547 +/- 0.2063
#3: p[3]: 11798.8692 +/- 42.1169
#4: p[4]: 6586.4289 +/- 0.0253
#5: p[5]: 13.0215 +/- 0.0483
#6: p[6]: 6566.5382 +/- 0.0506
#7: p[7]: 9833.1764 +/- 55.6459

Chi-squared: 134.735
```

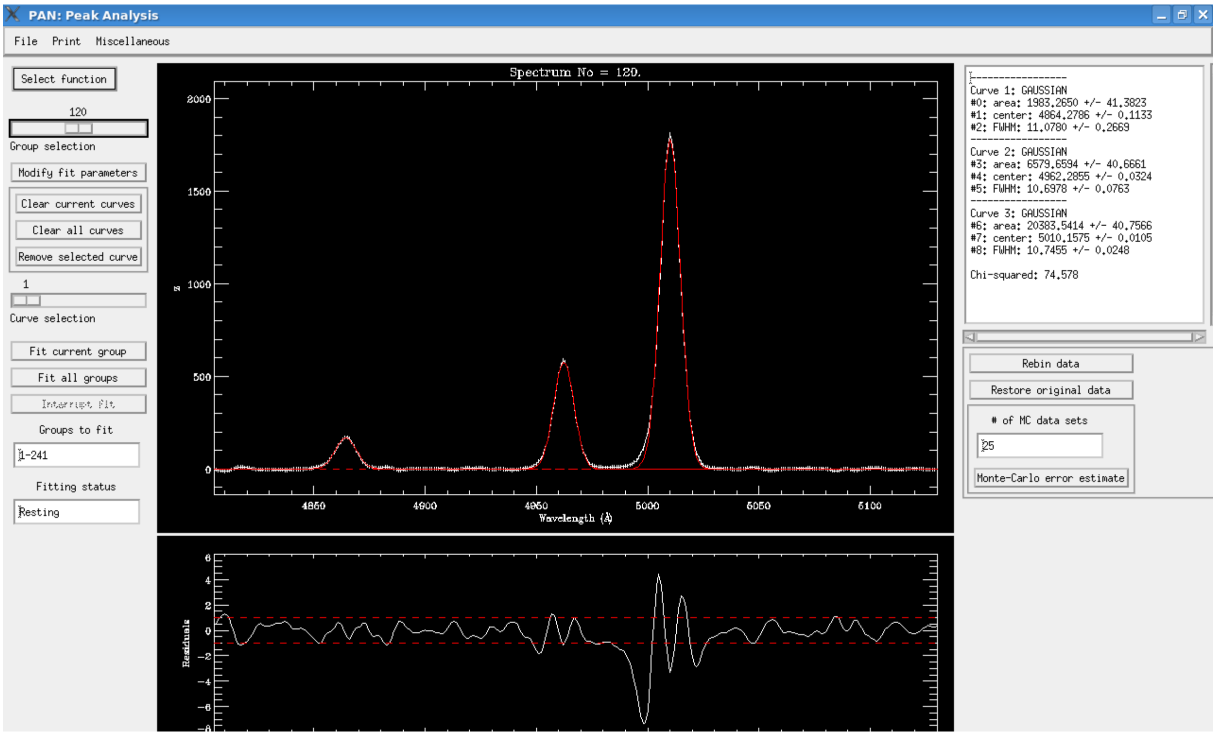

Group selection: 120

Curve selection: 1

Groups to fit: 1-241

Fitting status: Resting

# of MC data sets: 25

```
-----------------
Curve 1: GAUSSIAN
#0: area: 1983.2650 +/- 41.3823
#1: center: 4864.2786 +/- 0.1133
#2: FWHM: 11.0780 +/- 0.2669
-----------------
Curve 2: GAUSSIAN
#3: area: 6579.6594 +/- 40.6661
#4: center: 4962.2855 +/- 0.0324
#5: FWHM: 10.6978 +/- 0.0763
-----------------
Curve 3: GAUSSIAN
#6: area: 20383.5414 +/- 40.7566
#7: center: 5010.1575 +/- 0.0105
#8: FWHM: 10.7455 +/- 0.0248

Chi-squared: 74.578
```

FIGURE 2.20— Two examples of the graphical interface of PAN. Upper panel: the case of Hα+[N II]. Lower panel: the case of Hβ+[O III]. The observed spectrum is in white, the fit is in red. The lower box shows the residual spectrum. The right box shows the results of the fit: area, central λ and FWHM for each Gaussian component.

does not allow to control or modify the fit while the fit is running. Furthermore we cannot see in the multi-Gaussian fitting the different components (for example in the case of [N II] and Hα), but only the sum of them, so we are not able to control the single components if we use a formula for [N II] and Hα.

It is difficult to use this software when we need to separate more component in the same emission line. This was the case of [O III] in the high resolution data of NGC7212 and of [O III] and Hα and Hβ in the high resolution data of MRK6. Furthermore we need to apply a multi-component fit also for some central spectra in MRK3 and in MRK78. When we needed to check each fit or to be able to see the components, we used XAlice of MIDAS. In particular we used XAlice for the nuclear spectra of MRK 78 for [N II] and Hα and for [S II] because in these cases we need to use more components for each emission lines, and we need to check the different components to be sure the fit was correct. We used XAlice also for the high resolution data of NGC 7212. We need to fit the [O III] emission lines with two components, a broad component and a narrow one. We want to apply a similar solution to all the spectra and to check the spectra and the fits one by one. Furthermore, the MIDAS task allows to re-apply the same solutions for the contiguous spectra, obtaining a more consistent solution.

3

NGC 7212

The first object we analysed is the nearby (z=0.0266, scale = 0.513 kpc/″) Seyfert 2 galaxies NGC7212 (Figure 3.1). We selected this object by comparing the narrow band [O III] image by Schmitt et al. (2003) and the NTT longslit spectrum by Bennert et al. (2006). They found a very extended [O III] emission in the longslit spectrum (20″ = 10 kpc), more extended with respect to the narrow band image (5″ = 2.5 kpc) so we decided to study the circumnuclear regions of this galaxy by means of integral field data, longslit and echelle spectra and *BVR* broad–band images.

In the first section the published information about NGC 7212 are collected, in the five following sections we describe the analysis of the emission lines ratios, the gas and stars kinematics and the properties of the ionization cones. A summary of the results is reported in the last section.

3.1 NGC 7212 in literature

NGC 7212 is a Seyfert 2 galaxy in an interacting system of three galaxies (Wasilewski 1981). Durret & Warin (1990) by means of optical longslit spectroscopy in the Hβ + [O III] spectral range found line emission from ionized gas extending for ~ 17″ along PA = 37° and 127°. They found a high excitation value R=I([O III])λ 5007+4959 /I(Hβ)=19 in the nucleus, and ranging from 5 – 28 in the ionized emission. In the polarized light of NGC 7212, Tran et al. (1992) found a broad Hα component (FWHM ~ 4000 km s^{-1}). However no obvious BLR component to NIR lines was found by Veilleux et al. (1997). Tran (1995) argues that a significant amount of polarisation is probably not intrinsic to the nucleus, but due to transmission through aligned dust grains in the host galaxy. This is supported by evidences, showing that dust obscuration plays a significant role in the source. He found a jet-like high-ionization feature extended up to 10″ from the nucleus at PA = 170° in ground-based [O III] and Hα image. This jet is exactly parallel to the axis of the small scale double radio source (0.7″ separation; Falcke et al. 1998), and roughly perpendicular to the optical polarisation (PA=93°), suggesting that the jet is collimated radiation from the hidden nucleus obscured by a torus.

Both galaxies in the pair exhibit multiple dust lanes, visible in the continuum image by Falcke et al. (1998). They found a NLR with an elongated and diffuse structure without a clear evidence of an

FIGURE 3.1— Broad–band image of NGC 7212 after composition process of *B*, *V* and *R* frames, obtained with SCORPIO at the SAO 6-mt telescope.

ionization cone, since the North side is partially obscured by the dust lanes. They suggested that the distribution of excitation to the South is consistent with a ragged inization cone.

Kotilainen (1998) published the B-I map of NGC 7212 showing a very blue and fan-shaped emission region extending from the nucleus to South (PA=165°) with total size 2.3″. This blue region is bisected by a red dust lane. A much redder narrow dust lane is situated on the other side of the nucleus, at closest distance, 3.7″ at PA=280°. HST [O III] images by Schmitt et al. (2003) showed that the [O III] emission is extended out of ~3″ from the nucleus along a P.A. = 170° with dimensions 2.1″ × 4.8″. The emission is diffuse and composed of several individual knots to the North and South of the nucleus. In 2003 Raimann et al. found that the nuclear stellar component of NGC 7212 is dominated by 10-Gyr metal rich (solar or above solar metallicity) stellar population, with a nuclear contribution from the 1-Gyr component of 15% of the total flux and a contribution from younger components (15% of 3-Myr) or by a featureless continuum. Bennert et al. (2006) found the [O III] emission extended out to 12″ from the nucleus along a PA of 170°, i.e. four times larger than the extension seen in the HST image in the same direction, but smaller than the maximum extent observed by Durret & Warin (1990) (PA of 127°and 37°). The excitation value observed in the central spectrum is R_{obs} ~17. The reddening corrected value in the centre is R_{dered} ~16 and varies between 6 and 17 in the central 24″ region. The reddening in the centre is rather low (E_{B-V} = 0.33 ± 0.01mag) and decreases to a value of ~0.07 mag at 1″ North-West of the nucleus. On both sides of this region, it increases and reaches its maximum value at 4″ South-East and 7″ North-West of the photometric centre (ΔE_{B-V} ~1 mag). These maxima may be attributed to dust lines seen in the continuum image by Falcke et al. (1998). At the X-ray range, the spectrum

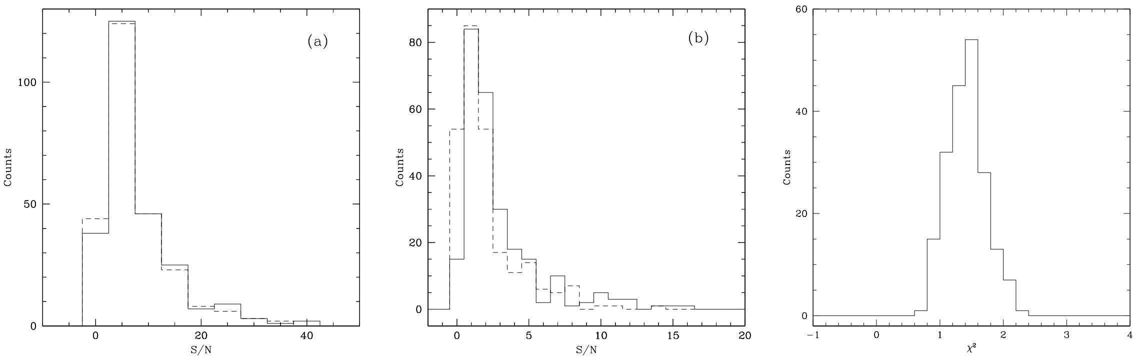

FIGURE 3.2— The S/N of the IFU low (a) and high (b) resolution data measured at 5500 Å (solid line) and at 7000Å (dashed line) and the histogram of the χ^2, evaluating the quality of STARLIGHT fit.

(Chandra/ACIS) of NGC 7212 have been fit by a pure Compton reflection component and a strong Kα iron line, suggesting that the source is Compton-thick (Bianchi et al. 2006).

3.2 Emission line analysis

We analysed both high (R = 1800, at λ = 5500 Å) and low (R = 900, at λ = 5500 Å) resolution IFU spectra. We analysed also longslit (R = 1400, at λ = 5500 Å) and Echelle spectra (R = 6500, at λ = 5500 Åand R = 8000, at λ = 5500 Å). The low resolution data were used to study the emission lines flux distribution and to analayze the gas physical properties and the ionization mechanisms in act, by means of the diagnostic maps and diagrams. The high resolution data were used to study the kinematics of the circumnuclear ionized gas, using only [O III] and Hα emission lines. From this analysis we derived maps of flux, velocity and FWHM for each line in the entire field of view.

By calculating the signal to noise ratio (S/N) of the continuum for MPFS data (see Figure 3.2), we can verify the reliability of our measurements. These data have small values of S/N: the median values for low resolution data are ~5.6 and ~5.4, measured at rest-frame 5500 Å and 7000 Å. The higher resolution data have smaller values: around 1.9 and 1.3, measured at rest-frame 5500 Å and 7000 Å, respectively. The χ^2 evaluates the quality of the fit of STARLIGHT: it should be peaked around 1. In our case it is peaked around 1.6 (see Figure 3.2), instead of 1 probably because the S/N ratio of the analysed spectra is not sufficiently high. Due to these small values of S/N for the high resolution spectra, we cannot apply STARLIGHT to these data. We calculated the flux errors, assuming that the determination of the position of the continuum level gives the main contribution to the errors when measuring the emission line fluxes. The errors ΔF are obtained dividing the reddening corrected flux $F_c(\lambda)$ by the S/N of each emission line, calculated as the ratio of the intensity of the peak of the line over the continuum (amp(λ)) divided by the standard deviation (rms(λ)) of the continuum in a spectral region near the emission line:

$$\Delta F = \frac{F_c(\lambda)}{S/N(\lambda)} \tag{3.1}$$

$$\frac{S}{N}(\lambda) = \frac{amp(\lambda)}{rms(\lambda)} \tag{3.2}$$

All the measured fluxes were corrected for Galactic extinction and needed to be corrected also for the internal reddening. This can be estimated using the Balmer decrement: assuming the theoretical value of the intensity ratio between Balmer emission lines, and comparing the measured values with the theoretical ones, we can estimate the absorption in $V-$band, A(V), applying the Cardelli Clayton and Mathis (1989, CCM) extinction law:

$$\mathrm{A}(V) = 7.2146 \times \log \frac{\mathrm{R_{obs}}}{\mathrm{R_{th}}} \tag{3.3}$$

where $\mathrm{R_{obs}}$ is the observed ratio between Hα and Hβ fluxes, and $\mathrm{R_{th}}$ is the theoretical one equal to 2.86. Once we obtained A(V), we can correct all the observed fluxes with the following expression:

$$\mathrm{F_{corr}} = \mathrm{F_{obs}} \times 10^{0.4\times \mathrm{A(V)}\times \mathrm{c}(\lambda)} \tag{3.4}$$

where c(λ) is calculated for each wavelength using the CCM extinction law, and corresponds to

$$\mathrm{c}(\lambda) = \mathrm{a}(\lambda) + \frac{\mathrm{b}(\lambda)}{3.1} \tag{3.5}$$

Clearly, the correction can be applied only where the Hβ emission line can be measured, therefore the reddening corrected maps are much less extended than original maps. To study the spatial distribution of extinction, we have reconstructed the A(V) map (see Figure 3.3 in which the stellar continuum contours are overlaid to the extinction map). We can see that higher extinction values (red colors indicate A(V) = 2 mag) are in the northern regions. We estimated the extinction from the stellar spectra by means of STARLIGHT, which gives as output also the A(V) values for each spectrum. By comparing the A(V) obtained from gas and stars, we can see that the distributions are peaked at different values, larger for the gas: the median value for gas is 1.38 mag and for stars is 0.68 mag. The extinction obtained from the gas is expected to be higher because the observed emission line spectrum is the sum of the stellar component plus the ENLR gas component. There is dust associated to stars, measured by means of STARLIGHT and dust associated to gas. The template-corrected spectrum has not stellar absorptions, but it is still affected by extinction. Therefore the extinction derived from the gas should be higher, as observed. If the ENLR gas was dust-free, than the A(V) measured by stars and gas should be the same.

Each reliable emission line in the reduced low resolution spectra was measured and the flux map reconstructed. These maps represent the spatial distribution of the emission for each spectral line. We measured the following 30 emission lines at least in the nuclear region: [O II] λ3727, [Ne III] λ3869, H8 λ3888, [Ne III] λ3968, [S II] λ4070, Hδ λ4102, [Fe V] λ4228, Hγ λ4340, [O III] λ4363, He I λ4472, [Fe III] λ4658, He II λ4686, [Ar IV] λ4711, [Ar IV] λ4740, Hβ λ4861, [O III] λ4959, [O III] λ5007, [Fe VII] λ5158, [N I] λ5198, [Fe VII] λ5721, He I λ5876, [Fe VII] λ6086, [O I] λ6300, [N II] λ6548, Hα λ6563, [N II] λ6584, [S II] λ6717, [S II] λ6731, He I λ6678. All the maps masked considering only spectra in which the emission line S/N is larger than 3 are shown in Figure 3.4. The maps of the brightest emission lines ([O II] λ3727, [O III] λ4959, [O III] λ5007, [O I] λ6300, [N II] λ6548, Hα λ6563, [N II] λ6584, [S II] λ6717, [S II] λ6731) show an elongated shape: the ionization gas is extended up to 13″ (corresponding to ~6.7 kpc) with a PA~0°, more extended in the North direction with respect to the South. The emission is not oriented as the stellar continuum emission which has the major axis at PA=45°, see for example the Figure 3.5 in which the [O III] and Hα emission line maps are shown with the overlaid contours of the stellar continuum emission at 5500 Å in black. The less intense [O III] λ4363

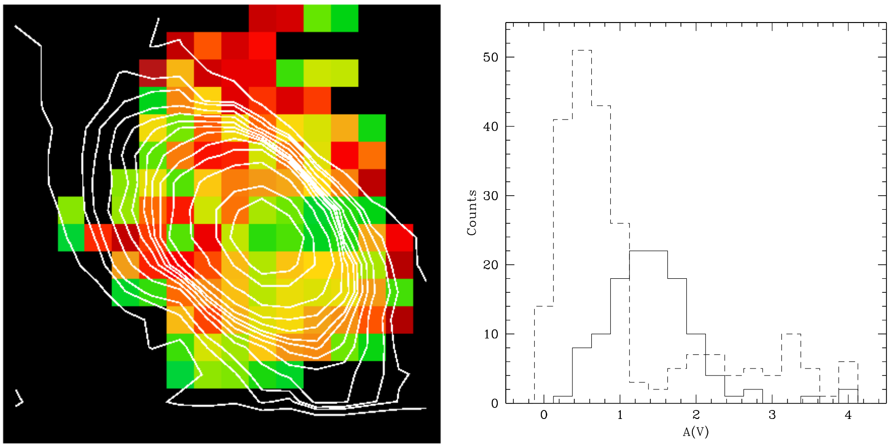

FIGURE 3.3— Left: A(V) map, obtained by applying the CCM extinction law to the ratio of the intensity of Hα and Hβ, with the stellar continuum contours overlaid (in white). Red colors correspond to A(V) values of 2 mag, yellow colors to 1.2 mag and green to 0.7 mag. North is up and East is to the left. Right: The histogram of the A(V) values obtained for gas (solid line) and stars (dashed line).

and He II λ4686 are clearly elongated with PA=0° and extended up to 9 – 10″ (corresponding to ~ 4.5 – 5 kpc). Fainter emission lines are visible not only in the very inner part, where the influence of the ionization source is more important, but also at 3″ – 6″ (1.5 – 3 kpc) from the nucleus. Also the coronal emission lines of iron with different ionization degree are detectable and were measured, but only in the central spectra, probably because here both the ionization and the S/N ratio are higher. We detected [Fe III] λ4658, [Fe V] λ4228, [Fe VII] λ5158 and [Fe VII] λ5721 and [Fe VII] λ6087.

3.3 Physical properties of gas and stars

By means of the usual emission line ratios, gas density and temperature were calculated, while by comparing our measurements with CLOUDY models (Vaona, PhD thesis 2010), we inferred an estimate of gas metallicity. The underlying stellar contribution fitted by STARLIGHT was used to study the stellar velocity field (see Section 3.5) and the distribution of the stellar population with different ages.

We calculated the density with the TEMDEN IRAF task, by using both the [S II] λ6717/λ6731 ratio and the [Ar IV] λ4711/λ4740 ratio. The [S II] and [Ar IV] lines have different values of critical density, indeed we can assume that these lines are emitted by gas in different physical conditions. The [Ar IV] ratio gives information about higher density and higher ionization gas, while lower density gas can be studied by means of the [S II] ratio. We used an input value of temperature T=10^4 K and we calculated the density for each spectrum in which we measured the ratios. Unfortunately, the [Ar IV] lines can be measured only for few central spectra, giving not significant information about the spatial distribution of the high density gas. So we calculated the density using the ratio of the [S II] doublet, that is detectable in a more extended region (see Figure 3.6), we found a median value of ~ 450 e^{-1}/cm^3. The central density values obtained with [Ar IV] emission lines is ~ 2.2×10^3 cm^{-3} (assuming $T_e = 10^4$ K) and is in good agreement with the [S II] determination (~ 1.4×10^3 cm^{-3}, assuming $T_e = 10^4$ K). It is interesting that we found high density in the inner regions also for low ionization gas (where the [S II] low ionization

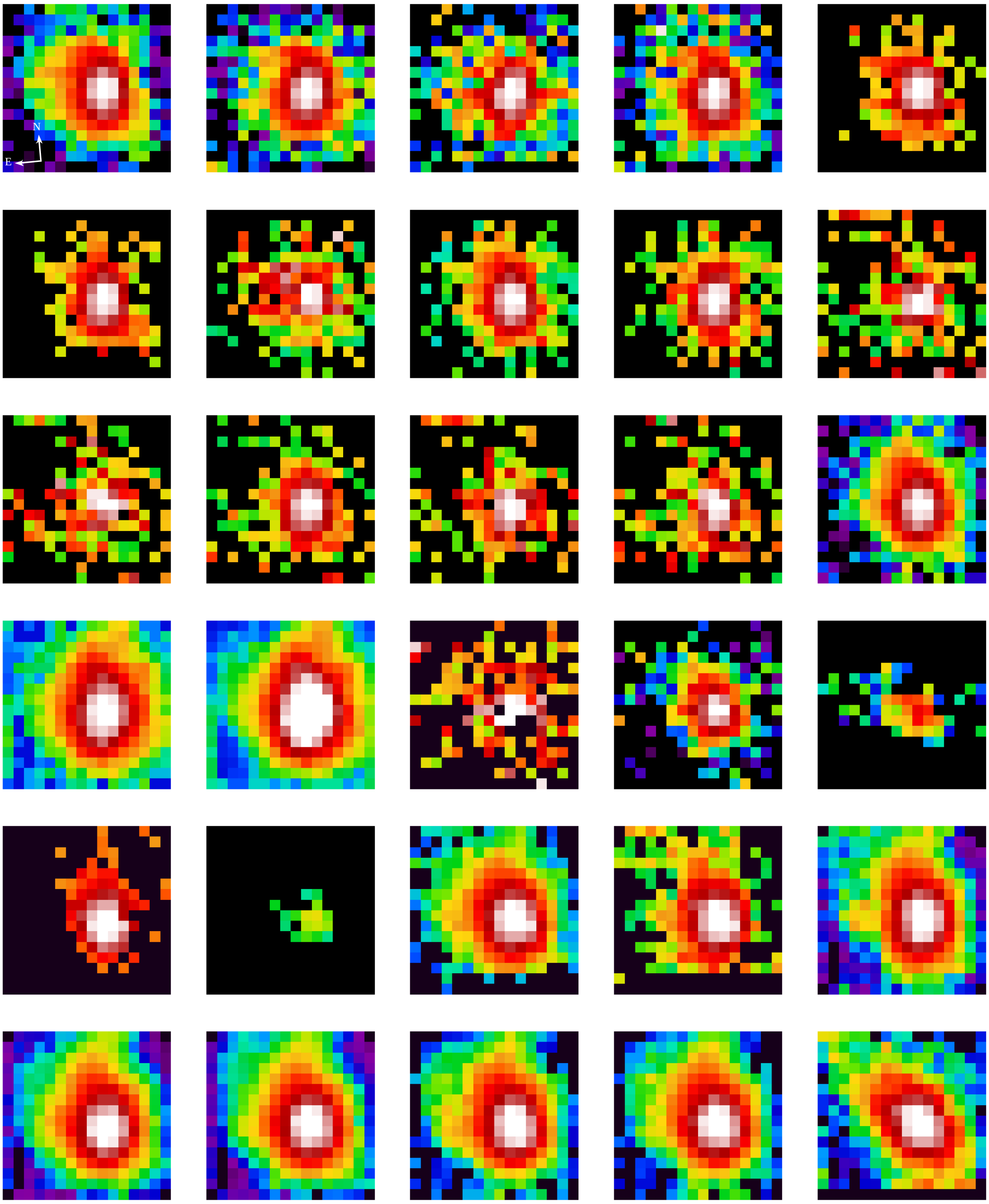

FIGURE 3.4— The measured emission lines and the reconstructed maps. All the data with S/N > 3 are shown. From up-left there are the following emission lines: [O II] λ3727, [Ne III] λ3869, H8 λ3888, [Ne III] λ3968, [S II] λ4070, Hδ λ4102, [Fe V] λ4228, Hγ λ4340, [O III] λ4363, He I λ4472, [Fe III] λ4658, He II λ4686, [Ar IV] λ4711, [Ar IV] λ4740, Hβ λ4861, [O III] λ4959, [O III] λ5007, [Fe VII] λ5158, [N I] λ5198, [Fe VII] λ5721, He I λ5876, [Fe VII] λ6086, [O I] λ6300, [N II] λ6548, Hα λ6563, [N II] λ6584, [S II] λ6717, [S II] λ6731, He I λ6678. The orientation shown in the first map is the same for all the maps: North is up and East is to the left.

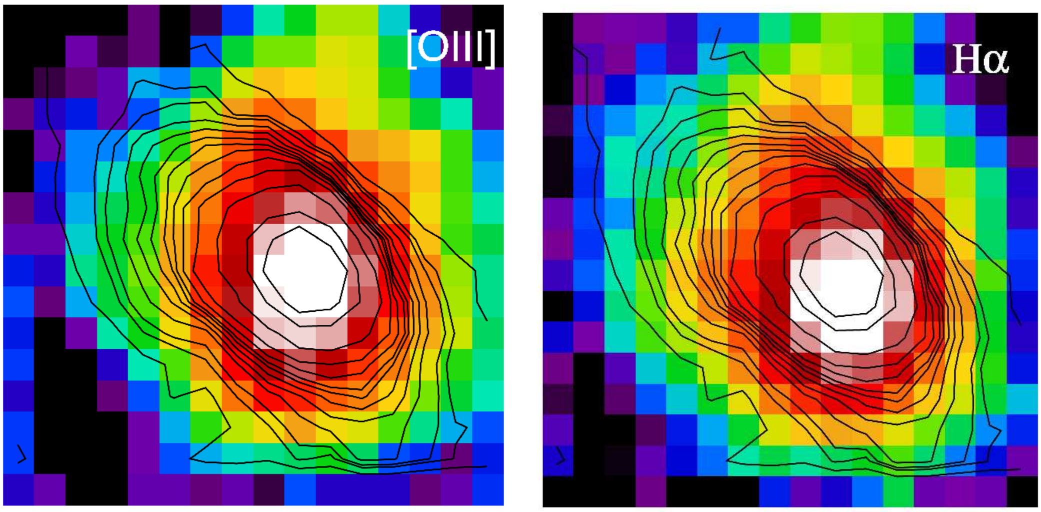

FIGURE 3.5— The [O III] (left) and Hα (right) emission lines maps with the overlaid contours of the stellar continuum emission at 5500 Å in black. North is up and East is to the left. The gas emission is oriented along PA = 0° and the stellar continuum is oriented along PA = 45°.

lines are emitted). These higher values of density ($1 - 1.4 \times 10^3$ cm^{-3}) are in an internal region oriented about East-West (see Figure 3.7). The gas temperature can be obtained using different emission line ratios: with our spectra we can use the [O III] lines at 4959 Å, 5007 Å and 4363 Å (by calculating the ratio between the flux of the [O III] 4959+5007 and the flux of the [O III] 4363), and the [S II] lines at 6717 Å, 6731 Å, 4068 Å and 4076 Å (by calculating the ratio between the flux of [S II] 6717+6731 and the flux of [S II] 4068+4076). We determined the temperature with these two ratios, in the case in which the λ4363 and the λ4068+λ4076 can be measured. So the temperature derived with this analysis are not characteristic of the whole f.o.v, neither of the whole gas, but only of the region where these lines are visible and of the gas emitting [O III] and [S II]. We derived temperature using TEMDEN, and the values of density calculated with the [S II] ratio. The histograms for the two determinations of temperature are shown in Figure 3.6. The median values are 1.8×10^4 K and 1.5×10^4 K for [O III] and [S II] ratios respectively. For high ionization gas, we should calculate the density using high ionization doublets, but in this case, we detected the [Ar IV] emission lines only in the inner part and we could estimate the density using this ratio only for few nuclear regions, so we used the [S II] density determination for the temperature estimate with [O III] ratio. Higher values (up to $2 - 3 \times 10^4$ K) are present in the North part of the f.o.v., in the central region we found lower values ($1 - 1.5 \times 10^4$ K), measured by [O III] ratio and even less measured by [S II] ratio ($4 - 9 \times 10^3$K), see Figure 3.7.

In HII regions and in star-forming galaxies, the metallicity can be measured through direct methods (Aller 1984) or by means of empirical metallicity indicators (Pilyugin & Thuan 2005), because in the stellar photoionization case, the ionization structure is known and the total abundances can be inferred once the ionic abundances are measured. On the contrary in case of ionization by a power-law spectrum, as for an AGN, the situation is more complicated and the ionization structure is very complex. There are not direct methods and to determine the metallicity photoionization models must be used. To estimate

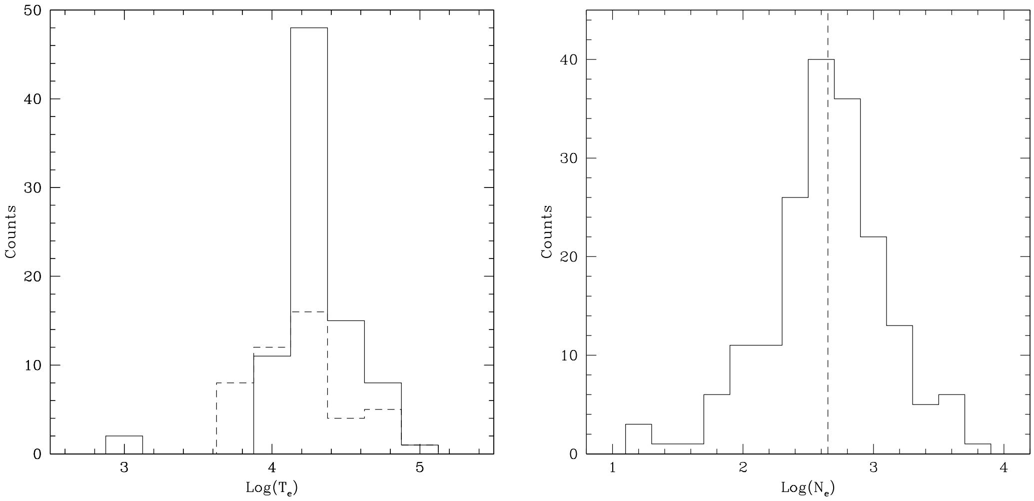

FIGURE 3.6— Histograms of temperature and density. Left: temperature obtained with [O III] (solid line) and [S II] (dashed line) ratio, the median values are 18000 K and 15000 K, respectively. Right: density obtained using a value of temperature of $T_e = 10^4$ K, the median value is 450 e^{-1} cm^{-3}.

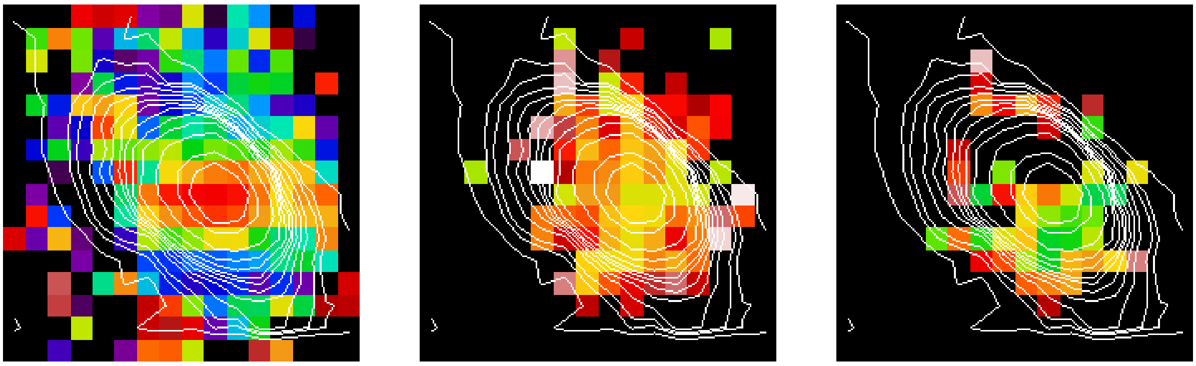

FIGURE 3.7— From left to right: the 2D maps of the density measured with the [S II] ratio and of the temperature obtained by means of [O III] and [S II] ratios, with the stellar continuum contour overlaid.

the gas metallicity, we compare the measured fluxes with values predicted by models from Vaona (PhD thesis 2010), using the emission lines ratios [N II] λ6584/[O II] λ3727 vs [N II] λ6584/[S II] λ6724, being this the best diagram sensitive to the metallicity. The models have a low resolution in metallicity because he used few $Z/Z\odot$ values, nevertheless the trend is clear. We used models with dust-to-gas ratio (D/G) equal to 1. The plot and the comparison between the observed values and the theoretical models allow us to estimate a sub-solar metallicity for the ionized gas in NGC 7212 (see Figure 3.8).

From the STARLIGHT output, we reconstructed the 2D maps of the stellar velocity field and velocity dispersion, as well as the 2D maps of the distribution of the stellar population with different ages and metallicities. The maps have been built using only the models in which the parameter adev$<$ 50. This parameter indicates the mean percentage of the deviation between the observed spectrum and the synthetic one. Then we used the S/N to decide which spectra can be considered, and we created mask in order to consider only the spectra with S/N$>$ 3. We obtained the distributions of the flux for stellar populations in different ranges of age: young (age $< 10^8$ yr), medium (10^8yr $<$ age $< 10^{9.5}$yr), and old (age $> 10^{9.5}$yr); and with different metallicities: sub-solar (Z=0.004), solar (Z=0.02) and super-solar (Z=0.05). We created the $B - R$ color image from the broad-band images obtained at SAO and we compared them with the 2D maps showing the stellar flux distribution. Old population is smoothly distributed in the whole field of view, as expected. Instead from the medium age population map, we stress that higher values are found in the interaction regions (N-E to the nucleus), this component could be the result of the on-going merger. The distribution of the young population does not match the color map, probably because it is not really light from a young population, but rather the scattered emission from the AGN. The detected young population could be an effect due to diffuse light from the cone. STARLIGHT does not distinguish from OB stars contribution and a power-law continuum. So even if in Seyfert 2 galaxy the AGN continuum is less important with respect to Seyfert 1, the determination of the young population could be wrong due to the contamination from the AGN continuum (see Figure 3.9).

3.4 The diagnostic ratios

The diagnostic ratios are useful to distinguish between ionization by power law and by stars or shocks. In this work we used the Veilleux-Osterbrock (VO) diagnostic ratios (Veilleux & Osterbrock 1987). By calculating the maps of emission line ratios ([O III]/Hβ, [N II]/Hα, [S II]/Hα) it is possible to investigate the ionization mechanisms in act in the ENLR. The 2D maps showing the spatial distribution of the diagnostic ratios (Figure 3.10) were created using the not-reddening corrected maps, in order to study a more extended field, not being limited by the small size of the Hβ emission. In fact, in this case we are interested in analysing the distribution of the diagnostic ratios in the whole field of view. Furthermore, the emission lines involved in each ratio are very near in the spectrum, so the extinction influence are expected to be similar and to be minimized or removed when we calculated the ratios. In each map, yellow-red colors imply large values of the ratio, instead green-blue colors imply small values. The 2D maps allowed us to detect for the first time an extended structure with high values (>10) of [OIII]/Hβ suggesting the possible presence of an ionization cone oriented as the galaxy minor axis (see Section 3.6). The ionization map ([O III]/Hβ) shows high values even far from the nucleus (red colors correspond to values of 10-12, green colors are equal to 4-5), this is inconsistent with the presence of photoionization as unique ionization mechanism. If there is only photoionization, the photon flux is diluted according to the distance, it does not keep high at large distance from the nuclear source. Maybe there are additional

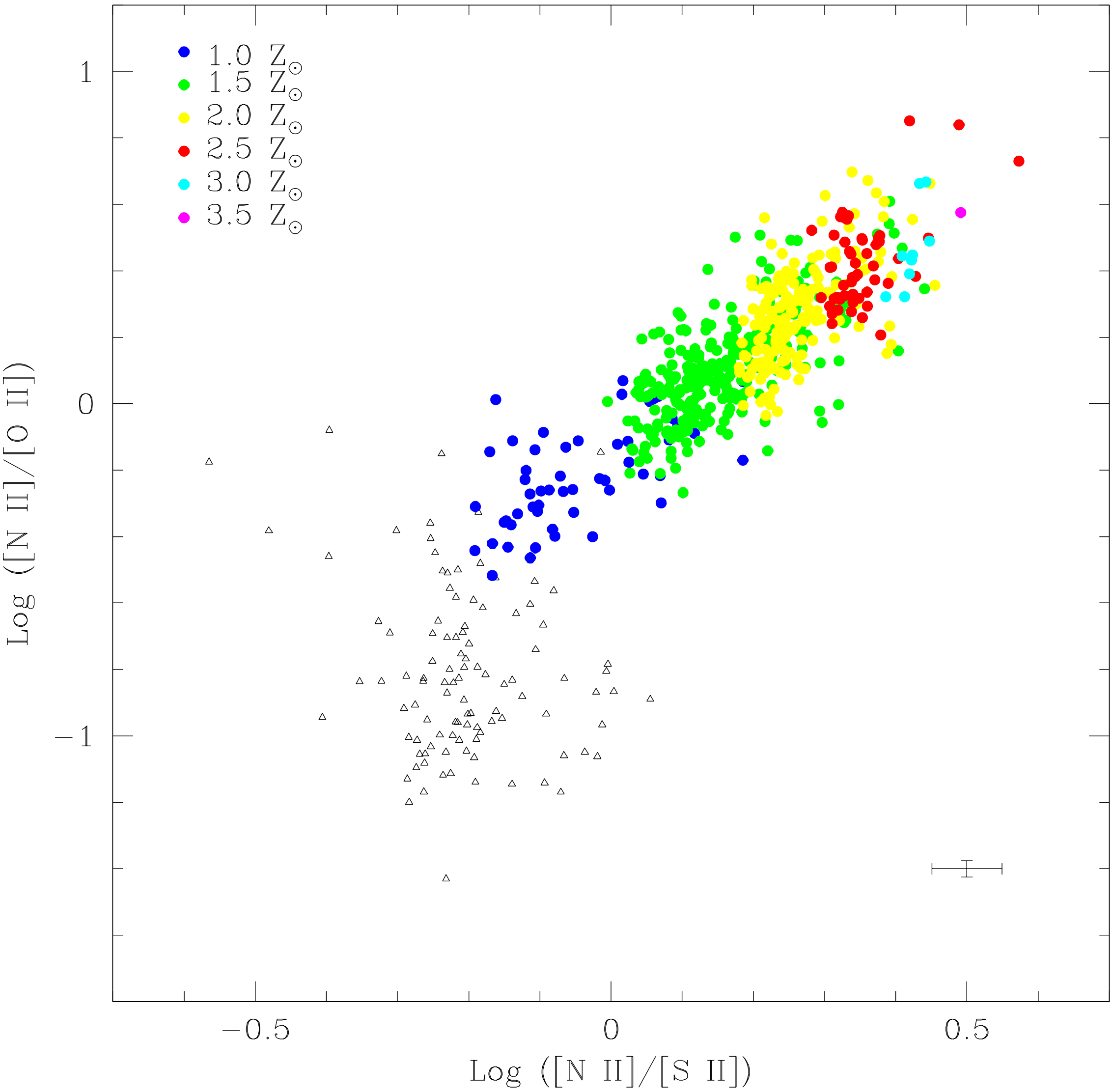

FIGURE 3.8— The graph of the log([N II]/[S II]) versus log([N II]/[S II]) compared with theoretical models by Vaona (2010) with D/G=1. From magenta (Z/Z⊙=3.5) to blue (Z/Z⊙=1) colors, the metallicity decreases. The observed values are black triangles.

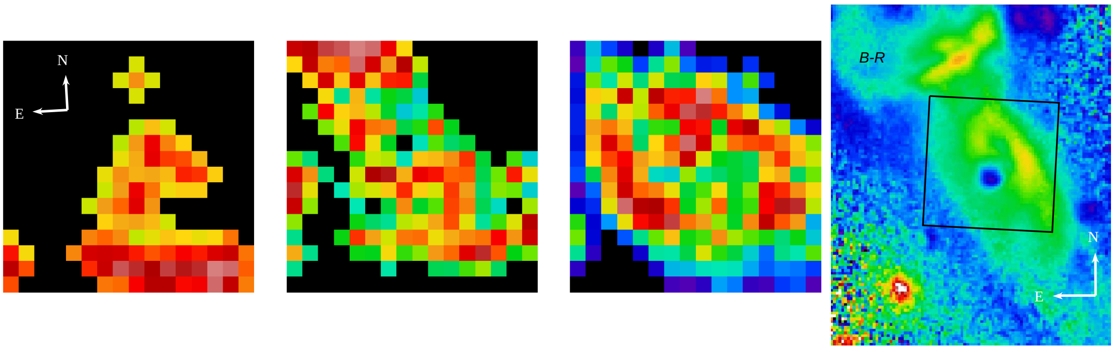

FIGURE 3.9— The 2D maps of the light distribution due to young, medium-age and old population, and the $B-R$ color from SAO images.

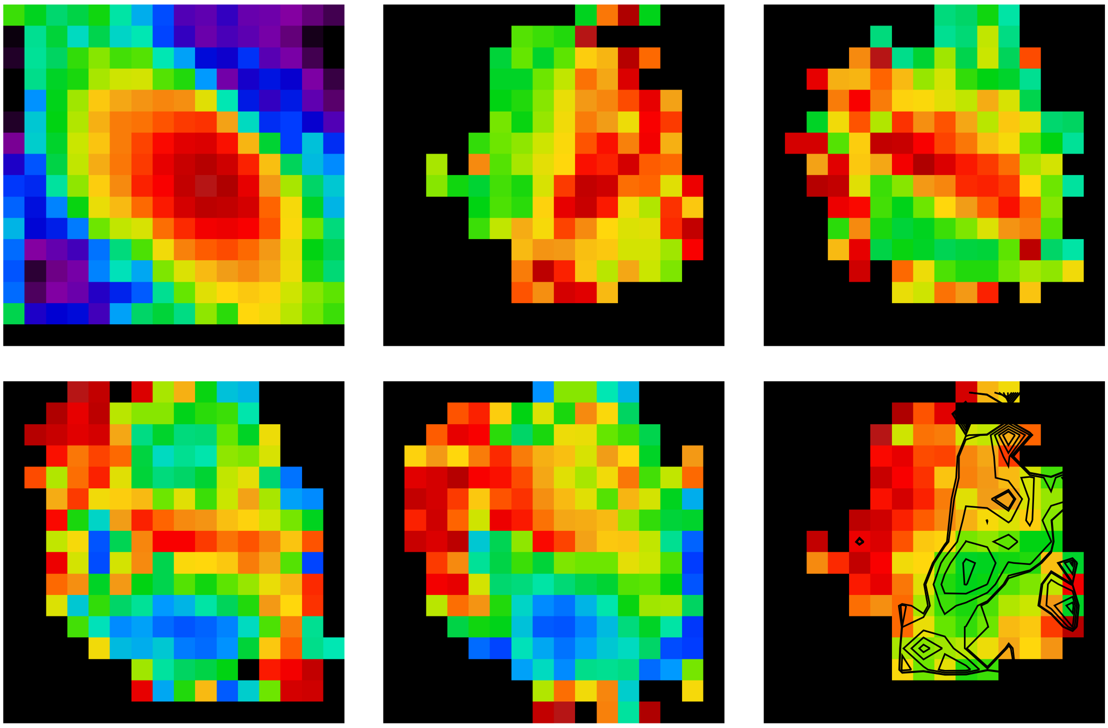

FIGURE 3.10— The continuum emission at λ 5500 Å (top left panel). The maps of the diagnostic ratios are shown: [O III]/Hβ, [O I]/Hα, [N II]/Hα, [S II]/Hα and finally [O II]/[O III] with the ionization cone contours overlaid. In each map, yellow-red color indicates larger values, instead green-blue colors corresponds to smaller values.

mechanisms, such as shocks. But there could be also a density effect, in fact the ionization parameter ($U = \frac{Q_{ion}}{cr^2 N_H}$) depends on the inverse of the density. So high values of U could be due to high values of ionizing photon flux (Q_{ion}=number of ionizing photons per second emitted by the source) or to low density. Inside the cone, we found low density, but without a gradient, the value is approximately the same along the whole size of the cone. So we can exclude that high values of U are due to density. We can invoke shocks, but this hypothesis need to be tested with photoionization+shocks models. Anyway, the ionization is strongly dominated by the AGN, as it can be seen from the calculation of the number of observed and theoretical ionizing photons. According to the very high values of [O III]/Hβ we can also exclude a contribution from star formation. The [O II]/[O III] map gives the same information of the ionization map. This ratio does not depend on the abundances, because it involves lines of the same element, and it is only an indication of the ionization parameter. This map shows a behaviour in good agreement with the ionization map ([O III]/Hβ), in fact where we have high ionization (inside the cone) we found low values of [O II]/[O III] (green colors means [O II]/[O III] ~0.2), instead outside the cone (in the North-East region) we found very high values of [O II]/[O III] (red colors means [O II]/[O III]~2) and lower ionization degree. Therefore the maps of [O III]/Hβ and [O II]/[O III] show emission with high ionization degree, oriented about along the galaxy minor axis.

The diagnostic ratios of [N II]/Hα and [S II]/Hα are not smoothly distributed, showing higher values (respectively ~ 1–1.3 and ~ 0.7–0.9) orthogonal to the cone and outside it. Furthermore these ratios show higher values in the North-East regions, namely in the interacting regions between the two galaxies. Here the ratios can be strongly influenced by interaction effects, such as shocks. This should be verified by applying photoionization+shocks models. The [O I]/Hα map is peculiar. It shows an elongated shape along the galaxy major axis, with high values (red=0.2 and green=0.1) oriented as the high density structure. High values of [O I]/Hα are related to collisions, because [O I] is a forbidden emission line. This emission line is formed in the recombination region, where we found O^+, H^+ and H, this region is more extended if the ionizing source has a power-law spectrum. This ratio is very useful to distinguish between photoionization by AGN or stars.

We plotted the VO diagnostic diagrams, using the reddening corrected fluxes, both for the regions inside and outside the ionization cones (see Figure 3.11). To separate the different regions in the diagnostic diagram (AGN, HII regions and LINERs) we used the expressions from Kewley et al. (2006):

$$\log\left(\frac{[\mathrm{OIII}]}{\mathrm{H}\beta}\right) = \frac{0.61}{\log\left(\frac{[\mathrm{NII}]}{\mathrm{H}\alpha}\right) - 0.47} + 1.19 \tag{3.6}$$

$$\log\left(\frac{[\mathrm{OIII}]}{\mathrm{H}\beta}\right) = \frac{0.72}{\log\left(\frac{[\mathrm{SII}]}{\mathrm{H}\alpha}\right) - 0.32} + 1.3 \tag{3.7}$$

$$\log\left(\frac{[\mathrm{OIII}]}{\mathrm{H}\beta}\right) = \frac{0.73}{\log\left(\frac{[\mathrm{OI}]}{\mathrm{H}\alpha}\right) + 0.59} + 1.33 \tag{3.8}$$

The errors to be associated to the diagnostic ratios were computed with these formulas:

$$\mathrm{err}\left(\log\frac{\mathrm{fl}_1}{\mathrm{fl}_2}\right) = 0.4343 \times \left(\frac{\mathrm{err}(\mathrm{fl}_1)}{\mathrm{fl}_1} + \frac{\mathrm{err}(\mathrm{fl}_2)}{\mathrm{fl}_2}\right) \tag{3.9}$$

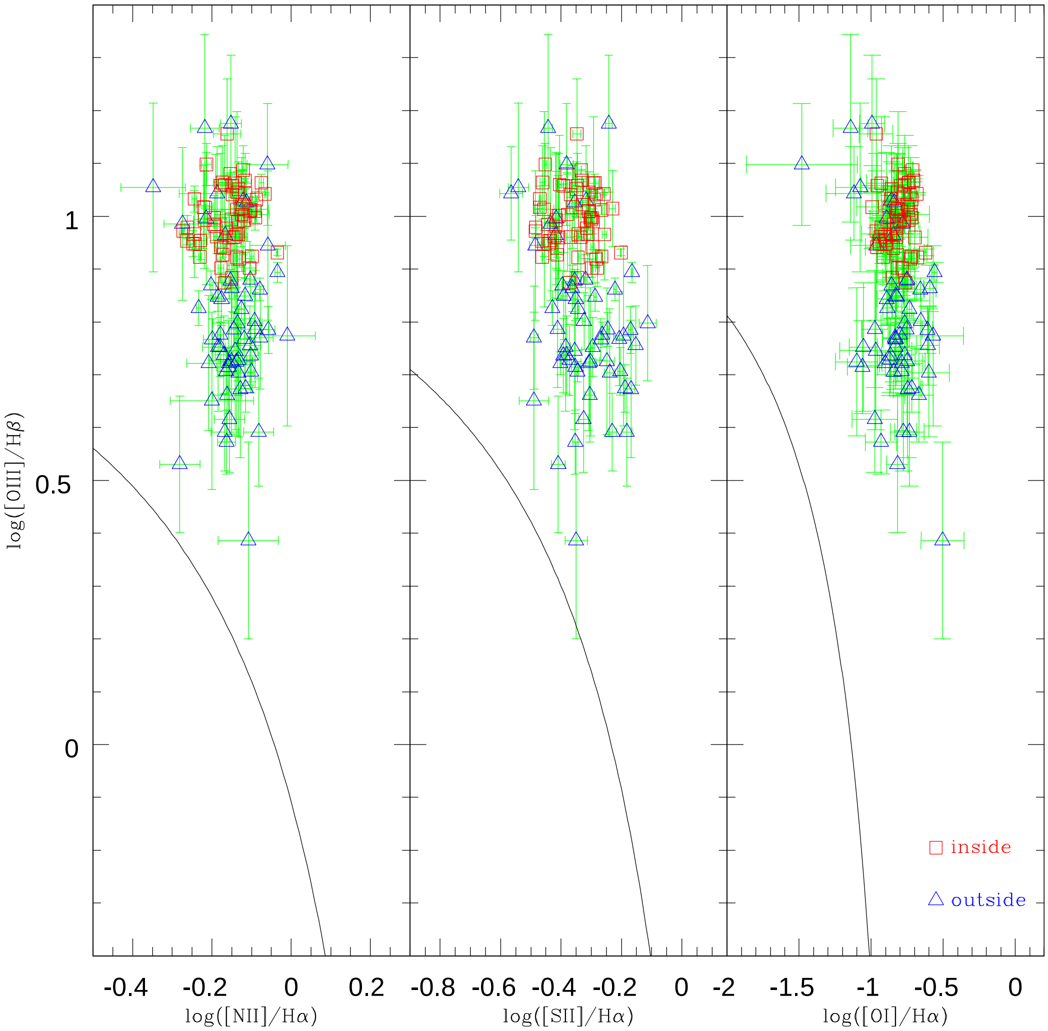

FIGURE 3.11— The VO diagnostic diagrams. Red squares are regions inside the cone, blue triangles are regions outside.

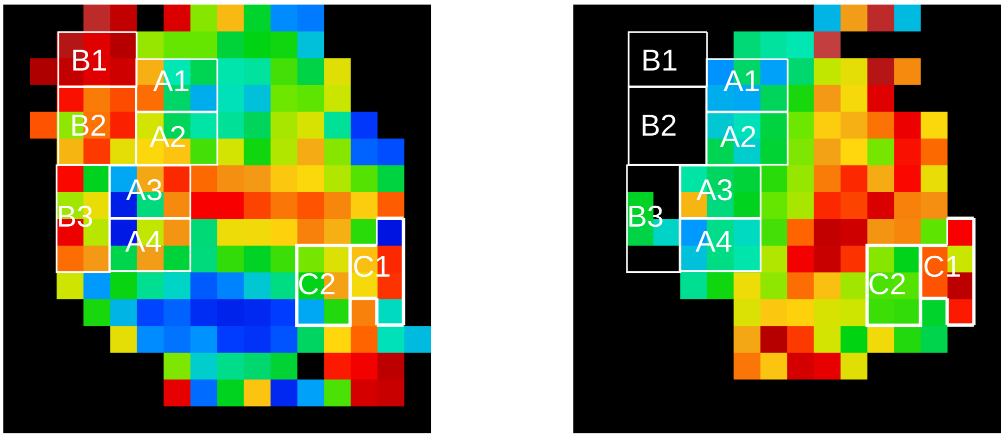

FIGURE 3.12— A, B and C regions selected by means of the diagnostic maps.

$$\mathrm{err}\left(\log\frac{\mathrm{fl}_1+\mathrm{fl}_2}{\mathrm{fl}_3}\right)=0.4343\times\left(\frac{\mathrm{err}(\mathrm{fl}_1)+\mathrm{err}(\mathrm{fl}_2)}{\mathrm{fl}_1+\mathrm{fl}_2}+\frac{\mathrm{err}(\mathrm{fl}_3)}{\mathrm{fl}_3}\right) \tag{3.10}$$

where fl_i and err_i are flux and relative error, calculated according to the Eq. 3.1.

By analysing these diagrams we noted that all the data in our field of view fill the AGN region. It is confirmed an AGN origin for the ionization source in the entire field of view. What is expected is that regions inside the cone, fall in the AGN area (upper-right part of the plot), instead for the regions outside the cone or we do not see them in the plot (if the AGN is the only ionizing source), or they should be ionized by HII regions (down-left part of the plot). So we can expect to see in the plot that the regions were distributed towards the HII regions area (bottom-left part of the plot). Instead, all the regions occupy the AGN area and are distributed vertically towards the shock region. This means that for each region, inside and outside the cone, the ionizing source has a power-law spectrum, it is not a thermal source; the only difference is that for the regions outside the cone the ionization decreases with increasing radius, instead inside the cone it remains high also far from the nucleus (see Figure 3.31). A possible explanation is that the ionizing photons from the cone are diffused, or the cone aperture angle is larger.

Starting from the maps of the diagnostic ratios, we selected regions to be deeper analysed (see Figure 3.12). We used the ionization map to select A and C regions, instead we selected B regions from the [N II]/Hα map. These regions were extracted in order to study the gas ionization mechanisms far from the nucleus and outside the ionization cones. We selected the spaxels and summed them to obtain a 1D spectrum for each region with higher S/N. The extracted and summed spectra for the 8 selected regions are shown in Figure 3.13, the regions A1, A2, A3, A4, B1, C1 and C2 have area equal to 6 arcsec^2, the region B2 has area equal to 9 arcsec^2 and the region B3 has area equal to 8 arcsec^2. The A and B regions could be ionized by both AGN and shocks, probably due to the merger in act. To test this hypothesis, we applied STARLIGHT to these spectra, obtaining information about the age of the stellar component; in particular we found that the old population (age $> 3\times10^9$ yr) is the main component in

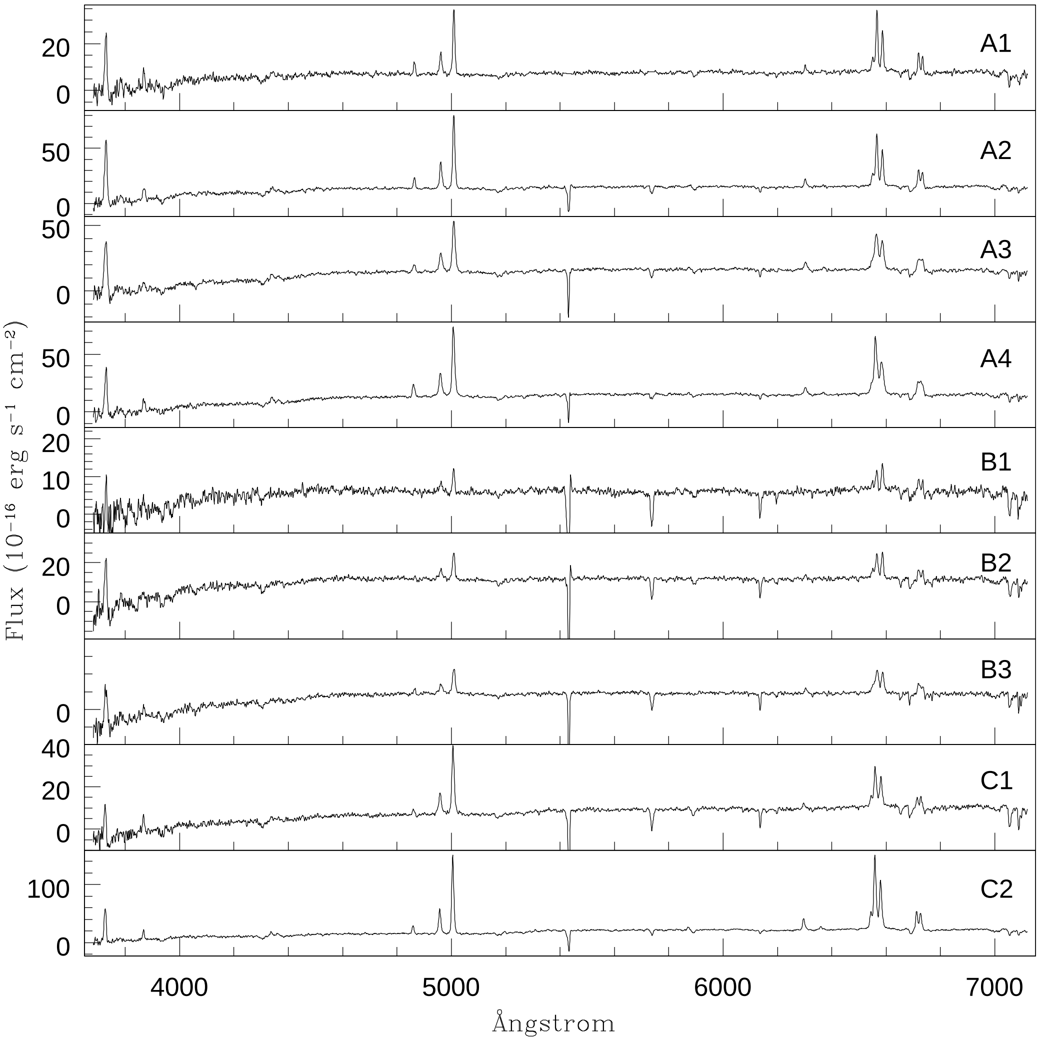

FIGURE 3.13— The 1D extracted and summed spectra for each selected region.

all the regions, but in A4 and moreover in B1 we found a percentage of medium age component (10^8 yr < age < 3×10^9 yr). We measured the emission lines after the stellar component subtraction and we constructed the diagnostic diagram for these regions (Figure 3.14). From these diagrams we see that the C1 and C2 regions are strongly ionized by the AGN source, this could be a hint supporting the idea that the ionization cone aperture angle is larger than 70° (likely 90° – 100°). The A and B regions have a similar lower ionization degree, with respect to the C regions, but are AGN dominated. Therefore, the AGN can ionize regions far from the nucleus ($d = 9.3'' = 4.8$ kpc) and in a direction orthogonal to the cone, this can be due again to an aperture angle of the cone larger than that shown by our [O III]/Hβ emission or to scattering of photons on a plane orthogonal to the cone. The star formation component cannot be excluded in these regions, being situated nearby the interacting regions of the galaxy (N-W), where it is possible to find star-formation. If it is present it is very low, as confirmed by the STARLIGHT output: the young population percentage is very small and we found intermediate age population only in A4 (4%) and in B1 (25%), the latter being the region nearest to the interaction. The distribution of the data in the diagnostic diagram suggests the possible presence of a combination of ionization by AGN and shock.

3.5 Kinematical analysis

For the main emission lines, we built also the 2D maps of velocity and FWHM (see Figure 3.15). The velocity values were corrected for the systemic velocity, considering as recession velocity the value obtained by measuring the nuclear spectrum (the spectrum with highest flux in the continuum map). The instrumental FWHM, obtained fitting some lines of the comparison lamp, have been subtracted from the measured values; for each spaxel, we subtracted the corresponding instrumental value, in order to take into account possible differences in the instrumental resolution in the field. We applied the usual formula:

$$FWHM_{corr} = \sqrt{(FWHM_{obs})^2 - (FWHM_{inst})^2} \tag{3.11}$$

The map of the velocity field shows values ranging from +200 km s^{-1} to -200 km s^{-1}, while the map of the FWHM, after the correction for instrumental width, shows values between 200 km s^{-1} and 700 km s^{-1}. The velocity maps show distortions East of the nucleus, especially in case of Hα, [N II] 6548,6584 and [S II] 6717,6731 lines, while [O III] 5007 line shows a more regular pattern. In particular, the Hα velocity map in that region has velocity values between 130 km s^{-1} and 200 km s^{-1}. This zone corresponds to an emission region with low surface brightness ($10^{-16} - 10^{-15}$ erg cm^{-2} s^{-1}) and high FWHM values, between 300 km s^{-1} and 600 km s^{-1}. In the HST image and in the SAO-6mt broad band image and color, this region shows no particular structure and has a low surface brightness. The anomalous regions in the maps of the velocity field of the gas appear to be located toward the interaction region, this could be an effect of the gravitational interaction between NGC 7212 and its companion galaxy. In the FWHM maps (see Figure 3.16) red colors indicate FWHM of 700-800 km s^{-1}, yellow colors values of 500-600 km s^{-1} and blue colors values of 200-300 km s^{-1}. In the [O I], [N II] and [S II] FWHM maps it is clearly visible an elongated structure, with higher values of FWHM ($\sim 700 - 800$ km s^{-1}), at about 90° with respect to the direction of the major axis of the emission, so almost aligned with the minor axis. This feature has been observed already in other Seyfert galaxies, like Mrk 3, Mrk 34, Mrk 1066, Mrk 348, Mrk 1, NGC 2992, NGC 5728 (Stoklasova et al. 2009). The explanation of this effect is still under debate. This structure is found also when we fit the high resolution [O III] emission

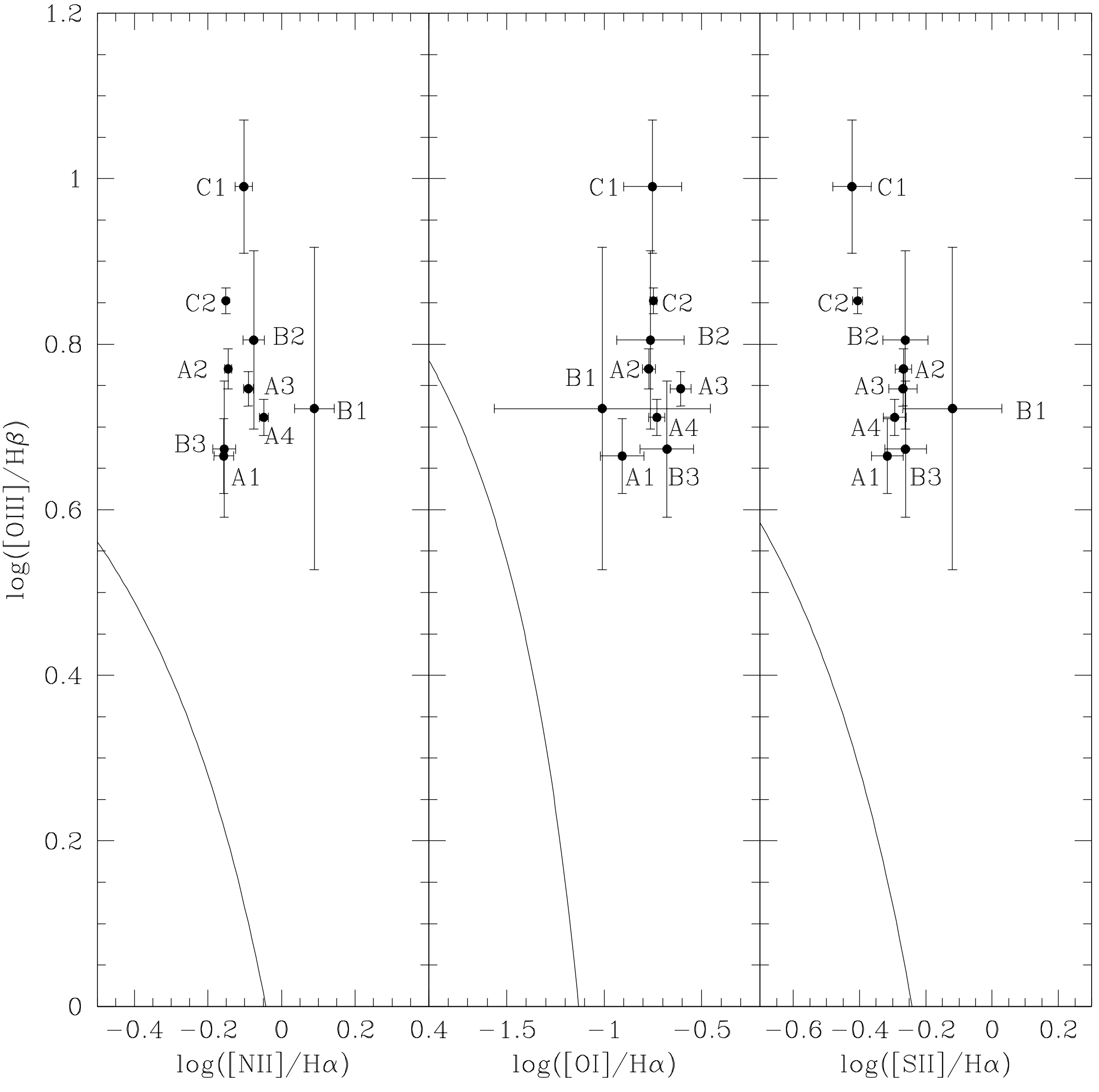

FIGURE 3.14— VO diagnostic diagrams for the extracted regions.

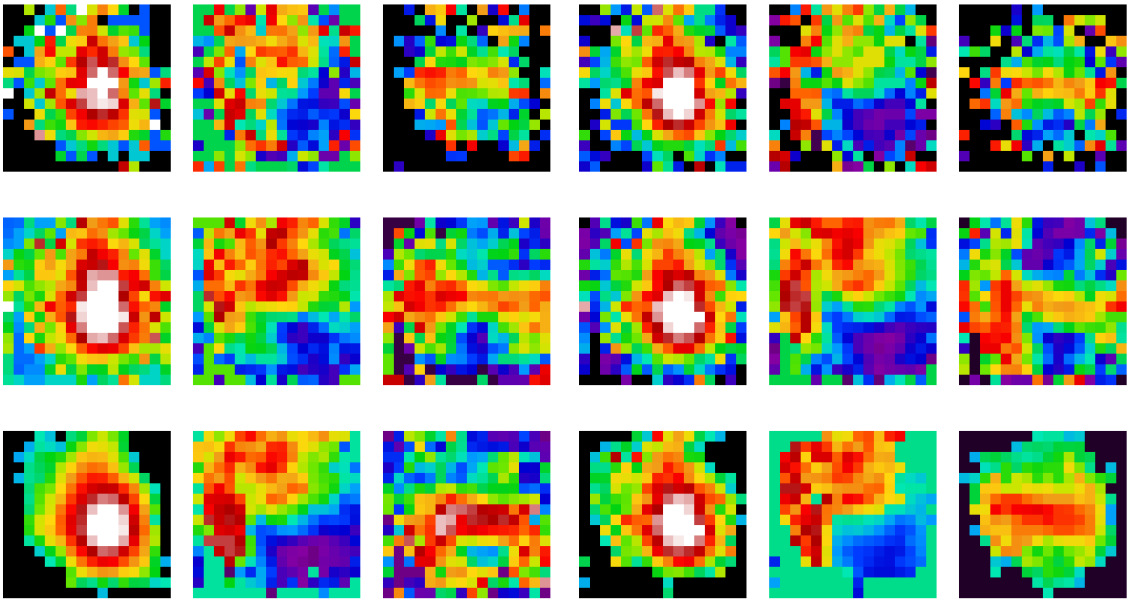

FIGURE 3.15— The 2D maps of the emission flux, velocity and FWHM for the main analysed emission lines. First line, from left to right, [O II] and Hβ; second line from left to right: [O III] and Hα; last line, from left to right:[N II] and [S II]. North is up and East is to the left.

line profile with two separate components. The minor axis of the stellar velocity field is aligned with the photometric minor axis, instead the gas velocity field is rotated with respect to the stellar one (Figure 3.17). From the analysis of the low resolution data we can see that stars and gas are not aligned, the [O III] emission is elongated along a direction orthogonal to the major axis of the galaxy. This could imply that the gas is not co-planar with stars. The extinction map shows dust lanes in the central part, also visible in the broad band images and in the color map. The density map is aligned as the FWHM maps. By comparing the high density (N_e = 700 – 1400 cm^{-3}) regions in the map and the FWHM maps (see Figure 3.18), we can see that in high density regions we found also high values of FWHM ($\sim$ 500 km s^{-1}), these are hints of compressed gas, or streaming of gas and can be consistent with shock. The N-E region with higher FWHM and a peculiarity in the velocity field is nearby the region of the merge between the galaxies. All the previous peculiarities could be caused by this interaction (see Figure 3.18).

From the analysis of the emission line profiles it is possible to point out the presence of asymmetries that can be due to additional and non-rotational kinematical components. With the low resolution data, we were not able to identify and analyze multiple components in the spectra line profiles, anyway some asymmetries in the line profile for the higher S/N spectra have been observed and as a consequence the fits were more difficult to be performed. From the higher resolution IFU data, first we fitted [O III] and Hα emission lines with a single component and we built the 2D maps of flux, velocity and FWHM. We used these maps as input for ROTCUR (Begeman et al. 1989), the task of GIPSY (Groningen Image Processing System) software to model the 2D map and to obtain the deprojected values of the velocity

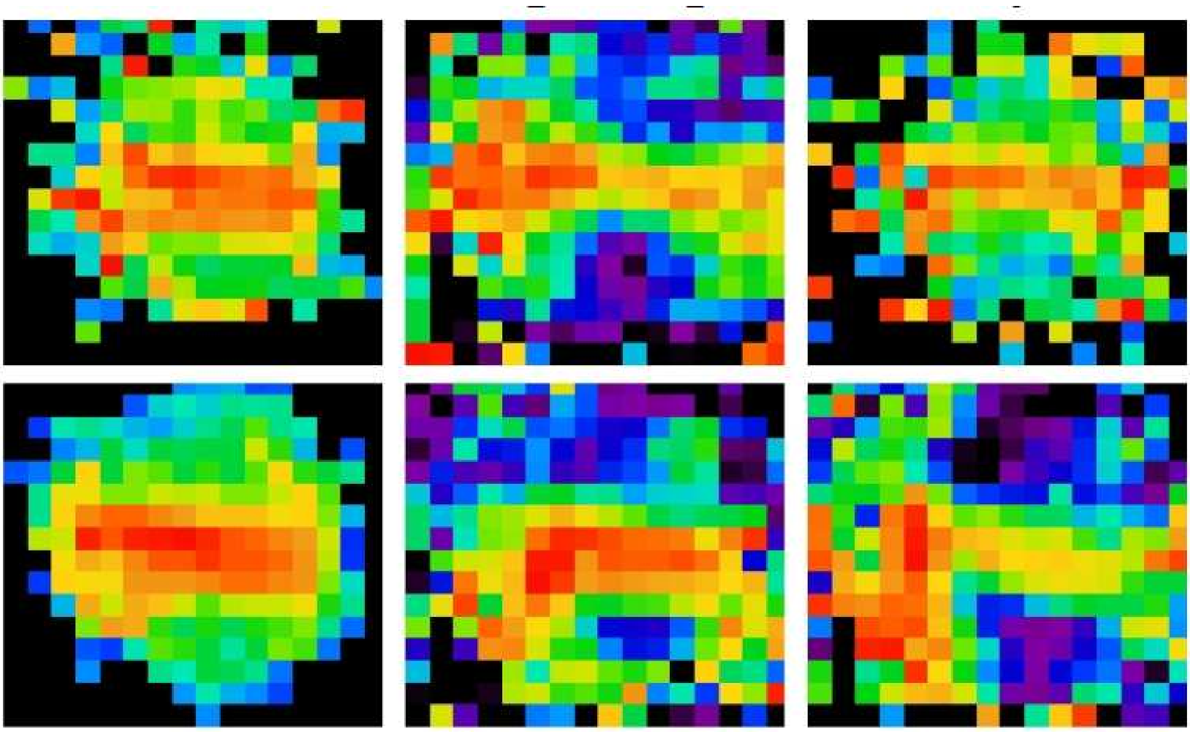

FIGURE 3.16— The FWHM maps for some emission lines. From top-left to bottom-right: [O I], [O III], Hβ, [S II], [N II], Hα. North is up and East is to the left.

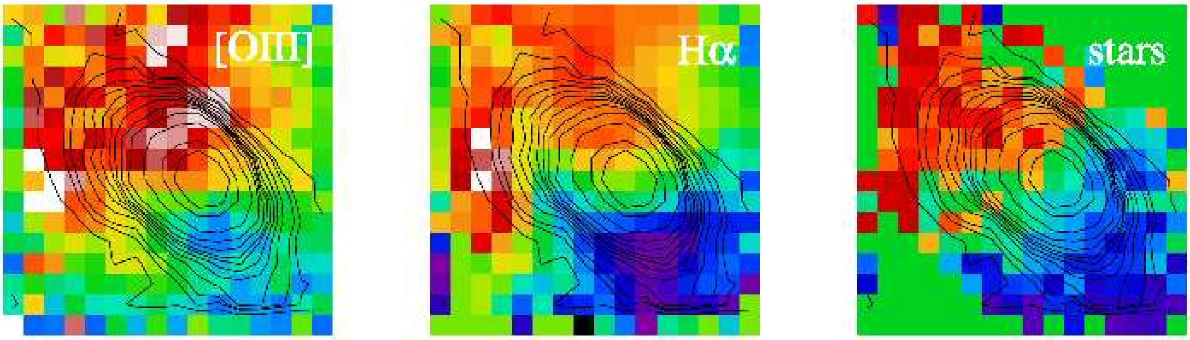

FIGURE 3.17— The velocity maps of gas ([O III] and Hα) and stars with the continuum contours overlaid.

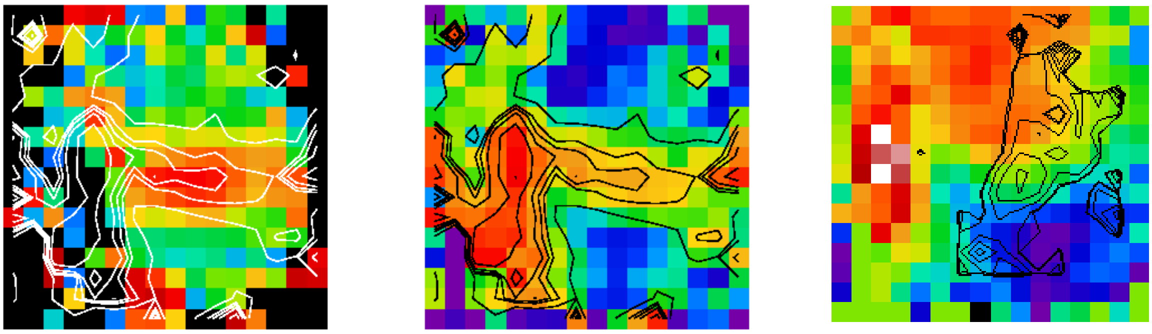

FIGURE 3.18— The maps of density and of Hα FWHM with the contour of Hα FWHM overlaid and the Hα velocity map with the cone contours overlaid.

to build the rotation curve. This task uses tilted-ring model to fit the velocity field, in the sense that it models the velocity map using concentric rings and taking into account the inclination on the line of sight. The observed velocity v(x,y) is reproduced by this formula:

$$\mathrm{v(x,y) = v_0 + v_c(R)\sin i \cos\theta} \tag{3.12}$$

where

$$\cos\theta = \frac{\mathrm{-(x - x_0)\sin\phi + (y - y_0)\cos\phi}}{\mathrm{R}} \tag{3.13}$$

$\mathrm{x_0}$ and $\mathrm{y_0}$ are the sky coordinates of the rotation center of the galaxy; $\mathrm{v_0}$ is the systemic velocity; $\mathrm{v_c(R)}$ is the circular velocity at distance R from the center; ϕ is the position angle of the major axis; i is the inclination of the galactic plane and θ is the azimuthal angle in the galactic plane. Before starting, we needed to calculate the inclination angle $i = \arccos\left(\frac{\mathrm{b}}{\mathrm{a}}\right)$, where a and b are the semi-major and semi-minor axis of the gas or stellar emission. We obtained i, by calculating the b and a values from an ellipse that matched the distribution of the emission. From this ellipse we also got the PA of the emission. We corrected the velocity maps for the systemic velocity, using the values obtained in the central spectrum. Once we determined the position angle (PA) and the inclination (i) from the maps of the emission line flux, we could run ROTCUR. We fixed the following input parameters: inclination i=40°, that was the same for the [O III] and Hα maps, the systemic velocity (0.0 km $\mathrm{s^{-1}}$), the expansion velocity (0.0 km $\mathrm{s^{-1}}$) and the coordinates (x, y) of the center of the galaxy. The other input parameters were radii of the concentric rings in arcsec, the first guess for the rotational velocity of each ring and the position angle, and we let them free. First we applied this task to the whole 2D velocity map, fitting both the approaching and receding side at the same time, this output was used as input for the task VELFI that reconstructs the model of the observed velocity field. This image is useful to be compared with the original one in order to check if the model can reproduce the velocity map. On the other hand, to get more accurate values of the deprojected velocity in order to build the velocity curve, the velocity maps were fitted in two steps, first the receding and then the approaching side. We compared the gas rotation curves with the stellar rotation curve, obtained applying ROTCUR to the stellar velocity map (i=54°). We found that the kinematical behaviour and the velocity values are similar for stars and gas and also the NTT longslit data show a similar behaviour, this implies that the kinematics of the ENLR gas and of the stars are

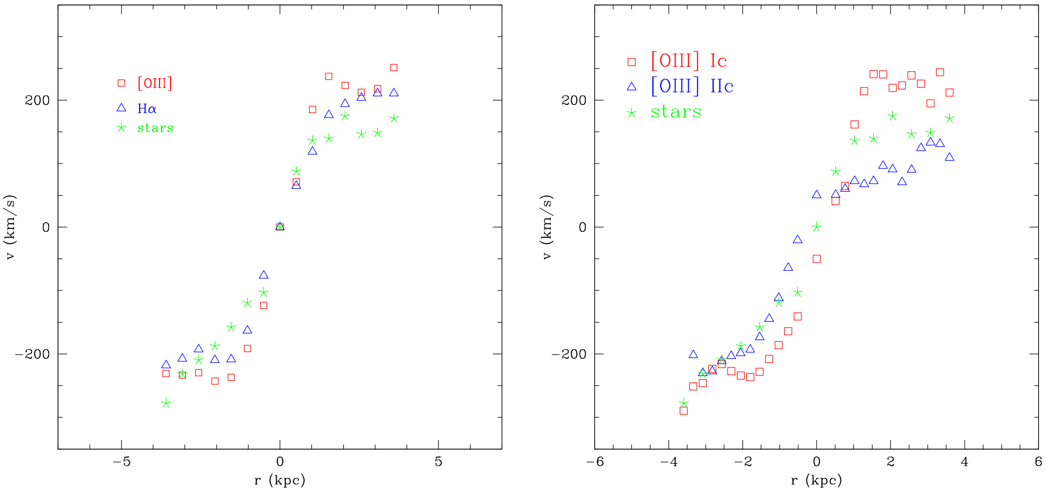

FIGURE 3.19— Rotation curve for stellar and gas components (left); rotation curve for the two components of the [O III] (right).

dominated by the same gravitational potential (see Figure 3.19). But looking at the 2D maps we have already seen that the kinematical axis of stars is inclined of around 30° with respect to that of the gas (Figure 3.17). This could be a projection effect: gas and stars could be distributed in a different way and in a different plane. Stars are in agreement with the continuum emission, instead gas velocity maps are oriented according to the gas emission. We derived the velocity map for the stellar component also using FXCOR task of IRAF, to check if the STARLIGHT determination was acceptable. We find similar results with FXCOR. We calculated the errors in velocity, by measuring the observed position of one or more sky lines. This assumes that the main contribution to the errors is due to wavelength calibration errors. When we found more sky lines we averaged the values, obtaining a single value (see Figure 3.20). We should take into account the S/N ratio of the emission lines (Corsini et al. 1999), in fact if the errors are due only to wavelength calibration, the error value should be the same in the whole f.o.v., instead we can see from the histograms that there is a distribution. In particular where the S/N is high, the error is due only to errors in calibration, instead where the S/N is low, the error is larger, because it is difficult to estimate the central λ. In our case, the S/N of these emission lines is high in the whole field and the errors are mainly due to calibration errors. The errors may be larger in presence of asymmetries. For the high resolution data we have also the error due to the fit of the two components.

By assuming that gas and stars are on circular orbits in a plane, we can fit the rotation curves with the following formula (Bertola et al. 1991):

$$v_c(r) = \frac{Ar}{(r^2 + c_0^2)^{p/2}} \tag{3.14}$$

where A, c_0, and p are parameters and r is the radius in arcsec. The p parameter is between 1 and 3/2. We fit the gas rotation curve, using both [O III] and Hα (see Figure 3.21) with A = 300 km s^{-1}, $c = 2.''5$ and p = 1.1. By fitting the stellar rotation curve (see Figure 3.21) we found A = 200 km s^{-1}, $c = 2''$,

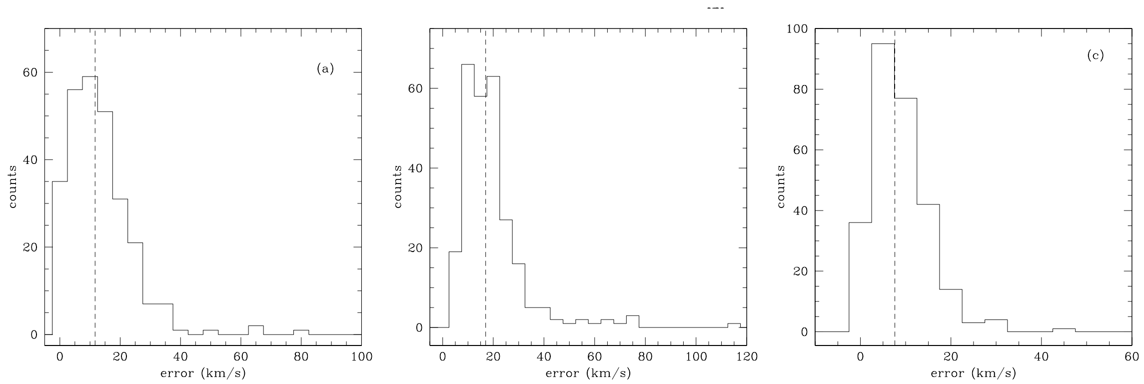

FIGURE 3.20— (a) Errors in the velocity determination for the [O III] rotation curve, median value = 12 km s^{-1}; (b) for the Hα rotation curve, median value = 17 km s^{-1}; (c) for the stellar rotation curve, median value = 8 km s^{-1}.

p = 1. By assuming a spherical potential, we can infer the mass distribution M(r) using the following formula and assuming that the maximum extension is r= 7″ (corresponding to 3.6 kpc):

$$\mathrm{M(r)} = \frac{\mathrm{r v_c^2}}{\mathrm{G}} = \frac{\mathrm{A^2 r^3}}{\mathrm{G(r^2 + c_0^2)^p}} \tag{3.15}$$

We found $M_{gas}(r < 7'') = 4.45 \times 10^{10}\ M_\odot$ and $M_\star(r < 7'') = 3.1 \times 10^{10}\ M_\odot$, where M_{gas} and $M_\star$ are the gravitational masses derived from gas and star velocity curves, respectively. From the analysis of the rotation curves we infer that the mass is $3 \times 10^{10} < M < 4.5 \times 10^{10}\ M_\odot$.

We analysed the NTT spectrum by dividing it into regions (see Figure 3.22), finding broad component in external regions. N, A1, A2, B1 and B2 cover a region of ~1″, B5 covers a region of ~ 1.65″, A4 and B4 cover a region of ~2.33″, B5 and B6 cover a region of ~ 3″. Broad components are visible in B4, B5, A3, A4. In B4 and in A4 it is asymmetric, this could imply the presence of more (at least 2) broad components in [O III] (Figure 3.23). By measuring the FWHM of the broad component, we found a value of 100 Å corresponding to ~$6{\times}10^3$ km s^{-1}. This is quite strange, in fact this broad component is not visible in the nuclear part, as in the case of more internal NLR, but only in the external regions. It is not a BLR component also because it is visible in [O III], less in Balmer lines. The velocity curve obtained with NTT data was deprojected: being the PA of the slit along the direction of the [O III] emission semi-major axis, we considered only the inclination, so the corrected velocity (v_c) was obtained from the observed velocity (v_{obs}) by applying the following formula:

$$\mathrm{v_c} = \frac{\mathrm{v_{obs}}}{\sin \mathrm{i}} \tag{3.16}$$

where i is the inclination with respect to the line of sight, obtained from the semi-major and semi-minor axes of the [O III] emission:

$$\mathrm{i} = \arccos\left(\frac{\mathrm{b}}{\mathrm{a}}\right) \tag{3.17}$$

The comparison between this rotation curve and the ones obtained from IFU data show a good agreement.

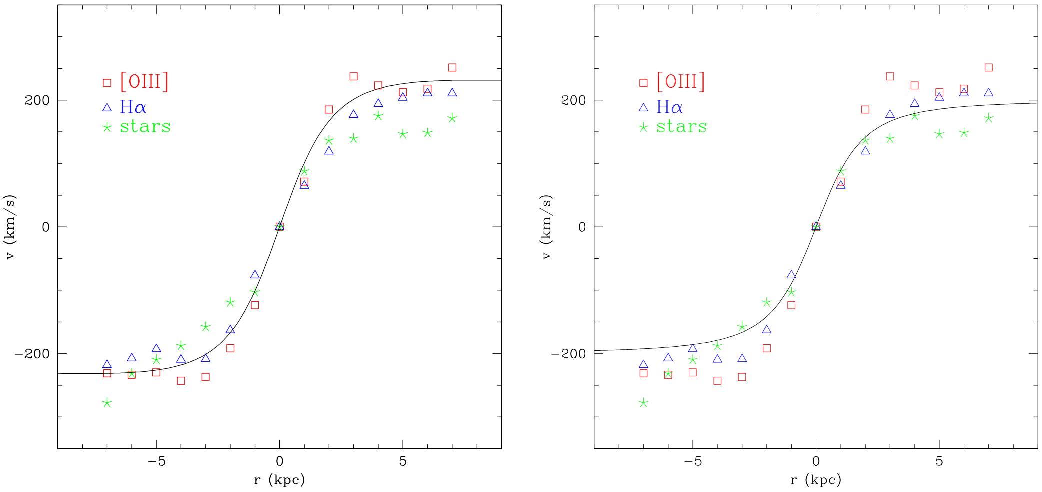

FIGURE 3.21— Fit of the rotaton curve to determine the mass from gas (left) and stars (right).

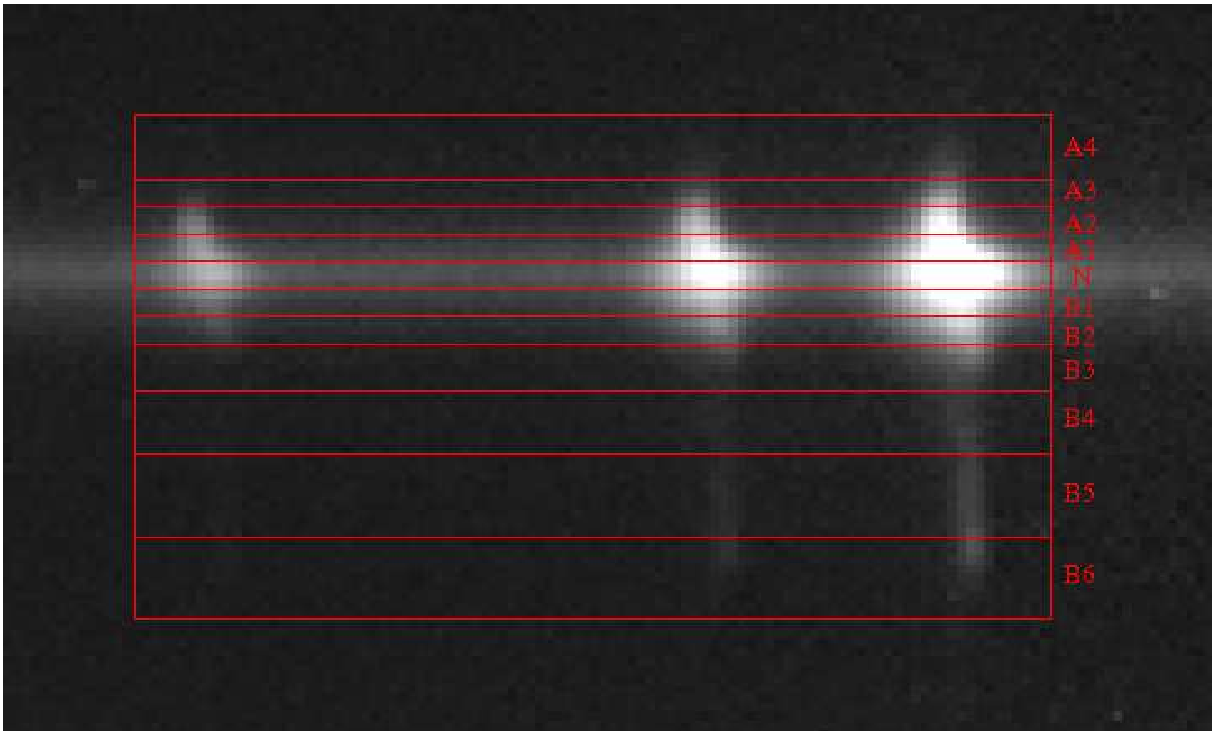

FIGURE 3.22— The NTT spectrum extracted regions. North is down.

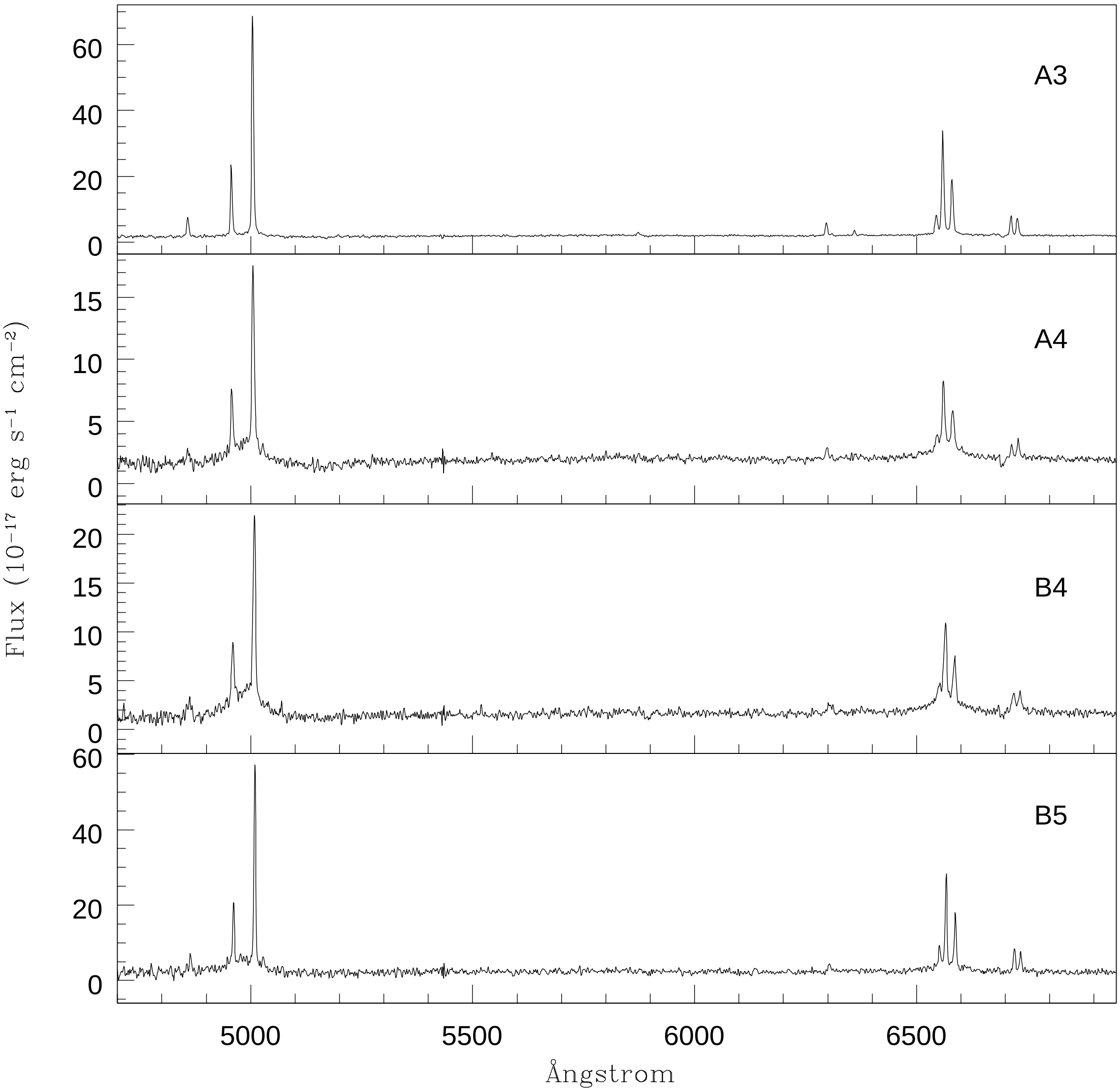

FIGURE 3.23— Spectra of the extracted regions showing broad [O III] component.

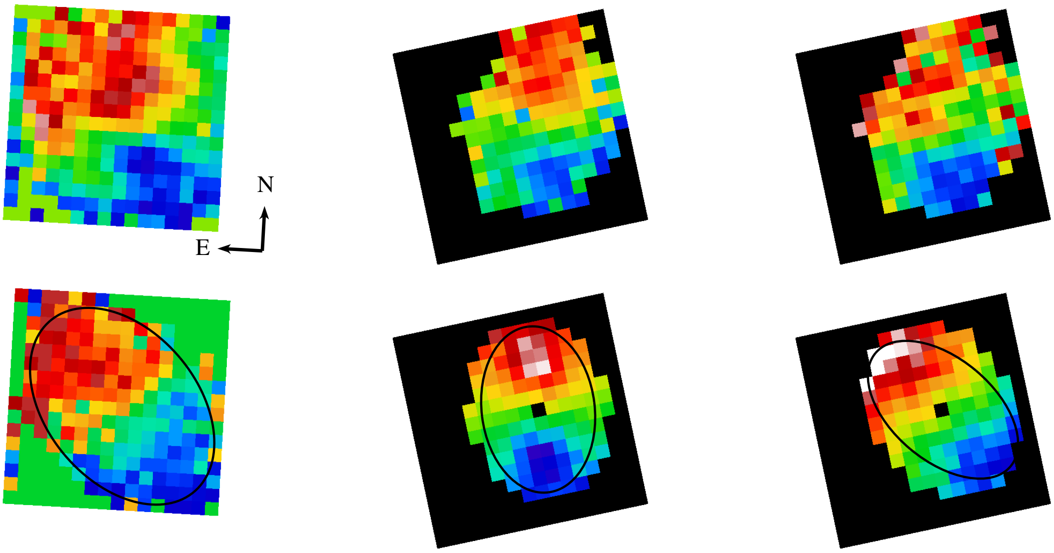

FIGURE 3.24— Comparison between the multi-component fit and the [O III] and stellar velocity maps. Top:[O III] velocity map obtained with a single component fit, the main component of the multi-Gaussian fit and the broader one. Bottom: stellar velocity map, and the ROTCUR models of the two [O III] components, with the ellipse used to estimate the PA of the kinematic minor axis, overlaid in black. North is up and East is to the left.

From the high resolution spectra a more accurate analysis of the kinematical behaviour of the ionized gas has been carried out. We decided to focus on the [O III] λ5007 line because it has the highest S/N and it is emitted by gas having a high ionization degree. We tried to identify more kinematical component, by using a multiple Gaussian fitting. In this way we were able to detect two components, the second broader than the main one. Their presence points out the complicate kinematic structure of the Extended Narrow Line Region. We tried to fit the high resolution MPFS spectra with PAN and two Gaussians, and considering only [O III] λ 5007, but the $\Delta\lambda$ between the two components were too small and PAN was not able to separate the components and often it exchanged the central wavelengths. So we decided to apply XAlice with MIDAS. From this analysis, we obtained the flux, velocity and FWHM maps for both narrow and broad components (see Figure 3.24 and Figure 3.25). The two components have different velocities and different inclinations of the minor axis. For the main component we found values ranging from -120 – -100 km s^{-1} (blue colors) and 150 – 170 km s^{-1} (red colors) and higher values of FWHM (red colors) equal to 350 – 400 km s^{-1}. The broader component has lower values, from -80 km s^{-1} (blue colors) to 120 km s^{-1} (red colors) and obviously larger values of FWHM, up to 700 – 750 km s^{-1}.

We compared the velocity fields of the two components with the stellar and the single-component [O III] velocity fields (Figure 3.24). As in the case of the single-fit [O III] velocity fields, the velocity maps of the two components are not aligned as the stellar velocity field. We showed also the models obtained with ROTCUR with the ellipse used to estimate the PA of the kinematic major axis overlaid in black. We found PA=130° for the stellar map and two different PA for the [O III] components: PA=97° for the narrower and PA=140° for the broader one. By comparing the FWHM of the [O III] components with the single-fit [O III] map we found (Figure 3.25) that the high turbulence region oriented as the minor

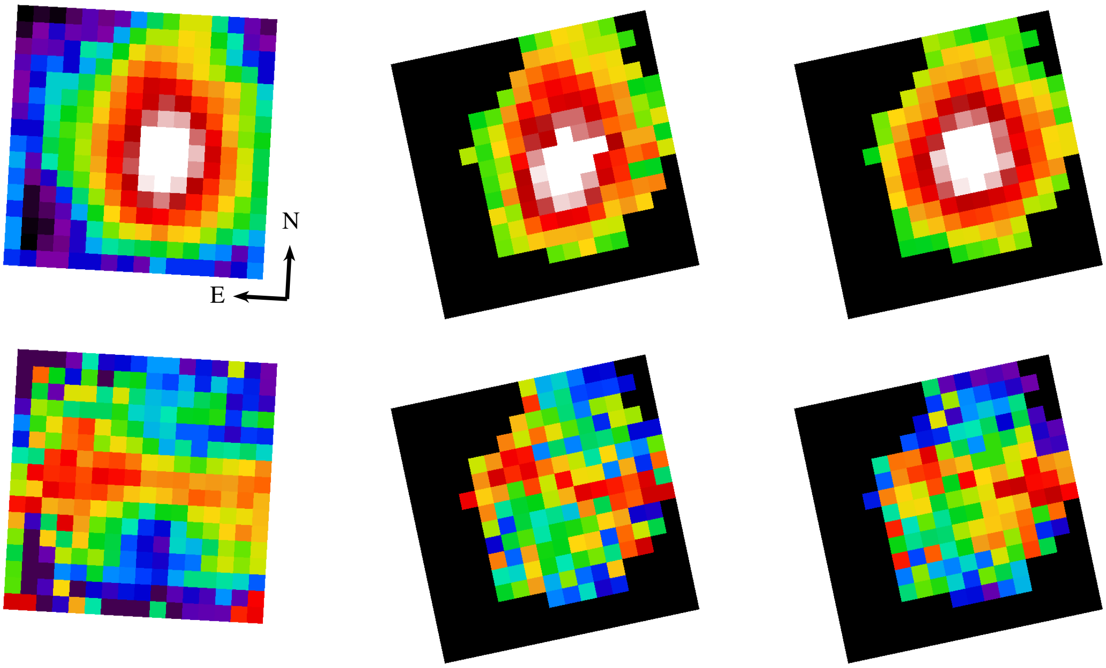

Figure 3.25— Top: The 2D maps of [O III] flux, for the single-component fit and for the two-components fit. Bottom: The 2D maps of [O III] FWHM for single-component and two-components fit.

axis of the gas emission is still present in both components.

We also found another component, a narrow peak, clearly visible in one aperture at a distance of 4″.2 (2.2 kpc) from the nucleus (see Figure 3.26), detected in Hβ, and in both [O III] λ5007 and λ4959. This component is visible also in three other apertures at distance of 4″ – 5″ (2 – 2.5 kpc) South to the nucleus, but the S/N of these spectra is very low. It is a small component in intensity but with high value of velocity, about 400 km s^{-1}. This indicates the presence of a radial motion that can be expected in such an interacting object.

To get the deprojected velocity (Figure 3.19) and to model the velocity field, we used ROTCUR. We subtracted from both the maps the value of the systemic velocity obtained from the velocity map of the narrow component. From the difference between the 2D velocity maps we can make some hypothesis about how significantly different the two velocity fields are. By considering the histogram (Figure 3.27) and the errors for the velocity determination (Figure 3.20) we can see that the median value of the difference is 77 km s^{-1} that is higher than 6 σ (the median error for these data is 12 km s^{-1}), so the difference between the two velocity maps is real.

After having found hints of multiple components in [O III] profiles, with high resolution MPFS data, we decided to explore the kinematics within the cone at higher spectral resolution. We analysed a high resolution (R∼8000, instrumental FWHM∼0.85 Å) echelle spectrum obtained with the slit oriented along the ionization cones. By only looking at the spectrum is clear that the emission is due to various sub-components at different velocities (see Figure 3.28). We can see from Figure 3.29 that the emission line

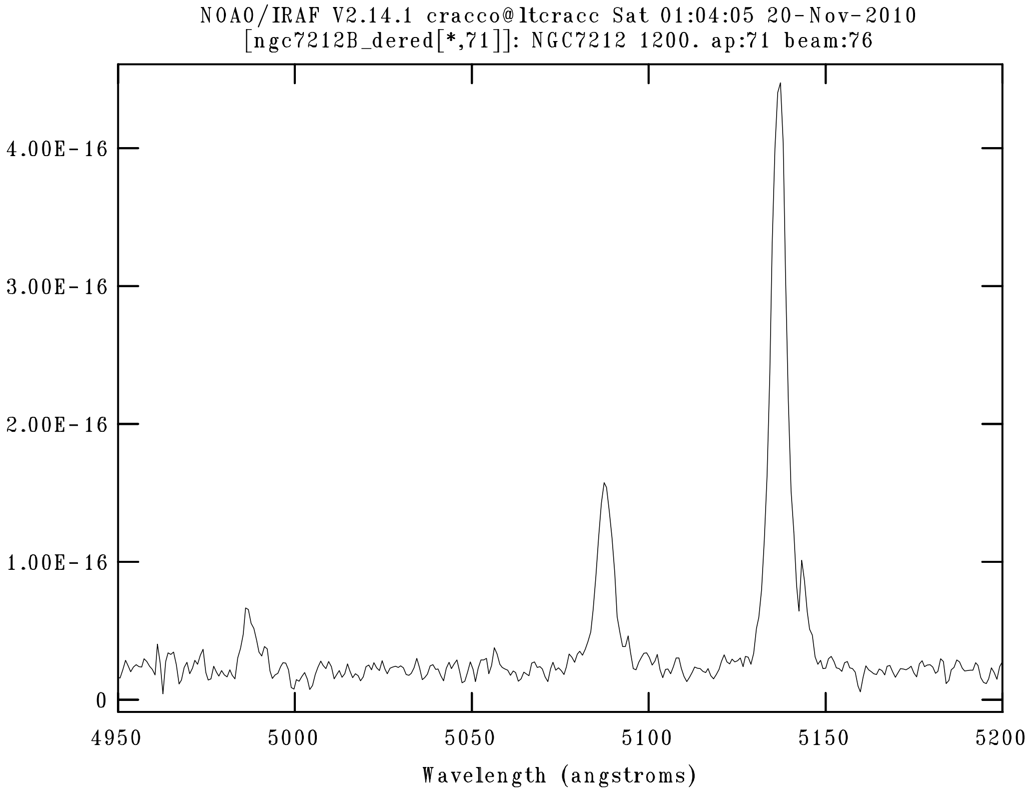

FIGURE 3.26— The MPFS high resolution data showing a component at v ~ 400 km s^{-1}. This component is visible in Hβ and [O III] emission lines.

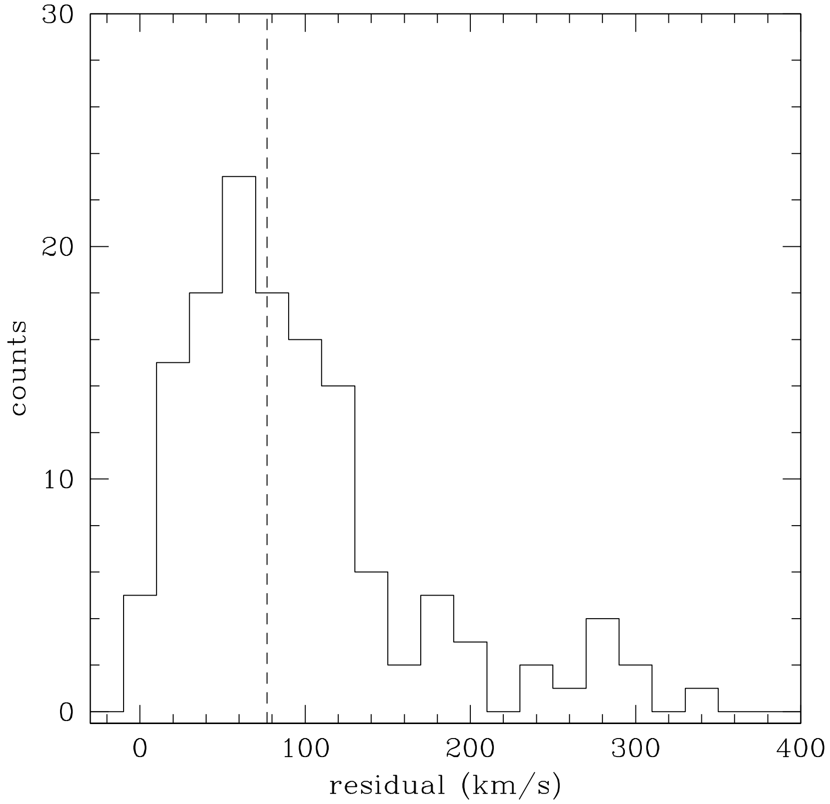

FIGURE 3.27— The histogram show the distribution of the difference between the velocity map of the two [O III] components. The vertical dashed line indicates the median value that is 77 km s^{-1}.

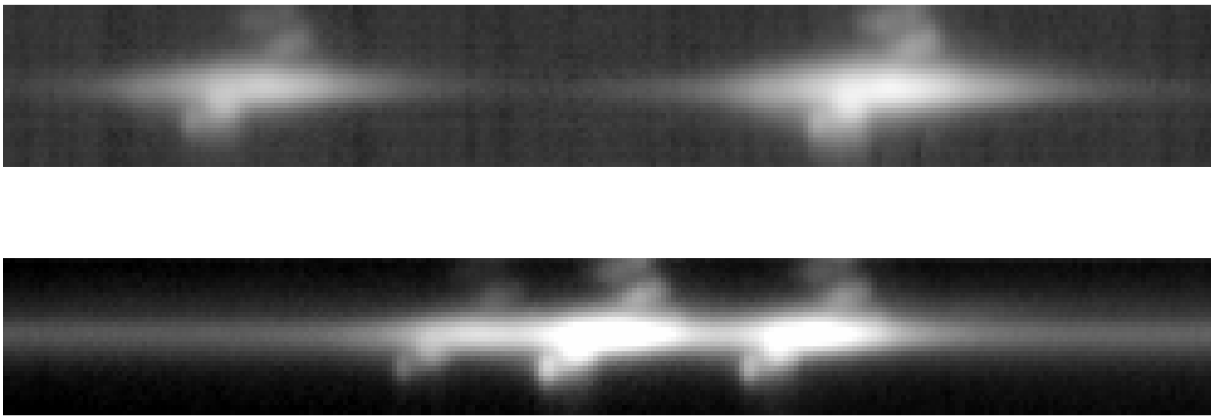

FIGURE 3.28— The echelle spectrum in the [O III] region (up) and Hα+[N II] region (bottom). The complex kinematics of the gas emission in this galaxy is clearly visible.

profile of [O III] is strongly variable and depending on the spatial position. It it difficult to reproduce such a profile in an authomatic way also because of the variability of the relative intensity of the components that makes hard to apply the same solution along the whole extended emission. Notwithstanding high spectral resolution, in the high ionization gas, the components of the emission line profiles are broad, so we decided to analyze the lower ionization gas, using the [S II] emission lines, in which the emission lines are narrower and it is less hard to identify and distinguish the different components. We found at least four components at different velocities (see Figure 3.30): $v_{11} \sim -300$ km s^{-1}, $v_{12} \sim -150$ km s^{-1}, $v_{13} = 0$ km s^{-1} and $v_{14} \sim 170$ km s^{-1}, for the [S II] λ 6716 Å. These components corresponds to the v_{21}, v_{22}, v_{23} and v_{24} of the [S II] λ6731. The FWHM of the central component of [S II]λ6716 is $\sim$ 4.6 Å, corresponding to $\sim$ 200 km s^{-1}. Maybe the lower velocity components are blended in the broad [O III] emission line profiles and are not detectable in lower resolution data.

The above mentioned higher velocity component ($\sim$ 400 km s^{-1}) is not visible in the [S II] λ6716 profile, because it is weak and it falls inside the [S II] λ6731 profile. This component could be in agreement with the highest velocity component found for the [S II] λ6731 at $v_{25} \sim 450$ km s^{-1}. It is worth noting that the ratio between the emission lines components is variable and is reversed, meaning that depending on the distance from the nucleus the physical conditions change. In particular, if [S II]6716/[S II]6731 $>$ 1, then the density is $<$ 500 e^{-} cm^{-3}, instead if [S II]6716/[S II]6731 $<$ 1, then the density is $>$ 500 e^{-} cm^{-3}. From HST images we see that the ENLR is formed by filaments, likely regions at different velocities that could be more easily seen with low ionization gas, because in this case the emission line are narrower, there is less turbulence and the components can be separated.

3.6 Ionization cones

From the ionization map we have detected an elongated and extended high ionization structure with high values (10–12) of [O III]/Hβ, up to 4 kpc from the nucleus, pointing out for the first time the presence of an ionization cone in NGC 7212 (see Figure 3.33) oriented as the galaxy minor axis. This is confirmed by the plot of the ionization degree as a function of the radius. The regions inside the cone are marked by red squares, while blue triangles represent the regions outside the cone. We built the plot of the trend of the [O III]/Hβ ratio with the distance from the nucleus, dividing the spaxels inside and outside the cone (Figure 3.31). We found that, as expected, outside the cone, the ratio decreases with the distance from the nucleus, instead inside the cone the ratio is high even far from the nucleus (up to 4 kpc). This could mean that inside the cone there are more mechanisms that ionize the gas. In order to understand if the AGN can account for such a high level of ionization, we considered the number of ionizing photons estimated from the observed Hα luminosity L(Hα) and compared these values with the number of photons emitted by the nucleus diluted by the covering factor. Firstly we calculated the L(Hα) from the reddening corrected Hα flux ($f_c(H\alpha)$) with the usual formula:

$$\mathrm{L(H\alpha)} = 4\pi d^2 f_c(\mathrm{H\alpha}) \ \ \mathrm{erg\ s^{-1}} \tag{3.18}$$

Then we derived the number of ionizing photons (N_{ph}) needed to observe these values of L(Hα), using:

$$N_{ph} = 7.3 \times 10^{11} \mathrm{L(H\alpha)} \ \ \mathrm{ph\ s^{-1}} \tag{3.19}$$

By means of these values we tried to estimate the intrinsic N_{ph}, by considering only the circumnuclear spaxels. In doing that, we are assuming that the central spaxel is along the line of sight, where the AGN

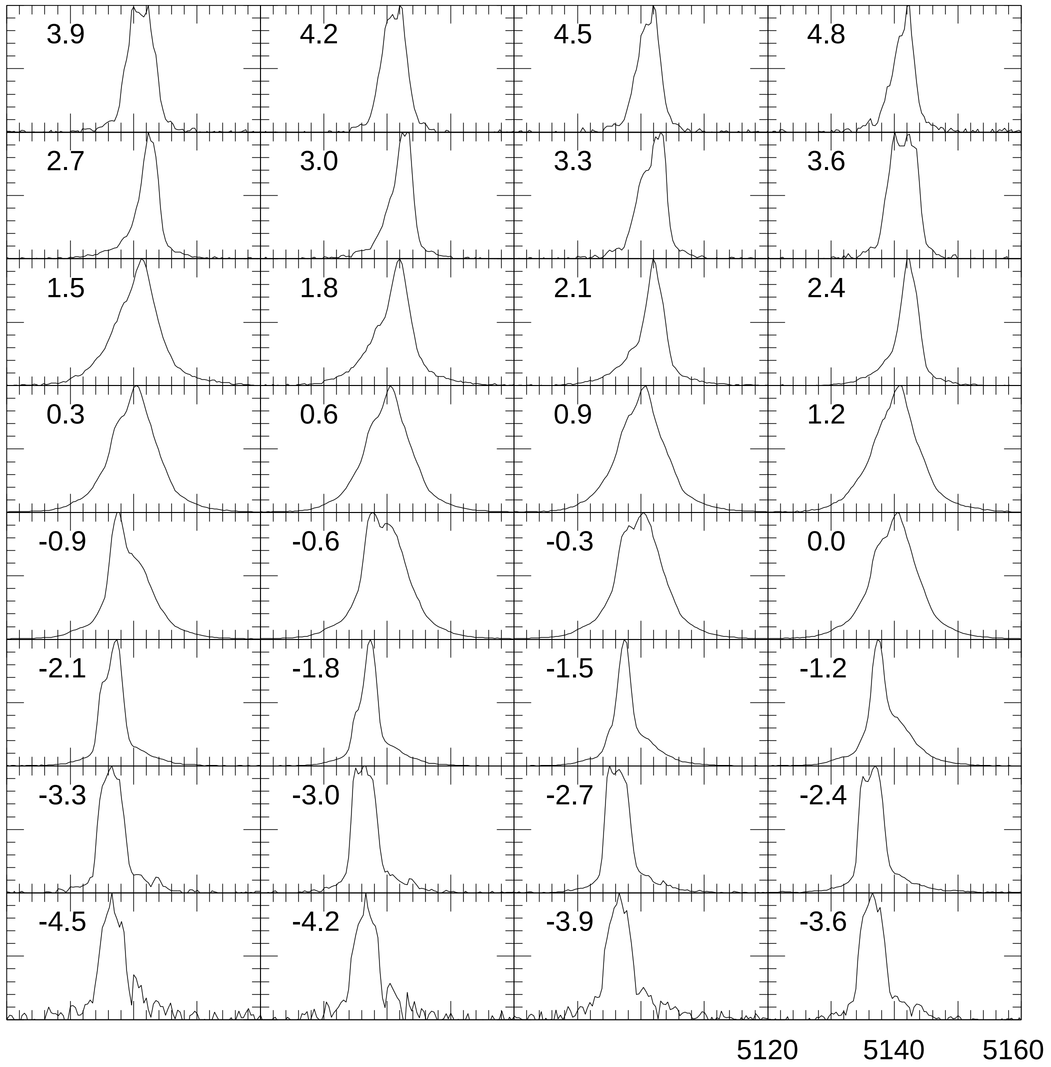

FIGURE 3.29— The [O III] emission line profiles at different distances (in arcsec) from the nucleus.

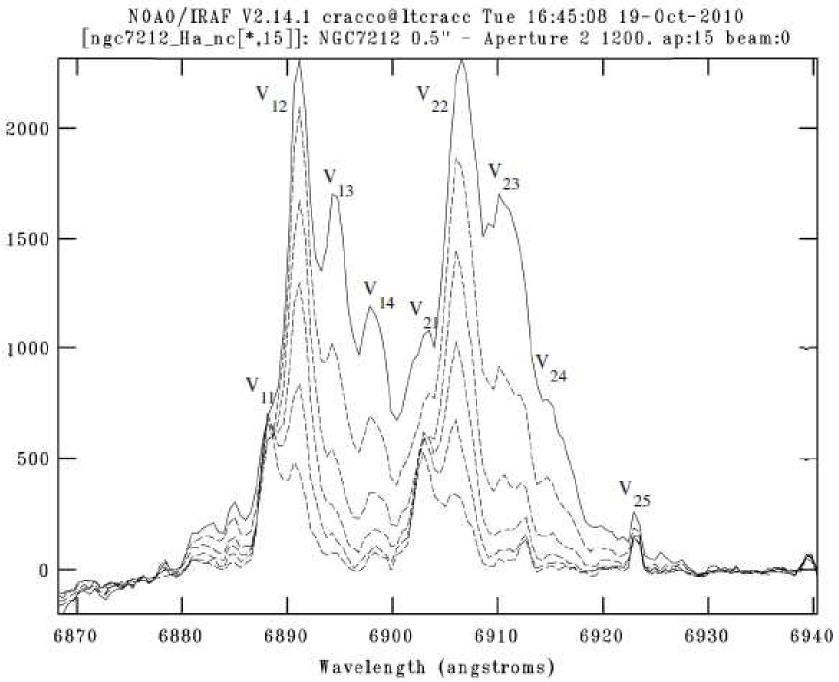

FIGURE 3.30— [S II] emission line profiles at differents distance from the nucleus. The peaks corresponding to the various components are consistent.

is obscured by the torus. Therefore in that direction we expect to have a luminosity value lower than the intrisic value. Assuming that the 3×3 circumnuclear spaxels are not obscured, we derived the observed N_{ph} value divided by the solid angle $(\Omega/4\pi)$, to get the total intrinsic emission. We used the values inside the cone, since we can expect that along the cone the radiation can flow, while orthogonally to the cone the radiation is absorbed. We found $N_{ph} = 9.4 \times 10^{53}$ s^{-1}. Then we compared the observed values with the intrinsic values diluted by the solid angle of each spaxel. We computed the ratio between the observed value and the diluted one and we found the distribution in Figure 3.32 and a median value of 0.84, indicating that the active nucleus is the dominant ionizing source of the regions within the cone. The ratio between observed and diluted values can be equal to 1, larger or lower. In the first case, the ratio is equal to 1 and this means that all the photons detected in a region come from the nuclear source. If the ratio is larger than 1 (as in few cases), this means that there are other ionizing sources, because we are measuring more ionizing photons than the ones coming from the nucleus; in other words, the photons coming from the nucleus are not enough to ionize the gas. Finally if the ratio is smaller than 1, the gas in that region has filling factor smaller than 1. In this case the AGN can sustain the observed ionization. We checked the spaxels with this ratio larger than 1 and we found that in most cases these are inside the cone, this assure that the AGN contribution is dominant. Assuming that the gas filling factor in all the regions is 1, we can get the lower limit of this value.

The aperture angle of the cone is ~70°, but, as we mentioned in Section 3.4 this angle could be larger, to account for the C1 and C2 region (showing very high values of the ratio, but not apparently belonging

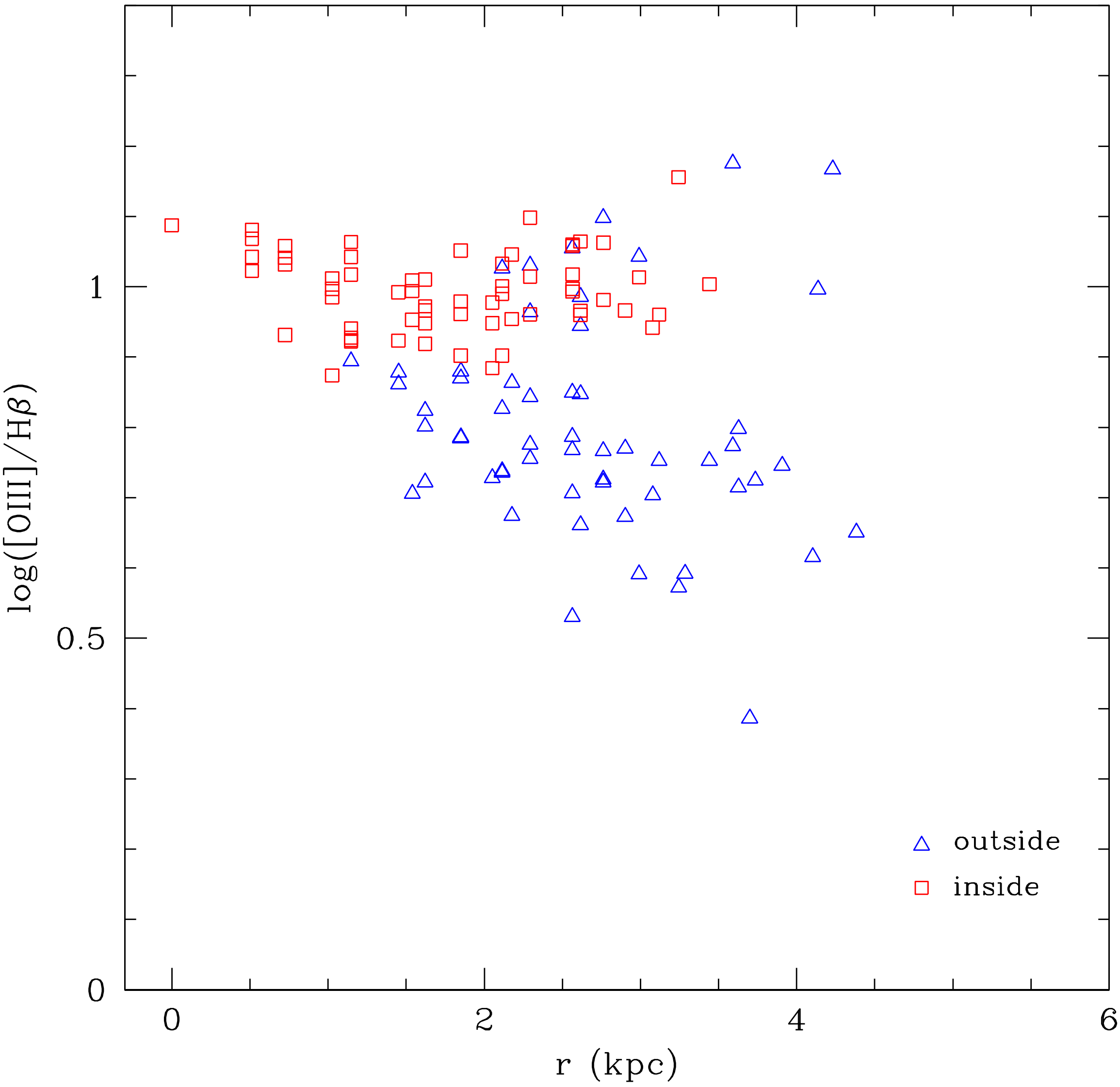

FIGURE 3.31— The trend of the ratio [O III]/Hβ and the distance from the nucleus, the red squares are the spaxels inside the cone, the blue triangles the regions outside.

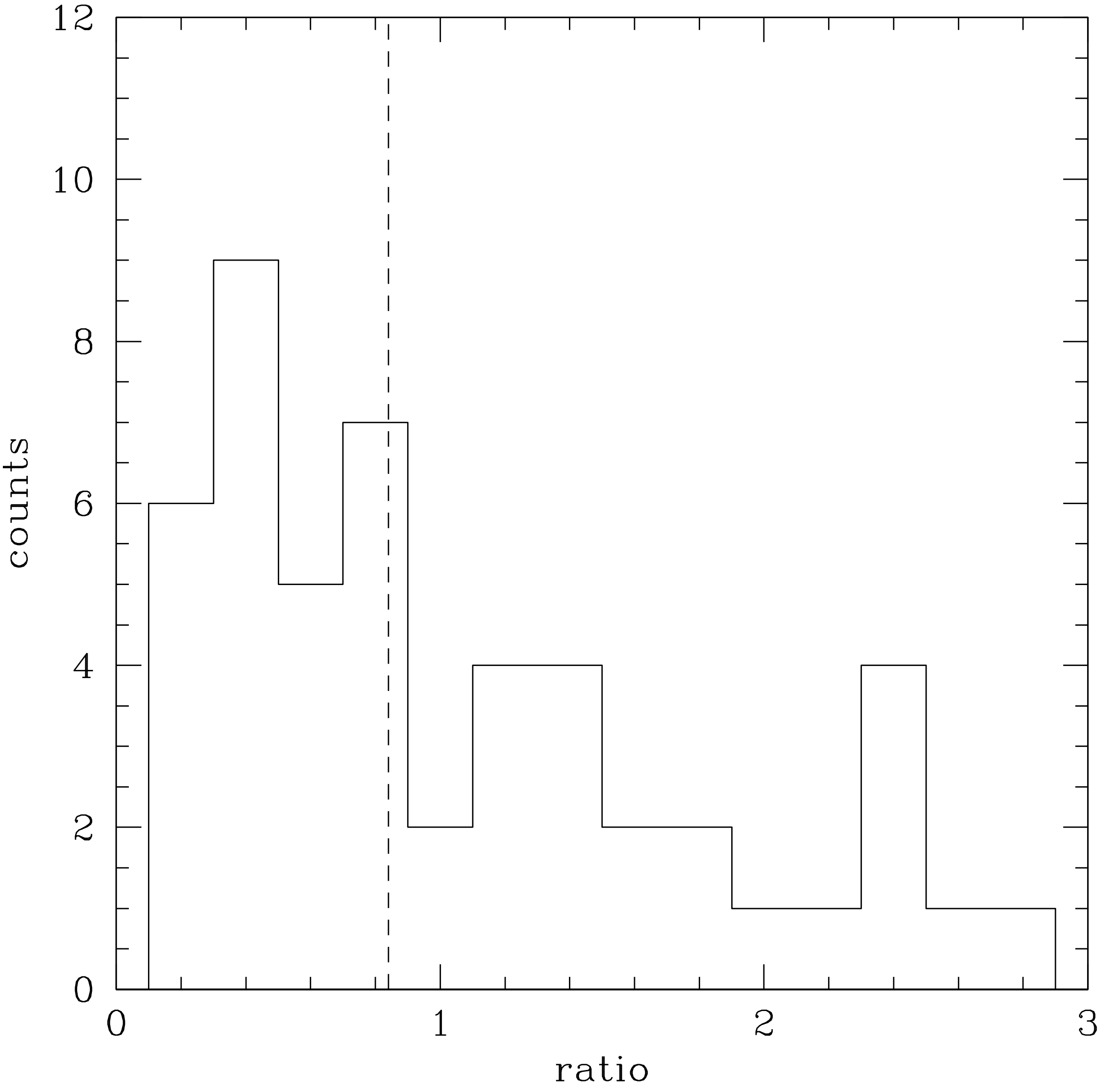

FIGURE 3.32— Histogram showing the distribution of the ratio between the observed and diluted photon number, the dashed line indicates the median value that is equal to 0.84.

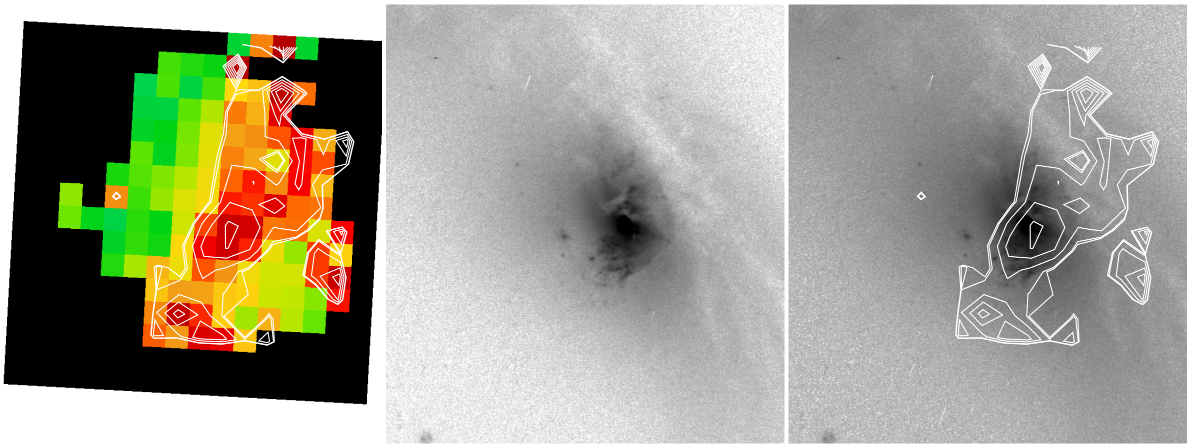

FIGURE 3.33— The ionization map with the cone contours overlaid, the WFPC2 image of NGC 7212 nucleus and the same with the cone contours overlaid.

to the cone) and the AGN-like ionization observed also far from the nuclues and in a direction orthogonal to the cones (see regions A, B and their diagnostic diagram). The total size is 12″ corresponding to ~6 kpc, oriented at PA=150°. The FWHM is around 200–300 km s^{-1} and the density is $< 10^3$ cm^{-3}, without a trend inside the cone (see Figure 3.34). We constructed also the 2D maps showing the distribution of the temperature and we overplotted the cone contours (see Figure 3.34), finding a gradient of temperature, with higher values in the norther region. The mass of the gas in the ionization cone was estimated following two methods. The first one makes use of the Hα luminosity (Ho 2009):

$$\mathrm{M(L_{H\alpha}) = 2.97 \times 10^3 \left(\frac{100cm^{-3}}{n_e}\right)\left(\frac{L_{H\alpha}}{10^{38}ergs^{-1}}\right)M_\odot} \tag{3.20}$$

The second method assumes a Galactic dust-to-gas ratio and makes use of the interstellar extinction (Fu & Stockton 2007):

$$\mathrm{M(A_V) = 1.5 \times 10^7 kpc^{-2} mag^{-1} A_V (s \times \theta)^2 M_\odot} \tag{3.21}$$

where s is the scale in kpc/″ and θ is the size of a region in arcsec. The results of the two methods are different, as shown by the two distributions in Figure (3.36) where the logarithm of the masses is plotted; in particular the second method gives larger values. The total values are $\mathrm{M(L_{H\alpha})} = 5.16 \times 10^6 \mathrm{M_\odot}$, $M(A_V) = 3.16 \times 10^8 M_\odot$. The reason of this discrepancy could be the fact that the e^{-1} density used in the first method is generally based on the [S II] line ratio, which fails in case of a very low density medium, that could constitute a large fraction of the mass of the gas in the ENLR. This could cause an underestimate of the ENLR mass with the first method. Estimating the mass of gas can give an idea of the origin of the gas, in fact a large amount of gas can be explained by acquisition of external material resulting from a merger or an interaction event.

By considering the work of Whittle (1985) about the emission line profiles and the asymmetry, we tried to calculate the asymmetry using the [O III] emission line of the higher resolution spectra. By calculating the area under the emission line and the wavelength corresponding to the 10% (λ_{10}), 50%

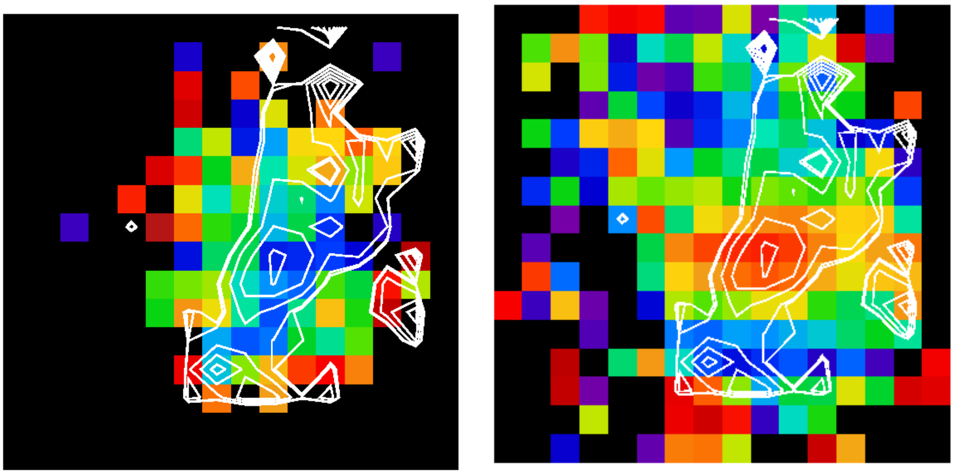

FIGURE 3.34— Map of the temperature obtained from [O III] ratio and of the density obtained from [S II] ratio, with the cone contours overlaid.

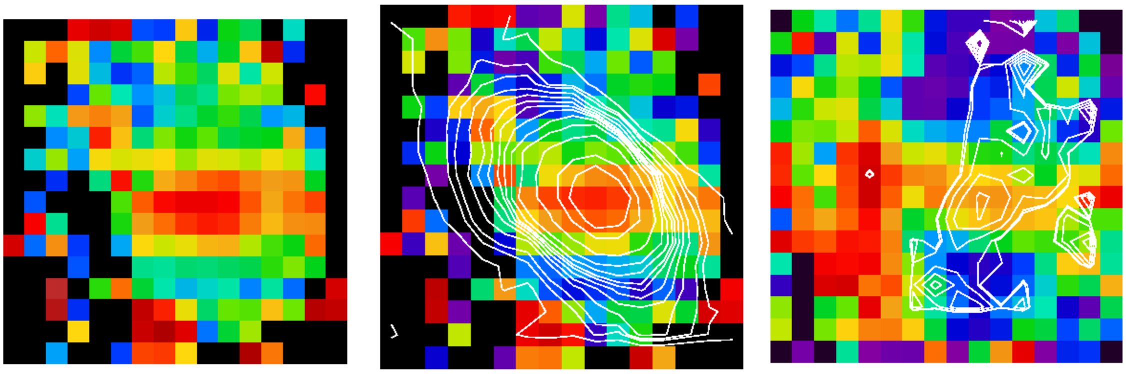

FIGURE 3.35— From left to right: density map, the same with the continuum emission at 5500 Å contour overlaid, the Hα FWHM map with the cone contour overlaid. Higher values of both density and FWHM are red coloured.

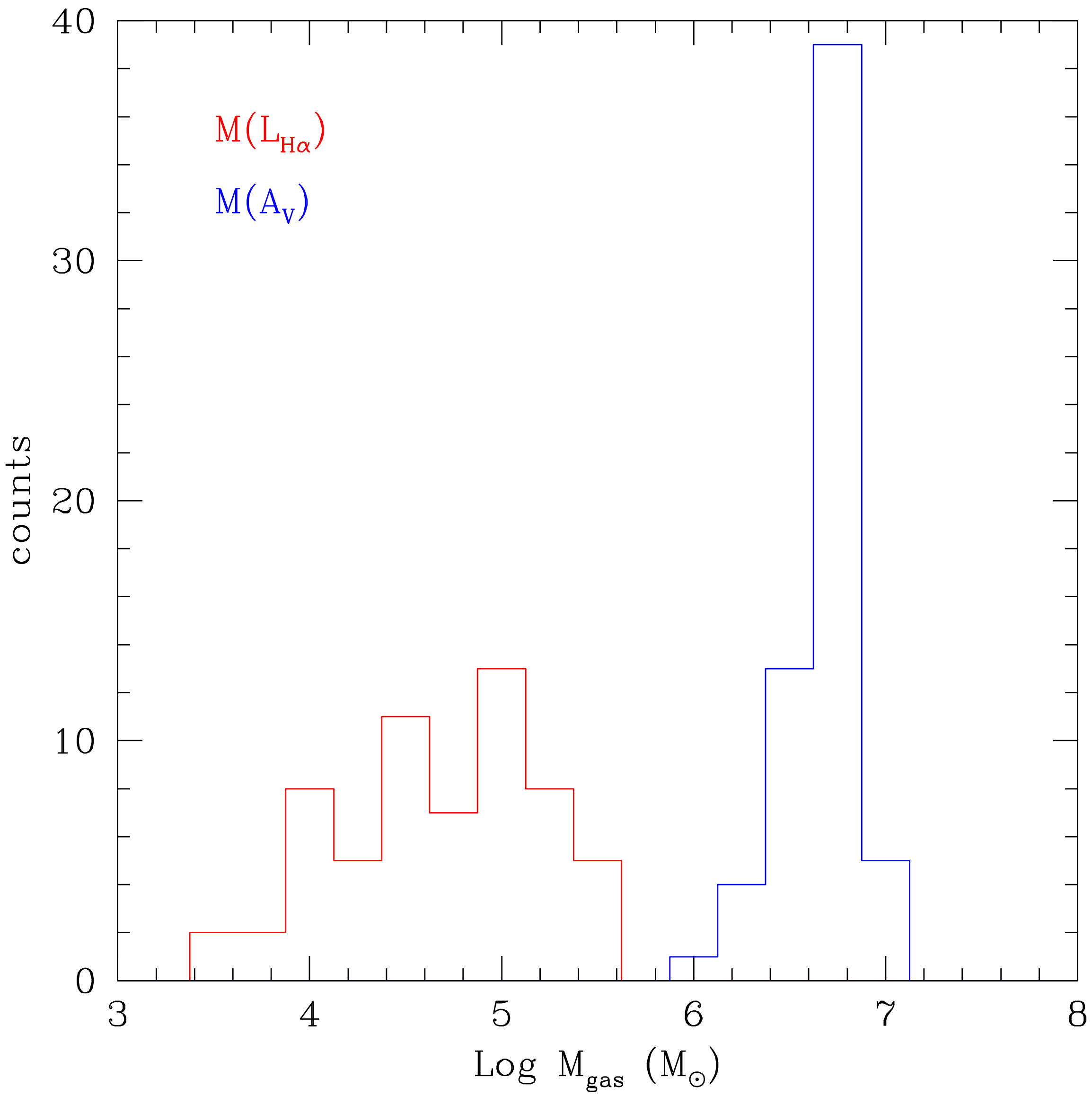

FIGURE 3.36— Logarithm of the mass distribution obtained with the two methods.

(λ_{50}) and 90% (λ_{90}) of the emission line area, we obtained the asymmetry (asym):

$$\mathrm{a} = \lambda_{50} - \lambda_{10} \tag{3.22}$$

$$\mathrm{b} = \lambda_{90} - \lambda_{50} \tag{3.23}$$

$$\mathrm{asym} = \frac{\mathrm{a} - \mathrm{b}}{\mathrm{a} + \mathrm{b}} \tag{3.24}$$

If there is a blue wing in the line profile, then $\mathrm{a} > \mathrm{b}$ and $\mathrm{asym} > 0$, instead if there is a red wing (blue colours in Figure 3.37), then $\mathrm{a} < \mathrm{b}$ and $\mathrm{asym} < 0$ (red colours in Figure 3.37). We reconstructed the asymmetry map (Figure 3.37) which shows two distinct regions, one with positive and the other with negative asymmetry. These two regions match the ionization cone contours. We found [O III] emission line profile with blue wings (red colours, see Figure 3.37) in the North part of the ionization cone, while the center-south part of the cone is characterized by [O III] with red wings (blue colours, see Figure 3.37). In the nucleus we found a symmetric profile (see Figure 3.37). This suggests the presence of gas in radial motions, outflow or inflow, inside the cone. The asymmetry is not correspondent to the higher FWHM regions, that is orthogonal to the cone, therefore these high values of FWHM is not an effect of multiple kinematical components.

3.7 Summary of the results

We studied the physical and kinematical properties of the circumnuclear gas in the nearby Seyfert 2 galaxy NGC 7212. We analysed this object by means of longslit, echelle and integral field spectra and broad–band images. By studying the VO diagnostic IFU maps we analysed the distribution of the ionization degree in the f.o.v. We pointed out for the first time the presence of an ionization cone in NGC 7212, with high values of [O III]/Hβ (up to 12), at a large distance from the nucleus (up to 3.6 kpc). The cone is oriented NW-SE direction, at PA = 150° close to the photometric minor axis of the galaxy, with an opening angle of about 70°. The cone is more extended in the North direction ($7'' = 3.6$ kpc) with respect to the South ($5''.5 = 2.8$ kpc), while both in [O III] HST images published by Schmitt et al. (2003) and Falcke et al. (1998), only the South high ionization emission was detected, showing a structure made of clouds or filaments (see Figure 3.33). The mass of the ENLR was calculated by means of two different methods based on the Hα luminosity and on the interstellar extinction. We found a value between 5×10^{6} and 3×10^{8} $\mathrm{M}_{\odot}$. This object is in an interacting triplet, with the two nearest galaxies in an on-going merger, in the N-E region. We found high values of [N II]/Hα and [S II]/Hα toward this interaction region: this could be related to shock effects, so we can have a combination of ionization by the active nucleus and by shocks. From the 2D velocity maps, we found differences between the stellar and gas kinematics. The velocity fields are misaligned, with the stellar kinematical minor axis aligned as the photometric minor axis, instead the gas kinematical axis is tilted of 30° with respect to the stellar one. We studied the asymmetry of the emission line profiles inside the ionization cone according to the work of Whittle (1985). We found [O III] emission line profiles with blue wings in the North side of the ionization cone, while the center-South side of the cone is characterized by [O III] with red wings. On the contrary in the nucleus the profiles are symmetric. This suggests the presence of gas in radial motions, which is confirmed also by the analysis of the high resolution spectra. Indeed studying the echelle data, we found that the ionization gas is characterized by multiple kinematical components at

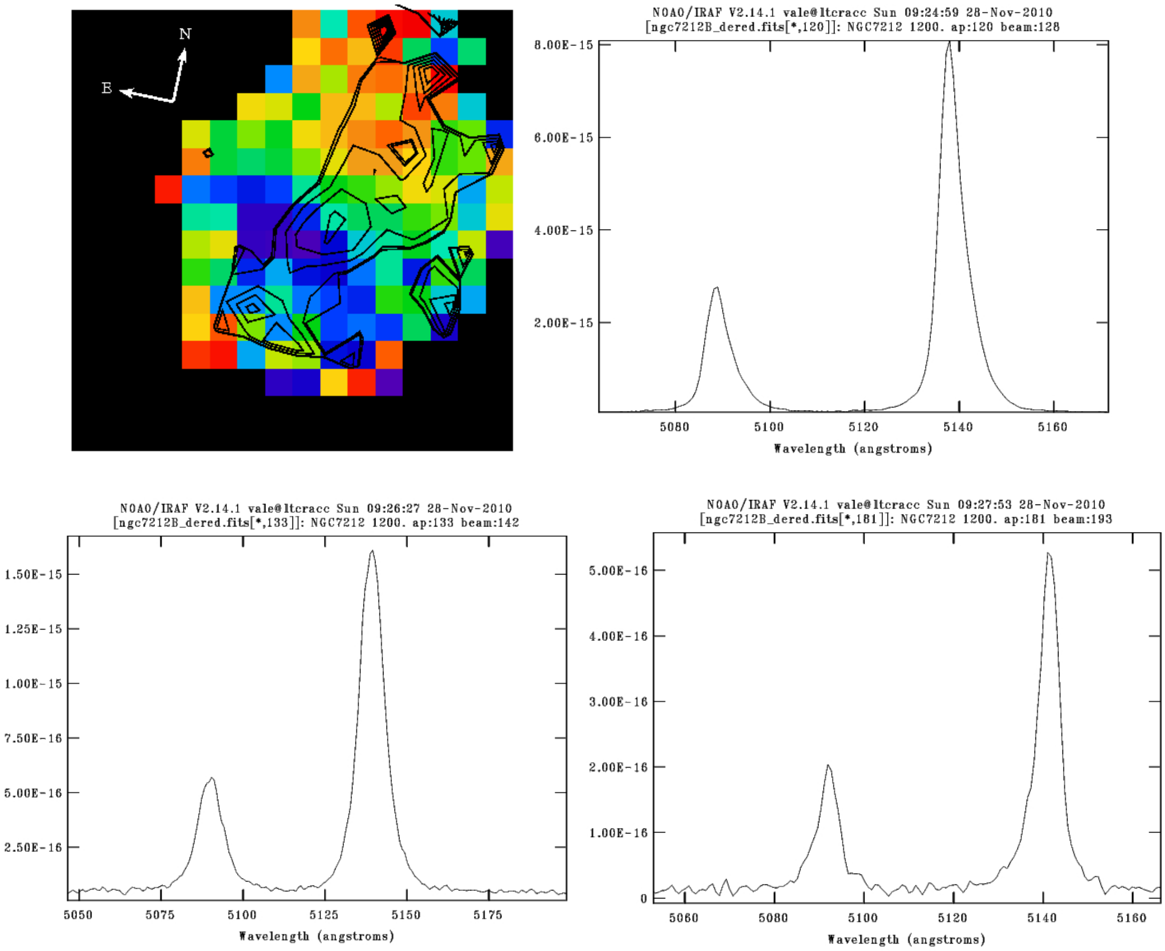

FIGURE 3.37— The asymmetry maps obtained by analysing the high resolution [O III] emission line profiles with the cone contour overlaid. Three examples of [O III] profiles in different regions of the f.o.v., from up to bottom, the asymmetry value ranging from negative to positive values. The first panel shows a spectrum in the blue part of the asymmetry map, with asymmetry equals to -0.14 with a red wing; the second panel shows an example of profile without asymmetry (green color in the asymmetry map); the last panel shows an example of red wing (asymmetry=0.21, red color in the asymmetry map).

different velocities, we found at least four components at v_1 = -300 km s^{-1}, v_2 = -150 km s^{-1}, v_3 = 170 km s^{-1} and v_4 = 450 km s^{-1}, with respect to the recession velocity. The ENLR gas metallicity was estimated by measuring the observed emission lines ratios and comparing them with CLOUDY models, obtaining sub-solar values.

In summary we found a large amount of low metallicity gas, kinematically disturbed and decoupled from stars, whose highly ionized component shows radial motions at different velocities proved by the complex profiles of the spectral lines. All these properties support the idea of an external origin of the ENLR gas in NGC 7212, likely due to gravitational interaction effects in act in this triple system.

4

MRK 6

The second interesting object we studied is the intermediate type Seyfert galaxies MRK 6 (z=0.0188, scale=0.385 kpc/′′). We selected this object by looking at the HST narrow band [O III] image by Schmitt et al. (2003) and the ground-based [O III] images (Kukula et al. 1996) showing a very extended emission. We took a longslit spectrum with AFOSC and then we decided to map and study the extended [O III] emission by means of integral field data, *g* and *r* broad-band images and AFOSC longslit spectra.

In the first section we report a summary of the information about MRK 6 taken from literature, in the five following sections we describe the analysis of the emission lines ratios, the gas and stars kinematics and the morphology of the galaxy. A summary of the results is reported in the last section.

4.1 MRK 6 in literature

Mrk 6 is an early-type (S0a) Seyfert 1.5 galaxy (Osterbrock & Koski 1976) with a compact variable nucleus, in a pair with IC 0451 located at 6′.5 to the North. Its optical hydrogen lines have a great deal of structure and have shown substantial profile variations (Khachikian & Weedman 1971), suggesting that much of the line-emitting gas has a spatially coherent bulk velocity field. It is also one of the Seyfert galaxies that have radio emission on both small and large scales. Using the Westerbork Synthesis Radio Telescope (WSRT), Baum et al. (1993) detected a pair of large weak radio lobes extending NE-SW and a smaller scale radio structure extending E-W. High-resolution MERLIN observations of the nuclear region by Kukula et al. (1996) revealed a well-defined jet extending in the N-S direction. This jet is nearly aligned with the ionization cone reported earlier by Meaburn et al. (1989) and the optical polarization position angle derived through spectropolarimetric observations (Smith et al. 2004). Kukula et al. (1996) also found some evidence of a pair of lobes on the sides of the jet that corresponded to the E-W radio structure observed by Baum et al. (1993) and Nagar et al. (1999). They carried out an extensive study with the Very Large Array (VLA) and found that the radio emission occurs on three different spatial scales: 7.5 kpc bubbles, 1.5 kpc bubbles, and a 1 kpc radio jet, all lying roughly orthogonal to each other. All the radio structures appear to originate from near the AGN core. They tried to explain radio morphology with a model of precessing jets.

Meaburn et al. (1989) used the Manchester echelle spectrometer/images on the William Herschel Telescope (WHT) to map the [O III] distribution in the nucleus of Mrk 6 and to measure the line profiles along the major axis of the [O III] structure. They found weak emission from ionized gas extending out to 22 kpc from the nucleus in a N-S direction, roughly aligned with the axis of the double radio source but tilted by 60° to the major axis of the elliptical contours of the outer optical continuum emission. The [O III] lines in this extended structure are much narrower than the typical values for a Seyfert NLR, and are indicative of material that is undergoing ordinary galactic rotation. Although the ENLR in MRK 6 does not exhibit the obvious biconical structure seen in some other Seyferts, it does have sharply defined edges suggestive of a wedge of ionized gas formed by the intersection of a cone of ionizing photons with the plane of a gas disc (Meurs 1989; Robinson et al. 1994). The unresolved intense optical nucleus probably lies between two radio sources separated by about 1″ and aligned with a PA = 177° (Ulvestad, Wilson & Sramek 1981; Ulvestad & Wilson 1984), embedded in a more extensive radio component which is 30″ across and aligned with PA=35°.

Kukula et al. (1996) carried out a ground-based study of the emission-line morphology of MRK 6, providing evidence for the existence of a large-scale radiation cone outside the jet. By means of HST emission-line observations obtained with the Faint Object Camera (FOC) in [O III] λ5007 and [O II] λ3727 together with the new high-resolution radio map, these authors revealed a jet-like emission line feature which extends 0″.5 from its nucleus.The central ridge of the jet shows a higher ionization that the surrounding diffuse emission. This optical jet is co-spatial with the radio jet and shares its bent morphology. These results strongly support the interpretation that the structure of the NLR of Mrk 6 is dominated by the compression and heating of the interstellar gas generated by shock waves formed by the supersonic radio ejecta (Pedlar et al. 1989; Taylor et al. 1992).

Absorption in the nucleus of Mrk 6 has been studied at radio, near-infrared, and optical wavelengths. In the radio band (Gallimore et al. 1998), H I (21 cm) absorption is detected only toward a bright, compact radio feature located, in projection, 1″ north of the optical nucleus. However, Gallimore et al. (1998) did not detect a clear radio candidate for the AGN core, and thus it is not clear that radio measurements have constrained absorption along the line of sight to the AGN. Several near-infrared and optical observations have been performed in attempts to constrain the reddening to the NLR of Mrk 6. Based on [O II] and [S II] line ratios, Malkan & Oke (1983) suggested an E(B-V) of 0.18±0.08, which corresponds to an absorption column density of $(1.0\pm0.4)\times10^{21}$ cm^2 by assuming a Galactic dust-to-gas ratio (Burstein & Heiles 1978).

Finally, Mrk 6 has been very poorly studied in the X-ray regime. The only X-ray detections are a possible Uhuru detection (as 4U 0638+74; Forman et al. 1978), a probable HEAO-1 detection (as 1H 0641]741; Grossan 1992), and a secure ROSAT All-Sky Survey (RASS) detection (as 1RXS J065209.8+742537; Voges et al. 1996). Nevertheless, Feldmeier et al. (1999) revealed a very interesting spectrum in the 0.69.5 keV band, showing heavy and complex intrinsic absorption in the AGN nucleus, a power law continuum of $\Gamma \sim$1.6 and an apparently broad 6.4 keV iron Kα line.

4.2 Data analysis

We analyzed both high (R = 1800, at λ = 5500Å) and low (R = 900, at λ = 5500Å) resolution IFU spectra. High resolution data were taken in two different field of views, the first centered on the galaxy nucleus and the other off-centerd by 8″ towards North (see Figure 4.1). In this way we were able to map

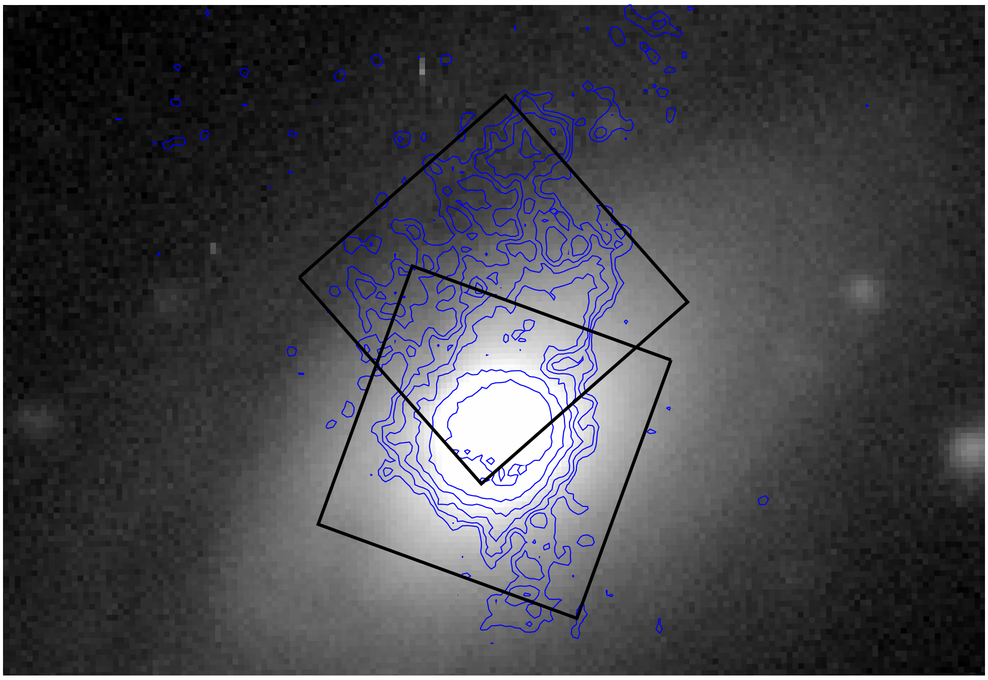

FIGURE 4.1— g-band image of MRK 6 with the [O III] contour (in blue) from Kukula et al. (1996) and the two MPFS f.o.v. (in black) overlaid.

and study both the nuclear and the extended gas emission, already found in Kukula et al. (1996). We took also longslit spectra (R ~ 370 at λ = 5500 Å) with AFOSC with the slit oriented at two different position angles (PA = 0° and PA = -30°). The low resolution data were used to study the emission lines flux distribution, the gas physical properties and to analyze the ionization mechanisms in act, by means of the diagnostic maps and diagrams. The high resolution data and the longslit spectra were used to study the kinematics of the ionized gas, using only [O III] and Hα emission lines.

MRK 6 is an intermediate type (1.2 – 1.5) Seyfert galaxy, indeed the emission we observed is a sum of BLR and NLR contribution. Since we are interested in the physics of the NLR gas, the BLR contribution must be subtracted. We started from the assumption that the BLR component can be represented as a point source, namely a 2D point spread function (PSF). This assumption is supposed to be correct because the BLR is an unresolved source. First we need to recreate the correct PSF. We fitted the line profiles of Hβ and Hα in the nuclear spectrum using NGAUSSFIT, which allows to perform a multiple Gaussian fitting. The 1D fit for the low resolution data is shown in Figure 4.2. We did not find a unique solution especially for Hβ, as shown in that figure, but finally we decided to use a similar solution for Hβ and Hα, with three broad components and one narrow component, since these lines originate from the same region. We tried to apply the same solution also for both centered and off-centered high resolution data. Then we rescaled these fits considering the light distribution in the f.o.v. of the PSF representing the BLR emission. We reconstructed 2D maps of the emission from the broad wings of Hβ and Hα (Figure 4.3) and we used them as PSF. We tried different spectral ranges to find out the best representation of the PSF, and then we normalized this map using the intensity value of the central spaxel. In this way

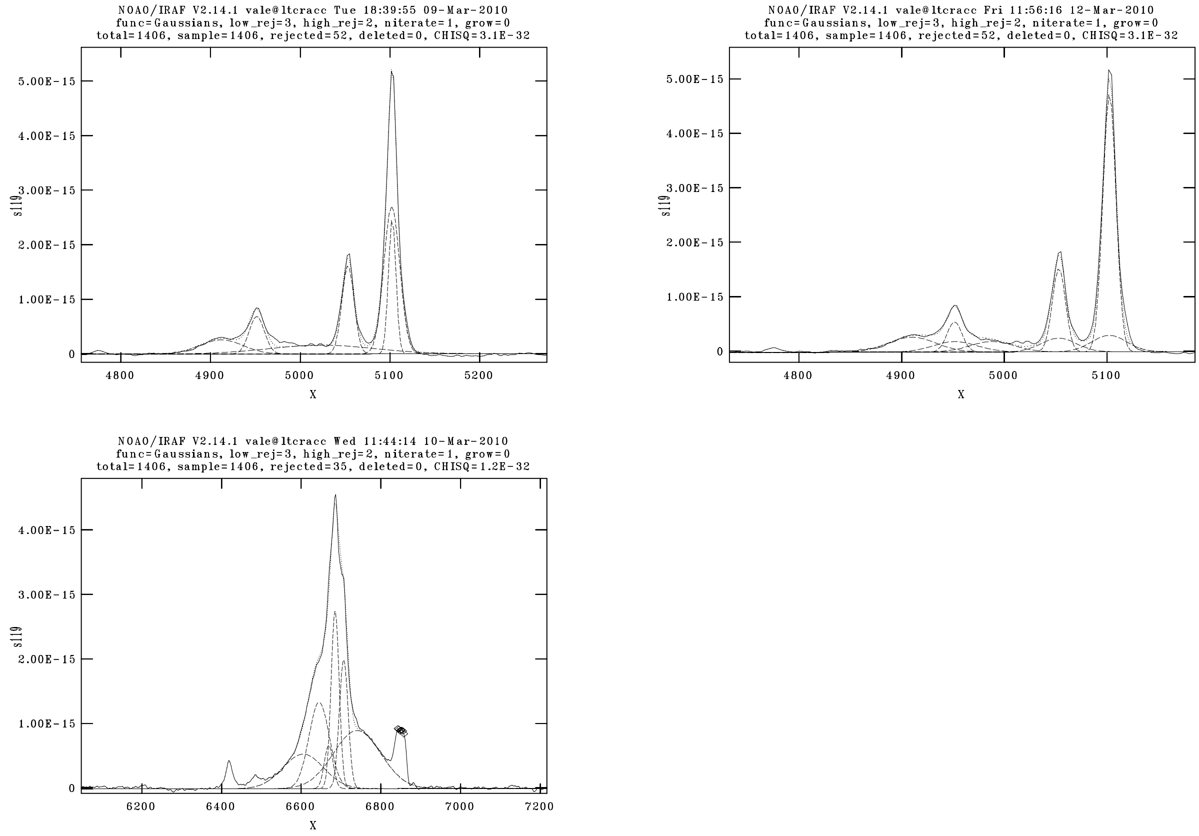

FIGURE 4.2— The 1D fits for the low resolution data are shown. Upper-left panel: the first attempt for Hβ with one broad component and another component between Hβ and [O III] λ5007. Upper-right panel: the final fit for Hβ with three broad components for Hβ and one broad component also for both [O III] emission lines. Lower panel: the final fit for Hα with three broad components.

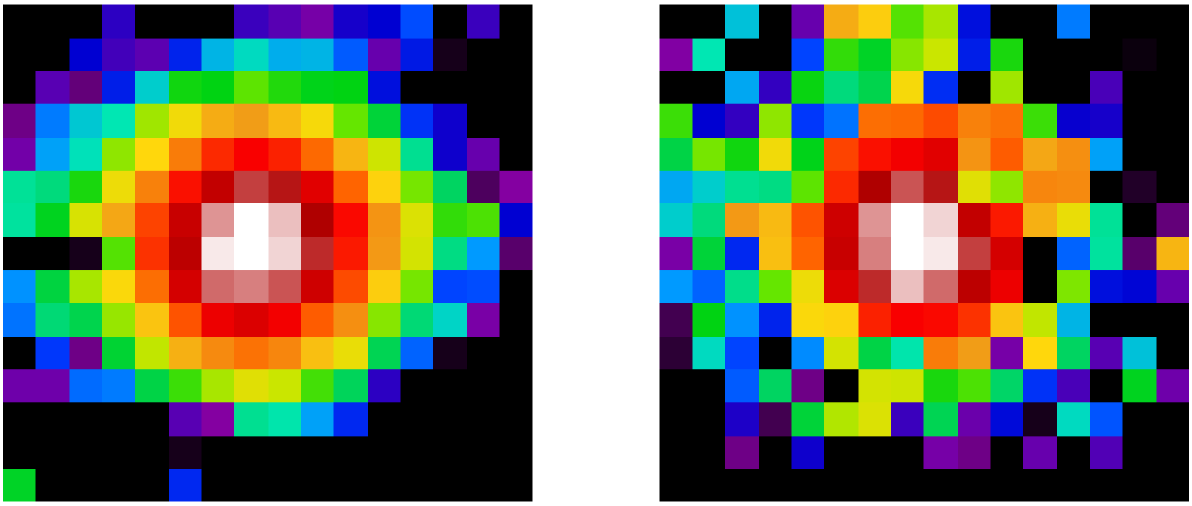

FIGURE 4.3— The 2D maps of the distribution of the point-like emission from the broad wings of Hα (left) and Hβ (right) lines.

we obtained a 2D map of the coefficients (between 0 and 1) to be multiplied for the 1D fit of the BLR profile in order to rescale it, according to the normalized PSF intensity. We reconstructed a 2D spectrum and we obtained for each spectrum the correct BLR contribution to be subtracted. Finally we subtracted from the original spectrum the BLR spectrum, obtaining only the NLR contribution (Figure 4.4). The subtraction is acceptable and allows us to better measure the narrow emission lines.

By analyzing these data we derived maps of flux, velocity and FWHM for each line in the whole field of view. In order to estimate the reliability of our measurements, we calculated the S/N of the continuum for MPFS data (see Figure 4.5). These data have low values of S/N: the median values for low resolution data are ~4.5 and ~6.3, measured at rest-frame 5500 Å and 7000 Å. The higher resolution data have smaller values: around 1.3 and 1.9, measured at rest-frame 5500 Å and 7000 Å, respectively. We tried to apply STARLIGHT to these data, but we did not get a good result, because of the low S/N of the continuum and also because in MRK 6 the continuum is dominated by the AGN contribution. Therefore we have no information about the stellar component for this galaxy. All the measured fluxes were corrected for Galactic extinction and should be corrected also for the internal reddening, using the Balmer decrement. Firstly we calculated the A(V), by means of the Hα/Hβ map and using the Cardelli Clayton and Mathis (1989) extinction law. We found high values of extinction, up to 4.5 – 5 mag, in the North-West region (5″ from the nucleus). In the nuclear region we found values of ~2 mag. We applied this correction, obtaining too high values for [O II] flux, not compatible with an ionizing source with a power-law spectrum: we found values 2 – 3 times more intense than [N II]. Furthermore the corrected flux distribution becomes asymmetrical, due to the strong asymmetry in the extinction map (see Figure 4.6). By comparing the A(V) map with the color map (see Figure 4.15), we did not find red structures in the North-West region, that could justify high values of A(V), instead we found dust lanes in the East part of the galaxy. These high values of A(V) could be due to a wrong subtraction of the broad component for Hβ and/or for Hα. To avoid introducing additional errors, we decided not to correct for

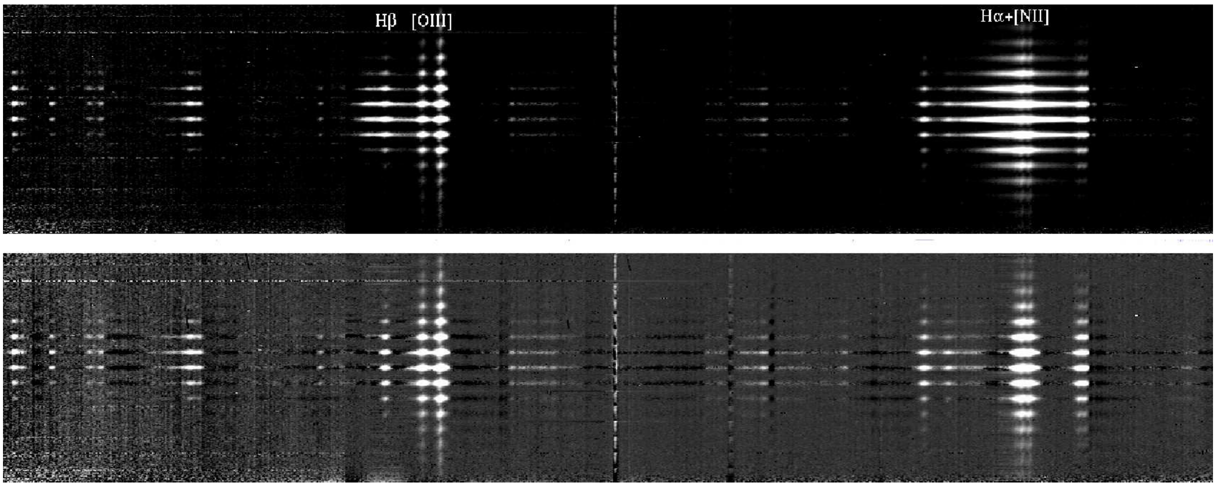

FIGURE 4.4— The MRK 6 multi-aperture spectrum, before (upper panel) and after (lower panel) the subtraction of the broad point-like contribution. The result is acceptable.

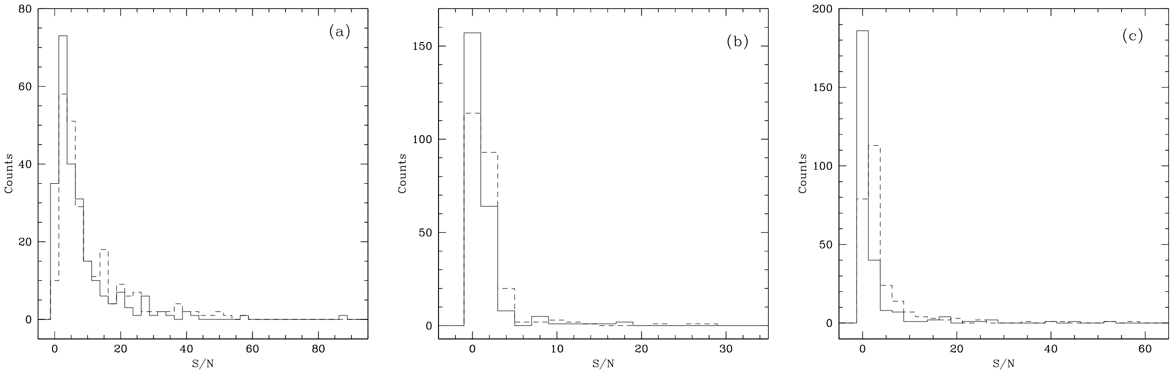

FIGURE 4.5— The S/N ratio for each dataset. Solid line indicates the S/N ratio measured at 5500 Å, and dashed lines indicated the S/N ratio measured at 7000 Å. We obtained the S/N distribution for low resolution data (a), high resolution data centered in the nucleus (b) and high resolution off-centered data (c).

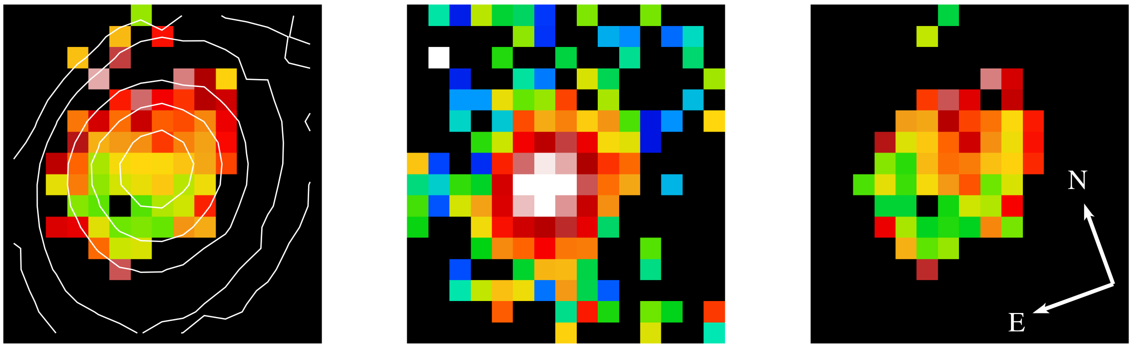

FIGURE 4.6— From left: the A(V) map with the continuum contour overlaid; the [O II] flux before and after the extinction correction. It is clear the strong difference in intensity and distribution of the [O II] emission.

internal reddening being the measurements of the Hα/Hβratios not so accurate. We estimated the flux errors, assuming that the determination of the position of the continuum level gives the main contribution in the errors measuring emission line fluxes. The errors ΔF are obtained dividing the reddening corrected flux $F_c(\lambda)$ by the S/N of each emission line, calculated as the ratio of the amplitude (amp(λ)) of the line divided by the standard deviation (rms(λ)) of the continuum in a spectral region near the emission line:

$$\Delta F = \frac{F_c(\lambda)}{S/N(\lambda)} \tag{4.1}$$

$$\frac{S}{N}(\lambda) = \frac{\mathrm{amp}(\lambda)}{\mathrm{rms}(\lambda)} \tag{4.2}$$

4.3 Emission line analysis

Each reliable emission line in the reduced low resolution spectra was measured and the flux map reconstructed. These maps represent the spatial distribution of the emission for each spectral line. We measured the following 20 emission lines at least in the nuclear region [O II] λ3727, [Ne III] λ3869, [Ne III] λ3968, [S II] λ4070, Hδ λ4102, Hγ λ4340, [O III] λ4363, He II λ4686, Hβ λ4861, [O III] λ4959, [O III] λ5007, He I λ5876, [O I] λ6300, [O I] λ6363, [N II] λ6548, Hα λ6563, [N II] λ6584, [S II] λ6717, [S II] λ6731, [Ar III] λ7135. All the emission line maps filtered considering only the spectra in which the S/N of the emission line is larger than 3 are shown in Figure 4.7. The most intense emission lines, such as [O III], [N II], [S II] and Hα, are extended for 12″–14″ (4.6 – 5.4 kpc) oriented along a PA$\sim$160°, the nuclear emission has a circular shape and its extension is probably limited by the f.o.v. The fainter emission lines, such as [O II], Hβ and [Ne III] , are extended for 3″–10″ (1.2–3.9 kpc) with the same position angle (Figure 4.8). The emission lines are not very extended except for the most intense ones, probably due to the low S/N ratio of the continuum emission. The major axis of the continuum is oriented at PA$\sim$130° (Figure 4.8).

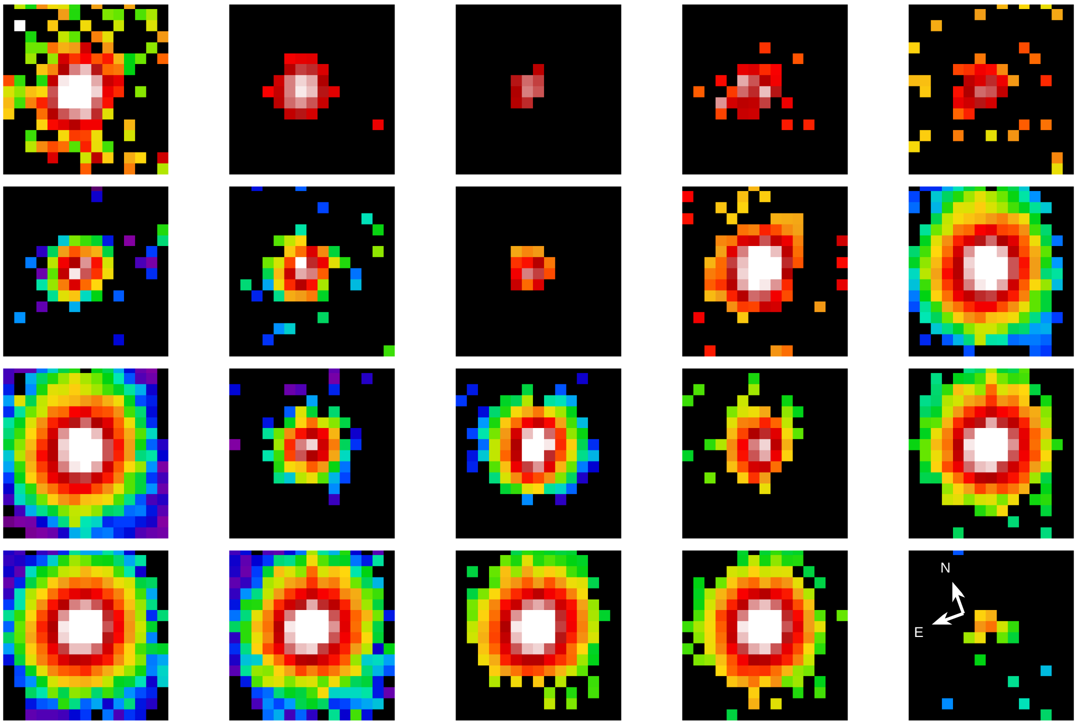

FIGURE 4.7— The measured emission lines and the reconstructed maps. All the data with S/N > 3 are shown. From up-left there are the following emission lines: [O II] λ3727, [Ne III] λ3869, [Ne III] λ3968, [S II] λ4070, Hδ λ4102, Hγ λ4340, [O III] λ4363, He II λ4686, Hβ λ4861, [O III] λ4959, [O III] λ5007, He I λ5876, [O I] λ6300, [N II] λ6548, Hα λ6563, [N II] λ6584, [S II] λ6717, [S II] λ6731, [Ar III] λ7135.

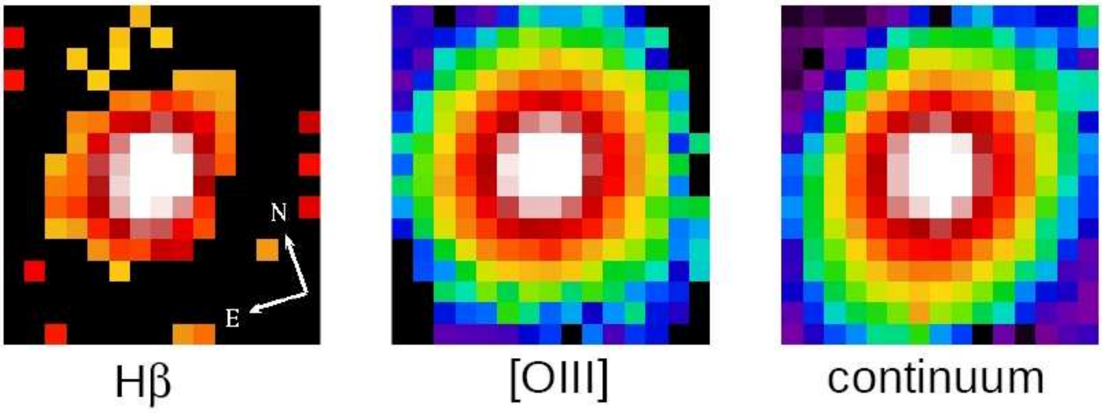

FIGURE 4.8— The distribution of the emission of Hβ and [O III] emission lines compared to the map of the stellar continuum emission.

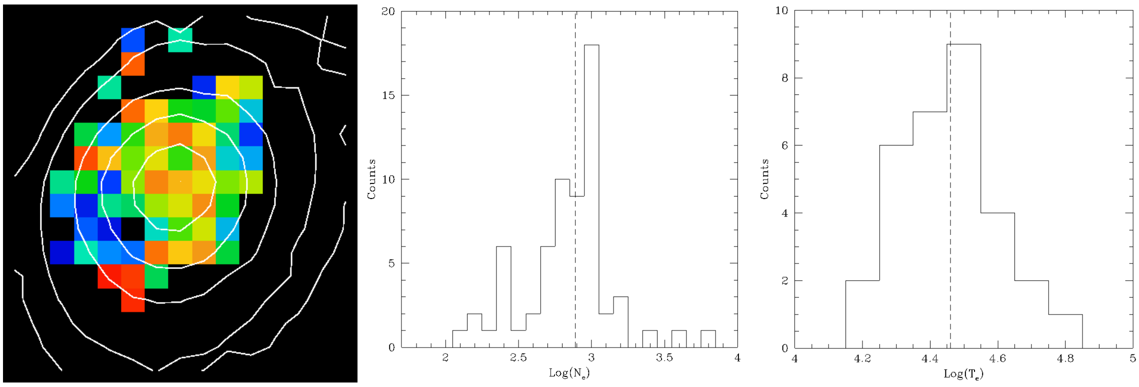

FIGURE 4.9— 2D map of the density measured with the [S II] emission lines, with the contours of the continuum emission at 5500 Å overlaid. The orientation is as in Figure 4.8. Histograms of density and temperature. Left: density obtained using a values of temperature of $T_e = 10^4$ K, the median value is ~780 e^- cm^{-3}. Right: temperature distribution, the median value is obtained with [O III] ~28000 K.

We analyzed gas physical properties: by means of the usual emission line ratios, gas density and temperature were calculated; by comparing our measurements with CLOUDY models, we inferred an estimate of gas metallicity. We calculated the density with the IRAF task TEMDEN, by means of the [S II] λ6717/λ6731 ratio, because the [Ar IV] lines were not detected. We used an input value of temperature $T=10^4$ K and we calculated the density for each spectrum in which we measured the ratios, obtaining a median value of ~ 780 e^- cm^{-3} (see Figure 4.9). In the central regions, the density value obtained with [S II] emission lines is ~ 10^3 cm^{-3} (assuming $T_e = 10^4$ K). We found high density in the inner regions and lower values in the outer regions both North-West and South-East to the nucleus (see Figure 4.9). The gas temperature can be obtained using different emission line ratios: with our spectra we can use the [O III] lines at λ4959, λ5007 and λ4363, by calculating the ratio between the flux of the [O III] λ(4959+5007) and the flux of the [O III] λ4363, and the [S II] lines at λ6717, λ6731, λ4068 and λ4076, by calculating the ratio between the flux of [S II] λ(6717+6731) and the flux of [S II] λ(4068+4076). We determined the temperature with these two ratios, in the case in which the λ4363 and the λ4068+λ4076 could be measured. So the temperature derived with this analysis is not characteristic of the whole f.o.v, neither of the whole gas, but only of regions in which these lines are detectable and gas emits [O III] and [S II]. We derived temperature using TEMDEN, and using the values of density calculated with the [S II] ratio. The [S II] λ4068 and λ4076 can be detected only in a small number of nuclear spaxels (6). We found a mean value of ~ 19000 K. The histogram for the [O III] determination of temperature is shown in Figure 4.9. The median value is ~ 28000 K, slightly higher than the [S II] determination. The study of metallicity for AGN is more problematic. In HII regions and in star-forming galaxies, the metallicity can be measured through direct methods (Aller 1984) or by means of empirical metallicity indicators (Pilyugin & Thuan 2005), because in the stellar photo-ionization case, the ionization structure is known an the total abundances can be inferred once the ionic abundances are measured. On the contrary in case of ionization by a power-law spectrum, as for the AGN, the situation is more complicated and the ionization structure is very complex. There are not direct methods and to determine the metallicity must be used photoionization models. We estimated the gas metallicity, by comparing the measured fluxes

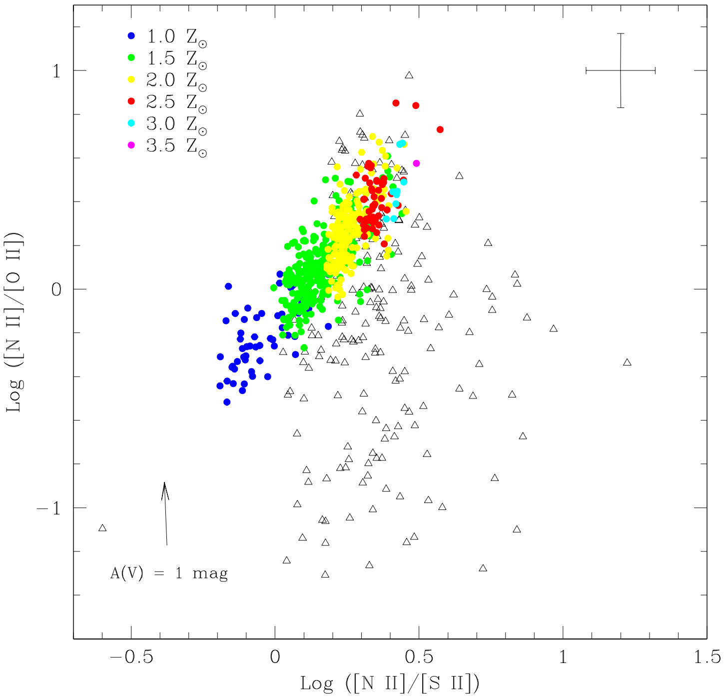

FIGURE 4.10— The diagram of log ([N II]/[S II]) vs log ([N II]/[O II]) compared with theoretical models by Vaona (2010) with D/G = 1. From red (Z/Z⊙=3.5) to purple (Z/Z⊙=1) colors, the metallicity decreases. The arrow indicates the direction and magnitude of the shift due to the extinction correction for A(V) = 1 mag. Black triangles are our data, coloured full circles are models by Vaona.

with values predicted by models from Vaona (PhD thesis 2010), using the following emission line ratios [N II]6584/[O II]3727 vs [N II]6584/[S II]6724, being this the best diagram sensitive to the metallicity. The models have a low resolution in metallicity because Vaona used few $Z/Z_\odot$ values, nevertheless the trend is clear. We used models with dust-to-gas ratio (D/G) equal to 1. We plotted the uncorrected ratios, because the extinction correction was uncertain, in particular in the case of [O II] 3727 Å. The arrow in Figure 4.10 indicates the direction and the magnitude of the shift due to the extinction correction for A(V) = 1 mag. 35% of the observed data could be fitted by the models, with high values of metallicity (1.5 – 3 $Z_\odot$). This disagreement is not an effect of extinction, indeed after the reddening correction the data are even more distant from the models. It should be due to a low S/N ratio of [O II] λ3727 emission lines, but by considering data with S/N > 5, most of the data are still distant from models. We need to build other models in order to interpret our observed data.

In order to distinguish between ionization by power law and by stars or shocks we used in this work the Veilleux-Osterbrock (VO) diagnostic ratios (Veilleux & Osterbrock 1987). By calculating the maps of emission line ratios ([O III]/Hβ, [N II]/Hα, [S II]/Hα) it is possible to investigate the ionization mechanisms in act in the ENLR. The 2D maps showing the spatial distribution of the diagnostic ratios (Figure 4.11) were created using the not-reddening corrected maps, in order to study a more extended

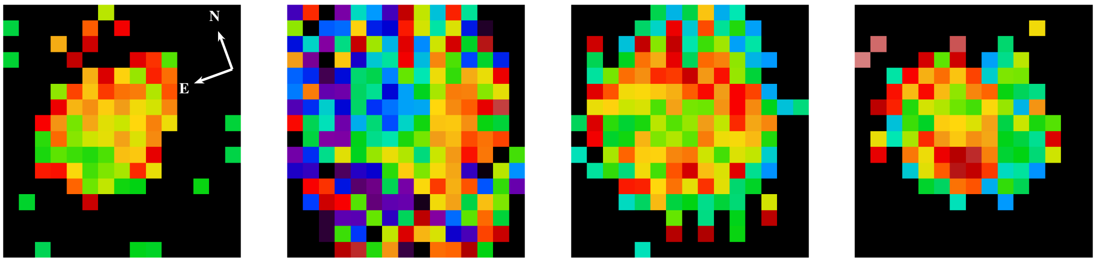

FIGURE 4.11— The VO diagnostic ratios maps are shown. Top: [N II]/Hα and [S II]/Hα. Bottom: [O I]/Hα and [O III]/Hβ. In each map, yellow-red color corresponds to high values, instead green-blue colors indicate low values.

field, not being limited by the small size of the Hβ emission. In fact, in this case we are interested in analysing the distribution of the diagnostic ratios in the whole field of view. Furthermore, the emission lines involved in each ratio are so closed in the spectrum, that the extinction influence is expected to be similar and to be minimized or removed when we calculate the ratios. In each map, yellow-red colors indicate high values of the ratio, instead green-blue colors correspond to low values. In the [O III]/Hβ map we find values larger than 6 and up to 18 (red-yellow colors indicate 9 – 15, green colors 4 – 7), but only in the central part where Hβ emission line was detected. [N II]/Hα shows higher values (up to 1.2 – 2.6) in the West region, instead [S II]/Hα shows a ring-like structure with high values (0.45 – 0.5), [O I]/Hα shows higher values (0.2) in the East region. We calculated also the VO diagnostic diagrams, for the whole sample (Figure 4.12), which show high excitation with all the ratios falling in the AGN region. The [N II]/Hα diagram shows a larger spread in the distribution of the regions, instead the two other diagrams are concentrated in a small range in x-axis and larger in y-axis. To separate the different regions in the diagnostic diagram (AGN, HII regions and LINERs) we used the expressions from Kewley et al. (2006):

$$\log\left(\frac{[\mathrm{OIII}]}{\mathrm{H}\beta}\right) = \frac{0.61}{\log\left(\frac{[\mathrm{NII}]}{\mathrm{H}\alpha}\right) - 0.47} + 1.19 \tag{4.3}$$

$$\log\left(\frac{[\mathrm{OIII}]}{\mathrm{H}\beta}\right) = \frac{0.72}{\log\left(\frac{[\mathrm{SII}]}{\mathrm{H}\alpha}\right) - 0.32} + 1.3 \tag{4.4}$$

$$\log\left(\frac{[\mathrm{OIII}]}{\mathrm{H}\beta}\right) = \frac{0.73}{\log\left(\frac{[\mathrm{OI}]}{\mathrm{H}\alpha}\right) + 0.59} + 1.33 \tag{4.5}$$

The errors to be associated to the diagnostic ratios were computed with this formula:

$$\mathrm{err}\left(\log\frac{\mathrm{fl}_1}{\mathrm{fl}_2}\right) = 0.4343 \times \left(\frac{\mathrm{err}(\mathrm{fl}_1)}{\mathrm{fl}_1} + \frac{\mathrm{err}(\mathrm{fl}_2)}{\mathrm{fl}_2}\right) \tag{4.6}$$

where fl_1 and fl_2 are fluxes and $\mathrm{err}(\mathrm{fl}_1)$ and $\mathrm{err}(\mathrm{fl}_2)$ are the relative errors, calculated according to the Equation 4.1.

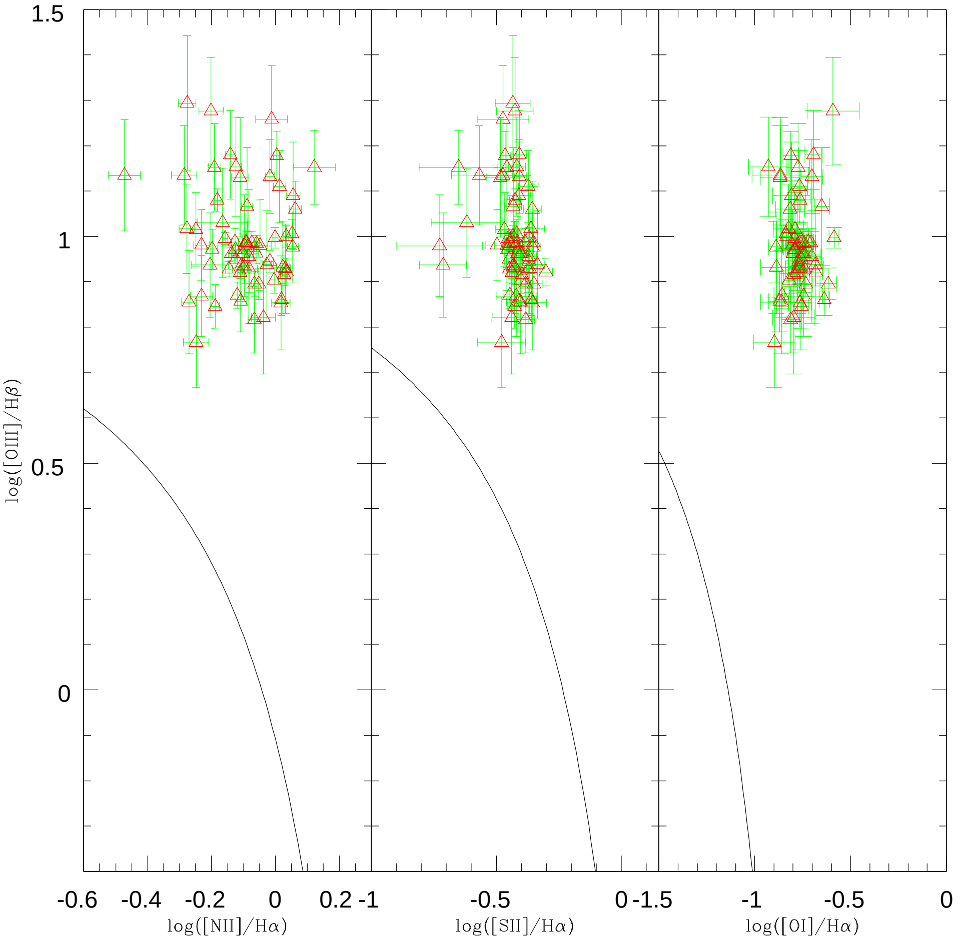

Figure 4.12— The VO diagnostic diagrams: all the regions fill the AGN zone in the diagrams.

4.4 Morphological analysis

We selected from Isaac Newton Group (ING) archive, *g* and *r* broad band images of MRK6, in order to study its morphology, looking for hints of interaction. Firstly, we modelled the isophote of the galaxy by means of IRAF task ELLIPSE. We applied a first ellipse with the following initial input parameters: PA=130°, ellipticity (e) = 0.5, semi-major axis (sma) = 100 px (~33″, the scale is 0.333″/px). We ran ELLIPSE with all parameters free and we used the so obtained output, to study the trend of the morphological parameters: PA, e, X_0 and Y_0, and B4 as a function of sma (see Figure 4.13). From the analysis of PA and e (top right panel in Figure 4.13) we did not find particular structures or evidence of a bar. From about 6″–7″ to the outer regions of the galaxy, both PA and e keep approximately constant with a value of ~130° and ~0.4, respectively. In the most inner regions, from 0″ to 7″, ellipticity raises from about 0.05 to 0.3 and PA decreases from ~170° to ~130°. To check the reliability of the parameters variations, we compared them with the seeing, that can be calculated, by means of the PSF image. We found a value of ~ 4.6 pixel, corresponding to 1.5″. Therefore, the very inner values (for r < 1.5″) cannot be considered reliable. Furthermore, in the very inner part there is also the problem of the saturated nucleus. The coordinates of the nucleus keep constant, with a Δx and Δy equal to zero up to r ~ 15″, while for r > 15″ $\Delta x = 2 - 4''$ and $\Delta y = 2 - 6''$, then for r > 55″ there are some fluctuations. The B4 coefficient (multiplied by 100) is used to estimate the boxy or disky shape of isophotes: B4> 0 indicates a disky profile and B4< 0 indicates a boxy isophote (Carter 1978; Jedrezjewski 1987). In this galaxy, B4 is between -2 and 8 for r< 2″, for r between 2″ and 4″ it ranges between 0 and 1. For r between 4.5″ and 10″ it decreases up to -3.5, then it raises up to 3, for r=20″ then it keeps negative up to ~50″. The median value of B4 is -0.28. These are hints of small boxiness in isophote shape. We ran again ELLIPSE holding the center constant, and we used these data to reproduce and analyze the 1D surface brightness profile. We tried to fit the observed data with a de Vaucouleurs profile, for the bulge component and a Freeman profile (exponential disk) for the disk. These are the equations:

- De Vaucouleurs profile:

$$\mathrm{I_{bulge}} = \mathrm{I_e} \exp\left\{-7.67\left[\left(\frac{\mathrm{r}}{\mathrm{r_e}}\right)^{1/4} - 1\right]\right\} \tag{4.7}$$

$$\mu_{\mathrm{bulge}} = \mu_{\mathrm{e}} + 8.325\left[\left(\frac{\mathrm{r}}{\mathrm{r_e}}\right)^{1/4} - 1\right] \tag{4.8}$$

- Exponential disk:

$$\mathrm{I_{disk}} = \mathrm{I_0} \exp\left[-\left(\frac{\mathrm{r}}{\mathrm{h}}\right)\right] \tag{4.9}$$

$$\mu_{\mathrm{disk}} = \mu_0 + 1.085\left(\frac{\mathrm{r}}{\mathrm{h}}\right) \tag{4.10}$$

- Sérsic law:

$$\mathrm{I_{bulge}} = \mathrm{I_e} \exp\left\{-\mathrm{b_n}\left[\left(\frac{\mathrm{r}}{\mathrm{r_e}}\right)^{1/\mathrm{n}} - 1\right]\right\} \tag{4.11}$$

  with

$$\mathrm{b_n} = 1.9992\mathrm{n} - 0.3271 \tag{4.12}$$

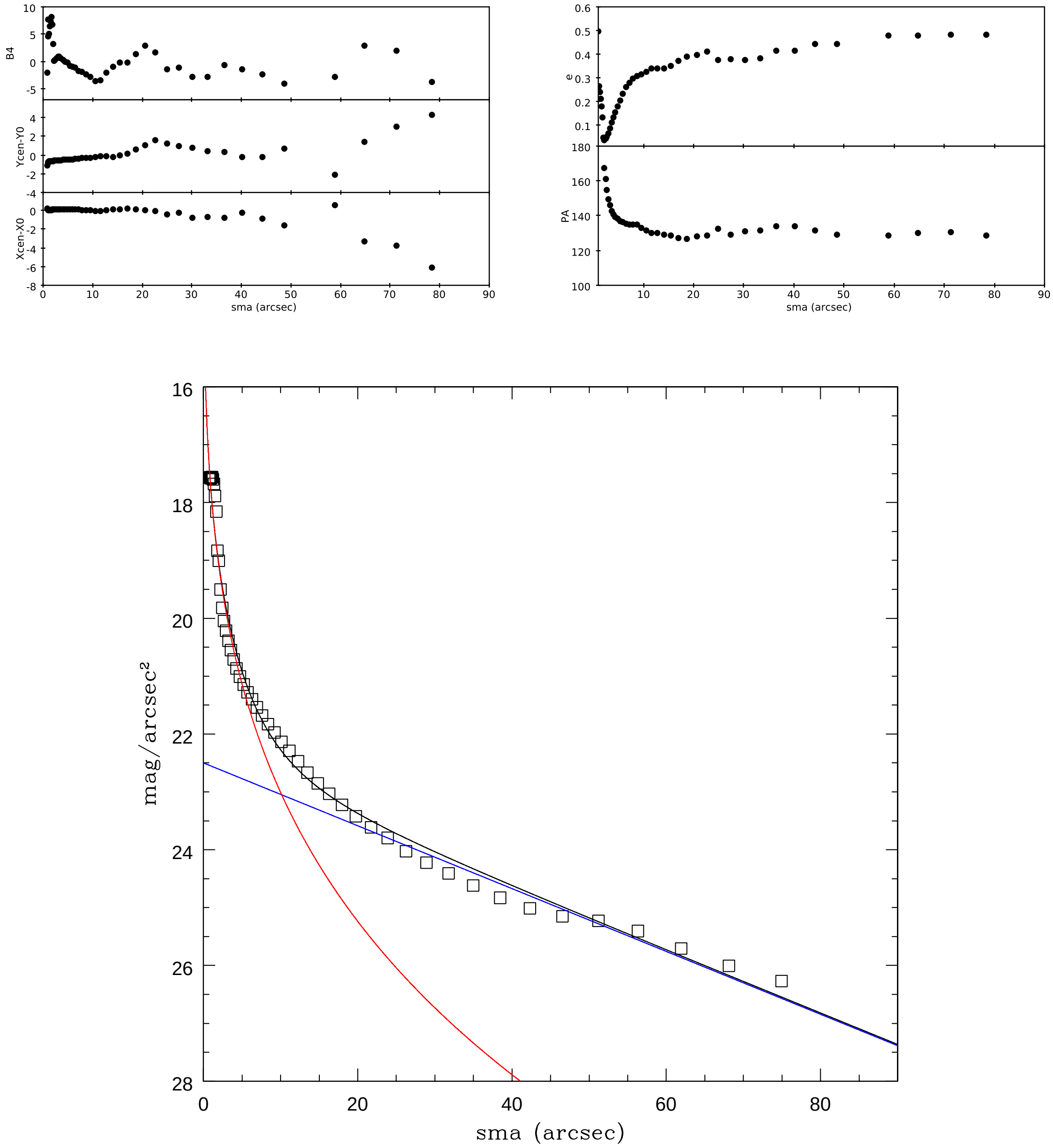

FIGURE 4.13— Morphological parameters in *g*-band. From top to bottom, the trends as a function of the semi-major axis in arcsec, the center of the galaxy (X,Y), the position angle (PA) and ellipticity (e) and the B4 coefficient (multiplied by 100) to estimate the boxy/disky shape of the isophote. The observed surface brightness profile as a function of the semi-major axis of the galaxy in arcsec, the de Vaucouleurs profile for bulge (red line), the exponential disk (blue line) and the sum of this two components that well reproduces the observed profile (black line).

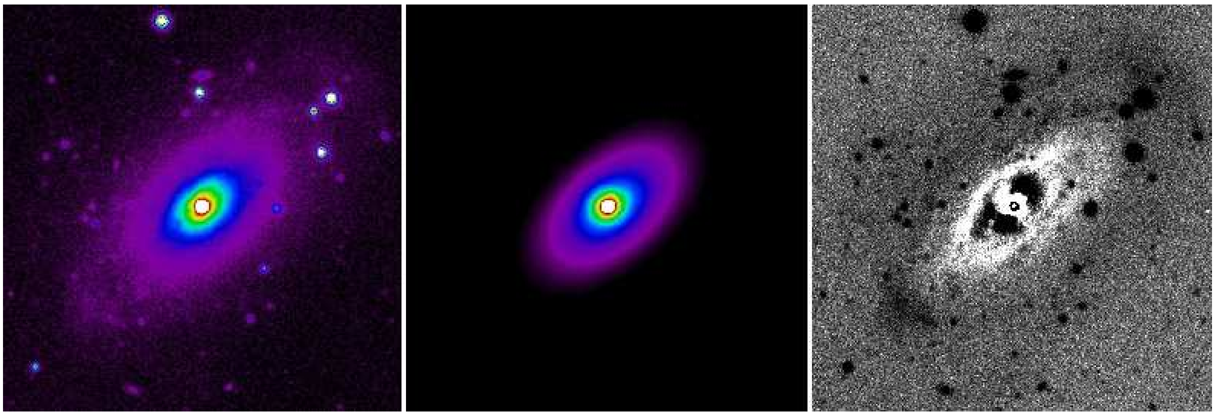

FIGURE 4.14— The results of the fit with GALFIT, from left: the original image, the model and the residual image. North is up and East is to the left.

We found the following best-fit parameters: I_e=150, r_e=2.5″ for bulge and I_0=10 and h=20″ for disk (see Figure 4.13). With these first results, we applied the GALFIT software (Peng et al. 2002) that allows to perform 2D models of the galaxy by means of analytic functions. Firstly, we modelled and reconstructed the PSF of the image, by means of some stars in the image. This is one of the input for GALFIT, that convolves the models with the PSF image in order to better reproduce the galaxy image. There are various functions to be combined to fit the galaxy image. We used a Sérsic profile for the bulge and an exponential disk for the disk. We did not use a point-like source to reproduce the AGN, because our broad-band images were saturated in the very inner part, for the strong intensity of the nucleus. Therefore, we were not able to reproduce the bulge component unless constraining the effective radius in a range of values (between 1″.65 and ~3″) and holding the Sérsic index fixed at n=4, according to the previous analysis. We obtained, as output, the parameters values shown in Table 4.1, a model image and a residual image, result of the subtraction of the model from the original image the model (see Figure 4.14).

The analysis of the residuals reveals over-subtracted regions North-East to the nucleus corresponding to dust lanes visible in $g - r$ image (see Figure 4.15). It is interesting to note that the extended [O III] emission from Kukula et al. (1996) well fit these regions. Also, two stellar shells are visible North-West and South-East to the galaxy. Stellar shells are often explained as an effect of gravitational interaction. Therefore, even if from the morphological parameters we did not find evidence of interactions, the dust lanes associated with the over-subtracted regions and the extended [O III] emission and stellar shells are hints of a merger episode.

	mag	r_e	h	b/a	n	PA	d/b
bulge	14.75	1″.67	–	0.85	4	119°	–
disk	14.72	–	14″	0.55	–	130°	0.16

TABLE 4.1— Fit parameters for bulge and disk. The last column indicates the diskiness (d) or boxiness (b) of the components, positive values indicates boxy isophotes.

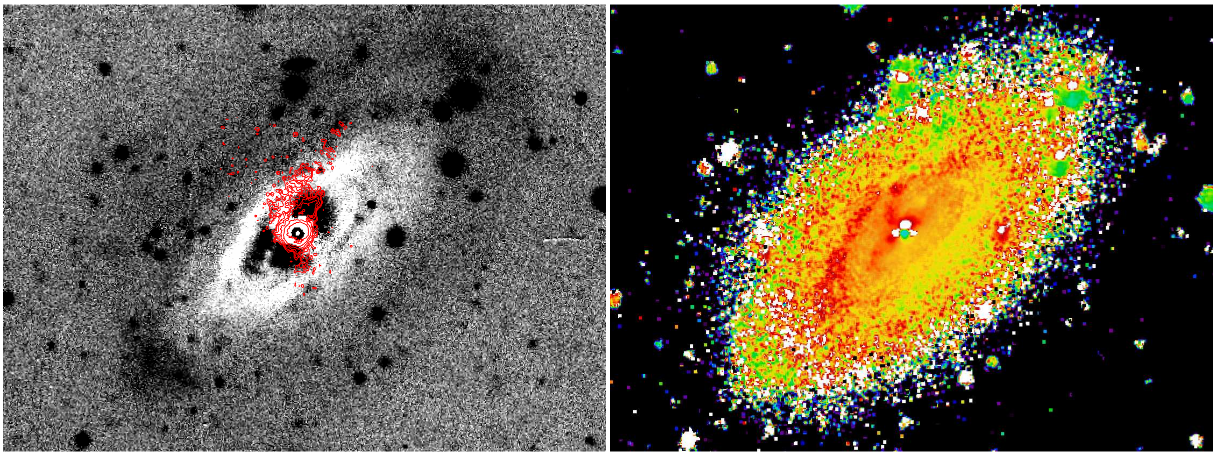

FIGURE 4.15— The comparison between the residual image, with the red contours from Kukula et al. (1996) and the $g-r$ color image. North is up and East to the left.

4.5 Extended high ionization emission

To fit [O III] λ5007 in the higher resolution data of MRK 6, we used two components because the emission lines of central spectra have profiles with a broad component plus a narrow one (see Figure 4.16). This broad component is due to the fact that MRK 6 is an intermediate type Seyfert galaxy and therefore we are looking deeper toward the AGN. This component still belongs to NLR component, we are probably observing emission from gas that is nearer to the center where the conditions of density are different and the influence of the gravitational potential of the central SMBH is stronger. Furthermore we see that this component is present only in the central spectra and the 2D image of its flux has a PSF-like shape. This confirm our idea that this is an unresolved component coming from the inner part of the NLR. We used PAN and we forced the two components to have different ranges of the FWHM (see Figure 4.16). Then we decided, both looking at the images and checking the spectra, which spectra really needed to be fitted with two components and we reconstructed the table for the broad and narrow component.

The higher resolution spectra were taken with two different f.o.v.: we were able to reconstruct the mosaic of the total [O III] detected emission, shown in the Figure 4.17 together with the [O III] contour from Kukula et al. (1996) and the continuum contour from *g*-band image overlaid. We can see that the central zone is really circular as in Kukula et al. (1996) contours, and the MPFS off-center emission perfectly matches this contour. The nuclear and circular [O III] emission is consistent with an emission ionized by the AGN seen face on, being the galaxy an intermediate type Seyfert. On the contrary from the *g*-band contour of the galaxy it is clear that the [O III] emission is not in agreement with the stellar emission. We tried to estimate the mass of the ionized gas from the Hα luminosity using the formula from Ho (2009):

$$\mathrm{M(L_{H\alpha})} = 2.97 \times 10^3 \left(\frac{100\ \mathrm{cm^{-3}}}{\mathrm{n_e}}\right)\left(\frac{\mathrm{L_{H\alpha}}}{10^{38}\mathrm{erg\ s^{-1}}}\right)\mathrm{M_\odot} \tag{4.13}$$

We derived the density from the centered and offset maps of [S II] , which show values distributed as in

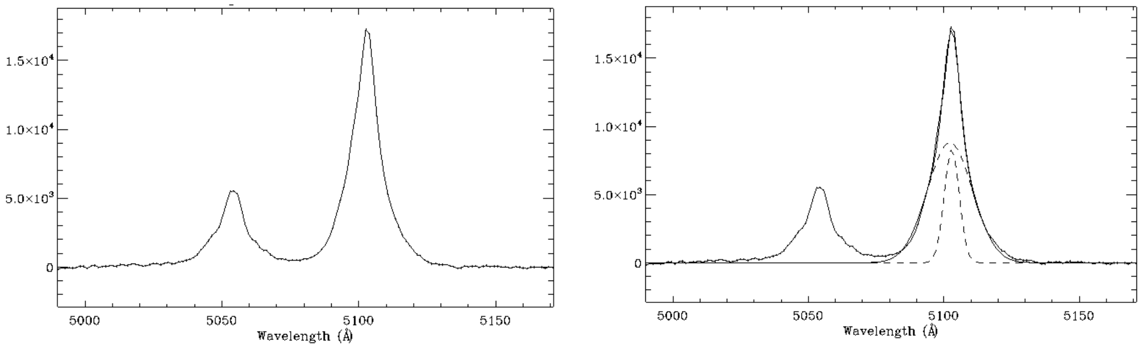

FIGURE 4.16— Broad component in [O III] for a circumnuclear spectrum of MRK 6 (left panel) and the two components fit (right panel).

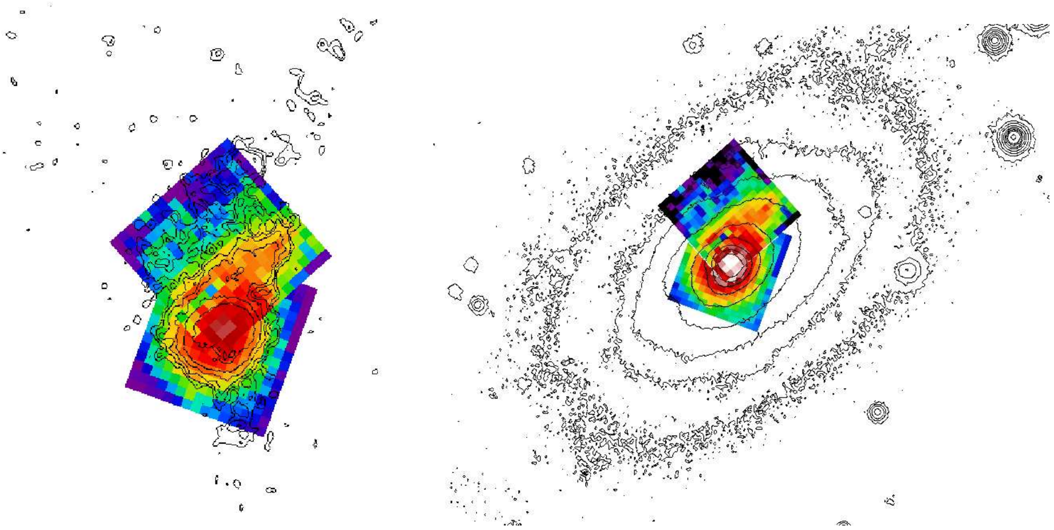

FIGURE 4.17— Total [O III] emission with the [O III] contour (left) from Kukula et al. (1996) and the *g*-band continuum contour (right) overlaid.

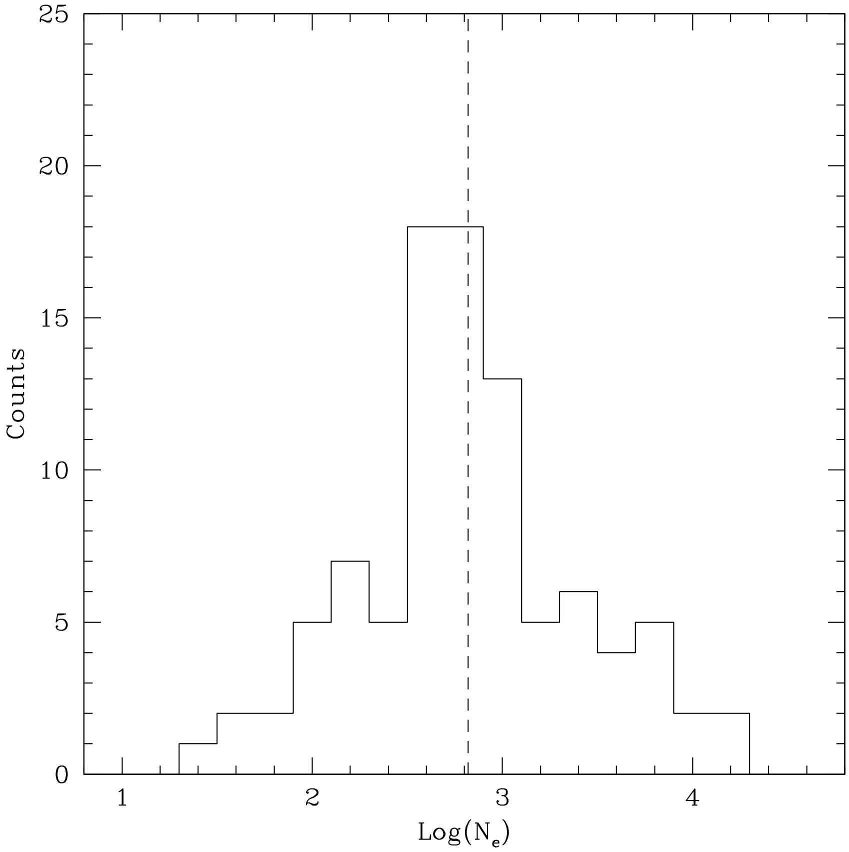

FIGURE 4.18— The histogram of the density in the centered and offcenter f.o.v. with the median value of N_e = 660 e^- cm^{-3}.

Figure 4.18, with a median value of N_e = 660 e^- cm^{-3}. We did not correct for extinction the Hα flux, because the Hβ map is less extended and also because the Hβ measurements are not completely reliable. Therefore we obtained a lower limit for the mass, equal to M = 3.2 $\times 10^6$ $M_\odot$. We also tried to apply an extinction of A(V) = 1 mag and A(V) = 2 mag to check the influence of reddening on the result and we obtained M = 6.8 $\times 10^6$ $M_\odot$ and M = 1.4 $\times 10^7$ M $_\odot$, respectively. The mass is dominated by the nuclear and circumnuclear emission within about 2 kpc (M ~ 3$\times 10^6$ $M_\odot$) instead the off-center lower intensity emission gives a smaller contribution (M ~ 6 $\times 10^4$ $M_\odot$). We tried to estimate also the ionization degree of the off-centered ionized gas, by reconstructing the [O III]/Hβ emission map of the offset f.o.v. (see Figure 4.19). While in the inner part, we found values of [O III]/Hβ ~ 5 – 6, in the North-West region we found an higher ionization with values of ~ 9 – 11 (see Figure 4.19). Unfortunately, the spectra have low S/N ratio, so it was not possible to reconstruct a complete map of the offset [O III]/Hβ emission, but the values we found are hints to a high ionization degree due to AGN.

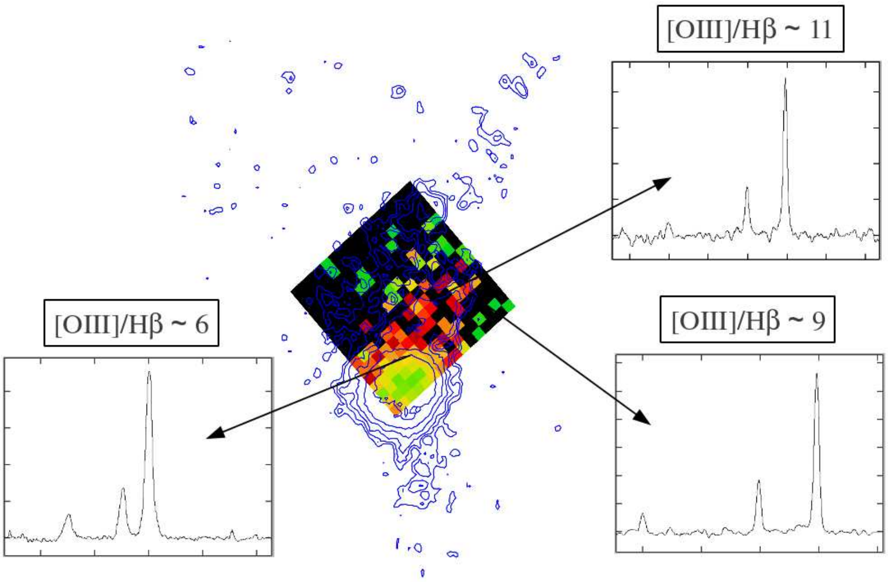

FIGURE 4.19— The offset map of the [O III]/Hβ and three examples of spectra in different regions showing different values of this ratio. North is up and East is to the left.

4.6 Kinematical analysis

For the main emission lines, we build also the 2D maps of velocity and FWHM (see Figure 4.20 for two examples: [O III] and Hα). The velocity maps were corrected for the systemic velocity, considering as recession velocity the value obtained by measuring some emission lines in the nuclear spectrum (the spectrum with highest flux in the continuum map). The instrumental FWHM values, obtained fitting some lines of the comparison lamp, have been subtracted from the measured values: for each spaxel, we subtracted the correspondent instrumental value, in order to take into account possible differences in the field. This is the usual formula:

$$FWHM_{corr} = \sqrt{(FWHM_{obs})^2 - (FWHM_{inst})^2} \tag{4.14}$$

The low resolution kinematics of high ([O III]) and low (Hα) ionization gas show velocity fields with different patterns (Figure 4.21): Hα and [O III] velocity maps are misaligned and have different velocity values. For [O III], the PA of the kinematic minor axis is 145° and the velocity values range from -250 km s^{-1} to 100 km s^{-1}. Instead for Hα, the PA is 120° and the range in velocity is between -150 km s^{-1} and 250 km^{-1}. The FWHM map, after the correction for instrumental width (see Figure 4.20), shows higher values in the inner part and in the central regions the FWHM reaches very high values, up to 1000 km s^{-1}.

A comparison between the Hα velocity field and the g-band contours shows that the kinematic minor axis of the low ionization gas is aligned with the photometric one (see Figure 4.22), so we can assume that the low ionization gas and the stars have the same kinematic behaviour. Instead the centered+offset [O III] velocity field has a peculiar non-axis symmetric pattern, which does not match the contours of the galaxy (see Figure 4.22). This is because the high ionization gas is elongated in North-South direction.

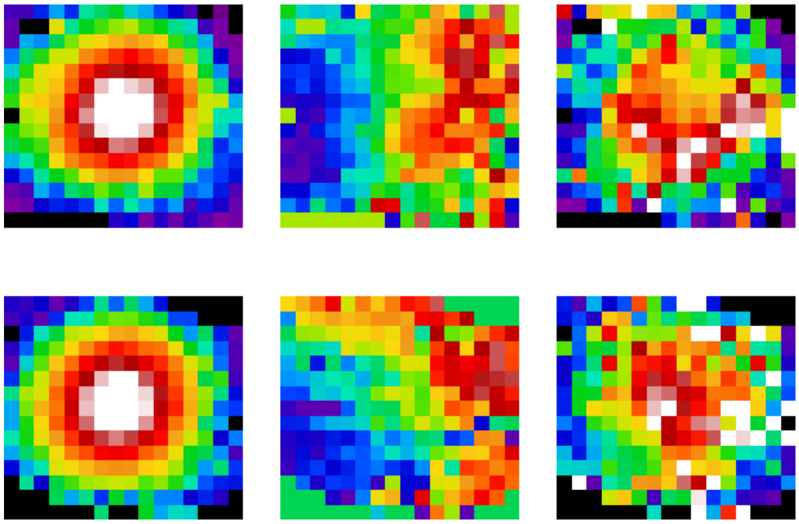

FIGURE 4.20— The flux, velocity and FWHM maps of [O III] and Hα emission lines obtained from low resolution data.

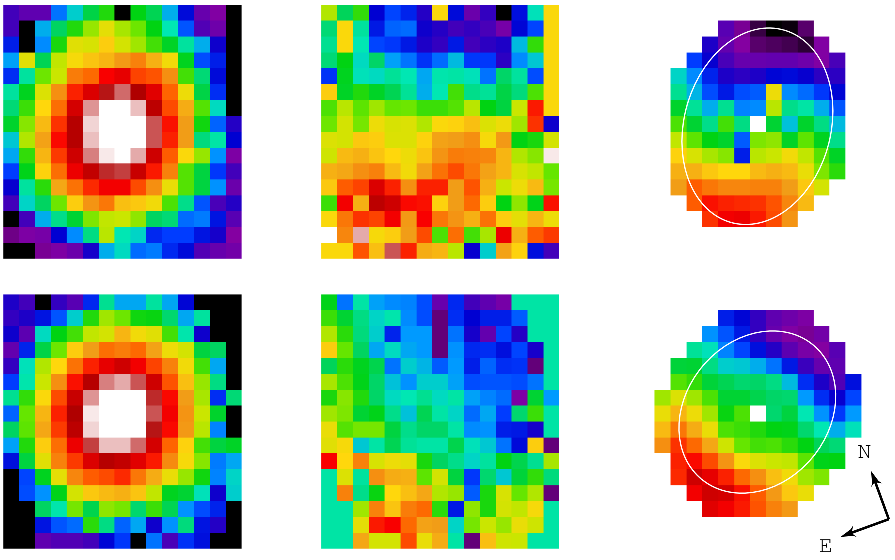

FIGURE 4.21— Flux, observed velocity and model of [O III] (top) and Hα (bottom), with the ellipse showing the inclination of the velocity field, overlaid.

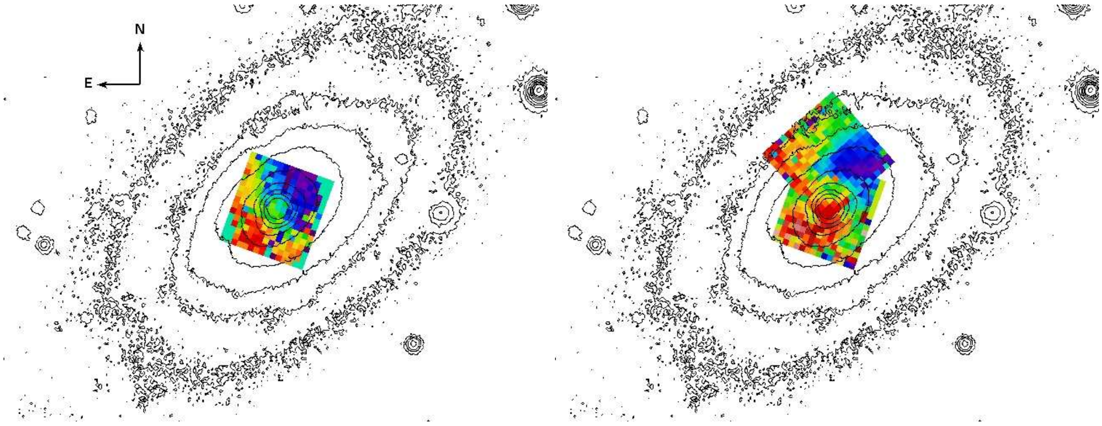

FIGURE 4.22— Hα velocity field with the *g*-band contour overlaid, and [O III] centered and off-set velocity field with the *g*-band contour overlaid.

The already published [O III] emission (Kukula et al. 1996) perfectly matches our integral field maps (see Figure 4.23). Moreover, the velocity values in the offset field are all negative: red colors correspon to velocity of 80 km s^{-1}, yellow colors to velocity of -100 km s^{-1}, green colours to velocity of -170 km s^{-1} and blue-purple colors to -300 – -400 km s^{-1}. The velocity field could be the combination of two kinematics. One component is rotating with a kinematic minor axis tilted with respect to the photometric minor axis of the galaxy (see Figure 4.20). The other seems to have a kinematic axis orthogonal to the previous one. We suggested two possible explanations: the gas is orbiting according to the galaxy potential and also spiralling; or the [O III] emission is formed by two parts on different planes, one is the galaxy plane and the other is outside the galaxy plane. We need additional information and models to confirm this hypothesis.

To the low resolution [O III] and Hα velocity maps and to the centered high resolution [O III] map, we applied ROTCUR (Begeman et al. 1989). For the offset [O III] map we tried to fit the 2D velocity map with ROTCUR, but according to our hypothesis that the [O III] velocity field is a combination of two velocity fields, we could not determine the correct PA and inclination, so we decided to only analyze the 2D maps but to use the AFOSC longslit spectra, for the rotation curve. ROTCUR is a task of GIPSY (Groningen Image Processing System) that models the 2D map allowing to obtain the deprojected rotation curve. This task uses tilted-ring model to fit the observed velocity field. It models the velocity map using concentric rings and taking into account the inclination on the line of sight. The observed velocity v (x, y) is reproduced by this formula:

$$\mathrm{v}\,(\mathrm{x},\mathrm{y}) = \mathrm{v}_0 + \mathrm{v}_\mathrm{c}\,(\mathrm{R}) \sin \mathrm{i} \cos\theta \tag{4.15}$$

where

$$\cos\theta = \frac{-(\mathrm{x}-\mathrm{x}_0)\sin\phi + (\mathrm{y}-\mathrm{y}_0)\cos\phi}{\mathrm{R}} \tag{4.16}$$

x_0 and y_0 are the sky coordinates of the rotation center of the galaxy; v_0 is the systemic velocity; $\mathrm{v}_\mathrm{c}(\mathrm{R})$ is the circular velocity at distance R from the center; ϕ is the position angle of the major axis; i is the inclination of the galactic plane and θ is the azimuthal angle in the galactic plane. Before starting, we

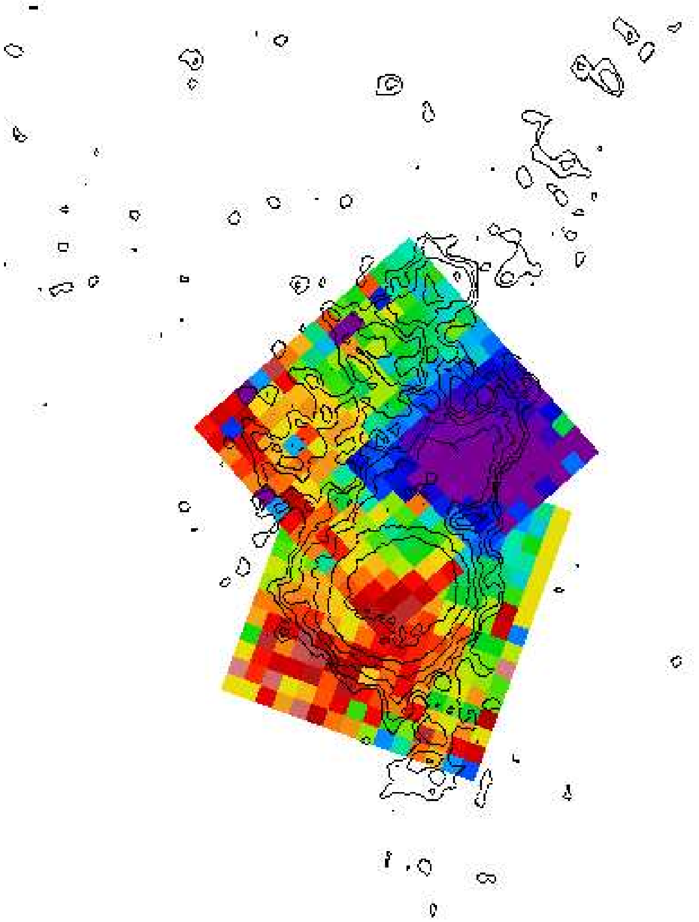

Figure 4.23— The centered+offset [O III] velocity field with the [O III] contours overlaid.

needed to calculate the inclination (i), that is i = arccos $\left(\frac{b}{a}\right)$, where a and b are the semi-major and semi-minor axis of the gas or stellar emission. We obtained i, by calculating b and a values from an ellipse that matched the distribution of the emission. From this ellipse we also got the PA of the emission. We corrected the velocity maps for the systemic velocity, using the values obtained in the nuclear spectrum. Once we determined PA and i from the maps of the emission line flux, we could run ROTCUR. We fixed the following input parameters: inclination, i=33.5° for [O III] and i=29° for Hα, the systemic velocity (0.0 km s^{-1}), the expansion velocity (0.0 km s^{-1}) and the coordinates (x, y) of the center of the galaxy. The other input parameters were radii of the concentric rings in arcsec, the first guess for the rotational velocity of each ring and the position angle, and we let them free. First we applied this task to the whole 2D velocity map, fitting both the approaching and receding side at the same time, this output was then used as input for the task VELFI that reconstructs the model image. This image is useful to be compared with the original one in order to check if the model can reproduce the velocity map (see Figure 4.21). On the other hand, in order to build the velocity curves, more accurate values of the deprojected velocity can be obtanied by fitting the velocity maps in two steps, first the receding and then the approaching side.

We analyzed also two AFOSC longslit spectra, the first taken with the slit along the PA=0° according to the [O III] image from Schmitt et al. (2003). By comparing the Schmitt et al. image, with our 2D maps, we see that the [O III] emission is elongated also along a different PA ~ -30°. So we took another spectrum deeper (exptime = 3 hours) and with PA = -30°, following the [O III] image from Kukula et al. (1996), (see Figure 4.24). The velocity curve obtained with AFOSC data were deprojected. To be consistent with the MPFS analysis, we considered as semi-major axis and inclination the ones obtained from MPFS [O III] emission map, PA=160° and i=33°.5. The deprojected velocity v_{circ} is:

$$v_{circ}(R) = \frac{v_{oss}(r)}{\cos\theta \times \sin i} \tag{4.17}$$

in which R and θ are the radius and the PA on the galactic plane, that can be obtained from the following equations:

$$\tan\theta = \frac{\tan\phi}{\cos i} \tag{4.18}$$

$$R = r\frac{\cos\phi}{\cos\theta} \tag{4.19}$$

where r and ϕ are the radius and the PA on the sky plane. The deprojected rotation curves are shown in Figure 4.25. From the ROTCUR output, we could build the rotation curves for low and high resolution data (see Figure 4.25) to be compared with the longslit rotation curves. We found a more regular behaviour in the MPFS rotation curves. This can be due both to the fact that ROTCUR in order to model the observed velocity field makes an average which produces a smoothing of peculiar properties, and that here we analyzed the central emission showing a more regular kinematics. Anyway, the curves are asymmetric as we found in AFOSC data and the [O III] kinematics is similar in both high and low resolution data, with values between -500 km s^{-1} and 150 km s^{-1}, while the Hα velocity curve is more symmetric and its values range from -200 km $^{-1}$ to ~ 350 km s^{-1}. In principal, a rotation due to gravitational potential should be symmetric. The AFOSC curves are very asymmetric and irregular, being more extended northward, where the [O III] emission is more extended, it ranges from -900 km s^{-1} to 100 km s^{-1} (PA=0°) and from -800 km s^{-1} to 200 km s^{-1} (PA= -30°), and it shows fluctuations, which suggest

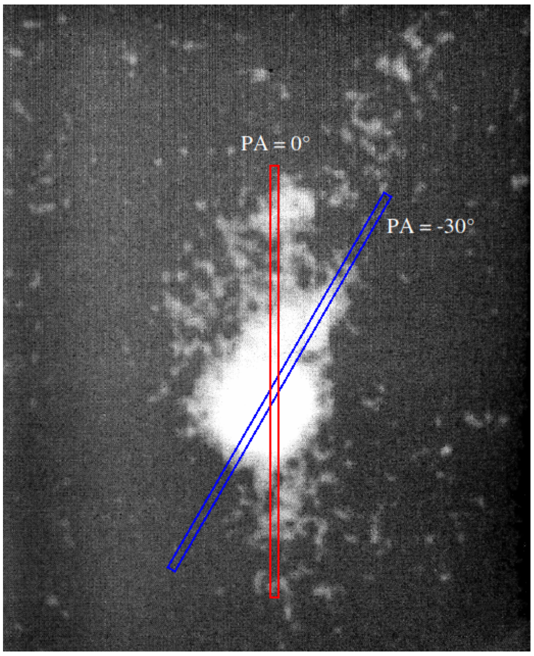

FIGURE 4.24— [O III] emission from Kukula et al. (1996) with the PA of AFOSC slit overlaid.

a peculiar kinematics. These fluctuations are due to the fact that the slit covers regions with various velocity with very negative values (up to -900 km s^{-1}).

We calculated the errors in velocity, by measuring the observed position of the only nightsky emission line detectable (at λ = 5577 Å). This assumes that the main contribution to the errors is due to calibration errors (see Figure 4.26). We should taking into account the S/N ratio of the emission lines (Corsini et al. 1999), in fact if the errors are due only to wavelength calibration, the error value should be the same in the whole f.o.v., instead we can see from the histograms that there is a distribution. In particular where the S/N is high, the error is due only to errors in calibration, instead where the S/N is low, the error is larger, because it is difficult to understand the peak position and the estimate of the central λ is difficult. In our case, the S/N of these emission lines is high in the whole field and the erros are mainly due to the errors in calibration. The errors may be larger in presence of asymmetries. For the high resolution data we have also the error due to the fit of the two components and for all the rotational curves we have errors due to ROTCUR fit. By considering the work of Whittle (1985) about the emission line profiles and the asymmetry, we tried to calculate the asymmetry using the [O III] emission line of the higher resolution spectra in the offcenter f.o.v. Our script calculates the area of the emission line, the wavelength corresponding to the 10% (λ_{10}), 50% (λ_{50}) and 90% (λ_{90}) of the emission line area and then it estimates the asymmetry (asym):

$$\mathrm{a} = \lambda_{50} - \lambda_{10} \tag{4.20}$$

$$\mathrm{b} = \lambda_{90} - \lambda_{50} \tag{4.21}$$

$$\mathrm{asym} = \frac{\mathrm{a} - \mathrm{b}}{\mathrm{a} + \mathrm{b}} \tag{4.22}$$

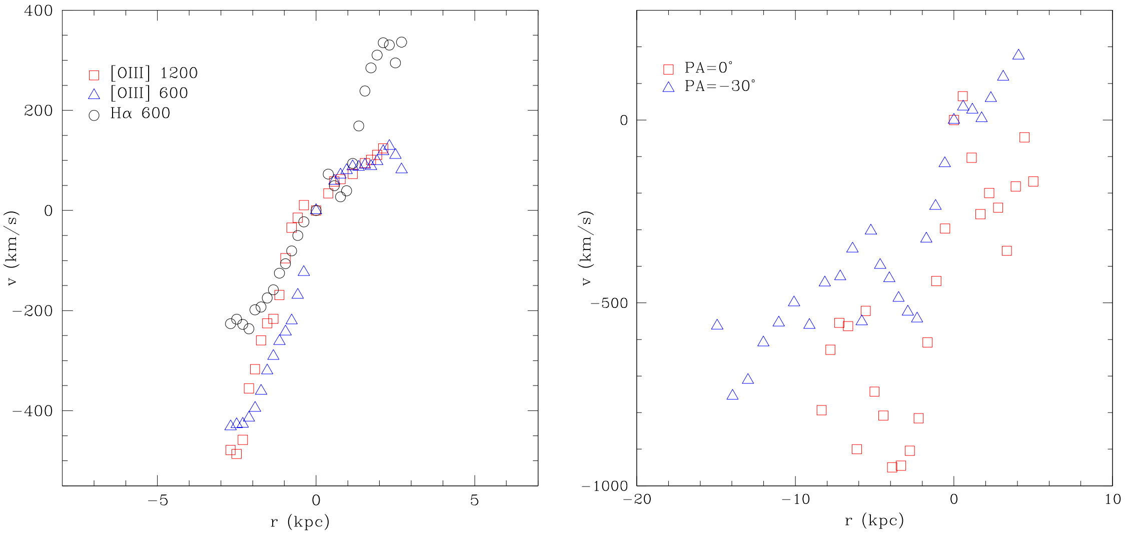

FIGURE 4.25— Rotation curves obtained from MPFS and AFOSC data.

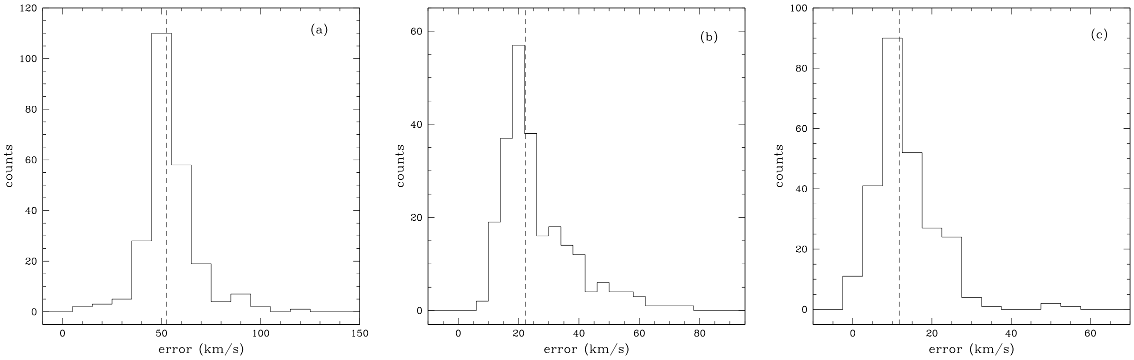

FIGURE 4.26— Histogram of the errors in the velocity determination, for MPFS data, in particular for (a) [O III] low resolution data, median value = 52 km s^{-1} (b) Hα low resolution data, median value = 22 km s^{-1} and (c) [O III] high resolution data, median value = 12 km s^{-1}.

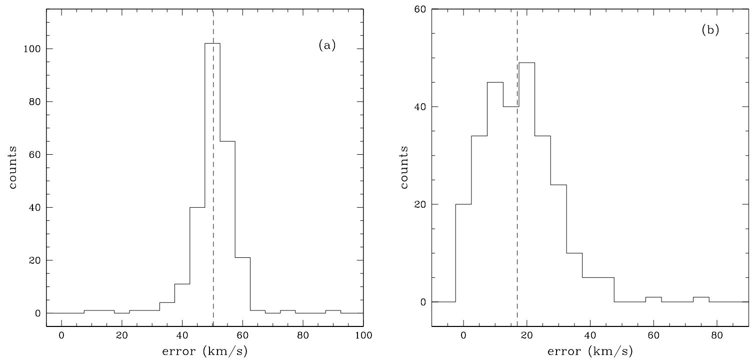

FIGURE 4.27— Histograms of the errors in the velocity determination for AFOSC data, in particular for [O III] obtained with old (a) and new dataset (c). The median values are 50 km s^{-1} and 17 km s^{-1}, respectively.

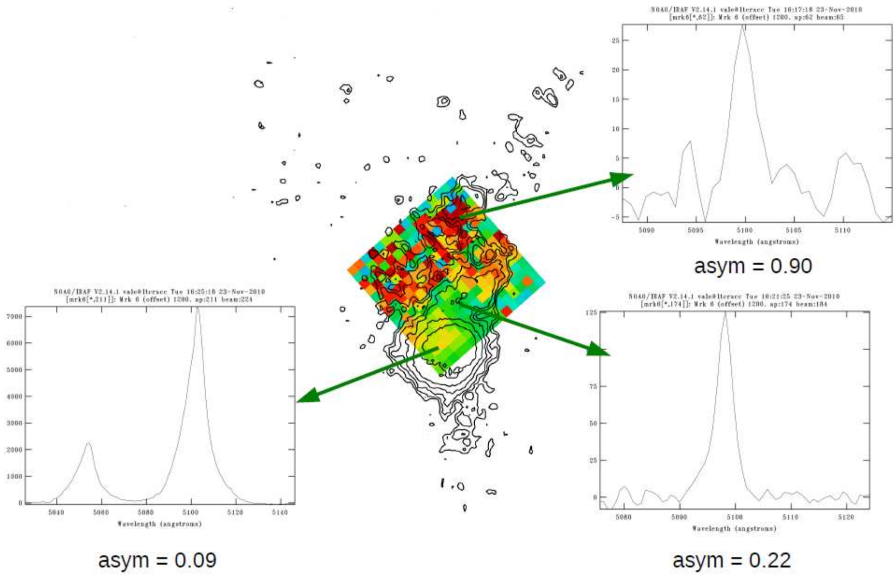

FIGURE 4.28— The asymmetry map for the extended [O III] emission, with three examples of spectra in different regions of asymmetry.

If there is a blue wing in the line profile, then a > b and asym > 0, instead if there is a red wing, then a < b and asym < 0 (red colours in Figure 4.28). We applied the asymmetry method suggesting by Whittle (1985) and reconstructed the asymmetry map for the extended [O III] emission (Figure 4.28). We found symmetric profile in the nuclear region (asym = 0.09) and positive values of asymmetry (green to red colors) in the extended emission (asym = 0.22 – 0.90), therefore the extended emission gas shows blue wings in the [O III] emission lines (Figure 4.28).

4.7 Summary of the results

We studied the physical and kinematical properties of the circumnuclear gas in the nearby intermediate type Seyfert galaxy MRK 6, showing an Extended Narrow Line Region. We analysed this object by means of longslit and integral field spectra and broad–band images. We mapped and studied both the nuclear and the extended gas emission, already found in Kukula et al. (1996). In particular we focused on the peculiar kinematics of this object and on the extended [O III] emission.

By analysing *g* and *r* band images of MRK 6 we found a not clearly disturbed morphology, but we pointed out the presence of dust lanes to the North and stellar shells at East and West edges of the galaxy. The analysis of the residuals reveals over-subtracted regions corresponding to dust lanes and to the extended [O III] emission from Kukula et al. (1996). All these findings are hints of a possible merger episode. We studied the extended [O III] emission by means of high resolution IFU spectra. We estimated a lower limit of the ionized gas mass, using the expression from Ho et al. (2009) and Hα luminosity not corrected for extinction, obtaining $M = 3.2 \times 10^6$ $M_\odot$. We estimated [O III]/Hβ, finding higher values in the North-West region (9–11) than in the inner part (5–6), values that confirms a photoionization due to AGN. The kinematical analysis revealed that high ionized gas has a disturbed kinematics. Low ionization gas, studied by means of Hα emission line, has a more regular behaviour and its kinematical minor axis is aligned with the photometric one. Instead, [O III] emission line shows a more complicated velocity field, with highly negative values and a pattern suggesting that its velocity field could be a combination of a rotating component, according to the gravitational potential of the galaxy, but with a kinematic minor axis tilted with respect to the photometric one, and a spiralling component. Indeed the longslit velocity curves are very asymmetric and irregular, with fluctuations consistent with a spiralling movement. This interpretation must be confirmed with further analysis. In summary, we confirmed that the extended [O III] emission is gas photoionized by the AGN forming an Extended Narrow Line Region with a complex kinematics and a mass indicating that it could be the result of a minor merger between MRK 6 and a gas-rich dwarf galaxy.

5

Sampling the Extended Narrow Line Region of Seyfert 2 galaxies

THIS chapter is based on a statistical study of the Extended Narrow Line Region (ENLR) properties in a sample of 12 Seyfert galaxies. These galaxies were observed at 6-mt telescope with the MPFS. We took advantage of the integral field data to study in detail the physical properties of the ENLR in this sample.

Firstly we described the method to select the sample and the analysis applied to the data, then we showed the physical properties of gas and stars in this sample and the properties derived from the emission lines analysis.

5.1 Sample selection

We selected the objects to be studied in this part of the work, from the Special Astrophysical Observatory (SAO) archive (ASPID). The objects were observed with MPFS, using the low resolution grating which gives a spectral range of $\Delta\lambda = 3700 - 7500$ Å and a resolution R = 850. We selected objects whose spectra show spectral lines with high S/N ratio, obtaining a sample of 12 Seyfert 2 galaxies. This sample is heterogeneous and not statistical, therefore we cannot consider our findings as globally valid. Nevertheless, this work is a useful test for a future analysis on a statistically selected larger sample. We explored the possibility of studying the ENLR at large distance from the nucleus and to analyze its physical properties as a function of distance from the nucleus. We also tested which parameters can be studied and we tried to understand the needed size of the field of view (f.o.v.), the best required S/N and the optimal redshift range to be able to study the radial trend of ENLR properties. This is a different approach with respect to other studies, for example with SDSS spectra which are integrated over a fixed $3''$ aperture and give only a partial or average information depending on the distance of a target.

The selected objects are listed in Table 5.1. Five galaxies are isolated, five are in a pair, one is in a triplet and one in a quintet. All the galaxies are nearby: the range in redshift is between z=0.006 (MRK 620) and z=0.037 (MRK 78). We reported also for each galaxy the size of the f.o.v. in kpc^2. The objects were observed with the MPFS with a f.o.v. of $16'' \times 16''$ or $16'' \times 15''$, the total sample consists of about 3200 regions, with a sampling of $1'' \times 1''$. To carry out an homogeneous analysis, we applied the following method: the spectra were reduced with P3d (Sandin et al. 2010), corrected for reddening and atmospheric refraction, then the stellar component was subtracted with STARLIGHT (Cid Fernandes et al. 2005; Cid Fernandes et al. 2007) and the emission lines were measured with PAN (Peak ANalysis). We decided to measure, where detectable, the following emission lines: [O II] λ3727, [Ne III] λ3869, [Ne III] λ3968, [S II] λ4070, Hδ λ4102, Hγ λ4340, [O III] λ4363, He II λ4686, [Ar IV] λ4711, [Ar IV] λ4740, Hβ λ4861, [O III] λ4959, [O III] λ5007, [N I] λ 5198, [Fe VII] λ5721, [N II] λ5755, He I λ5876, [Fe VII] λ6086, [O I] λ6300, [N II] λ6548, Hα λ6563, [N II] λ6584, [S II] λ6717, [S II] λ6731, [Ar III] λ7136. For each of the 12 galaxies, we have information from 256 or 240 spaxels, finally we constructed a table in which we listed for each object the following information: the measured fluxes, the central wavelength and the FWHM for each measured emission lines, the distance from the nucleus in arcsec and in kpc, the redshift, the distance of the object in Mpc, the spatial scale in kpc/$''$, the S/N ratio of the continuum at λ=5500 Å, the parameters from the starlight fit, such as the χ^2, the adev parameter, indicating the mean percentage of the deviation between the observed spectrum and the synthetic one, the estimated value of the total stellar mass, the velocity dispersion, the absorption in V band estimated from the stars, the percentage of the light emitted by the stellar populations, divided into the 15 different classes of age. By calculating the S/N of the continuum (see Figure 5.1), we verified the reliability of our measurements. The median value of the S/N of the continuum, measured at rest-frame 5500 Å is 19 and most of the spectra (77%) have S/N between 10 and 50. We believe that these data are sufficiently good for our analysis. The χ^2 evaluates the quality of the fit of STARLIGHT: it should be peaked around 1. In our case it is peaked around 1.4 (see Figure 5.1).

Object name	RA (J2000.0)	Dec (J2000.0)	z (NED)	scale (kpc/$''$)	Morphological type	Seyfert type	Isolated	f.o.v. (kpc^2)
MRK 348	00:48:47.1	+31:57:25	0.015034	0.2913	SA(s)0/a	Sy2	pair	4.66 × 4.66
MRK 1157	01:33:31.2	+35:40:06	0.015167	0.2974	(R')SB0/a	Sy2	yes	4.76 × 4.46
UGC 2024	02:33:01.2	+00:25:15	0.022342	0.4344	Sab	Sy2	yes	6.95 × 6.95
MRK 1066	02:59:58.6	+36:49:14	0.011946	0.2317	(R)SB0(s)	Sy2	yes	3.71 × 3.71
MRK 1073	03:15:01.4	+42:02:09	0.023343	0.4554	(R')SB(s)b	Sy2	yes	7.29 × 7.29
MRK 607	03:24:48.7	-03:02:32	0.008883	0.1794	Sa	Sy2	pair	2.87 × 2.87
MRK 3	06:15:36.3	+71:02:15	0.013509	0.2607	S0	Sy2	pair	4.17 × 3.65
MRK 620	06:50:08.6	+60:50:45	0.006138	0.1190	SB(r)a	Sy2	pair	1.90 × 1.90
MRK 78	07:42:41.7	+65:10:37	0.037150	0.7156	SB	Sy2	yes	11.45 × 11.45
MCG+03-45-003	17:35:32.7	+20:47:48	0.024323	0.4728	S	Sy2	pair	7.56 × 7.56
NGC 7212	22:07:01.3	+10:13:52	0.026632	0.5165	Sab	Sy2	triplet	8.26 × 8.26
NGC 7319	22:36:03.5	+33:58:33	0.022507	0.4346	SB(s)bc pec	Sy2	quintet	6.95 × 6.52

TABLE 5.1— The sample of galaxies.

All the measured fluxes were corrected for the internal reddening. This can be estimated using the Balmer decrement: assuming the theoretical value of the intensity ratio between Balmer emission lines, and comparing the measured values with the theoretical ones, we can estimate the absorption in $V-$band, A(V), applying the Cardelli Clayton and Mathis (1989, CCM) extinction law:

$$\mathrm{A}(V) = 7.2146 \times \log \frac{\mathrm{R_{obs}}}{\mathrm{R_{th}}} \tag{5.1}$$

where $\mathrm{R_{obs}}$ is the observed ratio between Hα and Hβ fluxes, and $\mathrm{R_{th}}$ is the theoretical one equal to 2.86.

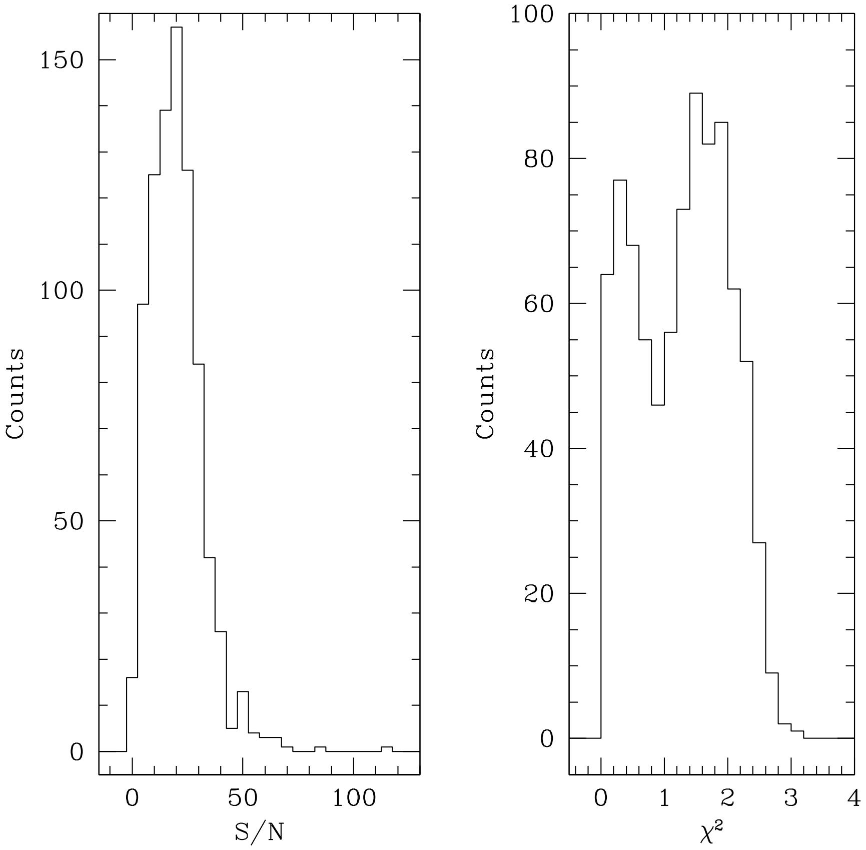

FIGURE 5.1— Histograms of the S/N of the continuum which gives an indication of the reliability of the measurements (left) and of the χ^2 evaluating the quality of the fit with STARLIGHT (right). The median values are 19 and 1.4, respectively.

Once we obtained A(V), we can correct all the observed fluxes with the following expression:

$$F_{corr} = F_{obs} \times 10^{0.4 \times A(V) \times c(\lambda)} \tag{5.2}$$

where c(λ) is calculated for each wavelength using the CCM extinction law, and corresponds to

$$c(\lambda) = a(\lambda) + \frac{b(\lambda)}{3.1} \tag{5.3}$$

Clearly, the correction can be applied only where the Hβ emission line can be measured. We calculated the flux errors, assuming that the determination of the position of the continuum level gives the main contribution to the errors when measuring the emission line fluxes. The errors (ΔF) are obtained dividing the reddening corrected flux ($F_c(\lambda)$) by the S/N of each emission line (S/N(λ)), calculated as the ratio of the intensity of the peak of the line over the continuum (amp(λ)) divided by the standard deviation (rms(λ)) of the continuum in a spectral region near the emission line:

$$\Delta F = \frac{F_c(\lambda)}{S/N(\lambda)} \tag{5.4}$$

$$\frac{S}{N}(\lambda) = \frac{amp(\lambda)}{rms(\lambda)} \tag{5.5}$$

In order to select the regions of the ENLR, we considered the S/N of Hβ and obtained a sub-sample with only those regions (1393 out of 3008) in which S/N(Hβ)>3. Then using this sub-sample, we built the VO diagnostic diagram (Veilleux & Osterbrock, 1987) [N II]/Hα vs [O III]/Hβ, to separate the different regions: the Seyfert regions (848, 61%), the HII regions (222, 16%) and the LINERs regions (316, 23%). We divided these sub-samples using the relation (Kewley et al. 2006):

$$\log \frac{[OIII]}{H\beta} = \frac{0.61}{(\log \frac{[NII]}{H\alpha} - 0.47)} + 1.19 \tag{5.6}$$

to separate the Seyfert-LINER regions from the HII regions; then we used this condition:

$$\log \frac{[OIII]}{H\beta} > 0.5 \tag{5.7}$$

in order to distinguish between Seyfert and LINER. Finally we used the Seyfert-subsample of 848 regions to study the properties of the ENLR. We need to point out that not every object has the same importance in the sample, indeed we have three objects (MRK 1066, MRK 620 and UGC 2024) that contribute to the whole sample of 848 regions for less than 2% each, and other galaxies (MRK 78, NGC 7212 and MRK 3) which are predominant in the sample contributing for ~15% each, the other galaxies contributing for ~6% to ~10%. The three predominant objects added together contribute for 44% of the whole sample. If the regions were uniformly distributed among the 12 galaxies, the mean percentage per object would be 8.2%. The percentage of the f.o.v occupied by the emission for each galaxy varies from about 3–6% (MRK 1066, MRK 620 and UGC 2024) and about 18–30% (MRK 348, MRK 607 and MCG+03-45-003) to about 35–54% in the remaining six galaxies.

To check the consistency of the sample selected by means of the [N II]/Hα diagram, we built the other VO diagrams (see Figure 5.2) in which we plotted two sub-samples, the AGN-like regions (blue triangles) and the HII plus LINERs regions (red squares). The curves dividing the regions are from Kewley et al. (2006) and the straight line indicates the AGN-LINERs separation at log([OIII])/(Hβ) > 0.5. The relations for the [S II] and [O I] diagnostic diagrams are:

$$\log\left(\frac{[\mathrm{OIII}]}{\mathrm{H}\beta}\right) = \frac{0.72}{\log\left(\frac{[\mathrm{SII}]}{\mathrm{H}\alpha}\right) - 0.32} + 1.3 \tag{5.8}$$

$$\log\left(\frac{[\mathrm{OIII}]}{\mathrm{H}\beta}\right) = \frac{0.73}{\log\left(\frac{[\mathrm{OI}]}{\mathrm{H}\alpha}\right) + 0.59} + 1.33 \tag{5.9}$$

The errors to be associated to the diagnostic ratios were computed with these formulas:

$$\mathrm{err}\left(\log\frac{\mathrm{fl}_1}{\mathrm{fl}_2}\right) = 0.4343 \times \left(\frac{\mathrm{err}(\mathrm{fl}_1)}{\mathrm{fl}_1} + \frac{\mathrm{err}(\mathrm{fl}_2)}{\mathrm{fl}_2}\right) \tag{5.10}$$

$$\mathrm{err}\left(\log\frac{\mathrm{fl}_1 + \mathrm{fl}_2}{\mathrm{fl}_3}\right) = 0.4343 \times \left(\frac{\mathrm{err}(\mathrm{fl}_1) + \mathrm{err}(\mathrm{fl}_2)}{\mathrm{fl}_1 + \mathrm{fl}_2} + \frac{\mathrm{err}(\mathrm{fl}_3)}{\mathrm{fl}_3}\right) \tag{5.11}$$

where fl_i and err_i are flux and relative error, calculated according to the Eq. 5.4. The histograms of the errors associated to diagnostic diagrams are shown in Figure 5.3, the errors are small, the median values for log([O III]/Hβ), log([N II]/Hα), log([O I]/Hα), log([S II]/Hα) are 0.03, 0.01, 0.06 and 0.03, respectively.

5.2 Physical properties of gas and stars

Gas density and temperature were calculated by means of the usual emission line ratios, while by comparing our measurements with photoionization models by Vaona (PhD thesis, 2010), we inferred an estimate of gas metallicity. We calculated the density with the IRAF task TEMDEN, by using the [S II] λ6717/λ6731. Unfortunately the [Ar IV] λ4711 and λ4740 could be detected only in 176 (21%) and 79 (~9%) out of 848 spectra, respectively, and their ratio could be measured only in 32 cases, so we did not use this ratio to calculate the density, because the obtained value is not characteristic of the whole sample. On the contrary, the [S II] ratio could be measured for 842 (99%) out of 848 spectra. The [S II] and [Ar IV] lines have different values of critical density, indeed these lines are emitted by gas in different physical conditions. The [Ar IV] ratio gives information about higher density and higher ionization gas, while lower density gas can be studied by means of the [S II] ratio. Unfortunately we could not calculate the values for the high density gas and we determined the density using an input value of temperature $T=10^4$ K and the ratio of the [S II] doublet. The density ranges between 40 and 4000 e^- cm^{-3} with a median value of ~360 e^- cm^{-3} (Figure 5.4). The gas temperature can be obtained using different emission line ratios: we used the [O III] lines at λ4959, λ5007 and λ4363, by calculating the ratio between the flux of the [O III] (λ4959+λ5007) and the flux of the [O III] λ4363, and the [S II] lines at λ6717, λ6731, λ4068 and λ4076, by calculating the ratio between the flux of [S II] (λ6717+λ6731) and the flux of [S II] (λ4068+λ4076). We determined the temperature with these two ratios, when both the λ4363 and the λ4068+λ4076 could be measured, that is respectively in 574 (68%) and 462 (54%) out of 848

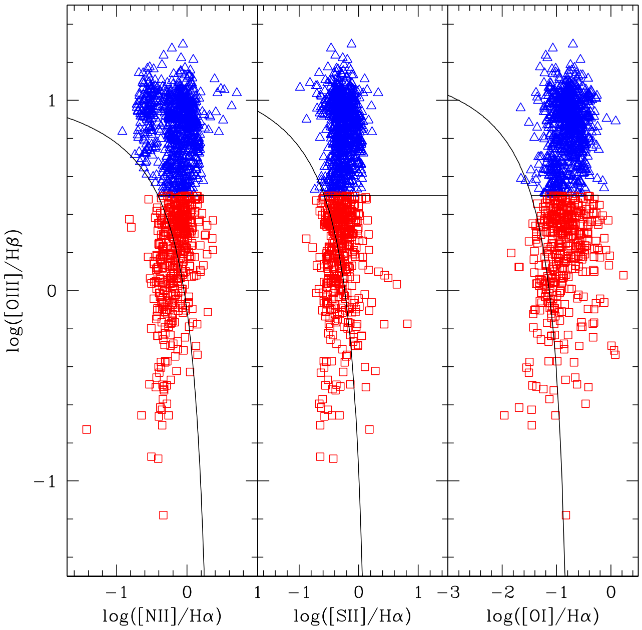

FIGURE 5.2— VO diagnostic diagrams with the regions divided in two samples, the AGN-like regions (blue triangles) and the HII regions+LINERs (red squares). The curves are from Kewley et al. (2006) and the straight line indicates the AGN-LINERs separation.

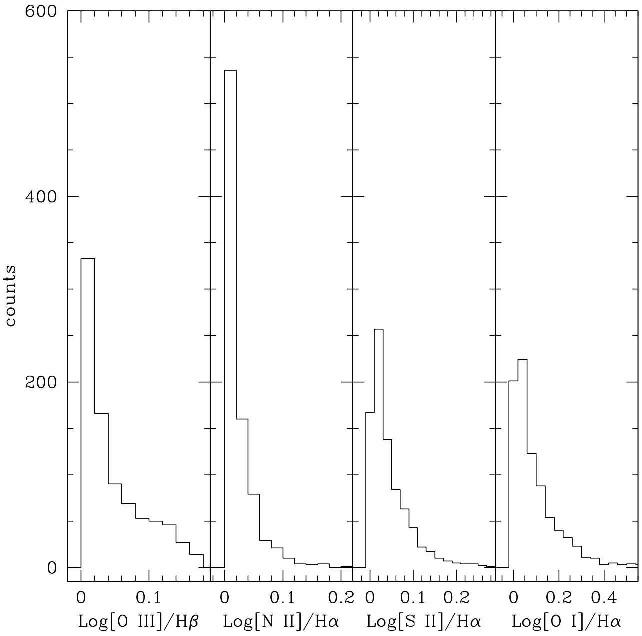

FIGURE 5.3— Histograms of the errors for the VO diagnostic diagrams.

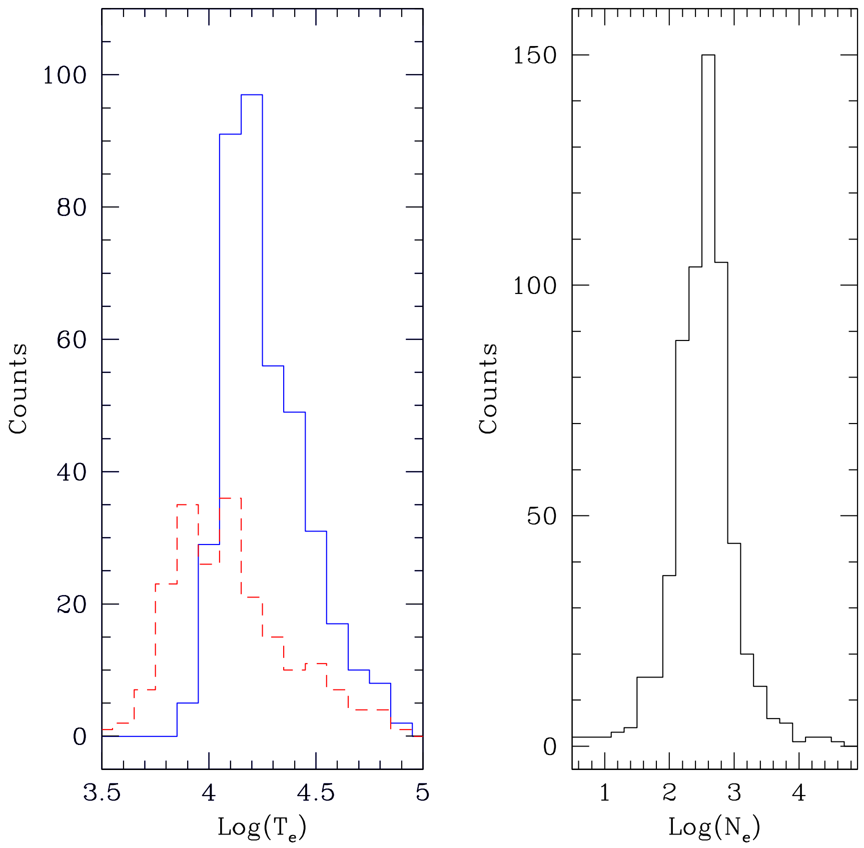

FIGURE 5.4— Histograms of temperature (left) and density (right). The red dashed line indicates [S II] distribution of temperature and the blue solid line identify the [O III] distribution.

spectra. We used TEMDEN, and the values of density calculated with the [S II] ratio, and we found for [S II] and [O III] median values of ~11500 K and ~16500 K, respectively. Their distributions are shown in Figure 5.4, where the red dashed line indicates [S II] distribution and the blue solid line indicates the [O III] distribution. The [S II] temperature varies between 5000 K and 40000 K, while the [O III] determination ranges between 8000 K and 60000 K. As expected, the temperature values obtained from [O III] are higher than the [S II] determinations. In Figure 5.5 we plotted the density and temperature as a function of the distance of each emission line region from its active nucleus. This graph shows that the temperature does not depend on the distance, while we can suggest a rather weak correlation with density: it seems that the density decreases with increasing radius, but the scatter is very large.

By comparing the extinction obtained from STARLIGHT with the A(V) derived by means of Hα/Hβ we studied the dust distribution in the interstellar regions and in the ENLR. We did not find any correlation with radius. Moreover, the extinction in ENLR is higher than in the interstellar medium, as expected. In fact, we can see that the distributions are peaked at different values, larger for the gas: the

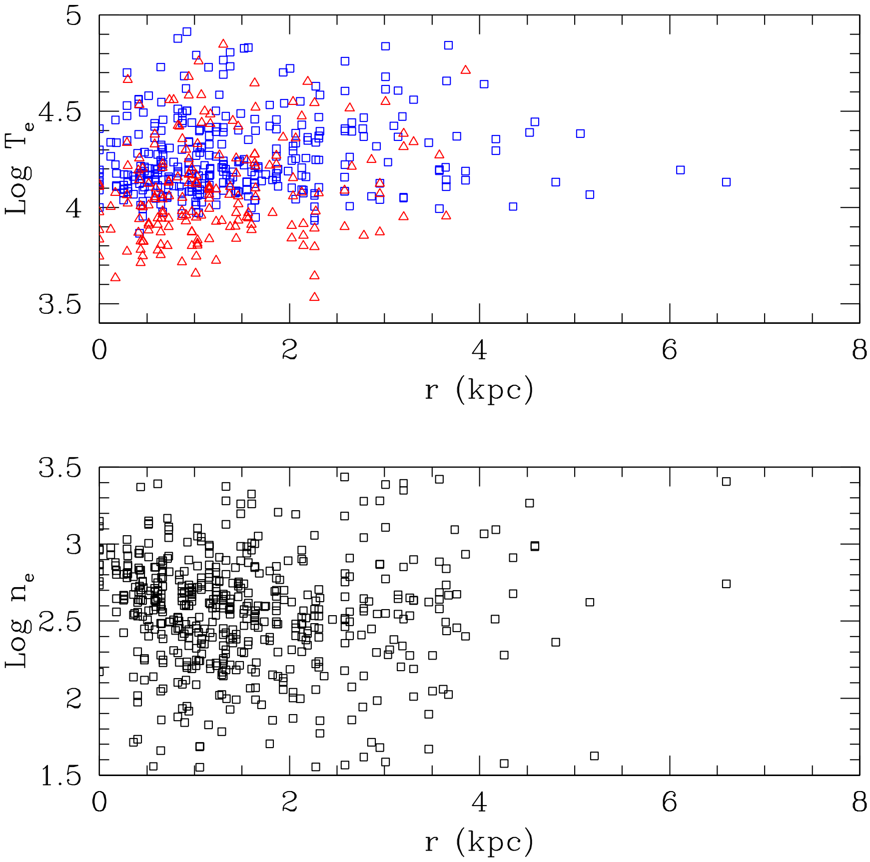

FIGURE 5.5— Radial trend of temperature (top panel) and density (bottom panel). Blue squares are [O III] temperatures, red triangles are [S II] temperatures.

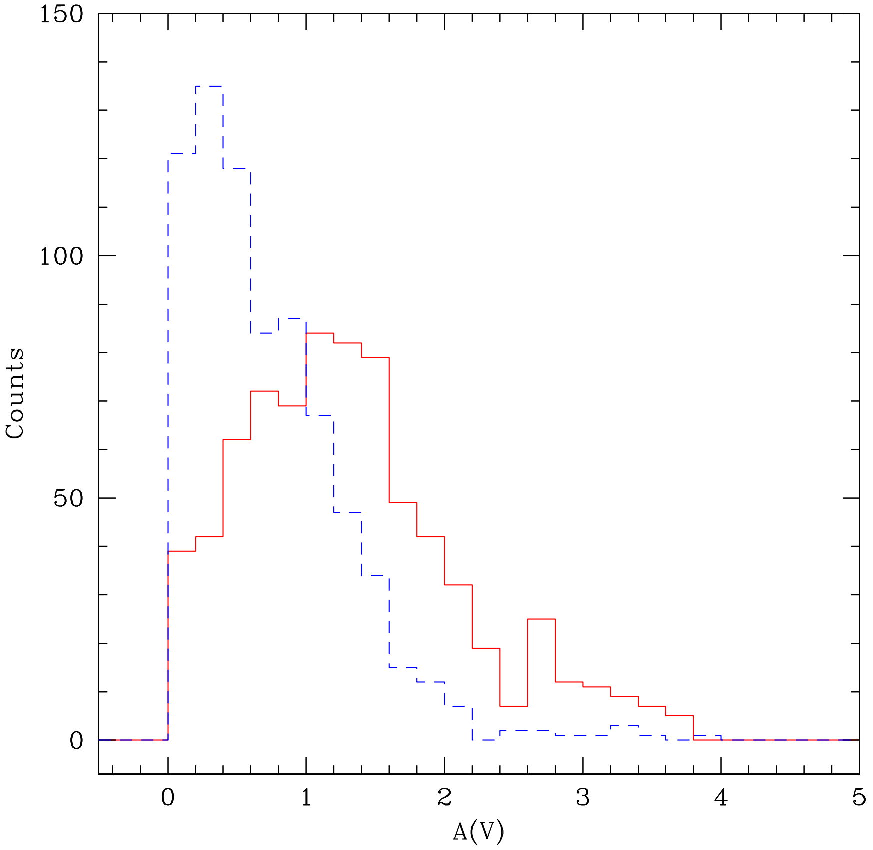

FIGURE 5.6— Histograms of the distribution of the extinction measured from the interstellar dust (blue dashed line) and from the ENLR dust (red solid line).

median value for gas is 1.2 mag and for stars is 0.6 mag (see Figure 5.6). The extinction obtained from the gas is expected to be higher because the observed emission line spectrum is the sum of the stellar component plus the ENLR gas component. There is dust associated to stars, measured by means of STARLIGHT and dust associated to gas. The template-corrected spectrum has not stellar absorptions, but it is still affected by extinction. Therefore the extinction derived from the gas should be higher, as observed. If the ENLR gas was dust-free, than the A(V) measured by stars and gas should be the same.

In case of ionization by a power-law spectrum, as in AGN, the determination of the metallicity is very complicated also because the ionization structure is very complex. There are not direct methods and to determine the metallicity photoionization models must be used. To estimate the gas metallicity, we compared the measured fluxes with values predicted by models from Vaona (PhD thesis 2010), using the emission lines ratios [N II] λ6584/[O II] λ3727 vs [N II] λ6584/[S II] λ6724, being this the best diagram sensitive to the metallicity. The models have a low resolution in metallicity because Vaona used few $Z/Z\odot$ values, nevertheless in Figure 5.7 the trend between super-solar values (red circles) and solar

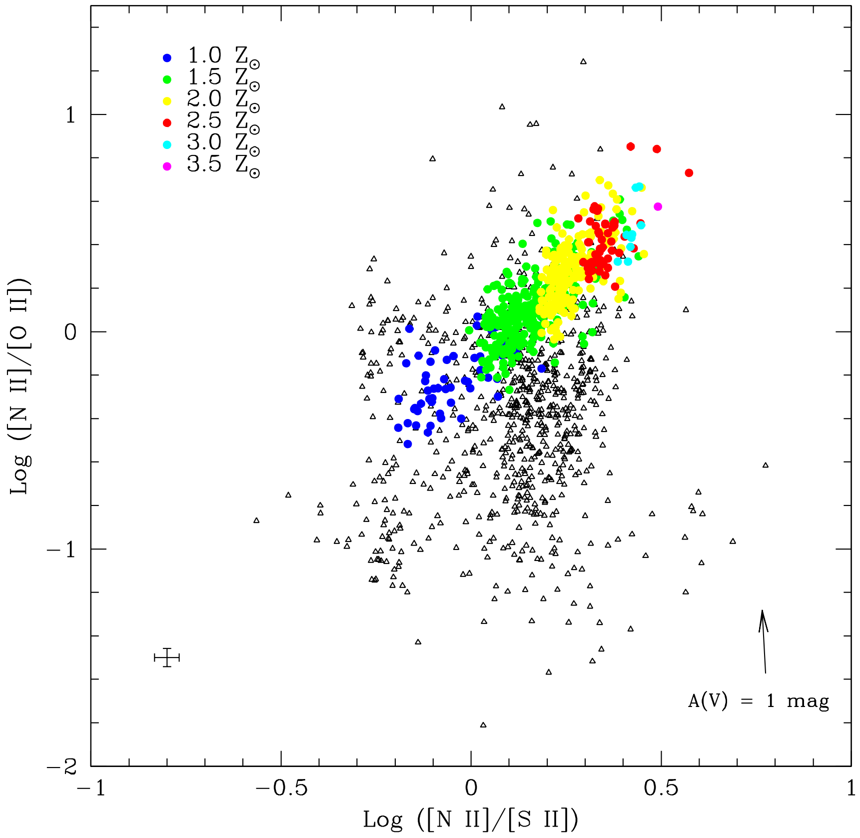

FIGURE 5.7— The graph of the log([N II]/[S II]) versus log([N II]/[O II]) compared with theoretical models by Vaona (2010) with D/G=1. From magenta (Z/Z⊙=3.5) to blue (Z/Z⊙=1) colors, the metallicity decreases. The observed values are black triangles. The arrow indicates the direction and magnitude of the shift due to the extinction correction for A(*V*) = 1 mag.

values (blue cirlces) is clear. We used models with dust-to-gas ratio (D/G) equal to 1. About 33% of the sample matches the models, with metallicity between 1 and 3 times the solar value, while most of the regions do not fit the models. A possible reason of this disagreement between observed data and models is the effect of the decreasing of the S/N ratio as increasing distance from AGN together with the errors due to our determination of the extinction, that affect the [O II] λ3727 more than the other emission lines involved in this diagram. Indeed, we verified that the data with larger scatter have also lower S/N ratio and are more distant from the nucleus. However, we should also build new photoionization models in order to better understand the distribution of the observed data.

STARLIGHT gives as output the percentage of light emitted by each of the 15 stellar populations × 3 different metallicities. For each population we summed the values obtained for the three metallicities and then we divided in three bins: young population, for t = 10^6 – 4 × 10^7 yr; medium population, for t = 10^8 – 1.3 × 10^9 yr; old population, for t = 2.5 × 10^9 – 1.3 × 10^{10}. We calculated the cumulative

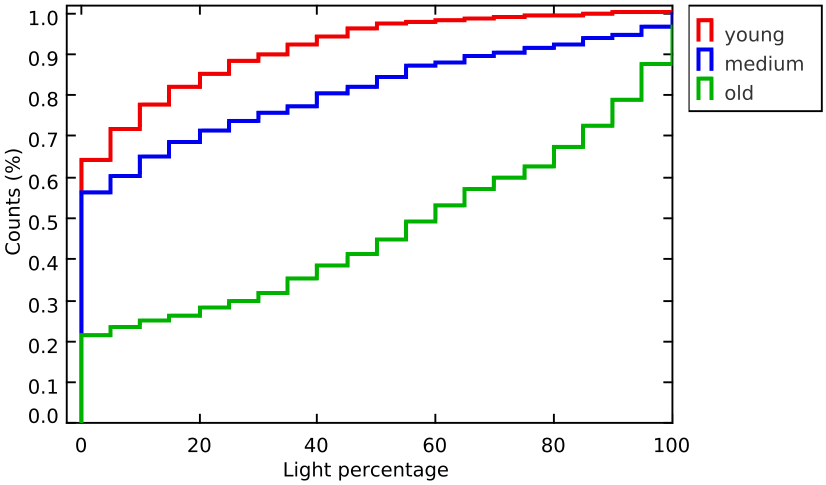

FIGURE 5.8— The cumulative distribution of the percentage of light for young (red), medium (blue) and old (green) stellar populations. See text.

distribution for these three bins and we found the result shown in Figure 5.8. In x-axis we plotted the light percentage emitted by old (green), medium (blue) and young (red) population, while in y-axis the fraction of the sample with a certain contribute from young, medium and old populations. For example, about 70% of the regions are characterized by a young population contributing to less than 10% of the total light, a medium population contributing to less than 20% and an old population contributing to less than 90%. As these are cumulative distributions, we do not expect that the sum of the light percentages corresponding to a certain fraction of the sample is 100%. The similar trends of the cumulative of young and medium populations indicates that in a small fraction of the sample we found a large contribution from young and medium populations. The flatter trend of the cumulative of old populations means that most of the regions show old stellar population.

For each region we calculated its distance in kpc from the active nucleus and we found a distribution peaked at small values (see Figure 5.9). The median is 1.5 kpc and 94% of the regions is at a distance r< 4kpc. This distribution seems to indicate that very extended emission line regions are rare and are present in few objects. Nevertheless we have to take into account that this result could be due to a relatively low S/N of our data that prevents us to detect and study more external fainter regions. In addition, these galaxies are very nearby and this can cause a detection of an ENLR with a small size because even if the emission was be more extended the small f.o.v. could not allow us to detect a large emission. In order to better check if this distribution is real, it is necessary to study Seyfert galaxies with IFU having larger f.o.v. and mounted on large diameter telescopes.

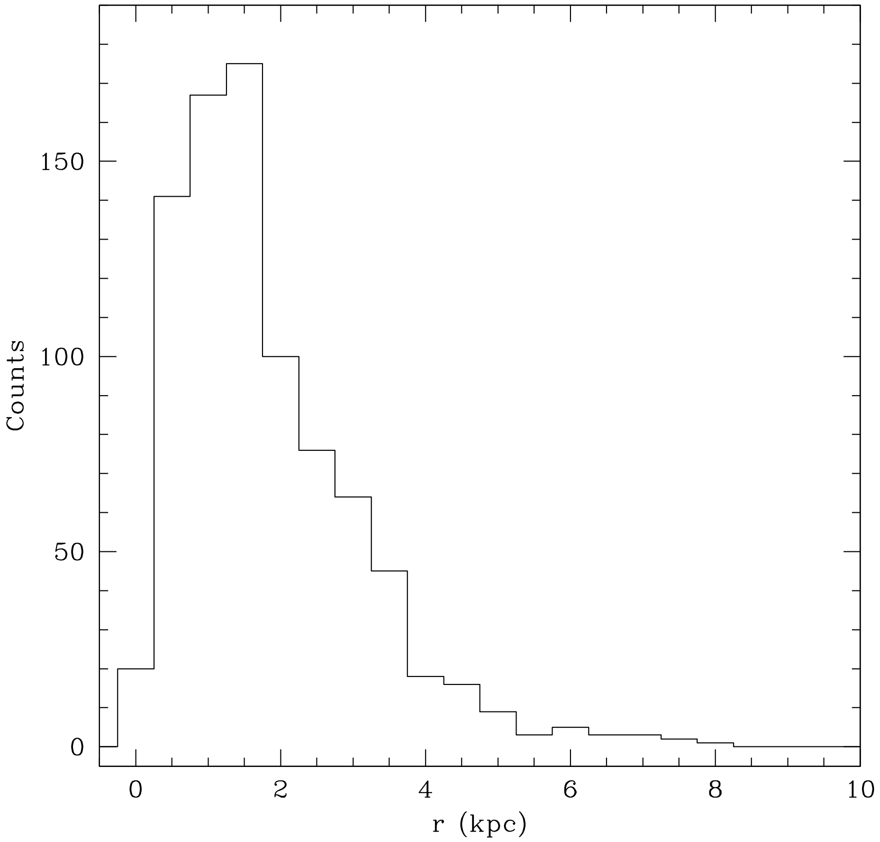

FIGURE 5.9— Histograms of the distance of each regions from its active nucleus.

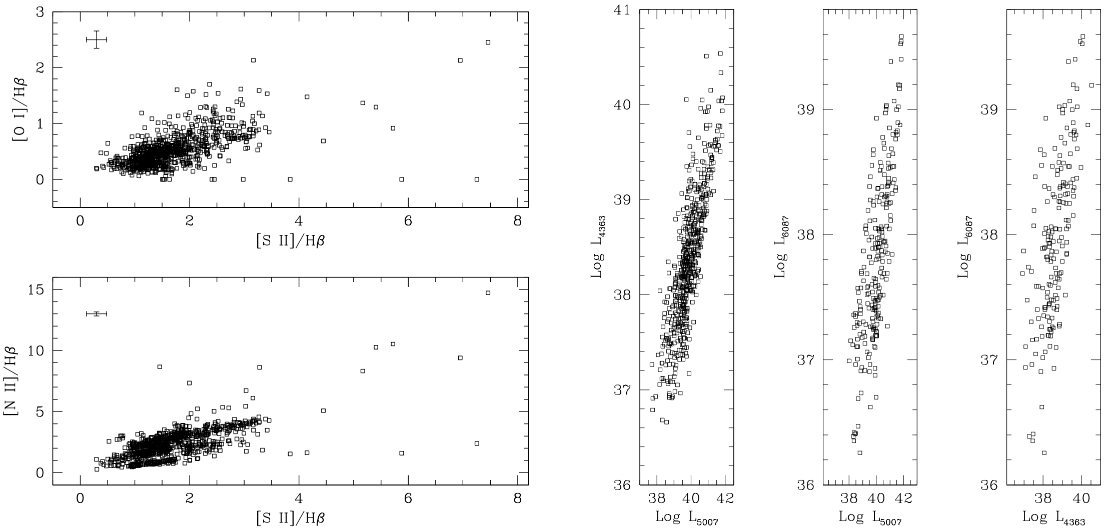

FIGURE 5.10— Left: Koski diagrams for low-ionization lines. [S II]/Hβ vs [O I]/Hβ (top) and [S II]/Hβ vs [N II]/Hβ (bottom). Right: Correlations between the luminosity of high ionization emission lines.

5.3 Emission line properties

We plotted the Koski diagrams (Koski 1978) finding a good correlation for the low ionization emission lines, [S II]/Hβ vs [O I]/Hβ and [S II]/Hβ vs [N II]/Hβ, with a correlation coefficient of 0.7. We found also a trend with the distance: the intensity decreases with increasing radius (Figure 5.10). Being the ionization parameter U depending both on distance and density, we checked if there is a trend with the density but we did not find any correlation. Therefore we can say that the trend with the distance is caused by a decreasing of the ionization degree with increasing radius. We tried to plot also the Koski diagrams for the high ionization lines, [O III]/Hβ vs He II/Hβ, [O III]/Hβ vs [Ar III]/Hβ, [O III]/Hβ vs [Ne III] /Hβ, but we did not find a good correlation, maybe because He II and [Ar III] are faint lines, much fainter than [O III] and are in the blue spectral range where the S/N is lower. However, we found good correlations, plotting the log of the luminosity of high ionization lines, [O III] λ5007 and λ4363, and [Fe VII] λ6087 (see Figure 5.10). The correlation coefficients are equal to 0.83, 0.77 and 0.68, respectively for the log(L_{5007}) vs log(L_{4363}), for log(L_{5007}) vs log(L_{6087}) and for log(L_{4363}) vs log(L_{6087}).

We studied also the distribution of [O III]/Hβ and [O II]/[O III] (see Figure 5.11). The former has a median value of 7.6 and shows very high values, like those observed in the ionization cones (10 – 20), in a small fraction of regions, about 19%. This ratio depends on the ionization degree, but also on the chemical abundances, while the [O II]/[O III] depends only on the ionization parameter (U), but ir is more sensitive to reddening. This ratio is peaked at 0.7, with a small standard deviation (0.7). Within 1σ we found 610 regions (72%) and within 2σ there are 694 regions (82%). While the [O III]/Hβ distribution shows a larger scatter with σ = 2.7 and 545 regions (64%) within 1σ and 808 regions (95%) within 2σ. The median values less than 1 indicates that the ionization degree is high, as expected if the ionizing source is an AGN. The fact that this distribution is peaked with a small spread indicates that a typical

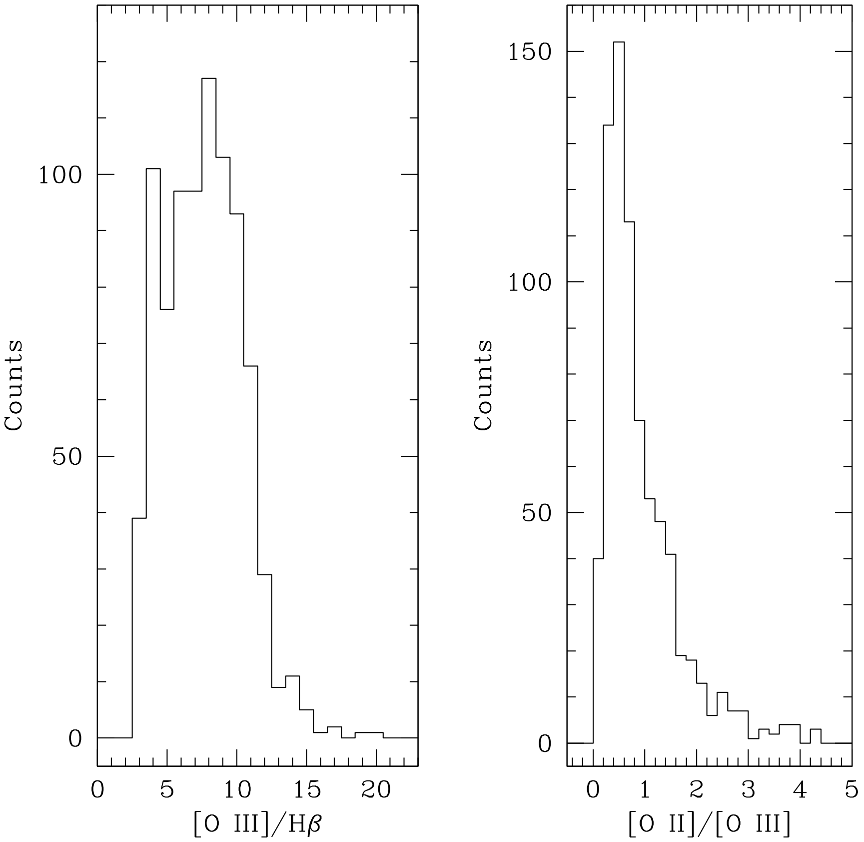

FIGURE 5.11— Histograms of the [O III]/Hβ and [O II]/[O III] ratios.

range of ionization parameters exists and that the spectral shape of the ionizing source for all the objects is similar.

We plotted the [O II]/[O III] ratio as a function of the distance for each galaxy, considering only regions in which S/N([O II]) was > 3 (Figure 5.12). These plots confirm the previous results: most of the regions show values of the ratio between 0 and 2, moreover in most of the cases the ratio keeps constant with radius, except for MRK 348, MRK 1157 and NGC 7319. It keeps constant in galaxies with very extended NLR. [O II]/[O III] is an indicator of the ionization parameter (U) that depends on r^{-2}, thus we should find higher values of the ratio for larger distance. But U depends also on N_e^{-1}. We plotted (Figure 5.5) the density vs the distance, finding a weak trend, with density decreasing as distance increases. In this case, the constant value of [O II]/[O III] can be explained by a density effect, while if the density is not depending on the distance, to justify the constant ratio we need to invoke other mechanisms, for example shocks, that can contribute to photoionization in order to keep high the ionization parameter even at large distance from the nucleus.

By plotting the luminosity of high ionization emission lines ([O III] λ5007, [O III] λ4363 and [Fe

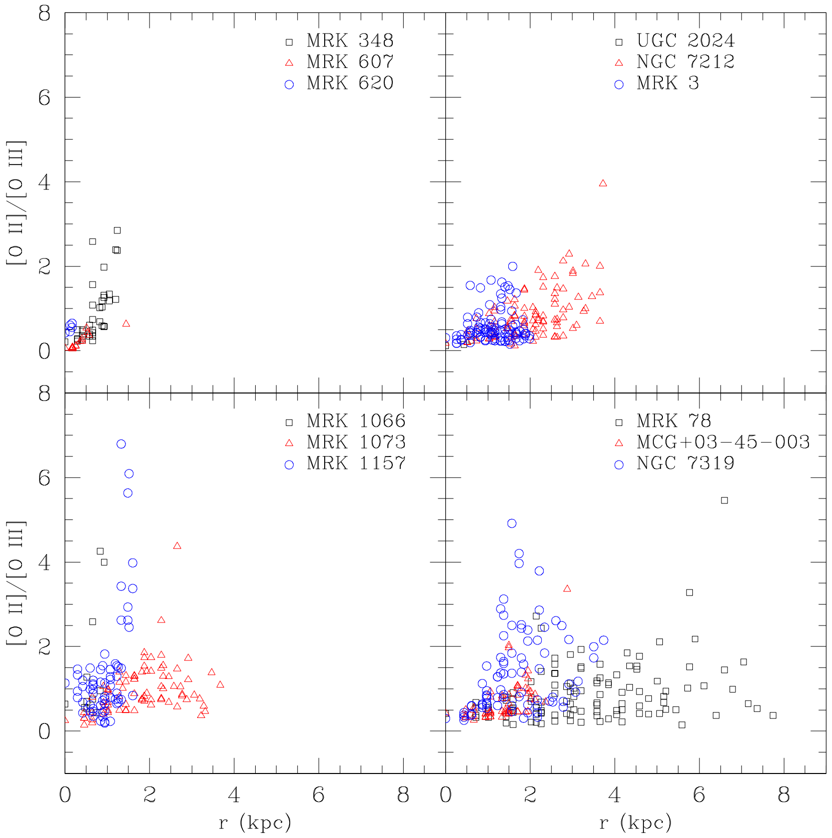

FIGURE 5.12— [O II]/[O III] ratio as a function of the distance from the nucleus for each object in the sample.

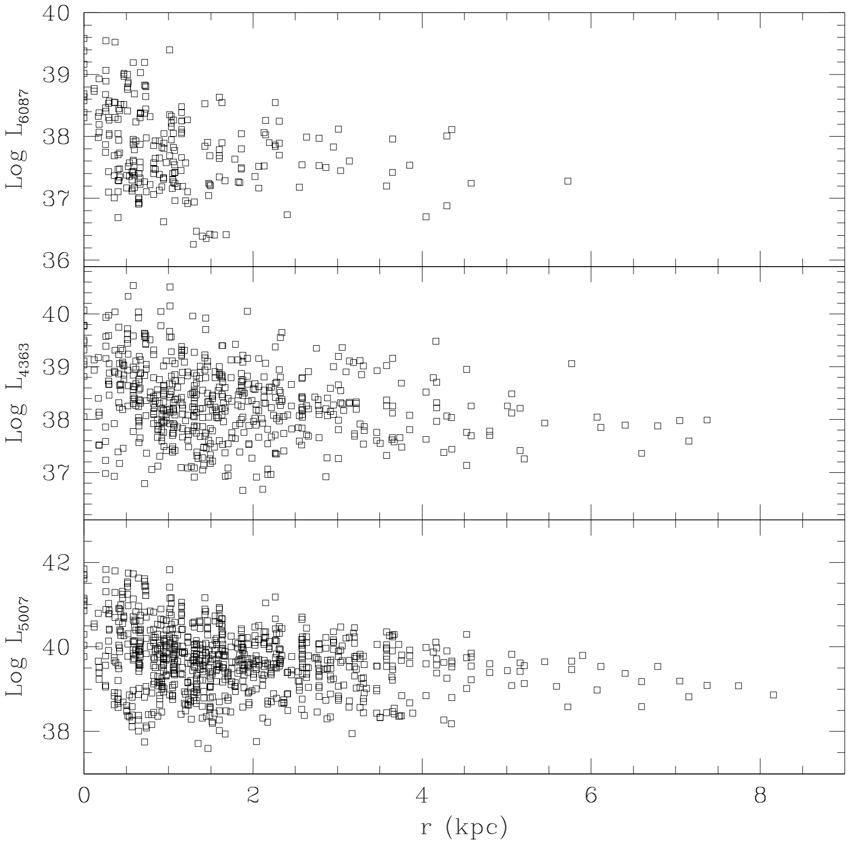

FIGURE 5.13— Luminosity of high ionization emission lines as a function of the distance from the nucleus. Top panel: luminosity of [Fe VII] λ6087; middle panel: luminosity of [O III] λ4363 and bottom panel: luminosity of [O III] λ5007.

VII] λ6087) as a function of the distance from the nucleus (Figure 5.13), we can see a weak trend with a large spread: the luminosity decreases with increasing radius. The values range from 4.0×10^{37} – 6.3×10^{41} erg s^{-1} for [O III] 5007, from 5.0×10^{36} – 3.2×10^{40} erg s^{-1} for [O III] 4363, and from 4.0×10^{36} – 4.0×10^{39} erg s^{-1} for [Fe VII] 6087. The spread is due to the fact that we are plotting sub-regions belonging to different galaxies: each galaxy has its peculiar nuclear luminosity (for example for [O III] λ5007 it is within 6.3×10^{39} – 6.3×10^{41} erg s^{-1}) and a different slope. This can be seen in Figure 5.14 in which the [O III] λ5007 luminosity is plotted against the distance for each object. Here the monotonic decreasing trend with increasing distance is clearly visible ($L_{5007} \propto r^{\alpha}$), even if with different slopes. In some cases, for example NGC 7212, MRK 1073, NGC 7319 and MRK 78 the luminosity keeps high at large distance from the nucleus. The slopes are very different, from -2.2 (MRK 620) to -0.3 (MRK 78), with typically steeper values, < -1 for objects with smaller NLR (MRK 1157, MRK 1066, MRK 620) and flatter values > -1 for objects with more extended NLR (MRK 1073, NGC 7212, MRK 3, MRK 78, MCG+03-45-003, NGC 7319).

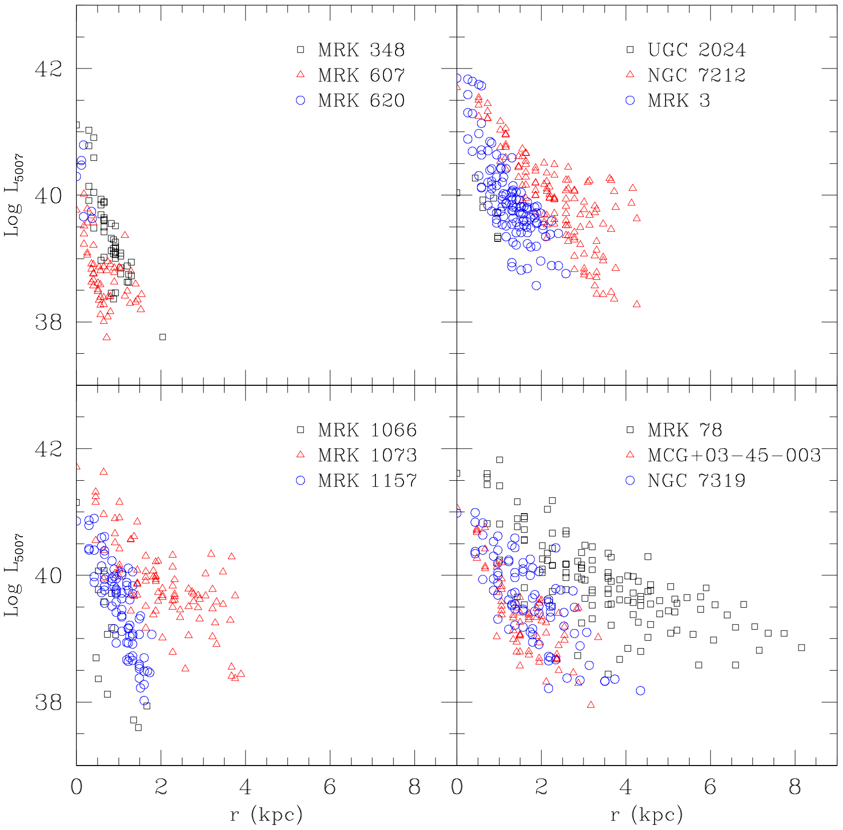

FIGURE 5.14— Luminosity of [O III] λ5007 as a function of distance from the nucleus for each galaxy of our sample.

5.4 Summary of the results

We performed a statistical study of the physical properties of ionized gas in a sample of 12 Seyfert galaxies by analysing their ENLR taking advantage of integral field data. Being the sample heterogeneous and not statistical, we cannot consider our findings as globally valid, nevertheless this work is a useful test to explore the possibility of studying the ENLR properties at large distance from the nucleus and to analyze its physical properties as a function of the distance from the nucleus.

We found typical values for temperature and density of the regions of ionized gas. The latter, measured with [S II] emission lines ranges between 40 and 4000 e^- cm^{-3}, with a median value of ∼ 360 e^- cm^{-3}; the former was measured both with [S II] and [O III] emission lines, obtaining values ranging between 5000 and 40000 K and 8000 and 60000 K, respectively, and median values of 11500 K and 16500 K. As expected (e.g. Vaona, PhD thesis 2010), we found that the dust content in the ENLR is higher than in the interstellar medium, with a median value of A(V) obtained for gas of 1.2 mag and for stars of 0.6 mag. By means of STARLIGHT, we studied the stellar populations and we found in a small fraction of the sample a large contribution from young ($t = 10^6 - 4 \times 10^7$ yr) and medium ($t = 10^8 - 1.3 \times 10^9$ yr) populations, while most of the regions show a significant contribution due to old ($t = 2.5 \times 10^9 - 1.3 \times 10^{10}$ yr) populations. The distribution of the distances from the nucleus of each region is peaked at small values: the median value is 1.5 kpc, with a range between 0.5 kpc and 4 kpc, and 94% of the regions is at distance $r < 4$ kpc. This result seems to suggest that very extended emission line regions are rare, nevertheless more distant and fainter regions in our sample could not be detected because of the relatively low S/N ratio of the data, and a possible bias introduced by the selection of nearby galaxy whose extended emission could not be detectable because of our small f.o.v. In order to better estimate this distribution, we need to use IFU with larger f.o.v., mounted on telescope with larger diameter. From the emission lines analysis, we found good correlation (correlation coefficient of 0.7) between the low ionization emission lines, with also a trend with the distance due to a decreasing of the ionization degree with increasing radius. We found also good correlations, between the luminosity of [O III] λ5007, [O III] λ4363 and [Fe VII] λ6087. The [O II]/[O III] distribution confirms an AGN origin of the ionizing radiation, even if possible additional ionization source, for examples shocks, cannot be excluded. The [O III]/Hβ distribution have a median value of 7.6, but only a small fraction of the regions (∼ 19%) shows high values (10 – 20), typically observed in the ionization cone. Finally the trend of [O III] luminosity with the radius is decreasing, but with different slopes in each object.

6

Conclusions

During the last twenty years several studies with broad-band UBVR and narrow-band interference filters at [O III] $\lambda5007$ and Hα have disclosed blue elongated structures with a conical or bi-conical shape in some Seyfert 2 galaxies. These structures, called ionization cones, are a proof of the validity of the Unified Model, which predicts an anisotropic escaping of photons from the AGN confined in a conical flow by the torus. Up to now, 25 galaxies have been found to show a bright Extended Narrow Line Region (ENLR). There are a a lot of problems concerning this topic that are still open, for example, the small number of ionization cones comparing to the predictions of the Unified Model. It is also important to verify if the ENLR emission is present in all Seyfert galaxies or only in particular galaxy types. Furthermore it is still not clear which is the origin of the ionized gas.

In this work we focused on this last open question. The ENLR gas could be part of the interstellar medium (ISM) of the host galaxy, photoionized by the active nucleus or material ejected by the nucleus in strong interaction with radio-jet, or acquired from intergalactic medium (IGM), or by means of gravitational interactions. This question is strongly related to the mechanisms of AGN feeding. There are not specific researches about this complex topic, but some works on single objects show a connection between extended ionized emissions and merger events (NGC 5252 Morse et al. 1998; MRK 3 Di Mille, PhD Thesis 2007; NGC 4388 Yoshida et al. 2002 and Ciroi et al. 2003; MRK 315 Ciroi et al. 2005). We proposed a possible approach to tackle the complicated issue of the gas origin in the ENLR, by means of a complete and deep analysis of ionized gas spectral properties, kinematics and metallicity. We stress that the most useful method for this science case is the 3D spectroscopy, that allows us to map the elongated emission visible in ionization cones, giving spectrophotometric and kinematical information of extended sources. Longslit spectra and broad band images are useful to complete the analysis and to interpret the results.

We applied this method to two Seyfert galaxies showing elongated [O III] emissions in longslit and narrow band [O III] filters, NGC 7212 a Seyfert 2 galaxy and MRK 6 a Seyfert 1.5 galaxy and we studied the physical and kinematical properties of the circumnuclear gas. We selected the Seyfert 2 NGC 7212 by looking at the HST narrow band [O III] image by Schmitt et al. (2003) and the NTT longslit spectrum by Bennert et al. (2006). The latter found a more extended emission (20″ = 10 kpc, $H_0 = 75$ km s^{-1} Mpc^{-1}) with respect to the narrow band image (5″ = 2.5 kpc). We observed this galaxy, which is in an interacting triplet showing an on-going merger in the N-E region, with MPFS mounted at the SAO 6-mt telescope. By means of the excitation map [O III]/Hβ we pointed out for the first time the presence of an ionization cone in this object with high values of [O III]/Hβ (∼12), oriented NW-SE direction with PA = 150° and an opening angle of ∼70°. The cone is extended 7″= 3.6 kpc in the North direction and 5.5″= 2.8 kpc in the South direction. The ionized gas mass is between 5×10^6 and 3×10^8 $M_\odot$ and the metallicity is sub-solar. The kinematics of gas and stars are decoupled. With high resolution IFU and echelle spectra we found asymmetrical [O III] emission line profiles and gas characterized by multiple kinematical components at different velocities, suggesting the presence of gas in radial motions. The large amount of low metallicity ENLR gas, with a disturbed kinematics, showing radial motions at different velocities has probably an external origin, likely due to gravitational interaction effects. We selected the Seyfert 1.5 MRK 6 by looking at the HST narrow band [O III] image by Schmitt et al. (2003) and the [O III] image by Kukula et al. (1996), then we observed MRK 6 with AFOSC at the 1.8-mt telescope of the Asiago Astrophysical Observatory . The [O III] image by Kukula and our longslit spectra show a very extended emission (up to 32″= 12 kpc) elongated in the N-S direction. We focused on the properties of this extended emission which was observed with MPFS in two different f.o.v., one centred on the nucleus and the other off-centred by 8″ towards North with respect to the nucleus. MRK 6 has a not clearly disturbed morphology, but we pointed out the presence of dust lanes to the North and stellar shells at East and West edges of the galaxy. We measured [O III]/Hβ, finding higher values in the North-West regions (9–11) than in the inner part (5–6), values that confirms a photoionization due to AGN. We obtained a lower limit of the ionized gas mass $M = 3.2 \times 10^6$ $M_\odot$. The kinematics of the highly ionized gas is clearly disturbed, showing a complicated velocity field, with highly negative values and a pattern suggesting a combination of rotation due to the gravitational potential of the galaxy plus a possible spiralling movement. On the contrary the low ionization gas has a kinematics with a more regular behaviour. All the spectrophotometric and kinematical information strongly suggest that the ENLR of MRK 6 could be the result of a minor merger with a gas-rich dwarf galaxy. Additional details can be found in Section 3.7 and Section 4.7. On the basis of these results we propose to carry out a systematic analysis on a larger sample of ENLRs, obtained by looking for extended [O III] emission in Seyfert 2 galaxies at $z \leq 1$. We plan to observe these galaxies with narrow band interference filters. We will select the sample from the work of Vaona (PhD Thesis, 2010). Assuming that the $L_{[OIII]}$ is an index of the power of AGN, we will choose only the objects with $L > 10^{42}$ erg/s from the 2153 Vaona's Seyfert 2 galaxies, obtaining a sample of 84 targets, 11 with $0.02 < z < 0.055$ and 73 with $0.06 < z < 0.1$. Not many instruments equipped with [O III] narrow band filters are available. A possibility is to use the Wide Field Imager mounted at the 2.2 mt telescope, ESO-La Silla, with [O III] medium band interferential filters #871(516/16),#875 (531/17), 549/16. These filters cover the following spectral ranges: 5050 Å – 5300 Å, 5200 Å – 5450 Å and 5380 Å – 5550 Å and allow to observe the [O III] λ5007 for objects at a redshift between z=0.0085 and z=0.0585 for the first filter, between z=0.0385 and z=0.0885 for the second filter and between z=0.0745 and z=0.1085 for the last one. The spatial scale for this instrument is 0.238″/px. At z=0.05 the scale is ∼ 1 kpc/″ and for z=0.1 the scale is ∼ 2 kpc/″. Assuming a seeing equal to 1″, an ionization cone extended up to 5 kpc is still detectable in a Seyfert at z=0.05, while for more distant galaxies only very extended ionization cones (> 10 kpc) will be visible. Therefore we stress that good seeing conditions are extremly important in order to achieve good results. Once the [O III] survey is concluded, the most promising targets will be observed with integral field spectrographs.

In the third part of this work we performed a statistical study of the physical properties of ionized gas in a sample of 12 Seyfert galaxies by analysing their ENLR taking advantage of integral field data. Being the sample heterogeneous and not statistical, we should consider our findings as a useful test to explore the possibility of studying the ENLR properties at large distance from the nucleus and to analyze its physical properties as a function of the distance from the nucleus. We analyzed the spectral properties of 848 $1'' \times 1''$ regions. These regions show the typical properties of the NLR and are dominated by the AGN photoionization. The median density is of the order of 10^2 cm^{-3} and the median temperature is about $1.0 - 1.5 \times 10^4$ K. The density seems weakly depending on the distance from the nucleus, but this relation must be confirmed. On the contrary, no correlation is found between temperature and the distance from the nucleus. The regions showing high values of the ionization degree, like those observed in the ionization cones, are rare, about one fifth of the sample. The stellar populations of the ENLR subregions are dominated by stars older than 3×10^9 yr, while the contribution of young and medium age populations is in general small. The size of the ENLR seems to be typically smaller than 4 kpc (in radius), but this result could be a combined effect of nearby targets, a limited f.o.v of the spectrographs and a low brightness of the emission lines far from the nucleus. Therefore we propose to select a larger sample of Seyfert 2 galaxies up to redshift 0.05 to be observed with integral field spectrographs having larger f.o.v., like VIMOS at ESO-VLT or WiFes at ANU 2.3-mt telescope. VIMOS allows to sample a f.o.v. of $27'' \times 27''$ with $0.67''$/spaxel, producing 1600 spectra in a wavelength range between 4000 and 11500 Å. Unfortunately, in this case the [O II] λ3727 cannot be observed which prevents the metallicity determination. On the contrary, the image slicer spectrograph WiFes is sensitive also in the blue/near UV range with a f.o.v. $25'' \times 38''$ and spatial sampling of $0.5''$.

In conclusion the results obtained in this work strongly suggest that the small number of Seyfert galaxies with kpc-scale ENLR could be due to the lack of particular conditions, like gravitational interactions between the active galaxy and possible satellite companions. This mechanism is able not only to trigger the activity in the nucleus but also to provide the sufficient amount of material mandatory to form a such extended region of ionized gas.

Appendix

Astronomical Observatory of Padova and Asiago

Vicolo dell'Osservatorio 5, I-35122 Padova, Italy – Phone: +39-049-8293411; Fax: +39-049-8759840

Application for Oberving Time with the 182cm Telescope of Cima Ekar

Publications based on Asiago propietary or archive observations have to give in a footnote on the first page of the article
Based on observations collected at Asiago observatory.

Send proposals to: **proposal@oapd.inaf.it** **PERIOD: May 2007 — Oct 2007**

1. Title (10 words maximum)
SEARCHING FOR IONIZATION CONES IN NEARBY SEYFERT 2 GALAXIES

2. Observing Mode
☒ Visitor
☐ Service

3. Name and address of the Investigators
PI: V. Cracco, Dipartimento di Astronomia, vicolo dell'Osservatorio, 2, Padova, Italia
valentina.cracco@studenti.unipd.it

Co–investigators:
S. Ciroi — Dip. Astronomia, Univ. Padova; F. Di Mille — Dip. Astronomia, Univ. Padova
Observer (name, phone, email):
Observing experinece):

4. Instrument(s) and requested set-up and number of nights

AFOSC 3+3		**ECHELLE**	
Filters:	*Slits:* 1.26,1.69,8.4	*Grat.:*	*Incl.:*
Grisms: 4		*Filter:*	*Slit:*

5. Moon
Dark ☐
Gray ☒
Any ☐

6. Special Requirements

7. Observing period restrictions:

Because of the coordinates of our targets, we ask to restrict the observing time to the August-October months, excluding the following period: August 27th - September 18th.

8. Proposal Category

☒ **Long Term Programme** ☐ **Short Term Programme** ☐ **Target of Opportunity**

9. Description of the proposed programme

Antonucci & Miller (1985, ApJ 297, 621) found for the first time an evidence of the validity of the Active Galactic Nuclei (AGN) unified model thanks to spectropolarimetric observations of the Seyfert 2 NGC 1068. According to this model, an AGN is formed by a central black hole which accretes matter and radiates across much of the electromagnetic spectrum. The black hole is surrounded by the Broad Line Region (BLR) and by the Narrow Line Region (NLR). The first one is formed by clouds of high density and velocity photoionized gas, which emit broad permitted lines, as we can see from spectra of the Seyfert 1 galaxies. The NLR is formed by lower density gas, and it is responsible for the emission of the narrow lines. Around the BLR a torus of gas and dust hides this region in Seyfert 2 galaxies.

Following this model, the AGN spectral classification is only due to different orientations with respect to our line of sight (Antonucci 1993, ARA&A 31, 473; Urry & Padovani 1995, PASP 107, 803).

Ionization cones are one of the most important evidences supporting the AGN unified model. These features are consistent with a dense nuclear gas hiding a strong central ionizing source. In fact, one of the aspects of the unified model is the confinement of the nuclear radiation into a double cone with an opening angle determined by the torus geometry (Pogge 1989, ApJ 345, 730). Indeed, some Seyfert 2 galaxies show their NLRs with a conical or biconical morphology extended up to several kiloparsecs (Pogge 1989; Mulchaey, Wilson & Tsvetanov 1996, ApJS 102, 309; Schmitt et al. 2003, ApJS 148, 327). This particular shape is easy to identify in some cases when we can clearly see sharp-edged bi-cones with a common nuclear apex. But other galaxies show quite compact emission line regions and in some cases the cone is visible only from one side of the nucleus (Wilson & Tsvetanov 1994, AJ 107, 1227). That last case is easily understood geometrically: the obscuring hidden material in the host galaxy may hide part of the emerging cones and the only part visible could be the one that comes from the nearer side of the host galaxies (Pogge 1989).

About the physical processes involved in the ionizing cones we need to investigate more; for example, one of the most important open question concerns the origin of the ionized gas: it can be a part of the host galaxies ISM or material ejected by the nucleus in strong interactions with the radio-jet, or it may be acquired from outside through gravitational interactions. The origin of the gas is also related to the mechanism of AGN feeding.

We are going to analyze a sample of nearby ($z<0.03$) Seyfert 2 galaxies showing an extended emission, visible through [O III]5007 emission line images. Considering that until now there are only few Seyfert 2 galaxies showing the ionizing cones predicted by the model, we want to increase their number looking for the presence of new ionizing cones in our sample of galaxies with extended emission. To this aim, we will try to position the slit along the direction of the extended emission, and we will map the flux ratios ([O III]5007/Hβ, [N II]6583/Hα, [O I]6300/Hα and [S II]6716+31/Hα) to identify the ionization mechanism. Later, we are going to analyze in detail the galaxies where we will find ionizing cones, mapping the kinematics of the NLR emission line clouds to understand the origin of the gas, since we expect that different origins of the NLR should affect the kinematics of its ionized clouds.

10. Justification of the requested number of nights and Target informations

We request 6 nights to observe our sample of galaxies (about 10 objects), which have magnitude $m_B \sim 14 - 15$. Considering that our objects are nearby, at $z<0.03$, which corresponds to a scale < 0.6 kpc/arcsec, assuming H_0=75 km sec^{-1} Mpc^{-1}) and a seeing of ~ 2 arcsec, we expect to have a typical resolution < 1 kpc. Such a resolution should be sufficient to map extended ionization cones.

We plan to use the low-resolution grism n. 4, which covers the range of 3500-8500 Å, and we need typical exposure times of 1–2 hrs for each object. During the night, we also need to observe spectrophotometric standard stars to perform flux calibration.

11. Description of the results from previous observations and list of recent publications

---

Asiago LaTeX style file v2.5 March 2007.

```
                LARGE TELESCOPE  TIME REQUEST

dead line
1st half year (Jan. 1 −Juny 30)   IId half year (July 1 − Dec.31)
September 10                      March 1

-----------------------------------------------------------------------------
Request ......     2009   1st  half year     6m  telescope
Received.......
-----------------------------------------------------------------------------
1. Program title:

   Exploring the physical properties of ionization cones in nearby Seyfert 2
   galaxies

-----------------------------------------------------------------------------
2. Brief statement of the program:

Several emission line imaging surveys of Seyfert galaxies, which are the
nearest and hence the most thoroughly studied AGNs, have shown some cases of
Seyfert 2 whose Narrow−Line Regions (NLRs) have just a conical and/or biconical
morphology. One of the open questions is the origin of the ionized gas of the
NLR. It is not yet clear whether this gas is simply part of the host galaxy
ISM photoionized by the active nucleus, or it is material ejected by the
nucleus itself in strong interaction with the radio−jet, or it is material
acquired from outside through gravitational interactions with companion
galaxies. These questions are strongly related to the mechanisms of AGN feeding.
We propose to take advantage of the integral−field spectroscopy to perform
two−dimensional observations of some nearby Seyfert 2 galaxies with known
ionization cones or at least extended highly ionized gas in order to map the
kinematics and flux ratios of the emission clouds populating the NLR of these
AGNs. Through the analysis of these data we expect significantly contribute to
the general understanding of the ionization cone nature and in particular to
the above mentioned open questions.

-----------------------------------------------------------------------------
3. Principal investigator:

   S. Ciroi, Department of Astronomy, University of Padova, Italy
-----------------------------------------------------------------------------
4. Co−investigators:(Dpt. Astronomy Padova, Italy)

   P. Rafanelli, Department of Astronomy, University of Padova, Italy
   S.N. Dodonov, Special Astrophysical Observatory, Russia
   V.L. Afanasiev, Special Astrophysical Observatory, Russia
   F. Di Mille, Department of Astronomy, University of Padova, Italy
   G. La Mura, Department of Astronomy, University of Padova, Italy
   V. Cracco, Department of Astronomy, University of Padova, Italy

-----------------------------------------------------------------------------
5. Request status: long−term program
-----------------------------------------------------------------------------
6. Number of nights (hours): 4 nights    Lunar phases: gray
periods (months) of observations:
Program type:   principal program, may be combined with other programs
Observing conditions (seeing etc.):   GOOD SEEING  (<2")
----------------------------------------------------------------------------
7. Mode of observations
focus: prime focus
optical equipment: MPFS+SCORPIO

spectral range:  3500 − 7500 A
```

spectral resolution: 4 A
required S/N or exposures: exposure time 2–4 hrs per target
recording system: CCD
additional requirements:

---

8. Scientific justification:

A. Scientific Rationale:

During the last two decades since the seminal paper by Antonucci & Miller (1985, ApJ 297, 621), who obtained the first evidence of the validity of the Active Galactic Nuclei (AGN) unified model with spectropolarimetric observations of the Seyfert 2 prototype NGC 1068, numerous authors have published relevant works on this important topic making use of both photometric and spectroscopic data in different wavelength bands. So at the present, the approximate structure of an AGN is known: a central supermassive black hole accreting matter is the ultimate source of the AGN luminosity, producing a large amount of high energy photons, which ionize spatially extended regions of gaseous clouds, named Broad Line Region (BLR) and Narrow Line Region (NLR). A thick dusty torus around the BLR hides it from our view when we observe the AGN along some line–of–sights. Therefore, the AGN type spectral classification is essentially depending on the orientation of the AGN (Antonucci 1993, ARA&A 31, 473; Urry & Padovani 1995, PASP 107, 803).

In fact, the situation is more complicated and until now not completely understood. One of the aspects of the unified model is the confinement of the nuclear radiation into a double cone with an opening angle determined by the torus geometry (Pogge 1989, ApJ 345, 730). Indeed, several emission line imaging surveys of Seyfert galaxies, which are the nearest and hence the most thoroughly studied AGN, have shown some cases of Seyfert 2 whose NLRs have just a conical and/or biconical morphology (see e.g. Pogge 1989; Storchi–Bergmann et al. 1992, ApJ 396, 45; Mulchaey, Wilson & Tsvetanov 1996, ApJS 102, 309; Schmitt et al. 2003, ApJS 148, 327).

The definition of an ionization cone, although clear in principle, is difficult to quantify. In some cases, sharp–edged bi–cones with a common nuclear apex are immediately obvious and striking. In other cases, the emission line gas may be quite compact and/or the cone may be seen on only one side of the nucleus (Wilson & Tsvetanov 1994, AJ 107, 1227).

The appearence of one–sided cones is easily understood geometrically. Given the large amounts of obscuring material that might be present in the host galaxy mid–planes, only the sides of the cones emerging more or less toward us from the near side of the host galaxies should be visible (Pogge 1989).

One of the open questions is the origin of the ionized gas. It is not yet clear whether this gas is simply part of the host galaxy ISM photoionized by the active nucleus, or it is material ejected by the nucleus itself in strong interaction with the radio–jet, or it is material acquired from outside through gravitational interactions with companion galaxies. These questions are strongly related to the mechanisms of AGN feeding.

The different origin of the NLR should affect the kinematics of its ionized clouds : in the first case the kinematics of the ionization cones should be dominated by rotational velocity driven by the gravitational potential of the host galaxy, while in the second and third cases the inflow/outflow processes should generate one or more significant nonrotational components.

Mrk 573, for example, shows an extended NLR (larger than 4 kpc) whose external side follows a smooth velocity field with very narrow emission lines, while the internal side is characterized by very disturbed kinematics with much broader emission lines especially in the areas where the radio ejecta lobes are located (Ferruit et al. 1999, MNRAS 309,1, and references therein).

Other famous AGN with large bright ionization cones have been spectroscopically observed. In a recent paper, Bennert et al. (2006, A&A 456, 953) carried out a deep analysis of the physical conditions within the NLR of few nearby Seyfert 2 galaxies, finding in some cases emission lines with asymmetric profiles, like blue or red wings, visible for several arcsec from the active nucleus, and believed to be originated by jet/NLR clouds interactions. The authors stressed that they had spectra with too low resolution (450−770 km/s) to perform a detailed study of the emission line profiles, and indeed their kinematic analysis showed essentially large scale velocity gradients suggestive of rotation.

A clear radio−jet/NLR association in the nucleus of Mrk 3 was shown by Capetti et al. (1995, ApJ 448, 600) with HST data. They proposed a scenario where the ionized gas is compressed by the shocks created by the passage of the supersonic jet, and supported this picture showing emission lines with broad (FWHM ~ 1200 km/s) and double−peaked profiles. Indeed, non−circular motions are also visible in a more extended NLR up to ~ 3 kpc from the center, both with low−resolution integral−field spectra (~ 500 km/s) and with high resolution long−slit spectra (~ 40 km/s), by means of which at least three independent components could be fit to the [O III]5007 lines (Di Mille et al. 2005, Mem. SAIt Suppl. 7, 38; Di Mille et al. 2007, in preparation).

Fabry−Perot observations of NGC 4388 revealed the presence of a bipolar outflow in the ionization cones (Veilleux et al. 1999, ApJ 520, 111). Indeed, Ciroi et al. (2003, A&A 400, 859) showed that its South−West cone is characterized by a mixture of low density colliding clouds and that the high ionization observed in the outer edges can be explained by a combination of photoionization and shock. Finally, Ciroi et al. (2005, MNRAS 360, 253) detected in Mrk 315 an extended region (up to 7 kpc) of highly ionized and collimated gas moving radially at high velocity (~ 500 km/s) with respect to the rotation of the galaxy and producing clear effects of gas compression and shock ionization.

B. Scientific aim:

On the basis of our experience, we plan to carry out an integral−field spectroscopic study of few nearby Seyfert 2 galaxies (z < 0.03) with known ionization cones, taking adavantage of the MultiPupil Fiber Spectrograph.
The targets have been extracted from the literature looking at [O III] emission line images obtained both from the ground and from space.
In particular, we used the HST snapshot survey by Schmitt et al. (2003, ApJS, 148, 327) selecting the objects showing elongated [O III] emission. We stress that in several cases the NLR size seems small and in principle not suitable for groundbased observations, but it must be taken into account that this survey is very shallow, as it is easily verifiable by comparing the [O III] map of the ionization cone in NGC4388, extended up to 5−6 arcsec from the nucleus, with our integral−field data where the cone appears extended more than 10 arcsec (Ciroi et al. 2003, A&A 400, 859). We believe that deep observations will help to investigate NLRs with a good spatial sampling, and a relatively reduced smoothing effect caused by the atmospheric seeing.

Our aim is to carry out a detailed exploration of the physical processes at work within the ionization cones, avoiding bias effects produced by long−slit alignments and compensating atmospheric refraction.
The strategy of the project will be to observe the targets with the maximum spectral resolution achievable with MPFS (~ 4 A). Two grating positions will be necessary to cover the entire spectral range (3500−7500 A) and for each position

we will apply relatively long exposure times (1−2 hrs) in order to obtain information with good S/N ratio both for emission lines but also for continuum.
Then, the emission line profiles will be carefully analyzed, measuring peak positions, FWHMs and fluxes. When possible, we will try to detect and separate different kinematic components, and to recontruct and model their velocity fields to point out the presence and the spatial distribution of non−circular motions. The kinematics of the gaseous component will be compared with the stellar kinematics to try to understand the origin of the ionized gas.
A higher spectral resolution can be reached with Fabry−Perot interferometer, but integral−field spectroscopy is more effective in our case,

since we want to cover a large spectral range including the brightest AGN emission lines, like H−beta, [O III]4959,5007, H−alpha, [N II]6548,6583 and [S II]6716,6731. In case of targets particularly intersting or strongly difficult to study, we will apply later for observations with FP.

We intend to calculate the H−alpha/H−beta emission line ratios to estimate the internal reddening and the diagnostic ratios [O III]/H−beta, [N II]/H−alpha,

and [S II]/H−alpha to investigate the nature of the ionizing sources through the comparison with models obtained through the application of photoionization and shock codes. About this last point, the [O II]3727/[O III]5007 will be fundamental to constrain the shock models. These models will be produced with SUMA code thanks to our strict collaboration with Prof. M. Contini (Tel Aviv University, Israel).

Moreover, we intend to observe the same targets with SCORPIO in imaging mode. The 6−m telescope has already shown us to be able to reveal very faint structures with low surface brightness around the galaxies, like stellar shells or filaments (see e.g. Ciroi et al. 2005, MNRAS 360, 253). Therefore, it is mandatory not to be limited by the field−of−view of MPFS centered on the active nucleus, but to collect deep information about the whole structure of the host galaxy and its environment, especially in case of interactive systems.

This would help to sustain new hypotheses about the extragalactic origin of the ionized gas within the cones.

Bibliography

Afanasiev V. L., Dodonov S. N., Moiseev A. V., 2001, sdcm.conf, 103

Aller L. H., 1984, ASSL, 112

Allington-Smith J. R., Content R., Dubbeldam C. M., Robertson D. J., Preuss W., 2006, MNRAS, 371, 380

Allington-Smith J., Content R., 1998, PASP, 110, 1216

Allington-Smith J., et al., 2002, PASP, 114, 892

Allington-Smith J. R., Content R., Haynes R., Lewis I. J., 1997, SPIE, 2871, 1284

Allington-Smith J. R., Dubbeldam C. M., Content R., Dunlop C. J., Robertson D. J., Elias J., Rodgers B., Turner J. E., 2004, SPIE, 5492, 701

Antonucci R. R. J., Miller J. S., 1985, ApJ, 297, 621

Antonucci R., 1993, ARA&A, 31, 473

Arribas S., Mediavilla E., Rasilla J. L., 1991, ApJ, 369, 260

Aspin C., et al., 2009, AJ, 137, 431

Böker T., Falcón-Barroso J., Schinnerer E., Knapen J. H., Ryder S., 2008, AJ, 135, 479

Bacon R., 1995, ASPC, 71, 239

Bacon R., et al., 1995, A&AS, 113, 347

Bacon R., et al., 2001, MNRAS, 326, 23

Bacon R., et al., 2004, SPIE, 5492, 1145

Baldwin J. A., Phillips M. M., Terlevich R., 1981, PASP, 93, 5

Baldwin J. A., Wilson A. S., Whittle M., 1987, ApJ, 319, 84

Barbosa F. K. B., Storchi-Bergmann T., Cid Fernandes R., Winge C., Schmitt H., 2006, MNRAS, 371, 170

Barden S. C., Wade R. A., 1988, ASPC, 3, 113

Baum S. A., O'Dea C. P., Dallacassa D., de Bruyn A. G., Pedlar A., 1993, ApJ, 419, 553

Begeman K. G., 1989, A&A, 223, 47

Bennert N., Jungwiert B., Komossa S., Haas M., Chini R., 2006, A&A, 456, 953

Bertola F., Bettoni D., Danziger J., Sadler E., Sparke L., de Zeeuw T., 1991, ApJ, 373, 369

Bianchi S., Guainazzi M., Chiaberge M., 2006, A&A, 448, 499

Bicknell G. V., Dopita M. A., Tsvetanov Z. I., Sutherland R. S., 1998, ApJ, 495, 680

Bland-Hawthorn J., McGrath A. J., Saunders W., Haynes R., Gillingham P., 2004, SPIE, 5492, 242

Boller T., Brandt W. N., Fink H., 1996, A&A, 305, 53

Bonnet H., et al., 2004, Msngr, 117, 17

Bower G., Wilson A., Morse J. A., Gelderman R., Whittle M., Mulchaey J., 1995, ApJ, 454, 106

Bower G. A., Wilson A. S., Mulchaey J. S., Miley G. K., Heckman T. M., Krolik J. H., 1994, AJ, 107, 1686

Bower R. G., et al., 2004, MNRAS, 351, 63

Burstein D., Heiles C., 1978, ApJ, 225, 40

Capetti A., Axon D. J., Macchetto F., Sparks W. B., Boksenberg A., 1996, ApJ, 469, 554

Capetti A., Macchetto F., Sparks W. B., Boksenberg A., 1994, ApJ, 421, 87

Cardelli J. A., Clayton G. C., Mathis J. S., 1989, ApJ, 345, 245

Carter D., 1978, MNRAS, 182, 797

Christensen L., Jahnke K., Wisotzki L., Sánchez S. F., Exter K., Roth M. M., 2006, A&A, 452, 869

Cid Fernandes R., Asari N. V., Sodré L., Stasińska G., Mateus A., Torres-Papaqui J. P., Schoenell W., 2007, MNRAS, 375, L16

Cid Fernandes R., Mateus A., Sodré L., Stasińska G., Gomes J. M., 2005, MNRAS, 358, 363

Ciroi S., Afanasiev V. L., Moiseev A. V., Botte V., Di Mille F., Dodonov S. N., Rafanelli P., Smirnova A. A., 2005, MNRAS, 360, 253

Ciroi S., Contini M., Rafanelli P., Richter G. M., 2003, A&A, 400, 859

Content R., 2006, NewAR, 50, 267

Content R., 1998, SPIE, 3354, 187

Corsini E. M., et al., 1999, A&A, 342, 671

Courtes G., 1982, ASSL, 92, 123

Covone G., Adami C., Durret F., Kneib J.-P., Lima Neto G. B., Slezak E., 2006, A&A, 460, 381

Davidge T. J., Beck T. L., McGregor P. J., 2008, ApJ, 677, 238

de Bruyn A. G., Wilson A. S., 1978, A&A, 64, 433

Dopita M., Hart J., McGregor P., Oates P., Bloxham G., Jones D., 2007, Ap&SS, 310, 255

Dopita M. A., 1995, Ap&SS, 233, 215

Dopita M. A., Sutherland R. S., 1995, ApJ, 455, 468

Durret F., Warin F., 1990, A&A, 238, 15

Eisenhauer F., et al., 2004, AN, 325, 120

Eisenhauer F., et al., 2003, Msngr, 113, 17

Eisenhauer F., Tecza M., Thatte N., Mengel S., Hofmann R., Genzel R., 2000, ESOC, 57, 292

Eisenhauer F., et al., 2003, SPIE, 4841, 1548

Emsellem E., et al., 2004, MNRAS, 352, 721

Evans I. N., Ford H. C., Kinney A. L., Antonucci R. R. J., Armus L., Caganoff S., 1991, ApJ, 369, L27

Evans I. N., Tsvetanov Z., Kriss G. A., Ford H. C., Caganoff S., Koratkar A. P., 1993, ApJ, 417, 82

Förster Schreiber N. M., et al., 2006, ApJ, 645, 1062

Falcke H., Wilson A. S., Simpson C., 1998, ApJ, 502, 199

Falcke H., Wilson A. S., Simpson C., Bower G. A., 1996, ApJ, 470, L31

Feldmeier J. J., Brandt W. N., Elvis M., Fabian A. C., Iwasawa K., Mathur S., 1999, ApJ, 510, 167

Ferruit P., Wilson A. S., Falcke H., Simpson C., Pécontal E., Durret F., 1999, MNRAS, 309, 1

Forman W., Jones C., Cominsky L., Julien P., Murray S., Peters G., Tananbaum H., Giacconi R., 1978, ApJS, 38, 357

Frank J., King A. R., Raine D. J., 1985, apa..book

Fu H., Stockton A., 2007, ApJ, 666, 794

Gallimore J. F., Holloway A. J., Pedlar A., Mundell C. G., 1998, A&A, 333, 13

García-Lorenzo B., Sánchez S. F., Mediavilla E., González-Serrano J. I., Christensen L., 2005, ApJ, 621, 146

Genzel R., et al., 2008, ApJ, 687, 59

Goto T., Kawai A., Shimono A., Sugai H., Yagi M., Hattori T., 2008, MNRAS, 386, 1355

Grossan B. A., 1992, PhDT

Groves B., Kewley L., Kauffmann G., Heckman T., 2006, NewAR, 50, 743

Haniff C. A., Wilson A. S., Ward M. J., 1988, ApJ, 334, 104

Harrison B., Pedlar A., Unger S. W., Burgess P., Graham D. A., Preuss E., 1986, MNRAS, 218, 775

Haynes R., et al., 1999, PASP, 111, 1451

Ho L. C., 2009, ApJ, 699, 638

Inskip K. J., Tadhunter C. N., Dicken D., Holt J., Villar-Martín M., Morganti R., 2007, MNRAS, 382, 95

Iserlohe C., et al., 2004, SPIE, 5492, 1123

Jedrzejewski R. I., 1987, MNRAS, 226, 747

Kenworthy M. A., Parry I. R., Taylor K., 2001, PASP, 113, 215

Kewley L. J., Groves B., Kauffmann G., Heckman T., 2006, MNRAS, 372, 961

Khachikyan É. Y., Weedman D. W., 1971, Ap, 7, 231

Kharb P., O'Dea C. P., Baum S. A., Colbert E. J. M., Xu C., 2006, ApJ, 652, 177

Kinney A. L., Antonucci R. R. J., Ward M. J., Wilson A. S., Whittle M., 1991, ApJ, 377, 100

Komossa S., Schulz H., 1997, A&A, 323, 31

Koski A. T., 1978, ApJ, 223, 56

Kotilainen J. K., 1998, A&AS, 132, 197

Krabbe A., Thatte N. A., Kroker H., Tacconi-Garman L. E., Tecza M., 1997, SPIE, 2871, 1179

Kriss G., Tsvetanov Z., Ford H., Evans I., 1992, AAS, 24, 1257

Kukula M. J., Holloway A. J., Pedlar A., Meaburn J., Lopez J. A., Axon D. J., Schilizzi R. T., Baum S. A., 1996, MNRAS, 280, 1283

López R., García-Lorenzo B., Sánchez S. F., Gómez G., Estalella R., Riera A., 2010, MNRAS, 406, 2193

Larkin J. E., et al., 2003, SPIE, 4841, 1600

Lawrence A., 1987, PASP, 99, 309

Le Fèvre O., et al., 2003, SPIE, 4841, 1670

Lee D., Allington-Smith J. R., Content R., Haynes R., 1998, SPIE, 3355, 810

Madau P., 1988, ApJ, 327, 116

Malkan M. A., Oke J. B., 1983, ApJ, 265, 92

Matteucci F., Padovani P., 1993, ApJ, 419, 485

McDermid R., Bacon R., Adam G., Benn C., Cappellari M., 2004, SPIE, 5492, 822

McGregor P. J., et al., 2003, SPIE, 4841, 1581

Meaburn J., Whitehead M. J., Pedlar A., 1989, MNRAS, 241, 1P

Mediavilla E., et al., 1998, ApJ, 503, L27

Meurs E. J. A., Unger S. W., Pedlar A., Axon D., Whittle M., Ward M. J., 1989, LNP, 334, 103

Morse J. A., Cecil G., Wilson A. S., Tsvetanov Z. I., 1998, ApJ, 505, 159

Morse J. A., Raymond J. C., Wilson A. S., 1996, PASP, 108, 426

Mulchaey J. S., Wilson A. S., Tsvetanov Z., 1996, ApJS, 102, 309

Murphy T. W. Jr, Soifer B. T., Matthews K., Armus L., Neugebauer G., 1999, AAS, 31, 1509

Nagar N. M., Wilson A. S., Mulchaey J. S., Gallimore J. F., 1999, ApJS, 120, 209

Netzer H., 1990, agn..conf, 57

Oliva E., Marconi A., Moorwood A. F. M., 1999, A&A, 342, 87

Osterbrock D. E., Koski A. T., 1976, MNRAS, 176, 61P

Osterbrock D. E., 1989, agna.book

Parry I., 1998, ASPC, 152, 3

Pasquini L., et al., 2000, SPIE, 4008, 129

Pedlar A., Meaburn J., Axon D. J., Unger S. W., Whittle D. M., Meurs E. J. A., Guerrine N., Ward M. J., 1989, MNRAS, 238, 863

Peng C. Y., Ho L. C., Impey C. D., Rix H.-W., 2002, AJ, 124, 266

Pilyugin L. S., Thuan T. X., 2005, ApJ, 631, 231

Pogge R. W., 1989, ApJ, 345, 730

Pych W., 2004, PASP, 116, 148

Raimann D., Storchi-Bergmann T., González Delgado R. M., Cid Fernandes R., Heckman T., Leitherer C., Schmitt H., 2003, MNRAS, 339, 772

Ramsay Howat S., Todd S., Wells M., Hastings P., 2006, NewAR, 50, 351

Relaño M., Monreal-Ibero A., Vílchez J. M., Kennicutt R. C., 2010, MNRAS, 402, 1635

Robinson A., et al., 1994, A&A, 291, 351

Robson I., 1996, agn..book,

Roth M. M., et al., 2005, PASP, 117, 620

Sandin C., Becker T., Roth M. M., Gerssen J., Monreal-Ibero A., Böhm P., Weilbacher P., 2010, A&A, 515, A35

Saunders W., et al., 2004, SPIE, 5492, 389

Schmidt M., Green R. F., 1983, ApJ, 269, 352

Schmitt H. R., Donley J. L., Antonucci R. R. J., Hutchings J. B., Kinney A. L., 2003, ApJS, 148, 327

Schmoll J., Dodsworth G. N., Content R., Allington-Smith J. R., 2004, SPIE, 5492, 624

Sharples R., et al., 2006, SPIE, 6269,

Sharples R. M., et al., 2004, SPIE, 5492, 1179

Sheinis A. I., 2006, SPIE, 6269

Sheinis A. I., Bolte M., Epps H. W., Kibrick R. I., Miller J. S., Radovan M. V., Bigelow B. C., Sutin B. M., 2002, PASP, 114, 851

Smirnova A. A., Gavrilović N., Moiseev A. V., Popović L. Č., Afanasiev V. L., Jovanović P., Dačić M., 2007, MNRAS, 377, 480

Smith J. E., Robinson A., Alexander D. M., Young S., Axon D. J., Corbett E. A., 2004, MNRAS, 350, 140

Stoklasová I., Ferruit P., Emsellem E., Jungwiert B., Pécontal E., Sánchez S. F., 2009, A&A, 500, 1287

Storchi Bergmann T., Pastoriza M. G., 1989, ApJ, 347, 195

Storchi-Bergmann T., Pastoriza M. G., 1990, PASP, 102, 1359

Sugai H., et al., 2004, ApJ, 615, L89

Sugai H., Kawai A., Hattori T., Ozaki S., Kosugi G., Shimono A., Okita Y., 2006, NewAR, 50, 358

Sutherland R. S., Bicknell G. V., Dopita M. A., 1993, ApJ, 414, 510

Tadhunter C., Tsvetanov Z., 1989, Natur, 341, 422

Taylor D., Dyson J. E., Axon D. J., 1992, MNRAS, 255, 351

Tran H. D., 1995, ApJ, 440, 578

Tran H. D., Miller J. S., Kay L. E., 1992, ApJ, 397, 452

Ulvestad J. S., Wilson A. S., 1984, ApJ, 285, 439

Ulvestad J. S., Wilson A. S., Sramek R. A., 1981, ApJ, 247, 419

Unger S. W., Pedlar A., Axon D. J., Whittle M., Meurs E. J. A., Ward M. J., 1987, MNRAS, 228, 671

Urry C. M., Padovani P., 1995, PASP, 107, 803

van Dokkum P. G., 2001, PASP, 113, 1420

Vanderriest C., 1998, ASPC, 152, 123

Vanderriest C., Lemonnier J. P., 1988, igbo.conf, 304

Veilleux S., Bland-Hawthorn J., Cecil G., Tully R. B., Miller S. T., 1999, ApJ, 520, 111

Veilleux S., Cecil G., Bland-Hawthorn J., 2005, ARA&A, 43, 769

Veilleux S., Osterbrock D. E., 1987, ApJS, 63, 295

Viegas-Aldrovandi S. M., Contini M., 1989, ApJ, 339, 689

Vila-Vilaro B., et al., 1995, A&A, 302, 58

Voges W., Gruber R., Haberl F., Kuerster M., Pietsch W., Zimmermann U., 1996, yCat, 9011, 0

Wasilewski A. J., 1981, PASP, 93, 560

Weitzel L., Krabbe A., Kroker H., Thatte N., Tacconi-Garman L. E., Cameron M., Genzel R., 1996, A&AS, 119, 531

Whittle M., 1985, MNRAS, 213, 1

Whittle M., 1985, MNRAS, 213, 33

Whittle M., Haniff C. A., Ward M. J., Meurs E. J. A., Pedlar A., Unger S. W., Axon D. J., Harrison B. A., 1986, MNRAS, 222, 189

Whittle M., Pedlar A., Meurs E. J. A., Unger S. W., Axon D. J., Ward M. J., 1988, ApJ, 326, 125

Whittle M., 1992, ApJ, 387, 121

Wilson A. S., 1988, A&A, 206, 41

Wilson A. S., Braatz J. A., Heckman T. M., Krolik J. H., Miley G. K., 1993, ApJ, 419, L61

Wilson A. S., Heckman T. M., 1985, aagq.conf, 39

Wilson A. S., Tsvetanov Z. I., 1994, AJ, 107, 1227

Wilson A. S., Willis A. G., 1980, ApJ, 240, 429

Wilson A. S., 1996, VA, 40, 63

Wilson A. S., Ward M. J., Haniff C. A., 1988, ApJ, 334, 121

Wisotzki L., Becker T., Christensen L., Jahnke K., Helms A., Kelz A., Roth M. M., Sánchez S. F., 2004, AN, 325, 135

Yoshida M., et al., 2002, ApJ, 567, 118

Acknowledgements

This research has made use of:

- IRAF (Image Reduction and Analysis Facility) *IRAF is distributed by the National Optical Astronomy Observatories, which are operated by the Association of Universities for Research in Astronomy, Inc., under cooperative agreement with the National Science Foundation. (http://iraf.noao.edu/)*
- NED *(NASA/IPAC Extragalactic Database) which is operated by the Jet Propulsion Laboratory, California Institute of Technology, under contract with the National Aeronautics and Space Administration. (http://nedwww.ipac.caltech.edu/)*
- CLOUDY *Calculations were performed with version 06.02 of Cloudy, last described by Ferland et al. (1998). (http://www.nublado.org/)*
- STARLIGHT *The STARLIGHT project is supported by the Brazilian agencies CNPq, CAPES and FAPESP and by the France-Brazil CAPES/Cofecub program. (http://www.starlight.ufsc.br/)*
- TOPCAT (Tool for OPerations on Catalogues And Tables) *The program is available under the GNU General Public Licence. It was initially developed within the now-termined Starlink project in the UK, and was more recently developed and supported by its author as part of the AstroGrid project. Its underlying table processing facilities are provided by STIL (http://www.star.bris.ac.uk/mbt/topcat/)*